2011

Heat Transfer And Friction Augmentation In A Narrow Rectangular Duct With Symmetrical And Non-symmetrical Wedge-shaped Turbulators

Michelle Valentino
University of Central Florida

HEAT TRANSFER AND FRICTION AUGMENTATION IN A NARROW RECTANGULAR DUCT WITH SYMMETRICAL AND NON-SYMMETRICAL WEDGE-SHAPED TURBULATORS

by

MICHELLE VALENTINO
B.S. University of Central Florida, 2010

A thesis submitted in partial fulfillment of the requirements
for the degree of Master of Mechanical Engineering
in the Department Mechanical, Materials, and Aerospace Engineering
in the College of Engineering and Computer Science
at the University of Central Florida
Orlando, Florida

Fall Term
2011

Major Professor Jayanta S. Kapat

ABSTRACT

The need for cleaner and more fuel efficient means to produce electricity is growing steadily. Advancements in cooling technologies contribute to the improvements in turbine efficiency and are used for gas turbines and for power generation in automotive, aviation, as well as in naval applications, and many more. Studies introducing turbulators on walls of internal cooling channels, which can be applied to hot gas components and in recuperative heat exchangers, have been reviewed for their ability to promote heat transfer in the channel while observing pressure loss caused by adding the features. Several types of turbulators have been studied; ribs, pin fins, dimples, wedges, and scales are some examples of features that have been added to walls of internal cooling channels or heat exchangers to increase heat transfer.

This study focuses on two types of wedge turbulator designs, a full symmetrical wedge and a half, or non-symmetrical right-triangular wedge for the purpose of disrupting the thermal boundary layer close to hot walls without causing large-scale mixing and pressure drops. There are two sizes of the wedges, the first set of full and half wedges have an e/Dh=0.10 with the second at e/Dh=0.40, a feature that fills the height of the boundary layer. There are six cases studied, two one-wall and four two-wall cases in a 2:1 aspect ratio channel at Reynolds numbers of 10,000, 20,000, 30,000, and 40,000. Two experimental setups are utilized: a segmented copper block and transient TLC, along with numerical simulation for computational flow visualization. Wall temperature data is collected from all four walls for the copper experimental setup and three walls on the transient TLC setup. The fourth wall of the acrylic test section for

the transient TLC tests is utilized for pressure testing, where static pressure ports are placed along the side wall.

Although the small features did not show large influence in heat transfer on the side walls as much as the larger features or as high of heat transfer on the featured walls, the minimal pressure loss in the channel kept overall thermal performance of the small two wall full wedge features very high. The case of the large half wedge on two walls also showed very high thermal performance, having pressure loss values nearly half of the same sized (length and height) full wedge feature while having the ability to incorporate side walls into the overall heat transfer enhancement. The results found in the experimental setups are supported by the visualization of flow characteristics from the numerical testing. Comparing the initial wedge study to recent full rib studies show the wedges have similar improvements in heat transfer to the full rib cases with friction augmentations 5 to 10 times lower than the full rib cases. Further improvements to wedge heat transfer and pressure drop can be done by determining optimal wedge size and orientation.

ACKNOWLEDGMENTS

Research for this thesis was conducted at the Center for Advanced Turbine and Energy Research, a Laboratory for Gas Turbine Heat Transfer, Aerodynamics, and Durability at the University of Central Florida's Siemens Energy Center under the guidance of Dr. Jayanta S. Kapat. This thesis could not have been written without the guidance and encouragement of Dr. Kapat. I would like to express my sincerest gratitude to him for his time and assistance investing in my future.

A special thanks to my thesis committee members Dr. J. Kapat, Dr. A. Kassab, and Dr. W. Deng for their time, assistance, and advice.

I would also like to acknowledge all my friends and colleagues at the lab for their inspiration, support, advice, and helping me keep my sanity for the past 3 ½ years: Bryan Bernier, Kaylee Dorman, Roberto Claretti, Michael Torrance, Perry Johnson, Josh Bernstein, Matt Golsen, Greg Natsui, Anthony Bravato, Sergio Quintero, and Sri Mahadevan.

I would also like to acknowledge the help and support from Dr. Mark Ricklick, whose constant push to strive for the best was inspirational.

My sincerest thanks goes to Lucky Tran who spent countless hours helping run tests, lending his expertise developing multiple MATLAB codes, and constantly giving encouragement for all my years at the lab.

Furthermore, this thesis could not have been completed without the funding and experience gained from the Laboratory for Turbine Heat Transfer, Aerodynamics, and

Durability at the Center for Advanced Turbine and Energy Research at the University of Central Florida.

Finally, I would like to thank my family. They undoubtedly supported me throughout my entire college career, gave me constant encouragement when I felt overwhelmed and never let me give up. Special thanks to my Mom, Dad, and my sisters Maria and Sarah, and my fiancé Ray, I love you all very much.

TABLE OF CONTENTS

LIST OF FIGURES

LIST OF TABLES

LIST OF ABBREVIATIONS

English Symbols

AR	Aspect Ratio = (H/W)
c	Specific Heat Capacity
D_h	Hydraulic Diameter
e	Height
f	Darcy Friction Factor
f_o	Darcy Friction Factor, Blasius Solution (Baseline)
h	Heat Transfer Coefficient
H	Channel Height
k	Thermal Conductivity; Thousand (i.e. 10k = 10,000)
L,ℓ	Length, Wedge Length
Nu	Nusselt Number = ((h*L)/k)
Nu_o	Nusselt Number from Dittus-Boelter Correlation (Baseline)
P	Pitch; Pixel
P_s	Static Pressure
Pr	Prandtl Number = (υ/α)
U	Fluid Velocity
$W_{channel}$, W	Channel Width, Wedge Width

Greek Symbols

α	Thermal Diffusivity
δ	Dimple Depth
υ	Kinematic Viscosity
ρ	Density
η	Thermal Performance Factor = $(Nu/Nu_o)/((f/f_o)^{1/3})$

Subscripts

o	Baseline Value
P	Constant Pressure

Superscripts

-	Averaged Value

Abbreviations

CFD	Computational Fluid Dynamics
FD	Fully Developed
GT	Gas Turbine
Re, Re_{Dh}	Reynolds Number
SW	Smooth Wall (Baseline)
TLC	Thermochromic Liquid Crystal
VG	Vortex Generator

CHAPTER 1: INTRODUCTION TO GAS TURBINES AND COOLING

Progress for the Future

A constant push for a cleaner, more fuel efficient energy supply to reduce harmful emissions as well as minimize strong dependence on natural gas consumption has been the focus of governmental, industrial, and educational research for many years past and will be for many years to come. Advancements toward improving clean and fuel efficient technologies can be applied to not only land-based power generation in gas turbines, but in smaller microturbines in automotive, aviation, as well as in naval applications, and many more. Applications may be almost limitless; however these progressions must be studied in detail prior to employing them into industrial, commercial, or governmental functions.

(a)

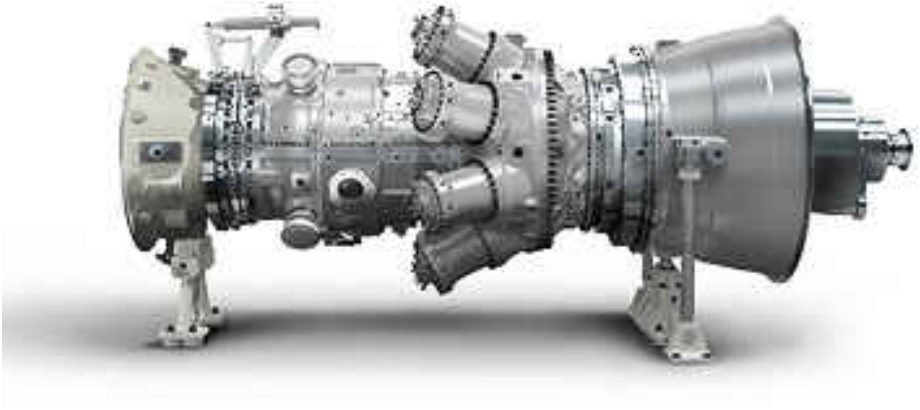

(b)

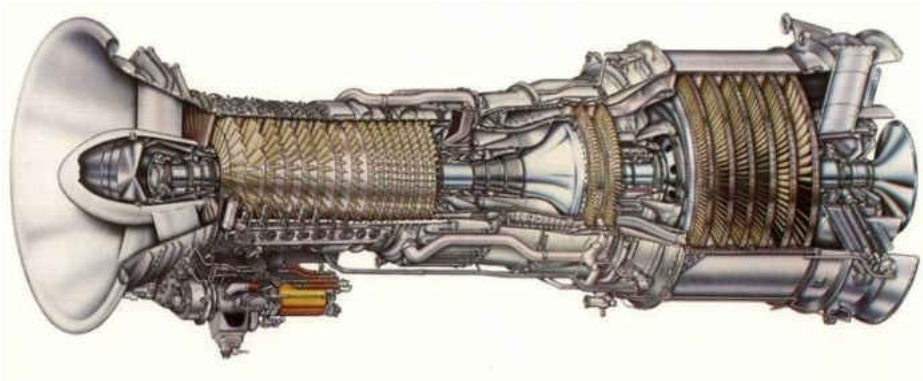

(c)

Figure 1: (a) GEnx Aviation (GE Aviation) (b) Siemens SGT-750 Power (European Petroleum Technology) (c) GE LM2500 Naval (Gas Turbine International, LLC)

Although there is a strong urge for developing sustainable energy as well, improvements upon existing technology may be implemented faster and for a lower initial cost. Returns on green-energy sources such as solar power are not seen for decades and have issues with maintaining constant output. They can be paired with existing fuel powered sources to offset the inconsistencies in output to develop a hybrid energy source, seen in Figure 2 with integrated solar combined cycle (Gas and Steam Turbines). Improvements, then, for the fuel-fed energy sources are still pertinent in

these cases as well, emphasizing the need to progress these technologies for better efficiency.

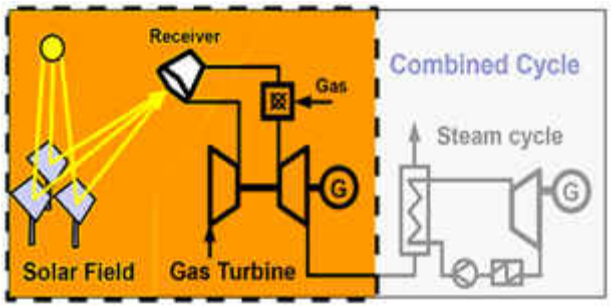

Figure 2: Hybrid Solar GT (& CC) (Solugas)

Figure 2 shows a solar field pre-heating compressor exit air, prior to the combustion chamber. Pre-heating could also be established from incorporating recuperative heat exchangers, which use the waste heat from the hot turbine exhaust to pre-heat the air before combustion.

Gas Turbine Efficiency

Advancements in heat transfer technology for cooling applications in gas turbines are continuously investigated in order to enhance gas turbine efficiency by either allowing for a higher turbine inlet temperature (at 3) or maintaining the same turbine inlet temperature while reducing amount of coolant flow and emissions (and hence fuel consumption in the combustion section) without compromising materials' durability. A gas turbine operates under the Brayton cycle, shown in Figure 3 below. From this figure, you can compare the path of the ideal Brayton cycle, to the actual for which is seen during the operation of a gas turbine, indicated by the prime numbers. From this figure, observe that the actual has increases in entropy, whereas for ideal stages 1-2

and 3-4 would be isentropic. There is also an added pressure loss throughout the system, where ideal shows constant pressure from 2-3. The lower pressure (constant between 4-1) remains constant in the case that the inlet and exhaust are to ambient air.

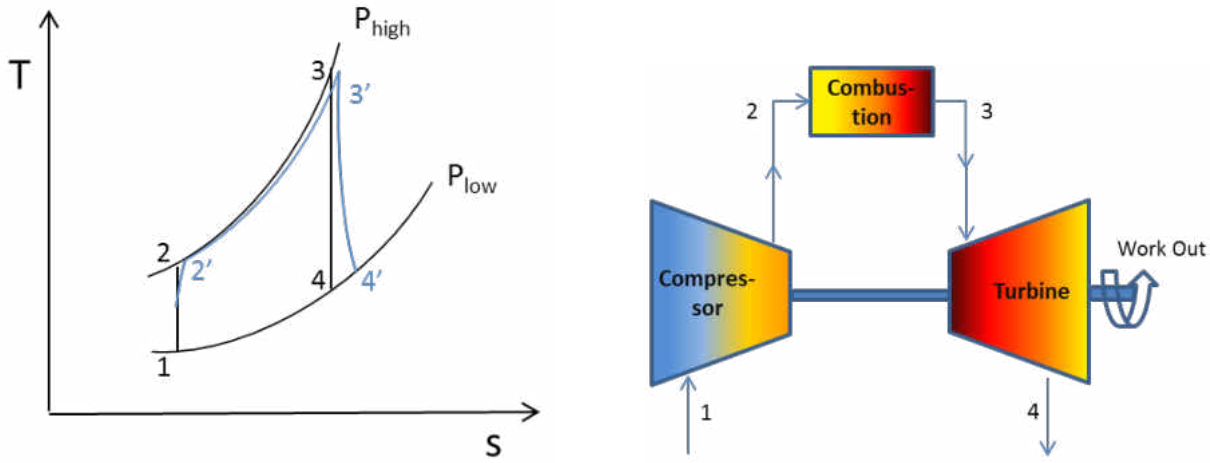

Figure 3: Ideal Brayton Cycle with Actual Deviation (left), GT System (right)

Useful work output occurs between stages 3 and 4. The heat input, in the combustion section, is then obviously between 2-3 in the chart. Any waste heat, then, is what is lost after the turbine section, after 4. The heat and work inputs and outputs are shown in Figure 4 below.

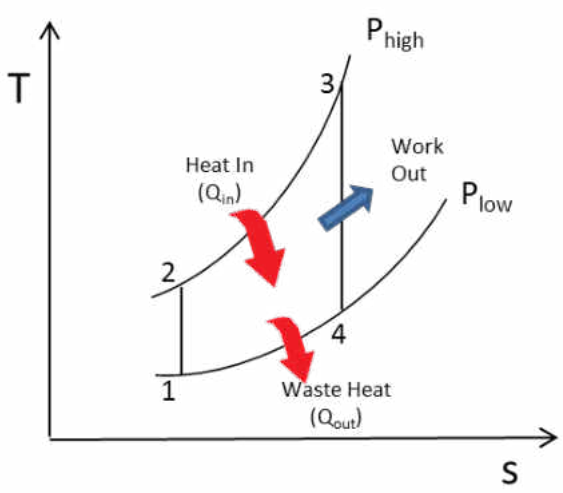

Figure 4: GT Work Output

Efficiency of the ideal Brayton cycle is the ratio of the net work to the heat input.

$$\eta_{th,Brayton} = \frac{w_{net}}{Q_{in}} = 1 - \frac{Q_{out}}{Q_{in}} = 1 - \frac{(T_4 - T_1)}{(T_3 - T_2)} = 1 - \frac{T_1}{T_2} = 1 - \frac{1}{(P_3/P_4)^{(k-1)/k}} \quad (1)$$

Another way of increasing gas turbine efficiency with small scale, or microturbines, is by introducing a recuperative heat exchanger, which uses the waste heat exhaust gas exiting from the turbine stage and pre-heats air entering the combustion section to reduce fuel consumption, shown in Figure 5. Improvements in this section (such as adding transport-enhancing features) can increase the amount of heat transferred from the hot exhaust to the cooler air exiting the compressor.

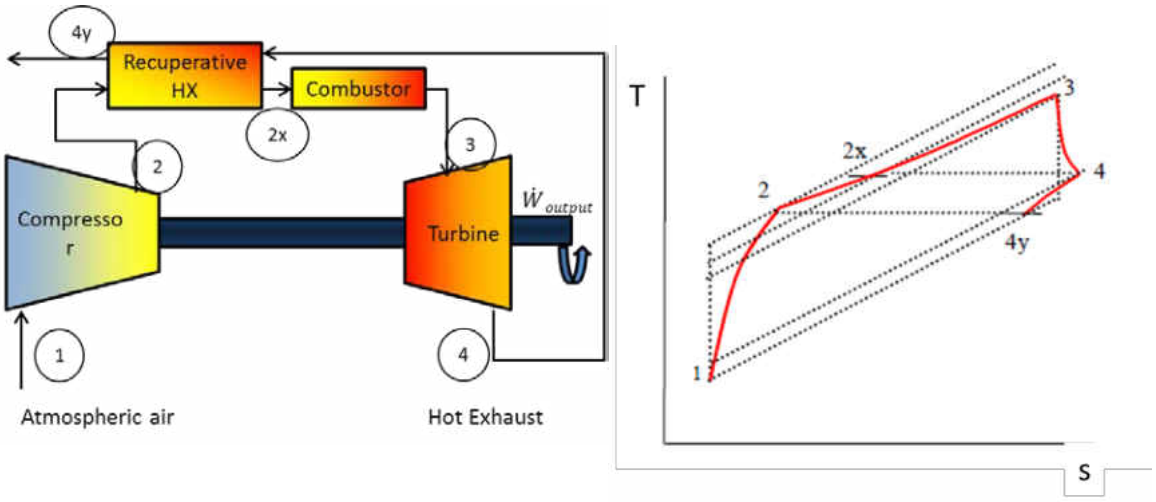

Figure 5: Recuperative Heat Exchanger In GT System (left); Cycle in T-S Diagram (Carman, Kapat, Chow, & An, 2002) (right)

For minimizing coolant flow and maintaining durability of the materials, several types of cooling techniques are studied, including film cooling, impingement cooling, and adding turbulators, or transport enhancing geometries. A variety of geometries have been introduced as surface enhancements for internal cooling channels or increasing heat transfer in heat exchangers; in the channels, the added roughness of the surface geometries break up the laminar sub-layer of the channel flow and promote mixing and secondary flows throughout the channel. Surface enhancements such as ribs, pin fins, swirl chambers, scales, and dimples have all been reviewed for contribution to mixing and secondary flows. Mixing in the channel, however, causes an increase in total pressure loss in the system. A balance between the two is then needed for optimization, observing thermal performance.

Literature Review

Previous studies reviewed in the following sections cover several types of positive, rib and rib-like turbulators for various applications with gas turbines. Emphasis is placed on those studies which contributed to insight for the current paper, where the progression of varying rib geometries led to a wedge-shape turbulator.

Rib Features

Ribs have been reviewed for their ability to disrupt flow and promote mixing throughout the channel. Ribs are positive features that can take up a majority (if not the entire) width of the channel that act to trip the flow, disrupting boundary layer formation and causing the formation of complex vortices and secondary flow patterns. This increased turbulence leads to a greater mixing of the flow and improvement in the advection of heat away from the channel walls. Typically, rib turbulators are rectangular in cross-section. Many other parameters such as approaching and departing angles, orientation angle to flow direction, channel blockage ratio, rib width, and rib spacing (pitch) can be varied such that an optimal design is achieved. A great deal of studies has been devoted to the application of these features to internal channel cooling designs.

In early rib studies, an experiment on the rib angle of attack was conducted by Han et al. who varied the attack angle from 90 degrees to 60, 45, and 30 degrees and investigated pressure drop and average heat transfer in a square duct with two opposite rib roughened walls (Han, Park, & Lei, 1985). Rib height to diameter ratio was kept constant where attack angle and pitch were varied; Reynolds number was varied from 7000 to 90,000. A comparison of thermal performance for the rib orientations concluded

the oblique angles of 45 and 30 degrees was about 10 to 20 percent higher than the rib oriented perpendicular to the flow direction. Han and Park expanded upon this study, testing the combined effect of rib attack angle and channel aspect ratio on local heat transfer coefficient in developing flow. Channel aspect ratio was varied from 1 to 2 to 4 and rib attack angle was varied from 90 to 60 to 45 to 30 degrees with two opposite rib roughened walls and varying Reynolds number between 10,000 and 60,000 (Han & Park, 1988).

In addition to observing effects of rib attack angle on thermal performance, studies followed that investigated effects of varying rib pitch, rib width, rib to diameter height, inlet conditions, arrangement, etc. onto rectangular cross-section ribs. Ligrani and Mahmood studied heat transfer and friction factors in a 4:1 aspect ratio channel of 45 degree angled ribs oriented in a crossed formation on two opposite surfaces (Ligrani & Mahmood, 2003). The study considered Nusselt numbers calculated both with and without three dimensional conduction considered within the test surface and were tested at Reynolds numbers based on channel height ranging from 10,000 to 83,700. The tests agreed, approximately, with other investigators studies for square channels with 45 degree angled ribs. With changes to the rib parameters, Wright and Gohardani investigated the effect of rib width and spacing (pitch) of 45 degree angled ribs in a 3:1 aspect ratio channel with Reynolds numbers 10,000, 30,000, 50,000, and 70,000 on thermal performance (Wright & Gohardani, 2008). The study concluded that increasing the rectangular width of the rib while increasing the spacing of the ribs increased thermal performance. Another method of observing rib orientations can be thought of with the variation of the number of ribbed walls. This study, observing heat transfer and

friction behaviors in a square channel with 90 degree angled ribs (perpendicular to the flow), Chandra et al. reviewed effects of applying the ribs on one, two, three, and all four walls (Chandra, Alexander, & Han, 2003). Both the highest Nusselt number augmentation and friction factor augmentations were seen with the four wall ribbed case.

Varying rib width in a 2:1 aspect ratio channel with one wall featured at 20,000, 30,000 and 40,000 Reynolds numbers was studied by Tran et al. using a transient TLC method (Tran, Valentino, Ricklick, & Kapat, 2011). The study examined heat transfer and friction augmentation for rib aspect ratios of 1, 3, and 5. Results from this study showed decreasing both heat transfer augmentation and friction factor augmentation with increasing rib width. A comparison of the ribs to the current study for heat transfer augmentation and friction augmentation is found in Chapter 5.

Taslim et al. studied twelve different rib-roughened channels with varying channel cross section, square as well as trapezoidal channel cross-section, with ribs applied on two or all four walls of a channel staggered (Taslim, Li, & Spring, 1998). Channels were designed to mimic the cross-section for mid-chord cooling cavities in small aircraft engines. The rib geometries were oriented perpendicular to the flow (90° angle of attack) and spanned with entire width of the featured wall. This work utilized liquid crystals for temperature measurements and characterized the heat transfer and friction factor of each channel and geometry. Taslim, Li, and Spring concluded from this study that applying ribs to the partition walls (side walls so that all four walls are rib-roughened) not only increases heat transfer to those walls, but consequently improves heat transfer on the other two (primary) walls. The addition of extra rib-roughened walls

of course increases the friction factor as well, however the overall thermal performance still increased for four wall ribbed channels over the two ribbed wall channels.

Delving further into variations on the rib, new rib shapes were created to offset the frictional issues of the square or rectangular cross-sectioned rib; rib-variation features were developed.

Rib-Variation Features

Variations of the typical rectangular rib shape include trapezoidal, triangular, or V-shaped and delta-shaped features. Several studies were conducted to compare the typical rib shape to these newly developed rib-variation shapes, a few of which are described below.

An expansion on the angled rib, a V-shaped rib (or chevron) is formed with two angled ribs that meet in the center of the channel. Taslim et al. studied heat transfer and friction in a 2:1 rectangular channel with two opposite rib-roughened walls, comparing 90 degree angled ribs to 45 degree angled ribs and 45 degree angled V-Shaped ribs (Taslim, Li, & Kercher, 1996). The study concluded that the lowest blockage ratio of the 45 degree V-shaped ribs produced both the highest heat transfer and highest friction factors, over the 90 degree attack angle ribs; higher friction factors of the V-shaped rib corrupted thermal performance for the V-shape, where the 45 degree angled ribs showed improved results.

Han et al. altered the typical rib shape to create a right triangle and a wedge-like feature which were called wedge shaped and delta shaped ribs, respectively (Han, Huang, & Lee, 1993). Images of these ribs are shown in Figure 6. The study conducted

tests at Reynolds numbers from 15,000 to 80,000 on two opposite walls, both aligned and offset configurations were observed.

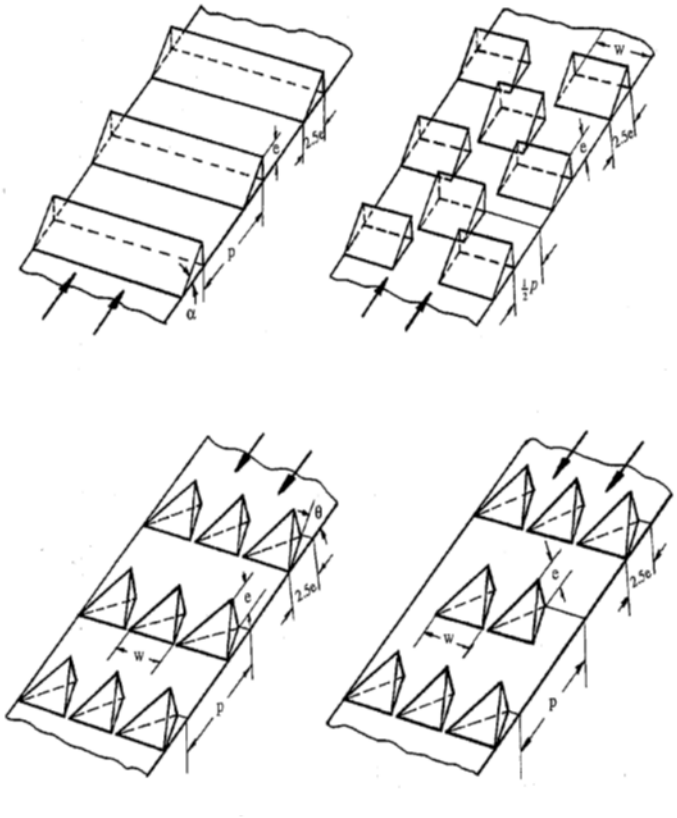

Figure 6: (Han, Huang, & Lee, 1993)

The study concluded the backward delta-shaped offset rib configuration produced the lowest pressure drop penalty and the highest heat transfer was found with the aligned rib configuration of the same case. This feature is the ‘wedge’ feature discussed in this study as well as expanded with several other authors in the wedge features section below.

The wedge-rib (right triangular rib) roughened channel was coupled with a winglet vortex generator at the entrance of the channel for a study conducted by Chompookham et al. with two opposite rib-roughened walls in a high aspect ratio

(AR=10) channel with Reynolds numbers based on the inlet D_h from 5000 to 22,000 (Chompookham, Thianpong, Kwankaomeng, & Promvonge, 2009). A winglet vortex generator geometry is a thin surface into the flow path shaped for this case, as a right triangle angled into the flow and further winglet tests are found in the wedge features section; the winglet vortex generators have a similar (un-filled) shape to the wedge features tested in the current study and are typically created with a punch through the thin material in heat exchangers. The combination study by Chompookham et al. studied the triangular winglet vortex generators at the entrance for wedge ribs pointing downstream and pointing upstream of the flow. The study determined that the collaboration of winglet vortex generators with the downstream pointing wedge ribs resulted in the highest increase in both friction factor and heat transfer, with the highest performance seen in with the upstream pointing wedge.

Thianpong et al. reviewed thermal performance over ribs shaped as isosceles triangles, spanning the width of the channel (Thianpong, Chompookham, Skullong, & Promvonge, 2009). The study investigated varying the triangular rib height in staggered and aligned rib arrangements on two walls of the channel, in a high aspect ratio (AR=10) channel with Reynolds numbers ranging from 5000 to 22,000. The results for heat transfer and friction factor were shown. As expected, the ribs with the highest e/H and at the in-line arrangement produced the highest frictional losses, but also the highest heat transfer. The best performing case, in terms of thermal performance at constant pumping power was the lowest e/H triangular rib in the staggered array.

Promvonge and Thianpong determined thermal performance of four rib shapes in staggered and aligned arrangements for a high aspect ratio (AR=15) channel for cooling

channels or channel heat exchanger design (Promvonge & Thianpong, 2008). The rib variations included a rectangular cross-section, a triangular cross-section, and wedge cross-section ribs spanning the entire width of the channel. The wedge ribs were tested sloped both towards and away from the flow direction and all ribs were tested at Reynolds numbers from 4000 to 16000. The study concluded that the wedge rib pointing downstream (sloped away from the flow direction) yielded the highest increase in Nusselt number but also in friction factor, where the triangular shaped rib yielded the highest thermal performance with the staggered arrangement.

Wedge Features

Further manipulating these shapes or perhaps viewing the wedge ribs in a broken rib design, turbulators with similar cross-sections that did not span the entire width of the featured wall were developed. These 'partial rib' features can consist of full-bodied vortex generators, punched vortex generators, or winglet vortex generators. A punched or winglet vortex generator will not be a full-feature as a rib turbulators, but a thin slice of material protruding into the flow. The full-bodied vortex generator, used for the current study, is more comparable to the rib, as a partial rib, in that it is a full 'filled' feature as well.

The alteration to the full wedge rib to the partial rib wedge shape was discussed first above in the rib variation section by Han et al. (Han, Huang, & Lee, 1993). Early studies of similar shaped features were of the winglet vortex generators and include a study of the development of longitudinal vortex pairs embedded in a turbulent boundary layer, a study by Pauley and Eaton (Pauly & Eaton, 1988). This study investigated the mean streamwise development of pairs of longitudinal vorticies as well as arrays of

longitudinal vorticies in a turbulent boundary layer following 16 different vortex generator pair configurations and two regular arrays. They concluded that a close proximity of counter-rotating vorticies developed from the VGs does not increase the loss of vortex circulation, but rather it affects the spreading of the vorticity.

Punched vortex generators are typically for use in fin and tube heat exchangers, where the shapes are easily manufactured and are added to promote heat transfer as with previously discussed vortex generator applications. Tiggelbeck et al. studied flow structure and heat transfer in a channel with single and double rows of delta half-wing punched vortex generators. (Tiggelbeck, Mitra, & Fiebig, 1994). There were two general shapes tested with this study, the delta wing and the rectangular wing. The delta wing (or delta winglet pair) represented a shape similar to the test in this current study, unfilled. The winglet pair however was sloped toward the direction of the flow, where the delta wing, more similar to the current design, is sloped away from the direction of the flow. These vortex generators were tested at Reynolds numbers between 2000 and 9000 with local heat transfer coefficients determined from utilizing the liquid crystal technique in a 2:1 aspect ratio channel. The study concluded that the winglet pairs (and more particularly the delta winglet pairs) contributed to the highest performance. The four wings and winglet pairs tested by Tiggelbeck et al. are shown in Figure 7.

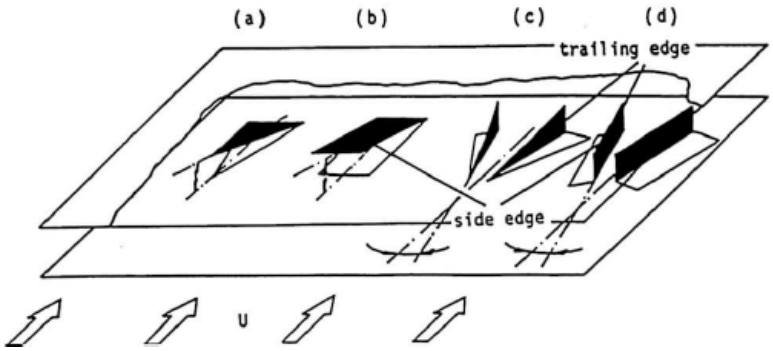

Figure 7: (a) Delta Wing, (b) Rectangular Wing, (c) Delta Winglet Pair, (d) Rectangular Winglet Pair (Tiggelbeck, Mitra, & Fiebig, 1994)

Chen et al. studied heat transfer enhancement of finned tubes with staggered punched longitudinal vortex generators (Chen, Fiebig, & Mitra, 2000). Punched vortex generators in this study and the fin and tube arrangement can be seen in Figure 8(b). Visible in this image, the orientation of the winglet pair forms a similar shape to the full bodied wedge vortex generator in more recent, and the current, studies.

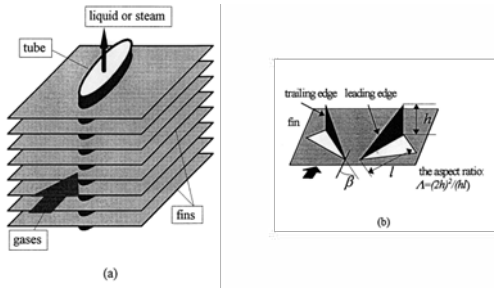

Figure 8: Chen et al. 2000

Chen et al. in this study presented and compared the velocity field, pressure distribution, vortex formation, temperature fields, local heat transfer distributions, and global results for the fins with the punched winglets. The study examined both aligned (shown in Figure 8b) and staggered winglet configurations. Chen et al. concluded staggered winglets were more effective than an in-line configuration for heat transfer enhancement.

Saha and Biswas conducted numerical simulation of turbulent flow with periodically mounted long VGs (Saha & Biswas, 2010). These VGs were oriented in a triangular fashion pointed toward the flow, similar to the wedge featured examined for this study, however no slope was developed in these VGs. Results showed streamwise velocity and vorticity at different spanwise locations. The study concluded the enhancement in heat transfer due to the mixing caused by the vortex generators are sustained over a long downstream zone.

The development of a full-bodied vortex generator for turbine cooling applications with similar shape and orientation of the winglets followed.

Liou, Chen, and Tsai followed with a study on twelve different shaped vortex geometries; included amongst these vortex geometries was a delta-wing vortex generator (Liou, Chen, & Tsai, 2000). Flow patterns were determined by use of laser-Doppler velocimeter, friction factors determined from pressure measurements with a pressure transducer, and local Nusselt numbers were determined using a transient TLC technique. The tests were conducted at one Reynolds number, 12000, on 12 configurations. Two of the better performing cases, a delta wing and 45°V rib were reviewed further in detail for fluid flow and heat transfer characteristics. The study concluded that the direction and strength of the secondary flows with respect to the heat transfer wall have the strongest effect on heat transfer promotion.

More recent studies for a full bodied wedge-shaped vortex generator include Henze et al. in 2007 (Henze, Dietz, von Wolfersdorf, & Weigand, 2007). This study reviewed parallel and longitudinal arrangements of a wedge-shaped enhancement feature with sharpness of the edges on the features. Tests were conducted at Reynolds

numbers ranging from 150000 to 550000 with transient TLC thermometry along with numerical simulations to describe the flow field. In respect to the edge radii, as the radius increases, weaker vorticies are produced and in effect, lower Nusselt number augmentations resulted. In respect to the wedge arrangement, the study concluded that using several wedges in a row lead to an increase in heat transfer and the spacing of the wedges should be chosen to benefit vortex interactions.

Henze et al. examined flow and heat transfer characteristics behind a single vortex generator using a transient TLC method and PIV, flow characteristics behind this VG can be seen in Figure 9 (Henze, von Wolfersdorf, Weigand, Dietz, & Neumann, 2010). The combination of heat transfer and flow data describes the physical conditions in detail, and information was gathered at 300000 channel Reynolds number for validation of the numerical model. Local heat transfer coefficients are shown around the wedge and in the downstream region along with velocity and vorticity.

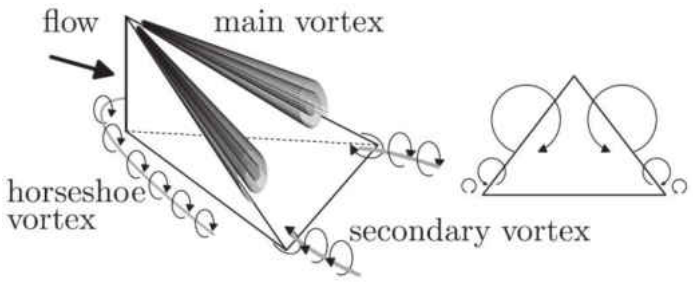

Figure 9: (Henze, von Wolfersdorf, Weigand, Dietz, & Neumann, 2010)

A following study by Henze and von Wolfersdorf depicted heat transfer behind a vortex generator with various approach flow conditions and Reynolds number of 150000 and 550000 (Henze & von Wolfersdorf, Influence of Approach Flow Conditions on Heat Transfer Behind Vortex Generators, 2011). An image of the local heat transfer behind a single vortex generator is shown in Figure 10.

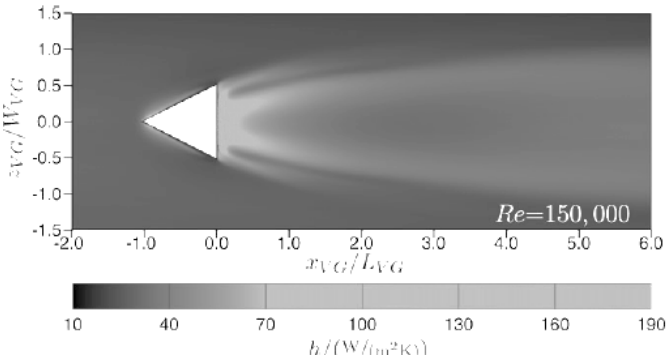

Figure 10: (Henze & von Wolfersdorf, Influence of Approach Flow Conditions on Heat Transfer Behind Vortex Generators, 2011)

General Introduction to Current Work

The current study will investigate thermal performance of the full wedge-shaped partial ribs (considered in this paper as 'full wedge' or 'symmetrical wedge' shapes) and extend the study to a comparison with a 'half wedge' (or 'non-symmetrical wedge') turbulator. These half-shaped wedge turbulator geometries, unlike previous studies, have a right-angled triangular footprint, rather than an isosceles-triangle shaped footprint. This study will also examine the effect of placing these wedge turbulators on two opposite walls in a staggered pattern to create mixing of flow between features on opposite walls and include evaluation of heat transfer enhancement to the surrounding smooth side walls in a 2:1 aspect ratio, rectangular channel. Six cases are studied; two cases studied will compare symmetrical and non-symmetrical wedges that have an e/D_h of 0.10, considered to be just more than a surface roughness feature, the remaining two cases have quadrupled the dimensions to develop a symmetrical and a non-symmetrical wedge that penetrate fully the boundary layer within the channel, observing

the two extremes with respect to e/D_h. The remaining two cases follow previous studies which place the full wedge shapes on one wall, so the same size full wedges tested in the two wall cases are also examined with the same spacing on one wall. To determine the effect of these features, two experimental setups will be utilized: transient TLC and a thermocouple embedded segmented copper-block setup. Experimental results will also be compared with computational results (for fluid flow only) from Star-CCM+.

Manufacturability

As a consequence of the complexity of the current tested wedge shape, the feature may contribute to difficulties manufacturing. However, progressions in manufacturing and materials could minimize or eliminate any production issues. Alterations to cooling channels in blade design and in heat exchangers including development processes, techniques, and materials allow for practicality of implementing more complex geometries, such as these wedge features.

The use of PDCs, or polymer derived ceramics, with a fabrication technique called micro-stereolithography for designing complex shapes in a recuperative heat exchanger was studied by Carman et al. in 2002 (Carman, Kapat, Chow, & An, 2002). The study concluded that the material and technique managed to successfully develop the complex channel design in multiple layers. This technique is one example of the possibility of implementing these complex features.

CHAPTER 2: EXPERIMENTAL OVERVIEW (METHODS AND MATERIALS)

Geometries

There are two basic shapes tested, each with two different sizes. The first geometry is a full symmetrical tapered wedge, which has an isosceles triangular footprint seen in Figure 11b below. The second geometry is a tapered half-wedge, or non-symmetrical wedge shape which has a right-triangle footprint seen in Figure 11a below. The figure also shows the orientation of the wedges with respect to flow and location in the channel. The blue or hatched triangles represent features on the bottom wall and the green or solid triangles represent features on the top wall of the channel. The first four cases on two walls created a staggered formation, where two times the pitch is measured from the base of a feature to the base on the next feature on the same wall, i.e. one pitch measures base to base of the nearest wedge, on opposite walls. The wedges slope away from the flow direction, where the slope angle remains constant for all cases and is shown in Figure 12. The two one wall cases orientation can then be represented by the blue hatched triangles in Figure 11b, with the green solid triangles removed.

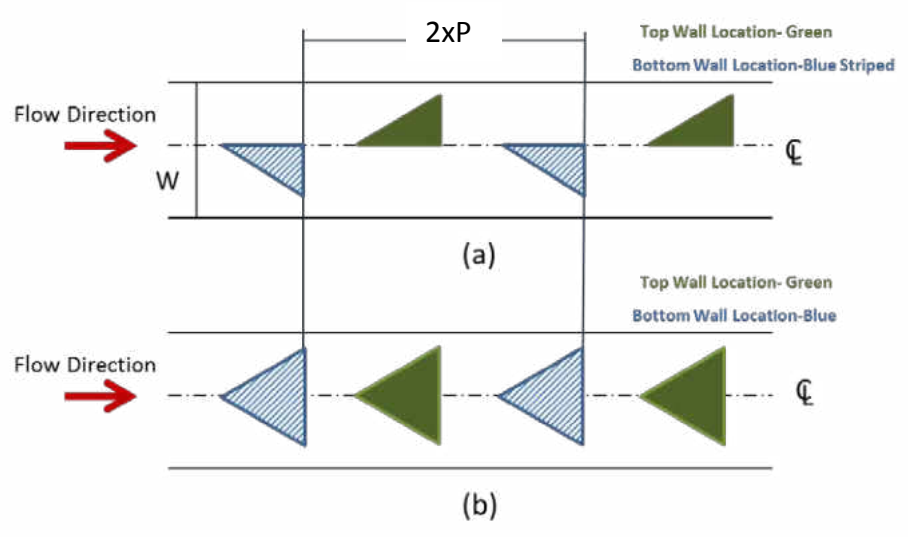

Figure 11: Configuration for (a) Non-Symmetric Wedge (b) Symmetric Wedge

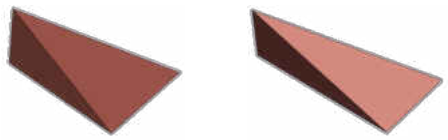

Figure 12: Geometries for Cases (A, C, E, F - right), (B, D - left)

The full wedge cases staggered on two walls are cases A and C, where case A is the low e/D_h. The half wedge cases staggered on two walls are cases B and D, where case B is the low e/D_h.

The two full wedge cases were also tested on one wall, succeeding tests in literature which follows the non-dimensional parameters of the experiments by Henze et al. (Henze, Dietz, von Wolfersdorf, & Weigand, 2007). The wedge for Case A, repeated for one wall is Case E and the wedge for Case C, repeated for one wall is Case F.

The wedge dimensions, given in mm for all cases are shown in Table 1, with descriptions of the dimensions in Figure 13. The smaller wedge cases (A and B) yield an e/H of 0.13, representing a height near surface roughness. Case C, Case F and

Case D dimensions are Case A, Case E and Case B dimensions scaled 4 times to increase side wall flow interactions as well as penetrate the entire boundary layer thickness. The wedges C, D, and F are just over half the channel height, e/H=0.52 (boundary layer thickness e/H=0.5) in order to keep consistent with all other parameters for placement on the modulated channel sections.

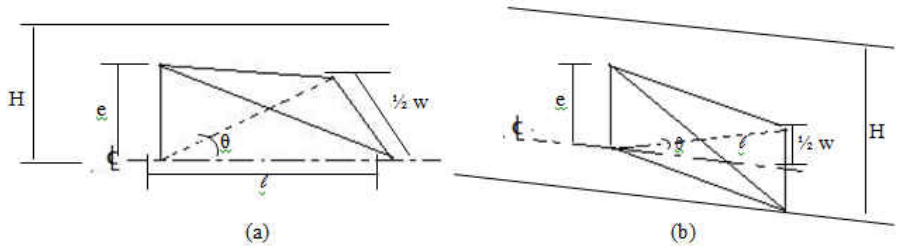

Figure 13: Description of Geometric Parameters (a) Non-Symmetric Wedge (Case B, Case D) (b) Symmetric Wedge (Case A, Case C)

Table 1: Wedge Dimensions (mm)

Dimension	Case A	Case B	Case C	Case D	Case E	Case F
Symmetric or Non	Non	Sym.	Non	Sym.	Non	Non
e	2.08	2.08	8.32	8.32	2.08	8.32
ℓ	5.20	5.20	20.80	20.80	5.20	20.80
e/ℓ	0.40	0.40	0.40	0.40	0.40	0.40
1/2-W	2.60	2.60	10.40	10.40	2.60	10.40
0.5W/ℓ	0.50	0.50	0.50	0.50	0.50	0.50
e/D_h	0.10	0.10	0.40	0.40	0.10	0.40
$W_{channel}$	32.0	32.0	32.0	32.0	32.0	32.0
H	16.0	16.0	16.0	16.0	16.0	16.0
e/H	0.13	0.13	0.52	0.52	0.13	0.52
D_h	20.90	20.90	20.90	20.90	20.90	20.90
P/e	6.11	6.11	6.11	6.11	6.11	6.11
P	12.70	12.70	50.80	50.80	25.4	101.6
Number of Featured Walls	Two	Two	Two	Two	One	One
Re_{Dh}	All: 10,000, 20,000, 30,000, 40,000					

Geometric Tolerances

From machining, the small wedge geometries all measured within 0.3mm of the design specifications and around 0.5mm of the design specs for the large wedge cases, with the exception of the width on the large full wedge, which on average measured just less than 1.5mm from the design specifications. Machining of the features was completing by electrical discharge machining (EDM). All wedges were measured by hand with a digital micrometer and results on the measurements are listed as follows (per case):

Table 2: Case A,E Wedge Dimension Measurements

	Length (ℓ)	Width (2*W)	Height (e)
Mean	4.94	4.91	1.99
Standard Deviation	0.07	0.06	0.02
Variance	4.84e-3	3.71e-3	4.23e-4

Table 3: Case B Wedge Dimension Measurements

	Length (ℓ)	Width (2*W)	Height (e)
Mean	5.09	2.51	2.02
Standard Deviation	0.06	0.31	0.04
Variance	3.59e-3	9.77e-2	1.48e-3

Table 4: Case C,F Wedge Dimension Measurements

	Length (ℓ)	Width (2*W)	Height (e)
Mean	20.96	19.31	7.89
Standard Deviation	0.31	0.30	0.08
Variance	0.093	0.088	0.007

Table 5: Case D Wedge Dimension Measurements

	Length (ℓ)	Width (2*W)	Height (e)
Mean	20.16	9.68	7.72
Standard Deviation	0.40	0.12	0.08
Variance	0.160	0.013	0.006

Friction Factor

The channel designed for friction factor testing was designed to run both the friction factor tests and the transient TLC tests. The channel was developed out of acrylic to allow for viewing the TLC. One side wall remained unaltered for side wall transient TLC measurements while the other side wall, the pressure-tapped side wall, was outfitted with 45 static pressure ports located along the mid-plane of the channel. The channel length is 40 inches to allow room prior to and following the test section to minimize any entrance or exit effects. The inlet box (which contains mesh heaters for the transient TLC tests) is connected to the beginning of the channel with an exit box, which is used to connect the rectangular cross section of the channel to the circular pipe exit, at the other end of the channel. An image of the entire channel and piping is shown in Figure 14.

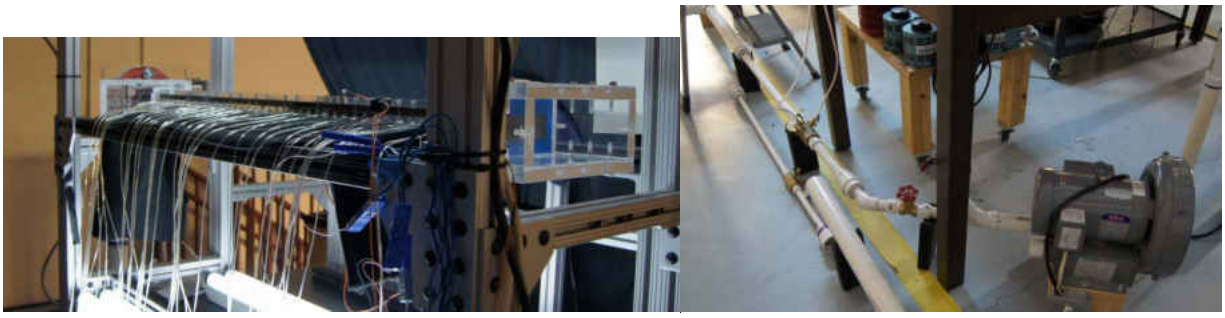

Figure 14: Pressure Taps (left) & Piping Setup (right)

The wedges are attached with double sided copper tape to two (top and bottom) acrylic inserts which slide into the acrylic channel. An image of the wedges (case A) on the acrylic insert is shown in Figure 15. Also visible in this image is the location of the TLC test section (where TLC data is collected) as indicated by the black paint, or black backing. The wedges are placed on the acrylic insert 5 inches from the inlet and the test section starts 10 inches from the inlet. The channel length that includes wedges in the channel is 20 inches.

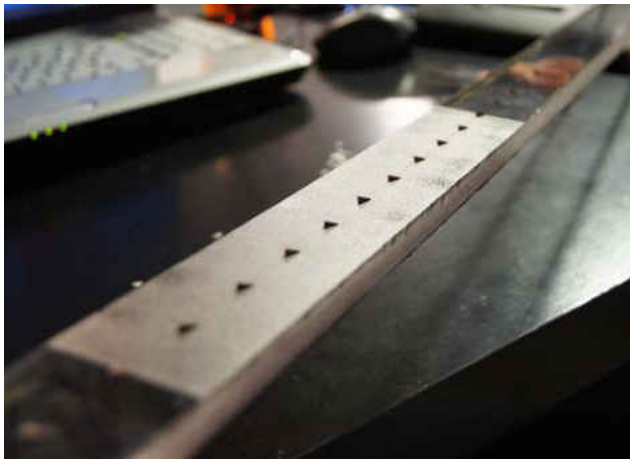

Figure 15: Case A on acrylic insert with TLC

The channel operates with a vortex blower under suction. A gate valve controls the flow rate while a calibrated venturi is used to measure the flow rate. Tests are conducted at 10,000, 20,000, 30,000, and 40,000 averaged Reynolds number, based on hydraulic diameter of the smooth walled channel. A 1”-38 calibrated venturi was used to measure flow rate for the 20,000, 30,000, and 40,000 Reynolds numbers while a ½”-20 calibrated venturi was used for the 10,000 Reynolds number case. Ample distance was added (>10 hydraulic diameters) in piping prior to the venturi for proper measurement. A digital handheld manometer was then used to measure the pressure

drop over the venturi which was then added into an excel sheet containing the calibration curve to determine SCFM, provided by Homer R. Dulin Co. The mass flow rate is determined from the SCFM, which is then used along with the channel perimeter and dynamic viscosity; found using temperature measured via a T-type thermocouple and handheld reader, to determine Reynolds number. The wedges are placed on the acrylic insert 10 inches from the inlet to allow for fully developed flow before the test section.

Static pressure taps start at 1.5 inches from the inlet of the channel and are spaced ½" apart for the first 4 inches, then one inch apart (except where a thermocouple is added at 1 inch, 5 inches, 9 inches, and 21 inches for bulk temperature measurement) until the end of the channel. Since the test section only consisted of 20 inches and starts 5 inches from the inlet, measurements were only taken from the 1.5 inches from the inlet to 28 inches (3 inches past the end of the test section). Measurements were taken using a Scanivalve™® in conjunction with a Data Acquisition Board (DAQ) and an in-house created data collection system using LabView. The setup is shown in Figure 16 below.

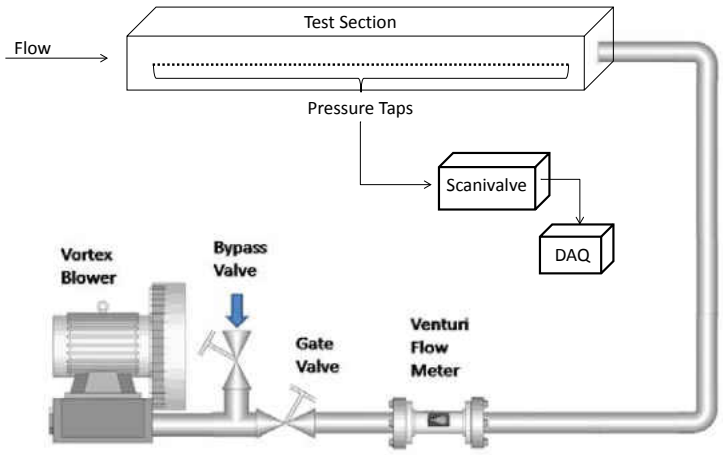

Figure 16: Static Pressure Measurements

Once data is collected using LabView, the software outputs an excel sheet with all of the static pressure measurements. The software is setup to collect ten samples from each static pressure port, which will be averaged in excel. The program also records the bias from Scanivalve™® (from three open ports) which is subtracted from the static pressure measurements prior to analyzing the data. Slope, or dP/dx, is then determined from the static pressures and the location of the measurements along the length of the channel.

To determine the experimental friction factor, the slope is used along with the density, velocity, and hydraulic diameter of the channel to determine the Moody friction factor in Equation (2) below.

$$f = \frac{\frac{dP}{dl} D_h}{\frac{1}{2}\rho U^2} \tag{2}$$

Validation of the channel was first conducted; prior to completing any of the wedge tests a baseline smooth-wall test was completed to validate the test section for friction factor. The setup was identical as described and shown above, where no wedges were taped to the acrylic inserts' surfaces. The experimental friction factors from Equation (2) in this baseline case where then compared to the theoretical value established by the Blasius solution for Friction Factor in a fully-developed, smooth-wall pipe flow, calculated using Equation (3).

$$f_0 = 0.316Re^{-0.25} \quad (3)$$

Results comparing the baseline test to Blasius smooth pipe solution and all case friction factor results are found in Chapter 3.

Segmented Copper Block

Flow is provided by a vortex blower operated under suction. A gate valve controls the flow rate while a calibrated venturi along with a handheld digital manometer is used to measure the flow rate. Tests are conducted at 10,000, 20,000, 30,000, and 40,000 averaged Reynolds number, based on hydraulic diameter of the smooth walled channel.

The heated test section is made up of segmented copper modules totaling a length of ~25 hydraulic diameters (based on the smooth wall area of the channel). Each module consists of 4 copper blocks: all four walls are originally smooth, and then features are attached to top and bottom walls. The wedge features are adhered to the smooth top and bottom walls with a double-sided copper tape. The copper tape thickness as reported by 3M (for 1182 double-sided copper tape) was 0.088 mm, so resistance between the copper block and attached wedge are considered negligible. An acrylic entrance section (~35 D_h) was created to ensure a hydrodynamically fully

developed flow before entering the heated test section. Incoming air at the inlet of the entrance section is from ambient. Three thermocouples are placed immediately at the inlet and exit of the heated test section to measure the inlet and exit bulk temperatures.

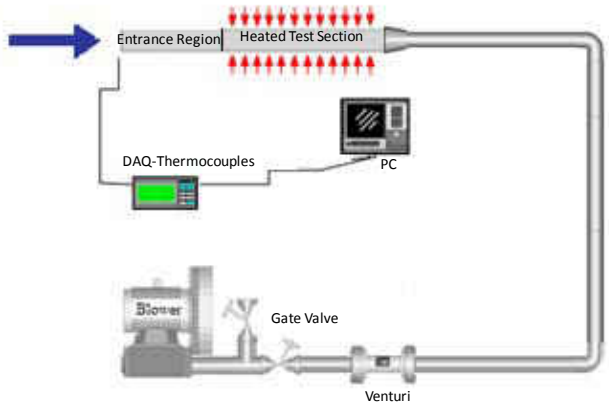

Figure 17: Copper Block Channel Setup

The modules of the heated test section are depicted in Figure 18, with the entire channel length (1-side and top wall removed) in Figure 19. The four copper blocks are held within an acrylic housing to form a 2:1 AR channel. The acrylic housing is also meant to provide a structure that will allow the copper to form a channel without physical contact between the four copper blocks of each modulated section to eliminate conduction between blocks of a module. To minimize conduction between adjacent blocks on each wall, the copper pieces are separated with cork insulation. The copper blocks contain two, for redundancy, T-type thermocouples inserted into machined holes in the back of the block, to measure wall temperature, held in place with high conductivity thermal cement. The thermocouple measurements are recorded using a Measurement Computing© data acquisition system.

Each copper block is backed by a thin foil heater, held to the block with double-sided Kapton™ tape. The heaters are manufactured to cover the entire surface of the copper block. Power is supplied to the heaters by a 300 Amp adjustable DC power source. Additionally, the top, bottom, and side heaters are each controlled by an array of rheostats such that the voltage applied to each heater can be individually controlled. The voltage applied to each heater is measured with a digital multimeter.

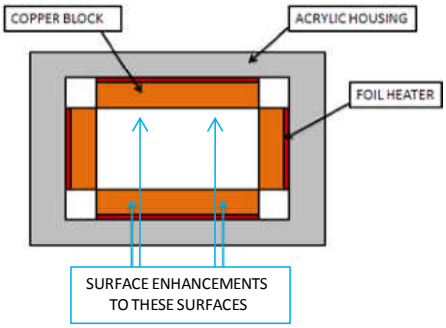

Figure 18: Copper Block Modular Section

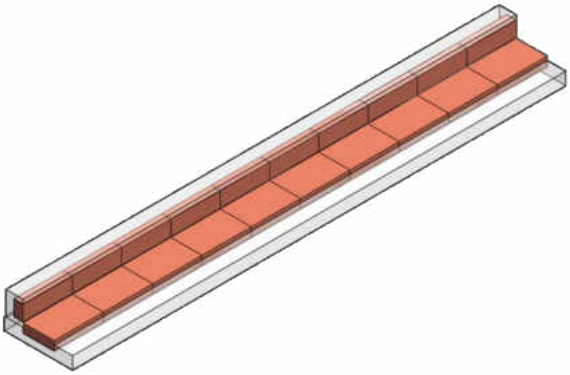

Figure 19: Segmented Copper Test Section

The full setup of the copper block test channel and the rheostats and DAQ boards are shown in the pictures below.

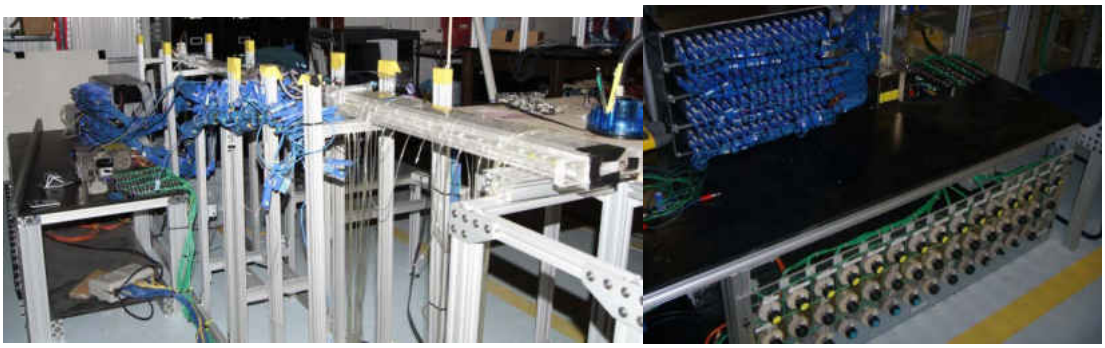

Figure 20: Copper Block Setup Pictures

Prior to conducting heat transfer tests, heat leakage tests are completed to determine heat lost through the acrylic housing as well as resistances for the heaters at three temperatures. To determine the heat lost, there is no flow and the channel is stuffed with insulation to ensure there is no natural convection in the channel. Heat is applied and adjusted so that the channel is isothermal. The test is run at three temperatures, 55°C, 65°C, and 75°C to establish a correlation (best fit curve) for both heat leakage and resistance in the heaters. For each test, data is collected once at steady state (no more fluctuation/increase in temperature) which usually takes approximately 8 hours once voltages have been set. Temperature data is collected from all thermocouples at ½ second intervals for 15 minutes (1800 samples). The calculated heat lost is then determined by $Q_{loss}=V^2/R$, where all Q_{loss} values determined are plot versus the temperature difference ($T_{wall}-T_{ambient}$) to determine a second order (0-intercept) curve fit for heat leakage. The resistance curve fit is a linear curve fit determined from plotting the measured resistances by the wall temperature. Both curve fits found here are then used in processing data for determining heat transfer coefficient after the heat transfer tests. A copy of the heat leakage Excel spreadsheet can be found in Appendix B.

Heat transfer tests are started by first setting the flow in the channel via the calibrated venturi. The flows are set to 10,000, 20,000, 30,000, or 40,000 Reynolds number. Once the flows are set, heat is applied. The rheostats are used to adjust the voltage to each heater so that the channel is isothermal. The channel is typically set to 70°C, so that ΔT=45°C. Once the channel temperatures are steady, the temperatures are recorded from all thermocouples (including the thermocouples installed at the channel exit to measure the bulk temperature), for 1800 samples; once every 0.5 seconds for 15 minutes. Voltages for each heater are manually recorded, read from a Keithley Meter. The temperature data is then processed in the heat transfer coefficient Excel spreadsheet. A copy of this spreadsheet can be found in Appendix B.

First, the temperatures are input to the sheet, averaged over each thermocouple for all 15 minutes. Then, the average for the block is determined by averaging the two thermocouples from the copper block; these are the wall temperatures. The flow rate information from recorded in the calibrated venturi sheet for each test is also added manually to the heat transfer coefficient sheet. The heat transfer coefficient sheet first calculates all the local properties, based on the local film temperature:

$$\boldsymbol{T_{film}} = \frac{\boldsymbol{T_{wall}+T_{bulk}}}{\mathbf{2}} \tag{4}$$

The voltages recorded are also entered into the heat transfer coefficient Excel spreadsheet. From this Excel file, all of the constant data is located on the first tab, which includes the curve fits for heat leakage and resistance. This curve fit data for the resistance is then used to calculate the resistance for each block's heater from the measured wall temperature.

Heat input from each copper block is then calculated as V^2/R, where the R is the resistance as the function of T_{wall}. The heat loss for each block location is also calculated via the curve fit, from the heat leakage curve fit as a function of $\Delta T = (T_{wall} - T_{ambient})$. Any lateral conduction between the blocks caused by any temperature difference is then calculated as:

$$\boldsymbol{Q_{lateral}} = \frac{\boldsymbol{T_{wall_{j+1}} - T_{wall_j}}}{\boldsymbol{R_{lateral}}} - \frac{\boldsymbol{T_{wall_j} - T_{wall_{j-1}}}}{\boldsymbol{R_{lateral}}}; \boldsymbol{R_{lateral}} = \frac{\boldsymbol{thickness_{insulator}}}{\boldsymbol{k_{insulator} * A_{contact}}} \quad (5)$$

The actual heat is then viewed at the input subtracting the losses, and adding in any lateral conduction from the previous block:

$$Q_{actual} = Q_{input} - Q_{loss} + Q_{lateral} \quad (6)$$

To determine the heat added to the flow, a different equation is used for the "Q_{added}" term. This is determined from the following method, which is also used for determining the bulk temperature. This method is used so that the T_{bulk} and Q_{added} are found at the centerline of each modular section, rather than the end of the block, or the beginning of the next block. The two terms are found using the control volumes outlined in the broken line, the four copper blocks are shown to represent the top and bottom walls, where the large arrow indicates the flow direction. The first control volume would be considered the first module in the channel, where only half of all information from the four copper blocks in that module is taken. All other center module copper blocks calculate the bulk temperature and heat added to the flow by Equation 7 and Equation 8.

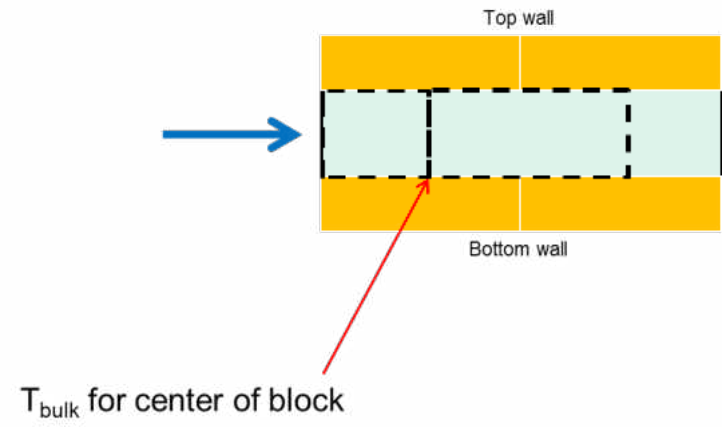

Figure 21: Calculation for T_{bulk} and Q_{added}

$$Q_{added} = Q = 0.5(Q_{current\ block}) + 0.5(Q_{previous\ block}) \quad (7)$$

$$T_{b_i} = T_{b_j} + \frac{\sum Q_{added}}{\dot{m} \times c_p}$$
$$j = i - 1 \quad (8)$$

The heat transfer coefficient is then determined from Newton's law of cooling:

$$Q_{added} = hA(T_{wall} - T_{bulk});\ h = Q_{added} / [A(T_{wall} - T_{bulk})] \quad (9)$$

Where the area is the smooth wall surface area (Baseline). Nusselt number is then:

$$Nu = \frac{h * D_h}{k_f} \quad (10)$$

The overall Nusselt numbers determined are the area-weighted averages of each wall's fully developed Nusselt number average. The results are then shown for the local and overall averaged Nusselt numbers in Chapter 3.

Thermal performance is obtained for each case and Reynolds number as well. The thermal performance is calculated for constant pumping power as identified below:

$$\eta = \frac{\frac{Nu}{Nu_o}}{\left(\frac{f}{f_o}\right)^{1/3}} \quad (11)$$

The thermal performance of each case and Reynolds number are presented in Chapter 3 and compared with the alternative testing method in Chapter 5.

Transient TLC

The channel used for the transient TLC measurements is the same as described and shown in the Friction Factor testing. The test section where the TLC data is pulled, is located 10 inches from the inlet of the channel to 20 inches from the inlet; the test section is 10 inches long. Three of the acrylic walls (two inserts on the top and bottom and one side wall) are painted with the sprayable Thermochromic liquid crystal coating, provided by LCR Hallcrest. The fourth wall is the pressure-tapped wall. The TLC paint has a green peak centered at 35 degrees C one degrees C bandwidth. The red peaks at 34.8°C, the green peaks at 35.1°C, and the blue peaks at 35.7°C. The sprayable TLC is then coated with a black backing, also provided by LCR Hallcrest, for easy viewing of the color change through the backside of the acylic (where the cameras are located).

Three cameras are set up, one perpendicular to each painted wall to capture the color changes in the paint. The three cameras are identical, all Panasonic PV-GS180. Recordings are started prior to turning on the heat for each test conducted. For the transient testing, two LEDs are placed in the viewing window for the cameras; the LEDs are connected to a switch with the power supply for the heater so that the light turns on as soon as heat is added to the flow and turns off once the heat is also turned off. All background lighting in the room was turned off for testing to avoid wash-out in the cameras. Four lights where then attached to the test rig to allow proper lighting for viewing the color changes in the cameras.

Mesh heaters (2) are used to heat the flow at the inlet section of the channel. The heaters are connected to a 7.5V,300A Xantrex DC power supply where voltage is regulated for each test. Setup with the cameras, lighting, and heater box are shown in the images below.

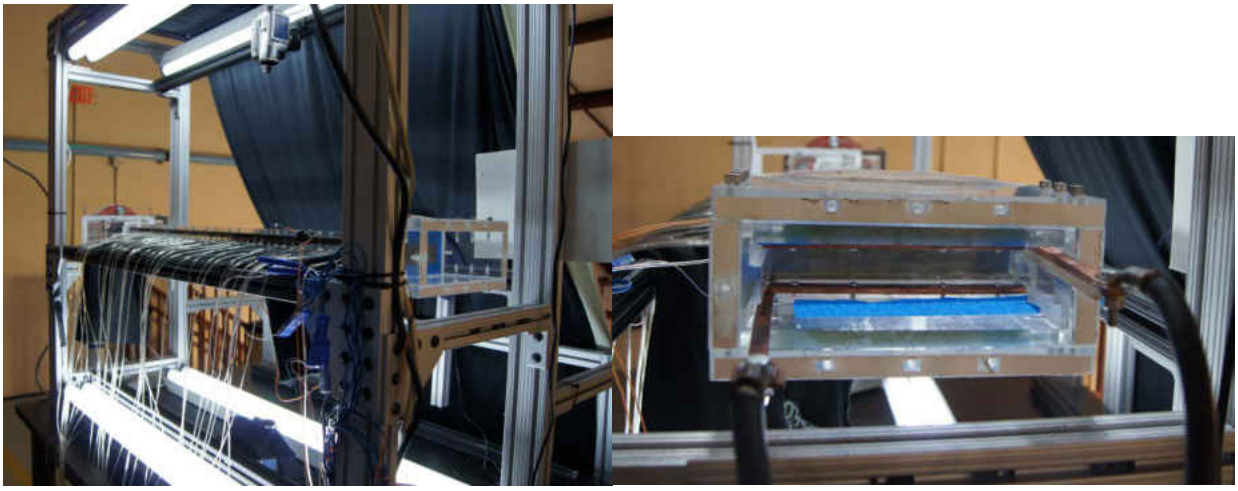

Figure 22: TLC Channel Setup & Inlet Heater Box

Four T-type thermocouples are placed at 1”, 5”, 9”, and 21” along the length of the channel in the center of the channel to capture the flow bulk temperature. The thermocouples are connected to a DAQ board and recorded with an in-house developed code in LabView at 0.25 second intervals for the entire duration of the test (typically 30-45 seconds until test completion). The output from LabView is an excel file, which is then converted to three columns (length from the test section inlet, time of each data point or temperature collected, and the temperature recorded) to determine the bulk temperature with a non-linear regression and curve fitting analysis program, NLREG. One example of the code and the output from NLREG can be found in Appendix A.

There are two temperature collections done for each test completed, one ‘starting temperature’ test and then the ‘actual heated’ test temperature collection. This temperature information is input to the NLREG code to output the bulk temperature curve fit used in the MATLAB code for determining the local heat transfer coefficients.

The videos from the cameras are downloaded via Panasonic MotionDV Studio. There will be three separate videos (one for each TLC coated wall) for each Reynolds number test with four Reynolds numbers and therefore there will be 12 videos for each case needed for post processing. The videos are then edited to create images of the TLC painted section only (eliminate any background) for the duration of the test (as indicated by the LED lights). These images are obtained using the Sony Vegas Pro software. Each test may have anywhere from 900 to 1400 images, depending on the time duration. These images are then imported into MATLAB to determine the local heat transfer coefficients and ultimately local, streamwise average, and overall Nusselt number augmentations.

There are 5 separate MATLAB codes used to determine the overall Nusselt number augmentations. An example of each code may be found in Appendix A. The first code is used to read all of the images into a .mat file for reading in the following MATLAB codes. This code will output information for the color in each pixel at each point in time. The next code is a filtering code; the filter code will eliminate any areas from the .mat files that exceed the input threshold and create a time step for all the frames in the .mat file for interpreting in the next code which determines the heat transfer coefficient at each pixel. After the filter code finishes, the heat transfer coefficient code is run. The heat transfer coefficient code utilizes the information

obtained in the filtering code, the time step, and then determines the bulk temperature, resolutions for each pixel location, and backs out heat transfer coefficient for each color peak (red, green, and blue) at each location from the information obtained and user defined (acrylic properties).

The local heat transfer coefficient over a surface coated with liquid crystals can be obtained from a transient test using the 1D semi-infinite solid model. This assumption is valid for sufficiently short test duration such that the heat penetration depth is less than the wall thickness; the maximum Fourier number of the longest test was calculated to be less than 0.02 to verify this assumption. The heat diffusion equation, for the one-dimensional case, reduces to Equation 12.

$$\alpha \frac{\partial^2 T}{\partial x^2} = \frac{\partial T}{\partial t} \tag{12}$$

The known boundary conditions are as follows:

$$@\ t = 0,\ T(x,0) = T_i)$$

$$@\ x = 0,\ -k\frac{\partial T}{\partial t} = h(T_w - T_b)$$

$$@\ x \rightarrow \infty,\ T(\infty,0) = T_i)$$

Equation 12 can be solved with the initial and boundary conditions to obtain the non-dimensional surface temperature at the convective channel surface in the form of Equation 13.

$$\frac{(T_w - T_i)}{T_b - T_i} = 1 - \exp(\beta^2)\,\mathrm{erfc}(\beta) \tag{13}$$

$$\textit{where} \quad \beta = \frac{h\sqrt{\alpha t}}{k}$$

The transient technique used is the so-called slow transient technique whereby the increase in flow temperature cannot be considered an ideal step-change; a typical

measurement of the centerline temperature at the start of the viewing window is shown in Figure 23. To account for this, Duhamel's superposition theorem is applied as suggested by Metzger and Larsen (Metzger & Larson, 1986). By segmenting the overall temperature change into a number of smaller temperature steps, the accuracy of the method can be maintained by use of Equation 14.

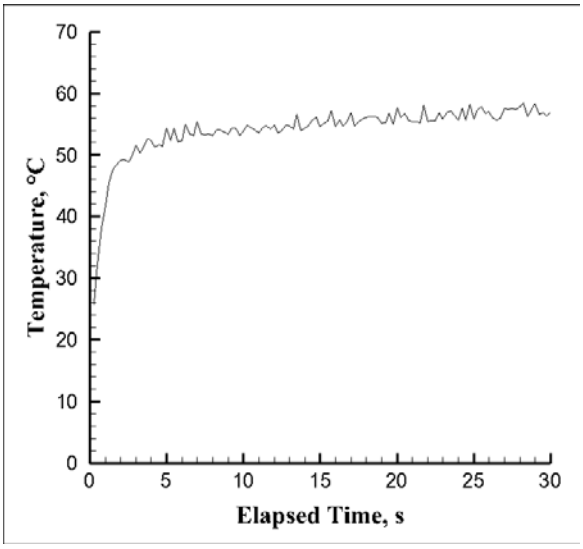

Figure 23: Centerline Entrance Temperature at Start of Viewing Window

$$T_w - T_i = \sum_{j=1}^{N} \left[1 - \exp\left(\frac{h^2 \alpha (t-\tau_j)}{k^2}\right) \operatorname{erfc}\left(\frac{h\sqrt{\alpha(t-\tau_j)}}{k}\right) \right] \left[\Delta T_{m(j,j-1)}\right] \quad (14)$$

The characteristic TLC temperature of the peak green color intensity is used for T_w. The channel bulk temperature, measured at steady state before the heat is provided, is used for T_i. The measured centerline temperatures from the thermocouples dispersed in the test section is used to curve fit the local time varying bulk temperature, using Equation 15, from NLREG to determine the curve fit parameters, T_f, A, B, and C.

$$T_b = \left(T_f - T_i\right)(Ax + B)(1 - e^{Ct}) + T_i \quad (15)$$

The elapsed time history of the color change of each pixel is obtained from the digitized recorded video images. The recorded RGB intensities are digitized using an 8-bit scheme. An example of the elapsed history of the green signal intensity is shown in Figure 24. A 3-point moving average filter is performed for each pixel location to filter out some of the noise in the recorded intensity versus time before a peak finding algorithm is used to determine the time since the test start at which the peak green intensity occurs for every individual pixel in the interrogation window. A 3x3 pixel block spatial average filter is performed to smooth the calculated peak times (t).

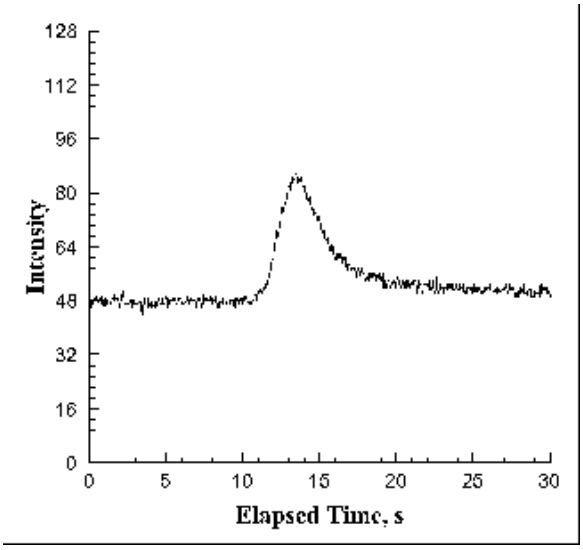

Figure 24: Recorded Green Intensity History

Knowing T_i, T_b, T_w, the thermophysical properties of acrylic, and the time at which T_w occurs (t) for each pixel, the heat transfer coefficient at each pixel location can be calculated using an iterative technique using Equation 14 and Equation 15.

For the featured channels; excluding the baseline, a mask code is run to determine the heat transfer over the copper features, using lumped capacitance, and

replace that information into the previously obtained heat transfer coefficient output in the next code. The mask is first created in Microsoft paint, where an image of the channel with the copper pieces still heated immediately following a test is input as a .bmp file, then the areas identified as copper are covered with white. The mask processing code then uploads this masked image and determines the heat transfer coefficient from the white areas using the user defined wedge dimensions and copper properties. The new copper values are input back to the original heat transfer coefficient output and replace the values at the identified locations (masked areas).

Calculation for these sections are done following Equation 16 for a constant bulk temperature; the Biot number of the copper rib is estimated to be less than 10^{-4} to support the validity of using the lumped model. Because the time scale of the color change of the copper rib is greater than the transient bulk temperature change, a superposition of the temperature steps is not necessary for the lumped capacitance portion. The surface area, *A*, used to calculate the heat transfer coefficient of the wedge portion is the surface area of the wedge base. This area is chosen in order to consistently evaluate the heat transfer of each different wedge channel relative to an equivalent un-ribbed, smooth channel. The actual average surface heat transfer coefficient of the wedge surface is correspondingly lower and can easily be calculated using the ratio of surface area of the exposed wedge surface and wedge base for each case.

$$h = \frac{\rho_{cu} V C}{tA} \ln\left(\frac{T_w - T_\infty}{T_i - T_\infty}\right) \tag{16}$$

The final code to determine the Nusselt number augmentations: local, streamwise averaged, and overall, is the post-processing code. The post processing

code will find the Nusselt numbers at each pixel location for all three color peaks (red, green and blue) for local Nusselt numbers found from heat transfer coefficient as in Equation 10, results reported for this study are from the values determined with the green peaks. Local augmentations are then found by dividing through by Nusselt number from Dittus-Boelter. Streamwise augmentations average the columns in the Nusselt number output and divide through by Dittus-Boelter; these streamwise augmentations are then plotted as a function of pixel location (x/P) and are shown in Chapter 3 for the green peaks. Overall augmentations then average the entire Nusselt number outputs to determine the Nu/Nu_o overall, shown to compare copper block results. All local Nusselt number augmentations are also shown in Chapter 3, which were plotted with Tecplot. The data for local Nusselt number augmentations are copied from MATLAB into Excel which uses a Tecplot add-in to create the color contoured local Nusselt number augmentation plots.

CFD

For further insight into flow characteristics, STAR CCM+ from CD-adapco was utilized. Prior to STAR-CCM+, geometries were first created in SolidWorks. The fluid zone for the small wedge cases were 2 inches long, showing 4 wedges for the two wall cases, and 2 wedges on the one wall case. The fluid zone for the large wedge cases were 4 inches long, showing 2 wedges for the two wall cases and one for the one wall case. Images of the Parasolids for each case used for importing into STAR-CCM+ are shown in Figure 25 to Figure 30 below, where the arrow shows the flow direction.

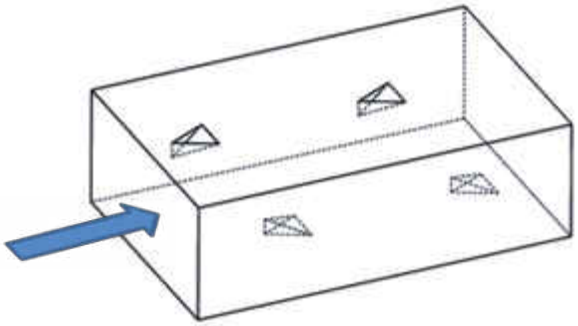

Figure 25: Fluid Zone Case A

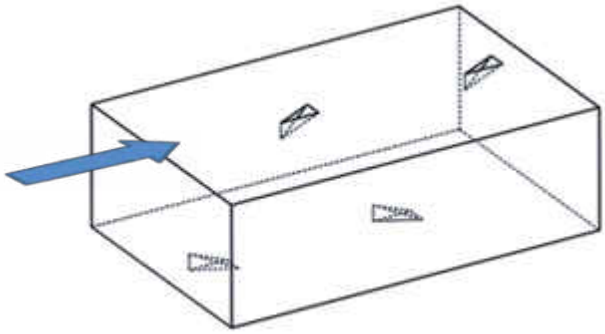

Figure 26: Fluid Zone Case B

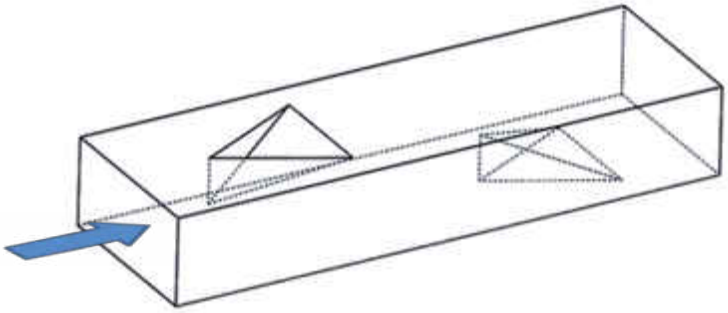

Figure 27: Fluid Zone Case C

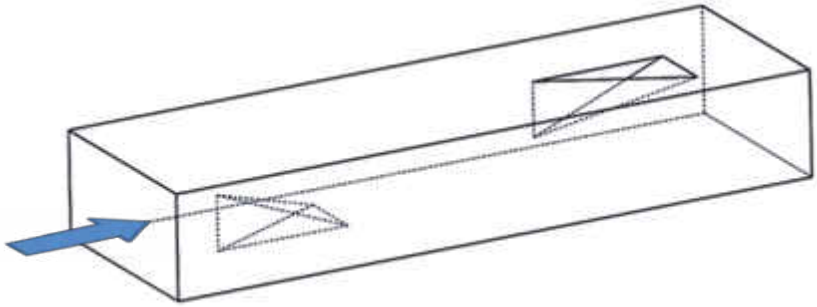

Figure 28: Fluid Zone Case D

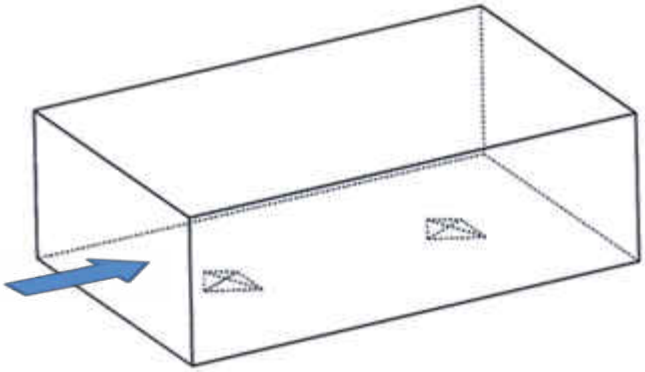

Figure 29: Fluid Zone Case E

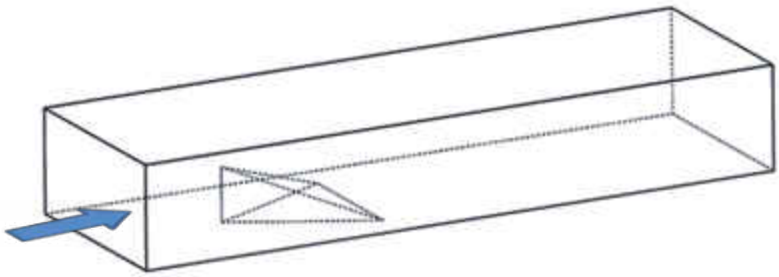

Figure 30: Fluid Zone Case F

Once all of the fluid zone parts had been created in SolidWorks and saved as parasolids, each figure was imported as a surface mesh into STAR-CCM+. Polyhedral

meshes were created in STAR-CCM+ by defining the meshing parameters in the mesh continua for prism layer mesher (defining boundary layer), polyhedral mesher, and surface remesher. The sizing of the mesh was determined from an in-lab created y+ MathCAD code, found in Appendix D. All meshes had a y+ of less than 5, where the highest y+ values were at the tips of the wedges on the bottom wall surface. One example of the y+ values on the surfaces is shown in Figure 31. Images of all case meshes are shown in Figure 32 to Figure 37 below. The meshes were between 2 to 4 million cells each, where the further from the wedge, the mesh became coarser. There were 6 prism layers used with a prism layer stretching of 1.5 (STAR default) and absolute prism layer thickness of 2.1E-4 (from y+ calculator sheet). The global settings for surface growth rate was 1.05, so that the cells grew slowly away from the wedges to minimize skewness, 5E-5 was the absolute minimum surface size and 2.54E-4 was the target surface size of the smaller wedge features and 4E-4 for the larger features. All other settings were left at the default in STAR-CCM+, however, some of the individual wedge surfaces were adjusted lower than the global size settings to reduce any skewed angles between the wedge and the surrounding surfaces so that the maximum skewness angle in the volume mesh was less than 85 degrees.

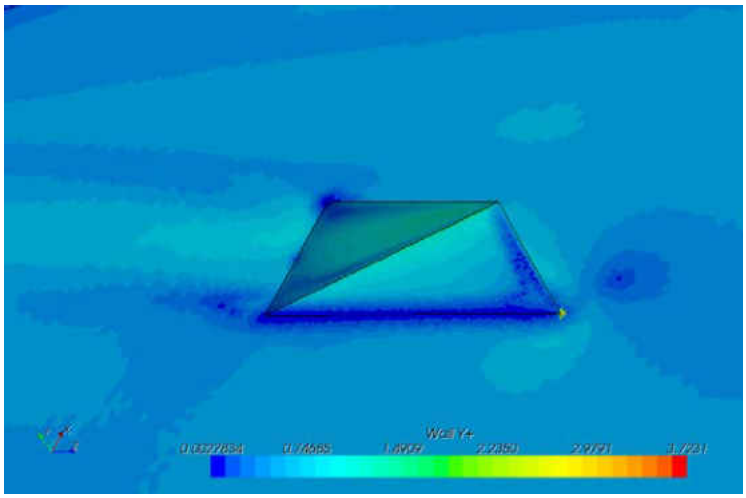

Figure 31: y+ Values on Wedge Surface

Figure 32: Case A Mesh

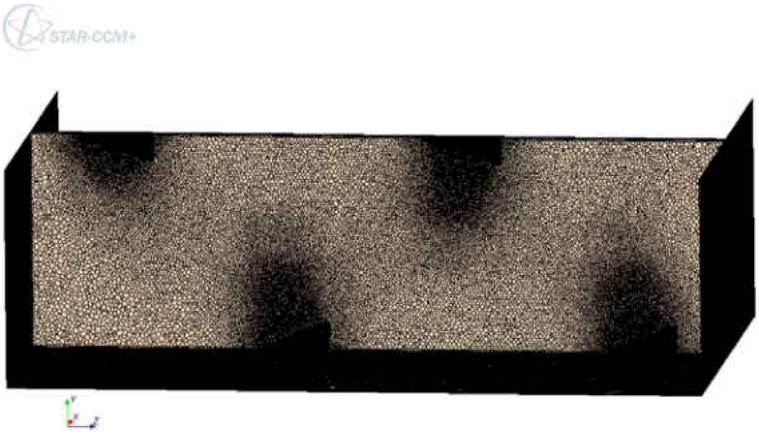

Figure 33: Case B Mesh

Figure 34: Case C Mesh

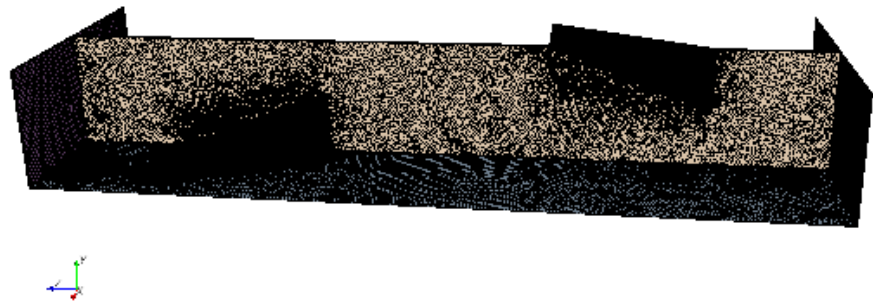

Figure 35: Case D Mesh

Figure 36: Case E Mesh

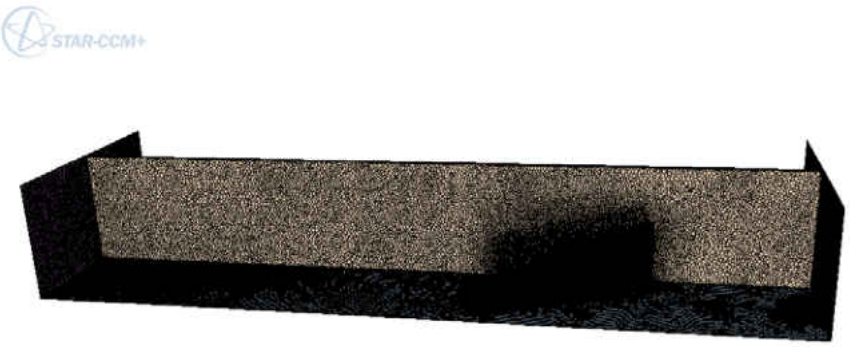

Figure 37: Case F Mesh

Multiple viewing planes and monitor points were also created prior to running the solution. The viewing planes were created to view the velocity vector plots at multiple locations along the streamwise direction as well as spanwise plans visualizing flow structures near the side walls, and top or bottom surface. The monitor points were placed at the top tip of the wedges and at the base of the wedges. The monitors determined maximum velocity at each point and were compared from all wedges in each case to check for fully developed flow. Mass flow rate for each case was also monitored to match with experimental cases after convergence.

The initial condition was set to the velocity for the 40,000 Reynolds number cases and the pressure drop as determined from the friction factor testing for each case was set in the periodic interface. The physics model selection or solution was set up with the parameters listed on the right in Figure 38. Realizable k-epsilon solvers were used for the RANS solution with constant density fluid (air) at steady conditions.

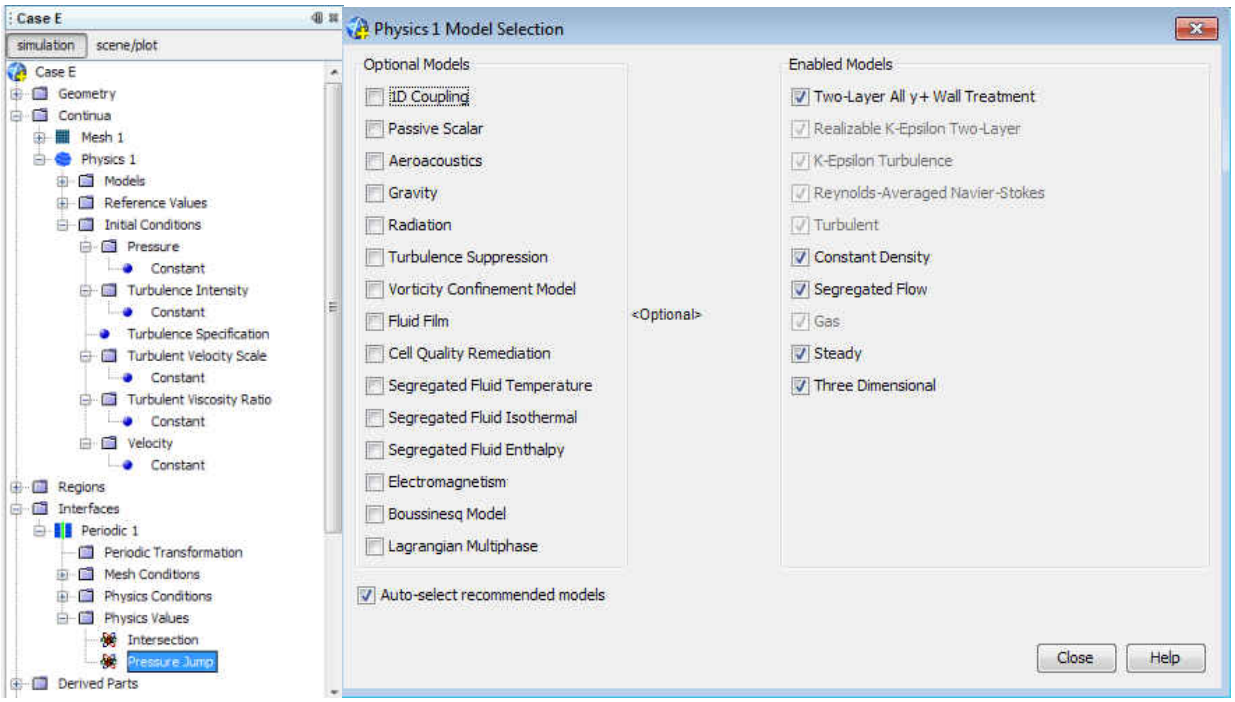

Figure 38: Physics Model Selection

Two plots were created when looking for convergence, the residual and the monitor points of maximum velocity. Reviewing the monitor points for maximum velocity, the system was converged once the velocities at all points stopped changing and showed the solution was fully developed because the values of points in corresponding locations on the wedges were aligned. Typically, the cases ran for 8,000 to 10,000 iterations for the results shown.

Images for the results were taken from the viewing planes created as velocity vectors to show the rotation of flow caused by the wedges, the interactions of the flows with the side walls, and the continuation of the secondary flows along the streamwise direction in the channel. These results are found in Chapter 3, listed for each case.

Uncertainty

The calculated experimental uncertainty for the overall heat transfer augmentation, friction factor augmentation, and thermal performance was performed using the procedures described by Kline and McClintock (Kline & McClintock, 1953).

$$u_R = \pm\sqrt{\sum_{i=1}^{L}(\theta_i u_{x_i})^2}$$

$$(95\%)$$

$$with$$

$$\theta_i = \left.\frac{\partial R}{\partial x_i}\right|_{x=\bar{x}};$$

$$i = 1,2,\ldots,L \qquad (17)$$

For the copper block experiment, the calculated experimental uncertainty for the overall Nusselt number augmentation was found to be 11%. To determine the highest possible uncertainty for all six cases, Case C at 10,000 Reynolds number results were used to calculate experimental uncertainty. The friction factor augmentation and channel Reynolds number uncertainties were 8% and 4%, respectively. The overall thermal performance for the copper block experiment was ~11%; exact values determined are in Table 6.

Table 6: Uncertainty (Copper-Block)

	Reynolds Number	Friction Factor Augmentation	Nusselt Number Augmentation	η
Uncertainty (%)	4.0	8.1	11.0	11.3

For the transient TLC experiment, the overall Nusselt number augmentation uncertainty was 21.4%. The MathCAD files, used to determine the uncertainty can be found in Appendix C.

Heat Loss into Acrylic for TLC

Calculation of the heat transfer coefficient for TLC results using lumped capacitance for the areas where copper features were attached to the acrylic does not account for heat loss into the acrylic. To determine the error in neglecting this loss, a transient conduction model was run in STAR-CCM+ using a large acrylic base with a copper wedge attached to the surface. Constant heat transfer coefficient was applied to all surfaces exposed to the flow and monitors to measure temperature were placed on non-featured areas as well as at the interface between the copper feature and the acrylic. Time and temperature from the monitor points were output to excel. An image of the transient conduction into the acrylic surface from STAR-CCM+ is in Figure 39.

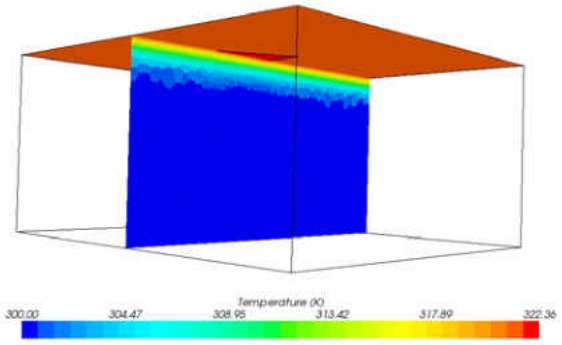

Figure 39: Transient Conduction into Acrylic

The curves for temperature as a function of time based on lumped capacitance (as calculated in the experiment), temperature as a function of time for the semi-infinite

model (non-featured areas), and the temperature as a function of time for the exact solution (as determined in STAR-CCM+ from the location at the interface between acrylic and copper) are shown in the plot below. A time correction coefficient was determined using the NLREG software and the exact data found for the semi-infinite (smooth wall) equation so that the exact solution for the heat transfer coefficient under the wedge features could be determined from the semi-infinite solution. The correction coefficient is multiplied by time in the semi-infinite Equation 14. This equation also includes the T_{bulk} step, which was not originally in the lumped capacitance calculation. Therefore to determine only the error with heat loss into the acrylic, lumped capacitance was calculated with stepping T_{bulk} first, then applying the correction to time. The results determined show <1% difference with the heat loss calculation added, but a 4% difference with the stepping T_{bulk} added. More error is associated with the T_{bulk} calculation in the original lumped capacitance calculation, increasing the overall Nusselt number augmentation by 4%, closer to the copper block results. The corrected semi-infinite solution is shown as SEMI-CORR in Figure 40. From this plot it is clear that the semi-infinite correction only works at short times (time <25 seconds), before deviating from the exact solution.

Table 7: Percent Errors with LC Calculations

Method	% Difference from Original Calculation for Nu Augmentation
Tbulk stepping	4.1%
Semi-infinite correction	3.8%

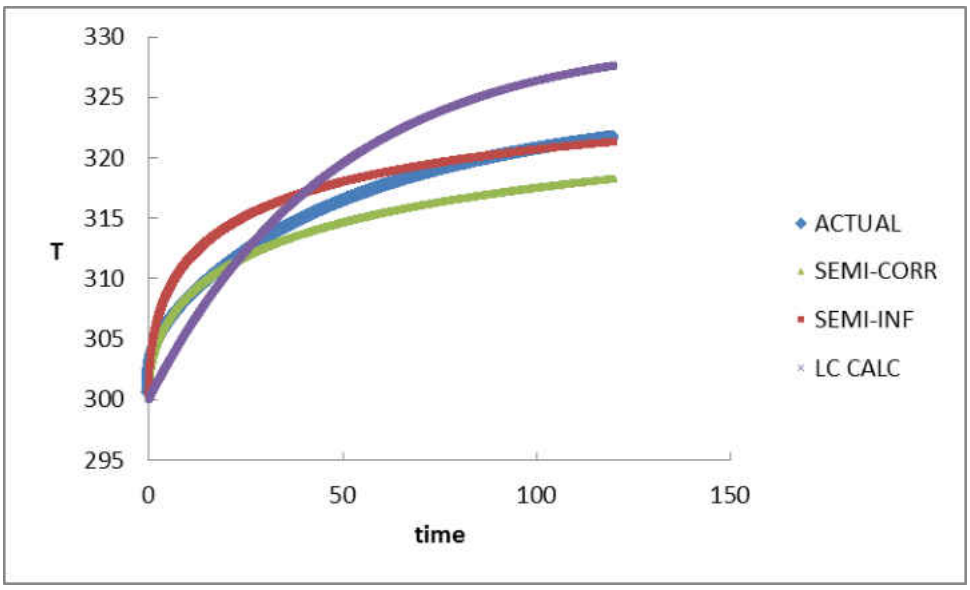

Figure 40: Heat Loss into Acrylic Correction

Since the semi-infinite correction does not follow the actual solution after a given amount of time, a second correction was determined for the time (in this example) after 25 seconds. The actual solution curve was found to match a semi-infinite curve for the time up to 25 seconds and a lumped capacitance curve after 25 seconds. A plot of the actual solution from STAR-CCM+ and the correction developed from the two functions is shown in Figure 41. The multiple function correction proposes difficulty in determining a general correction to implement into the MATLAB processing code. Further study is then necessary to determine the exact correction to be implemented, which will further raise the value for heat transfer coefficient following the curve for the semi-infinite correction used were time will be decreased to the exact solution, increasing heat transfer coefficient.

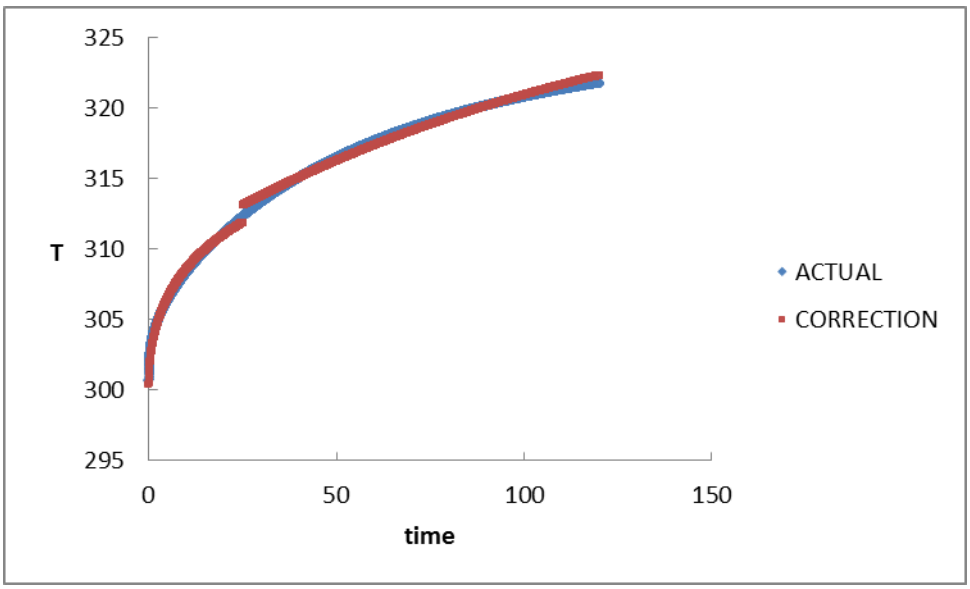

Figure 41: Heat Loss Correction Curve

Transient TLC Bulk Temperature

The method for which the bulk temperature is determined for the transient TLC tests makes a substantial difference in the results for heat transfer coefficient, up to 40 percent according to a study by Chyu et al. (Chyu, Ding, Downs, & Soechting, 1998). This study reviewed four methods for determining T_{bulk} and found one method to be particularly close to the exact solution. The best method found in this study consisted of using invariant local heat flux, where a conversion factor was determined to convert heat transfer coefficient based on inlet bulk temperature to a 'corrected' heat transfer coefficient. To determine the error associated with the nonlinear regression T_{bulk} calculation for the current study, the best solution as determined from the study by Chyu et al. is completed for the large full wedge two wall Case C. Values for overall Nusselt number augmentations as determined from 2 methods are reported in the tables below: marching bulk (as presented in results) and Chyu's conversion factor. The offset

associated with the bulk temperature calculation used in this study in comparison with Chyu's conversion factor helps the reader understand a large issue in comparing the TLC experiment to the copper block. The MATLAB codes for determining Nusselt number augmentation based on the conversion factor presented by Chyu et al. is in Appendix A.

Table 8: Case C Nu Augmentation from Tbulk Comparison (as % from Copper-Block) 20,000 Re

	Nu Aug	% from Cu-Block
Marching Tbulk	2.10	-6.5
Chyu Conversion	2.31	+2.4

The method proposed by Chyu however was not designed for use on the areas where lumped capacitance is used (underneath the wedge features). Once a correction using the semi-infinite equation for the exact solution under the copper wedge features is determined, the results for the Chyu method may vary.

CHAPTER 3: RESULTS

Friction Factor

Friction factor results determined at all four Reynolds numbers tested for all two and one wall cases as well as the baseline validation are shown in the following sections below, separated by case.

Baseline

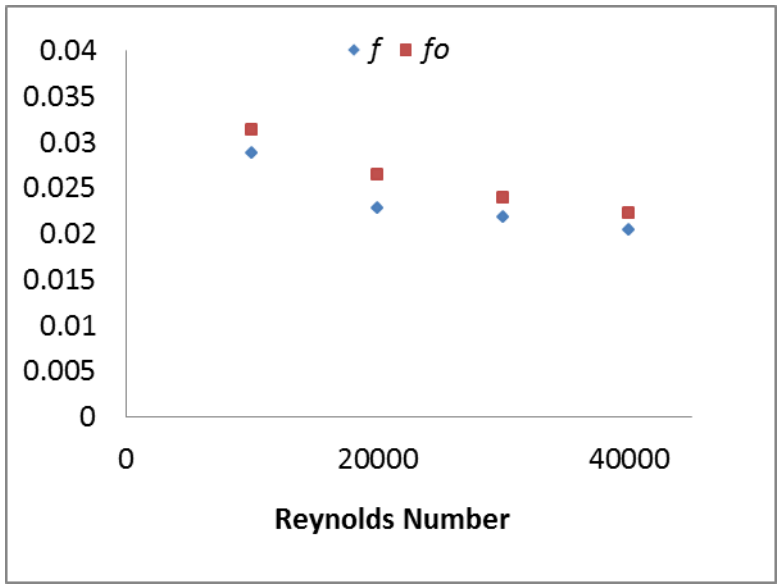

Figure 42: Friction Factor Results SW

Table 9: Friction Factor Augmentation SW

Nominal Reynolds Number	10,000	20,000	30,000	40,000
Actual Reynolds Number	10340	20400	29970	40150
Friction Factor Augmentation (f/f_o)	0.92*	0.87*	0.91*	0.92*

Results for the friction factor augmentations of all cases are augmented by the Blasius correlation for a smooth pipe. Results marked with an asterisk (*) indicate values that are less than one, resulting from augmenting with the Blasius solution,

rather than augmenting to the baseline case. These values should then be considered to be equal to one, i.e. no increase in friction over the smooth wall baseline case.

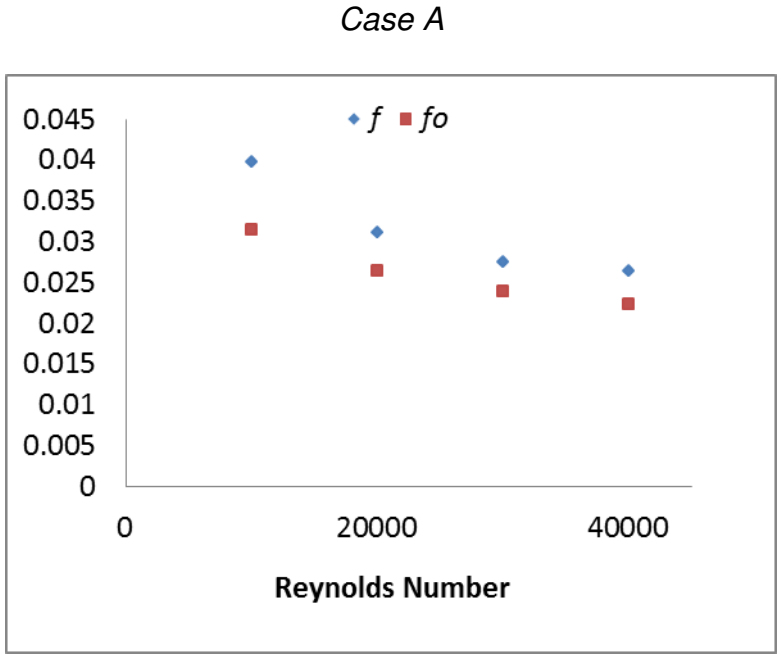

Figure 43: Friction Factor Results Case A

Table 10: Friction Factor Augmentation Case A

Nominal Reynolds Number	10,000	20,000	30,000	40,000
Actual Reynolds Number	10150	20290	29910	39920
Friction Factor Augmentation (f/f_o)	1.26	1.17	1.14	1.17

Case B

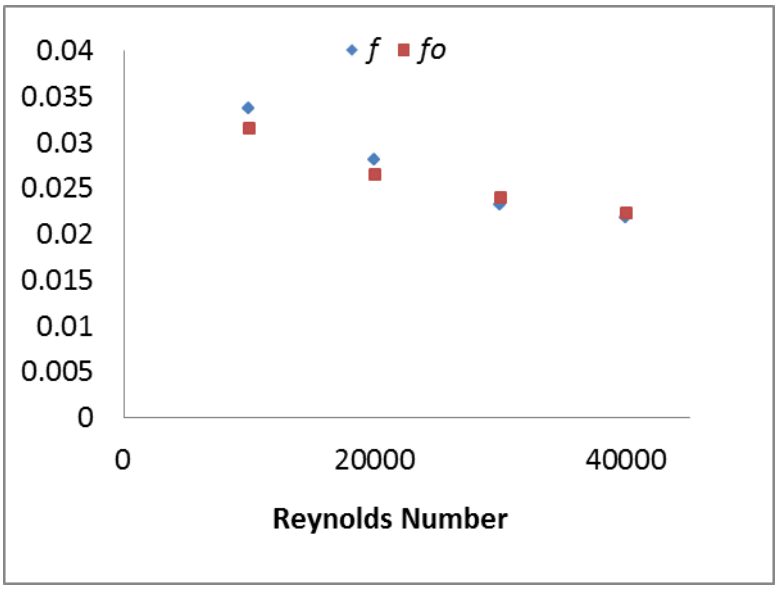

Figure 44: Friction Factor Results Case B

Table 11: Friction Factor Augmentation Case B

Nominal Reynolds Number	10,000	20,000	30,000	40,000
Actual Reynolds Number	10180	20230	30160	40060
Friction Factor Augmentation (f/f_o)	1.07	1.06	0.97*	0.98*

Case C

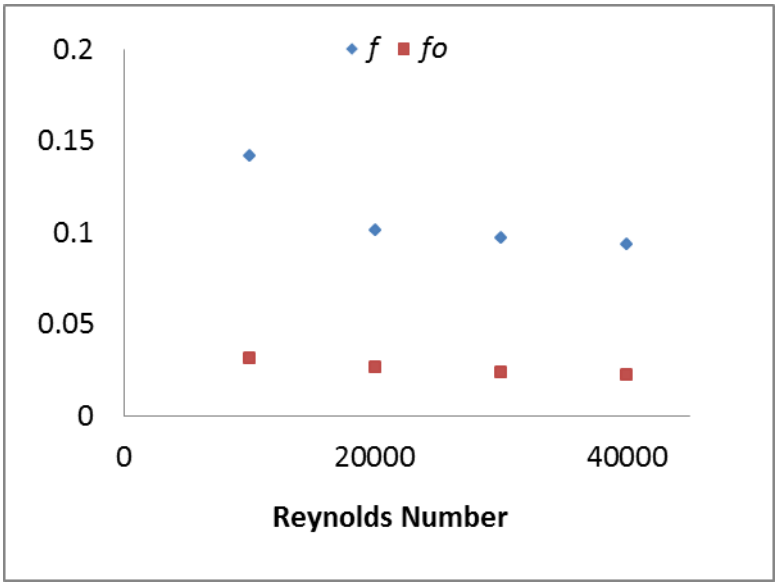

Figure 45: Friction Factor Results Case C

Table 12: Friction Factor Augmentation Case C

Nominal Reynolds Number	10,000	20,000	30,000	40,000
Actual Reynolds Number	10300	20130	29860	40080
Friction Factor Augmentation (f/f_o)	4.51	3.80	4.02	4.17

Case D

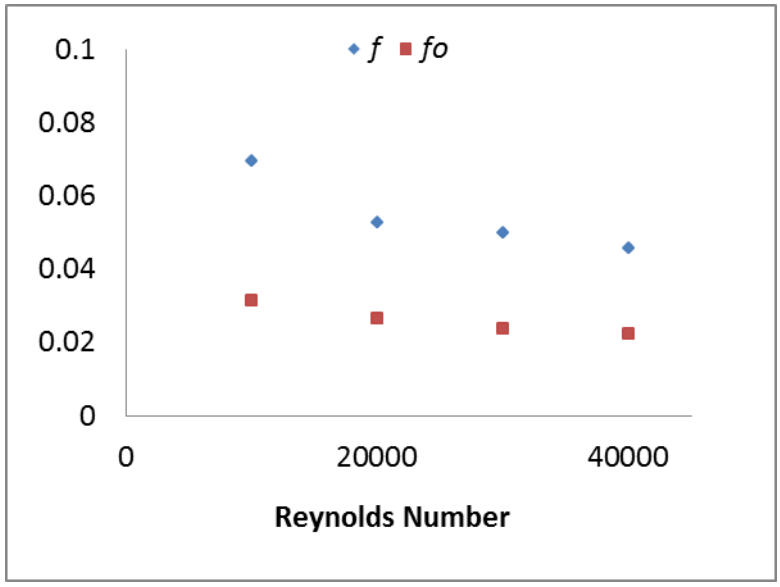

Figure 46: Friction Factor Results Case D

Table 13: Friction Factor Augmentation Case D

Nominal Reynolds Number	10,000	20,000	30,000	40,000
Actual Reynolds Number	10250	20220	29890	40120
Friction Factor Augmentation (f/f_o)	2.21	1.99	2.07	2.04

Case E

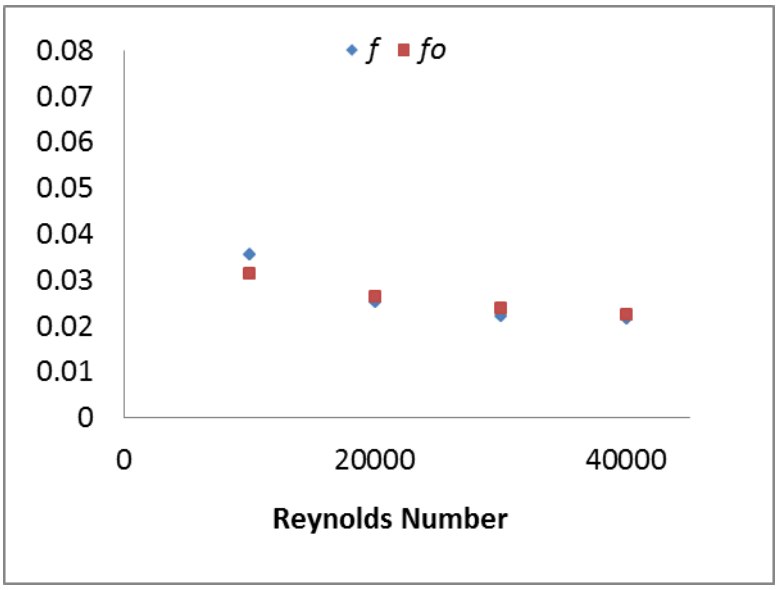

Figure 47: Friction Factor Results Case E

Table 14: Friction Factor Augmentation Case E

Nominal Reynolds Number	10,000	20,000	30,000	40,000
Actual Reynolds Number	10300	20210	30080	40140
Friction Factor Augmentation (f/f_o)	1.14	0.95*	0.92*	0.97*

Case F

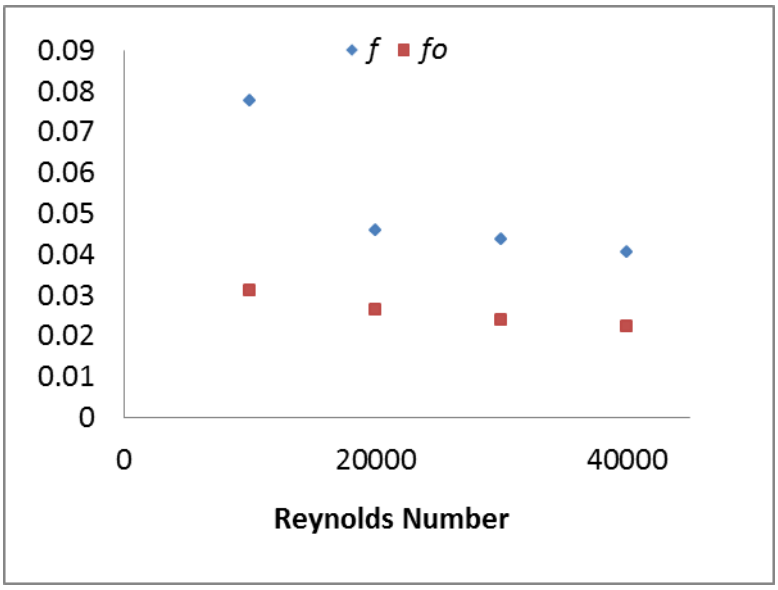

Figure 48: Friction Factor Results Case F

Table 15: Friction Factor Augmentation Case F

Nominal Reynolds Number	10,000	20,000	30,000	40,000
Actual Reynolds Number	10300	20250	29950	40140
Friction Factor Augmentation (f/f_o)	2.48	1.73	1.82	1.82

Segmented Copper Blocks

The results shown as Nusselt number for each modular location along with comparison to Dittus-Boelter for all Reynolds numbers are shown in the plots below, per case. The smooth side walls are averaged together and featured walls are averaged, top and bottom for the two wall cases, separated for one wall cases. Comparisons of overall Nusselt number augmentations and thermal performance are discussed and shown in Chapter 4.

Baseline

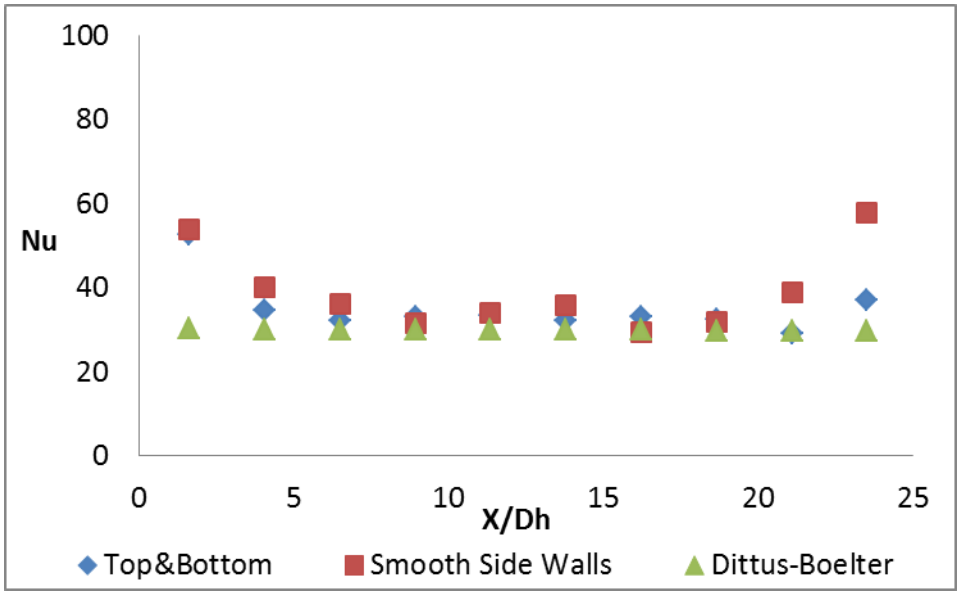

Figure 49: SW 10,000 Copper Block Nusselt Number

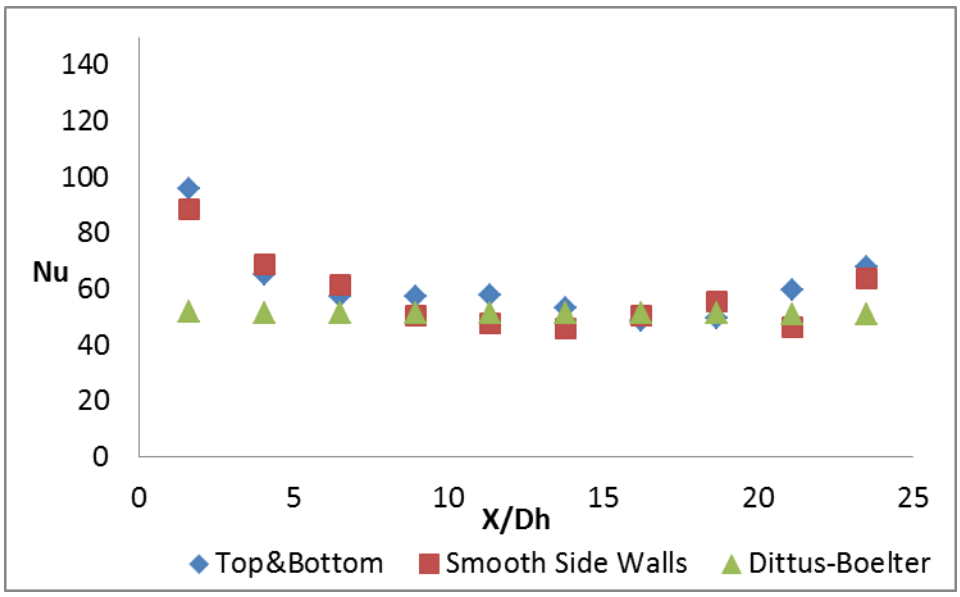

Figure 50: SW 20,000 Copper Block Nusselt Number

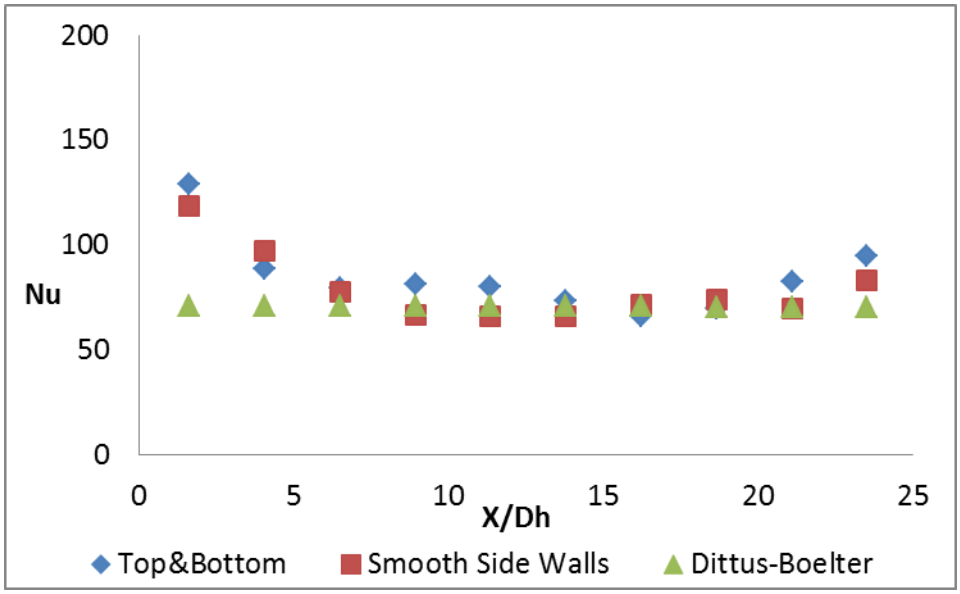

Figure 51: SW 30,000 Copper Block Nusselt Number

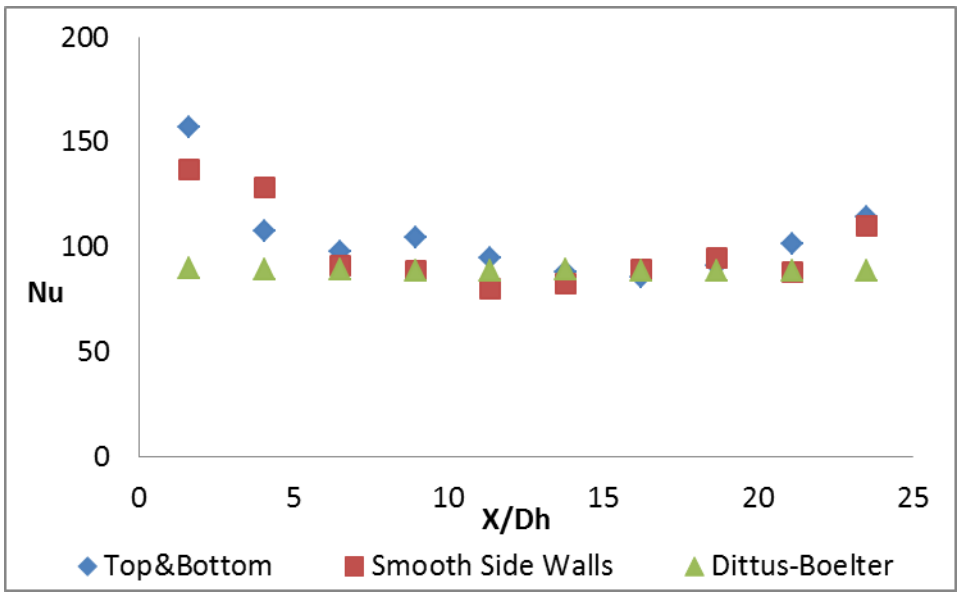

Figure 52: SW 40,000 Copper Block Nusselt Number

Table 16: Overall Augmentations SW Copper-Block

Nominal Reynolds Number	10,000	20,000	30,000	40,000
Actual Reynolds Number	9330	18300	27350	36320
$\frac{Nu}{Nu_{DB}}$	1.09	1.01	1.01	1.01

Case A

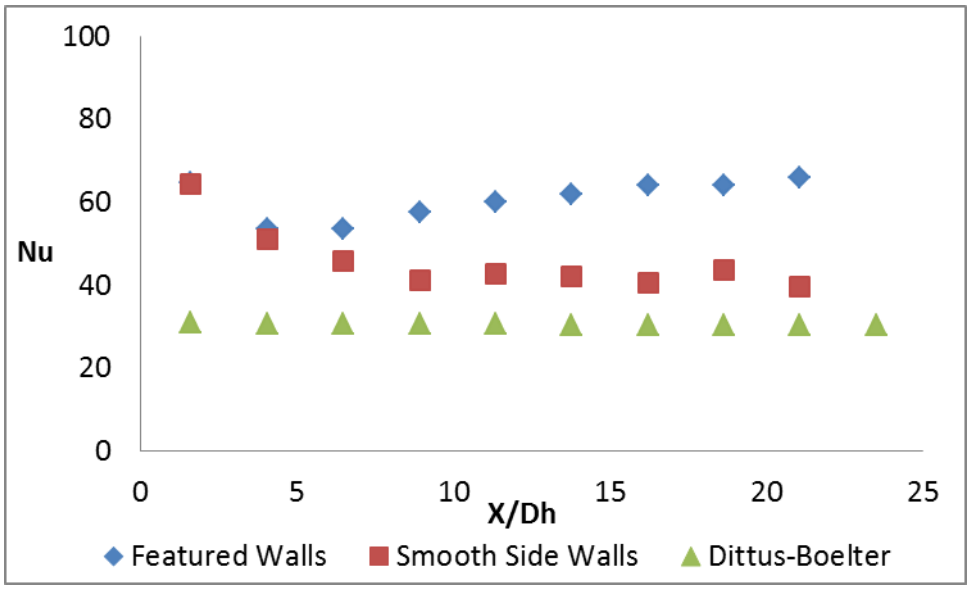

Figure 53: Case A 10,000 Copper Block Nusselt Number

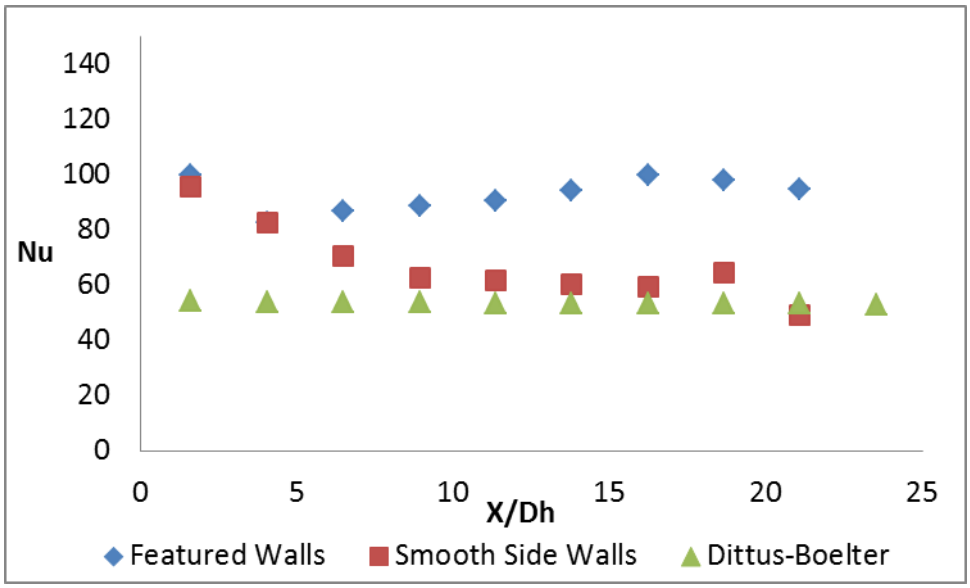

Figure 54: Case A 20,000 Copper Block Nusselt Number

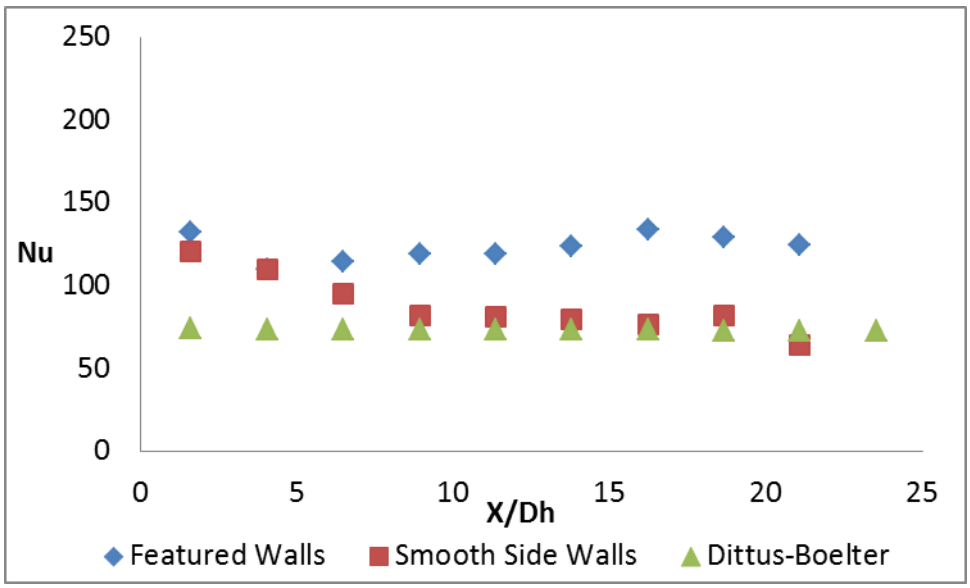

Figure 55: Case A 30,000 Copper Block Nusselt Number

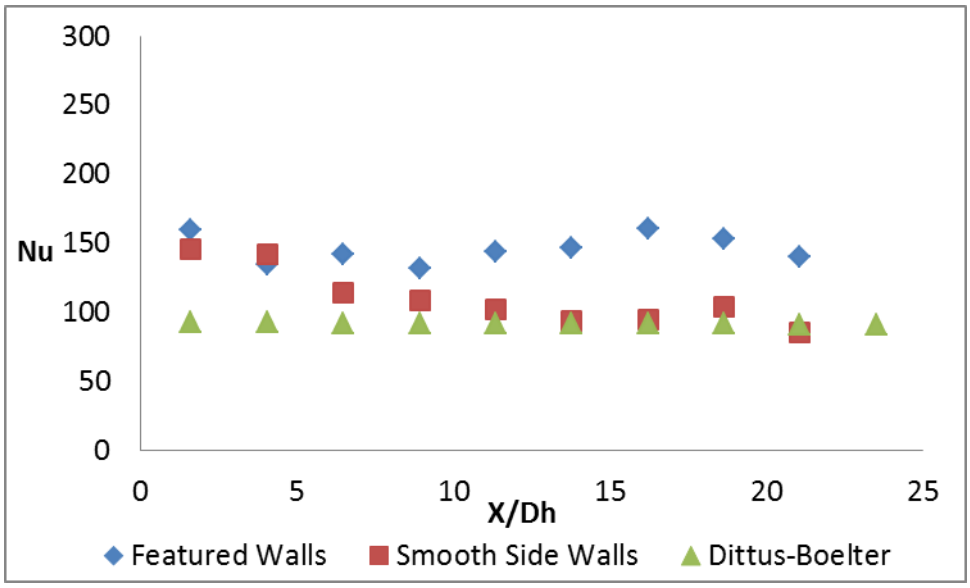

Figure 56: Case A 40,000 Copper Block Nusselt Number

Table 17: Overall Augmentations Case A Copper-Block

Nominal Reynolds Number	10,000	20,000	30,000	40,000
Actual Reynolds Number	9500	19200	28500	37700
$\frac{Nu}{Nu_{DB}}$	1.81	1.56	1.50	1.44

Case B

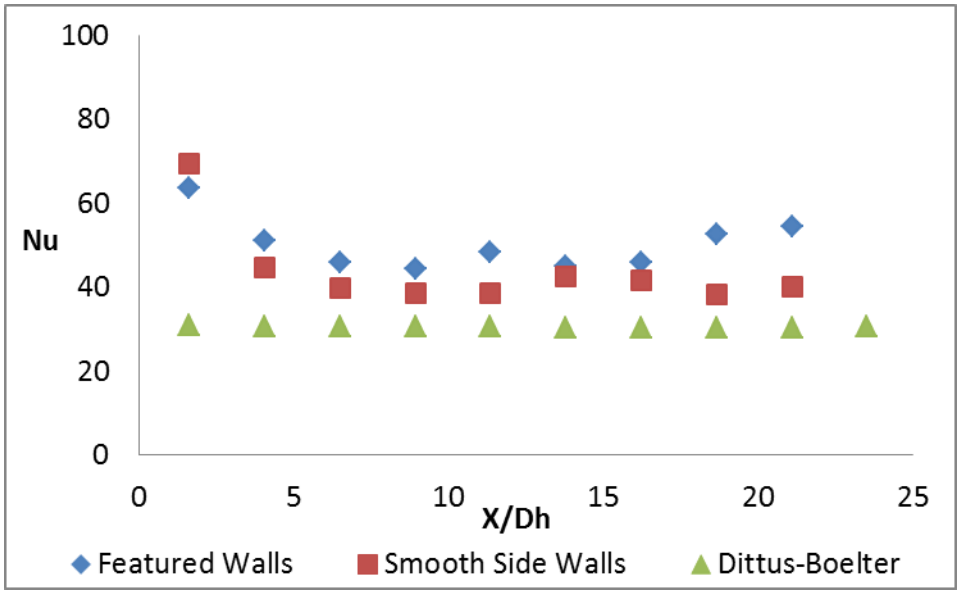

Figure 57: Case B 10,000 Copper Block Nusselt Number

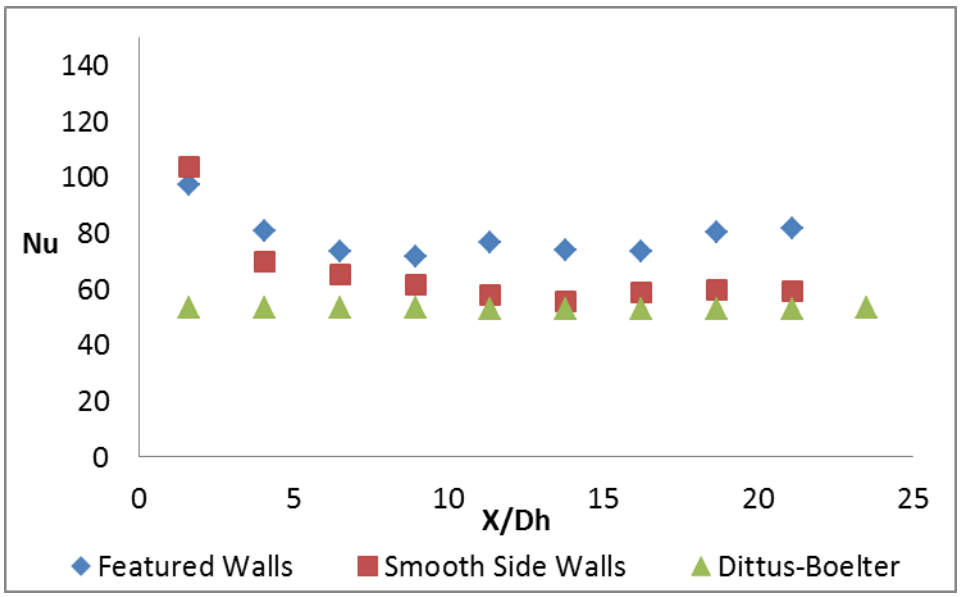

Figure 58: Case B 20,000 Copper Block Nusselt Number

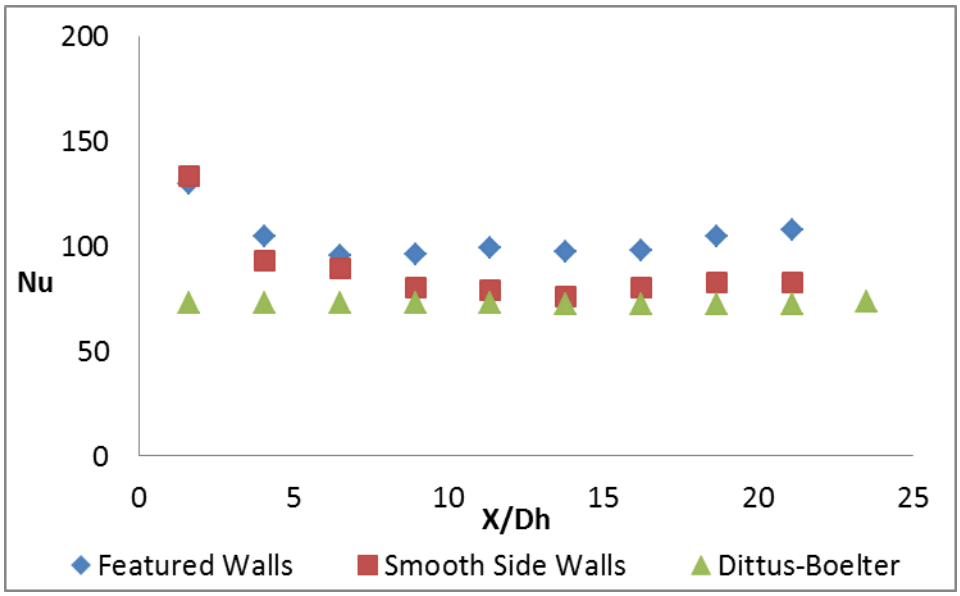

Figure 59: Case B 30,000 Copper Block Nusselt Number

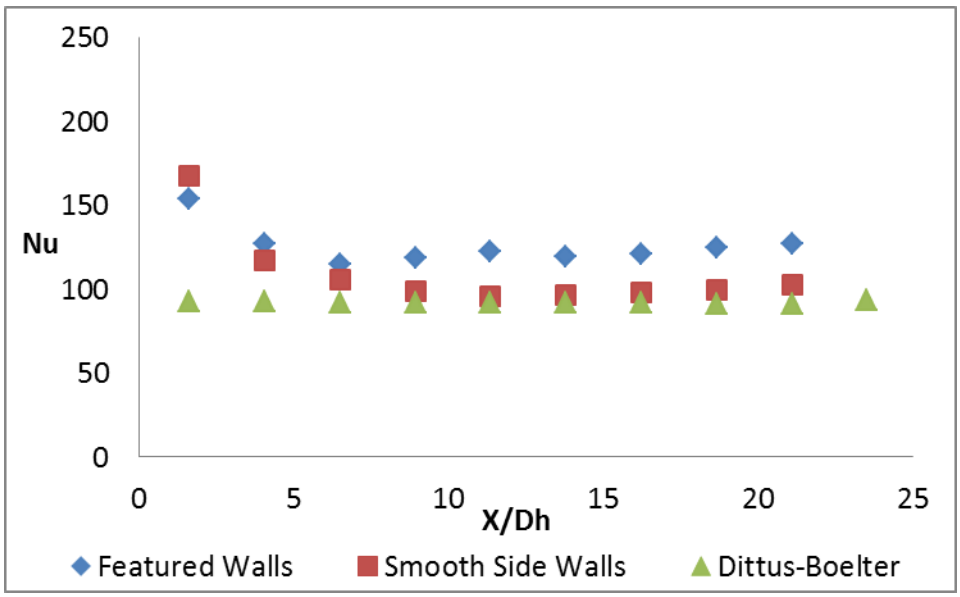

Figure 60: Case B 40,000 Copper Block Nusselt Number

Table 18: Overall Augmentations Case B Copper-Block

Nominal Reynolds Number	10,000	20,000	30,000	40,000
Actual Reynolds Number	9500	19000	28200	37800
$\frac{Nu}{Nu_{DB}}$	1.47	1.32	1.27	1.24

Case C

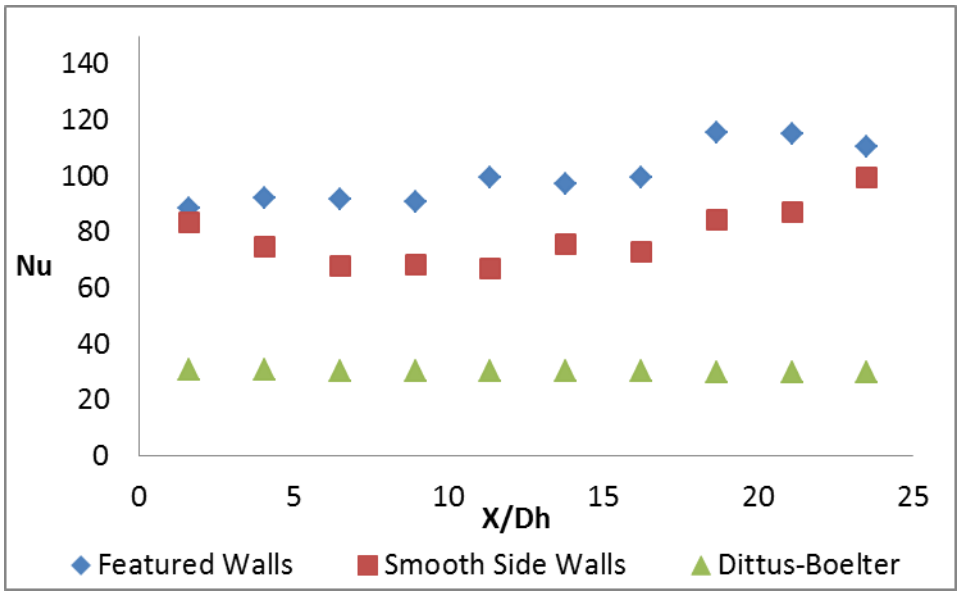

Figure 61: Case C 10,000 Copper Block Nusselt Number

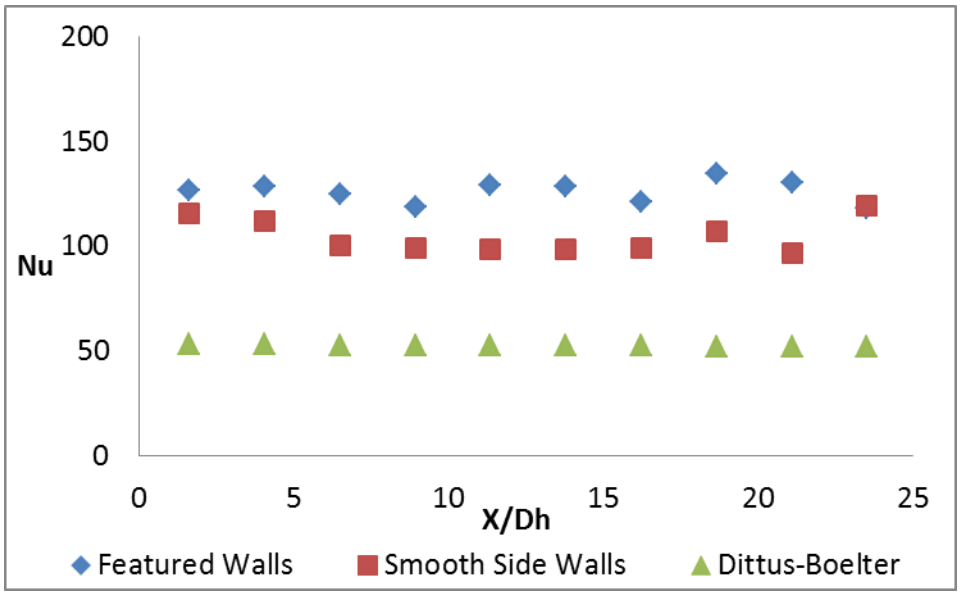

Figure 62: Case C 20,000 Copper Block Nusselt Number

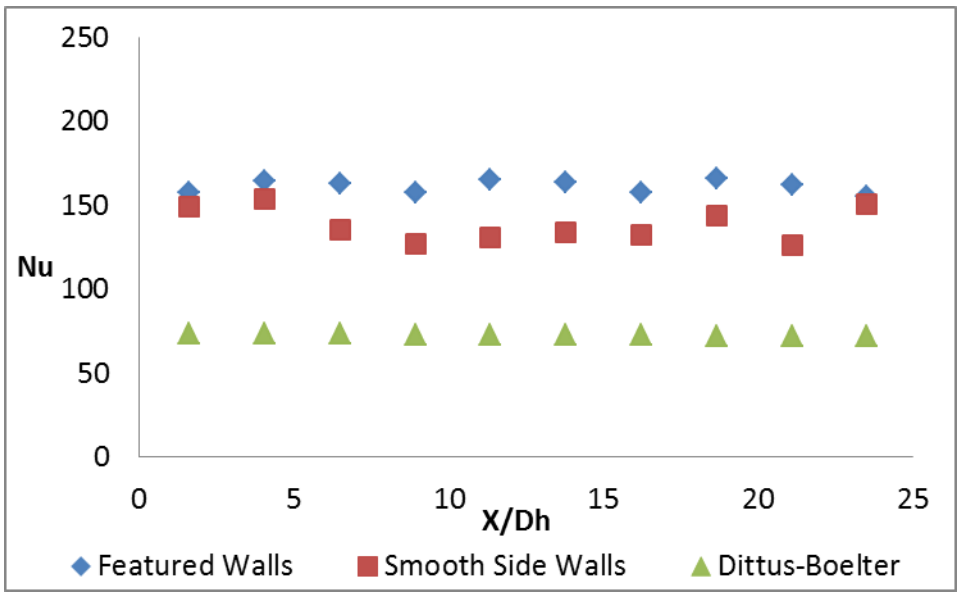

Figure 63: Case C 30,000 Copper Block Nusselt Number

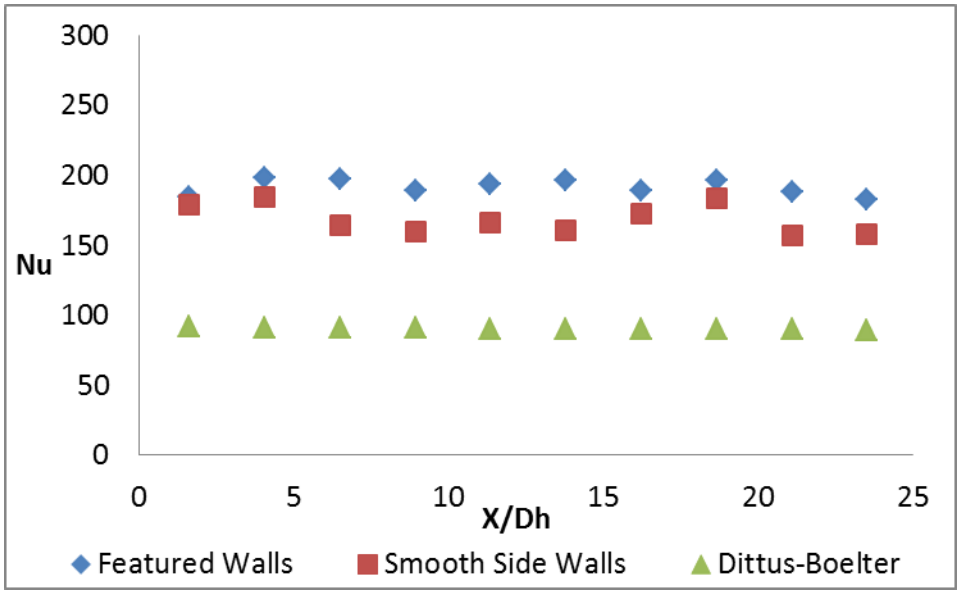

Figure 64: Case C 40,000 Copper Block Nusselt Number

Table 19: Overall Augmentations Case C Copper-Block

Nominal Reynolds Number	10,000	20,000	30,000	40,000
Actual Reynolds Number	9500	18900	28300	37100
$\frac{Nu}{Nu_{DB}}$	3.03	2.25	2.10	2.05

Case D

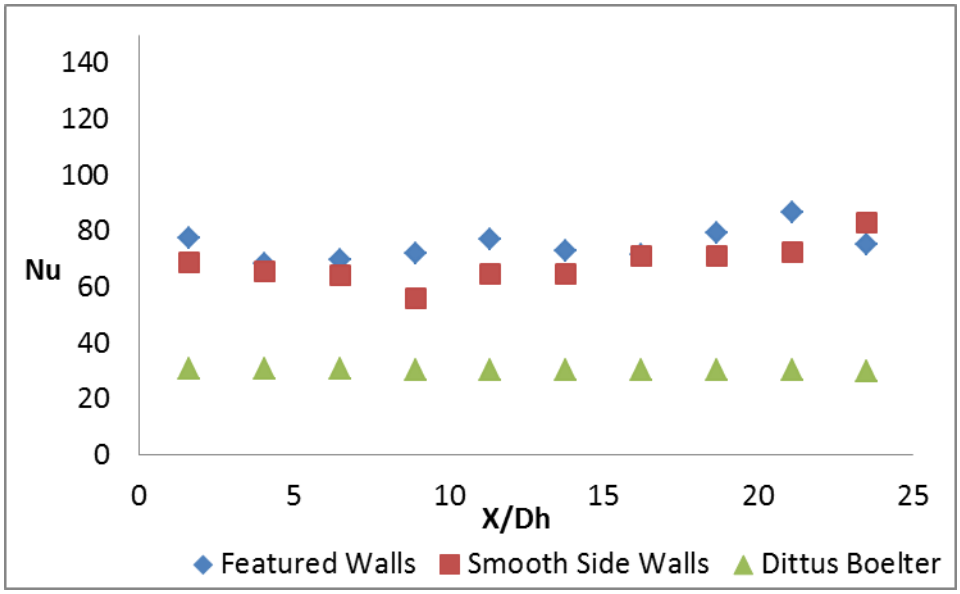

Figure 65: Case D 10,000 Copper Block Nusselt Number

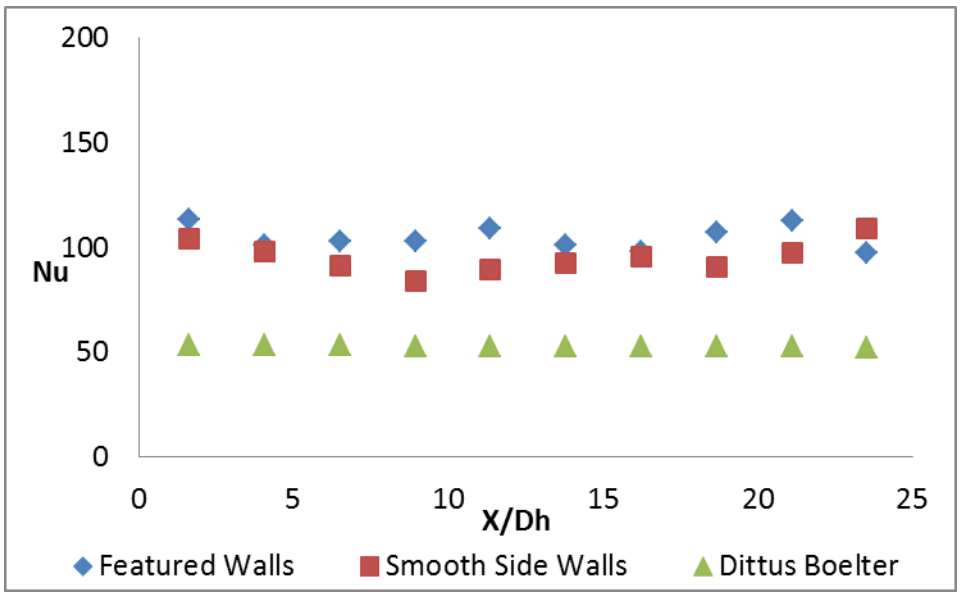

Figure 66: Case D 20,000 Copper Block Nusselt Number

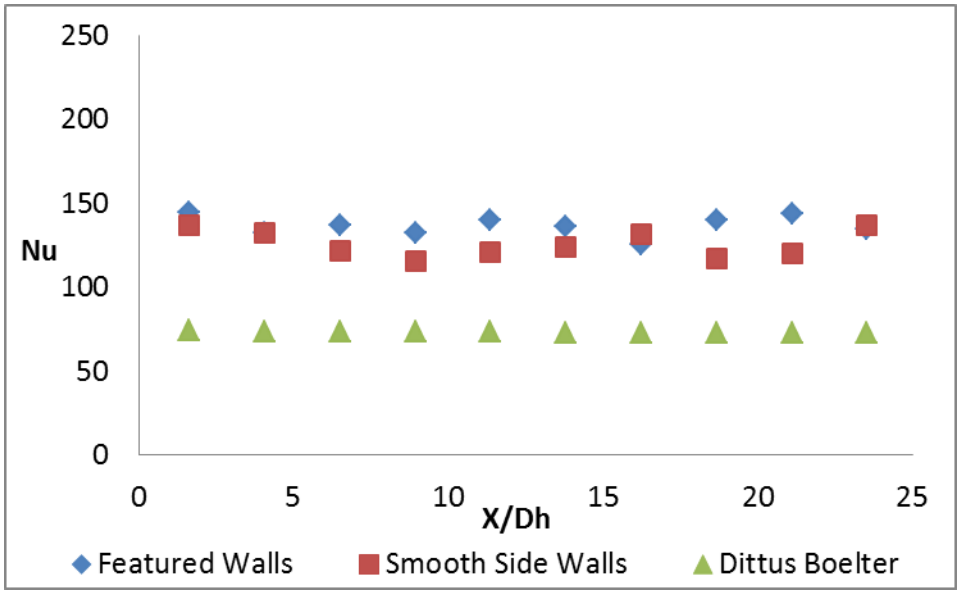

Figure 67: Case D 30,000 Copper Block Nusselt Number

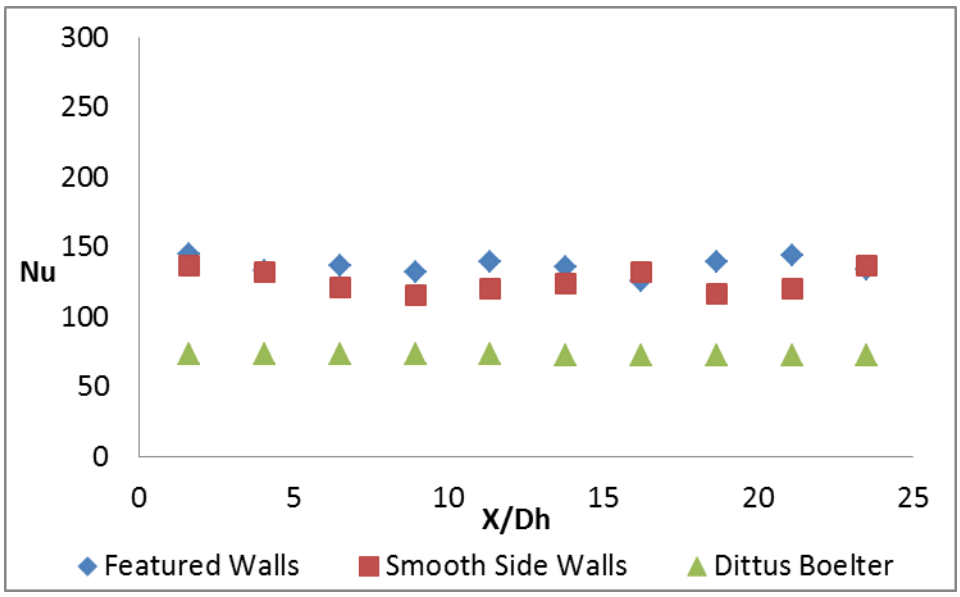

Figure 68: Case D 40,000 Copper Block Nusselt Number

Table 20: Overall Augmentations Case D Copper-Block

Nominal Reynolds Number	10,000	20,000	30,000	40,000
Actual Reynolds Number	9500	19000	28500	37500
$\frac{Nu}{Nu_{DB}}$	2.36	1.88	1.79	1.71

Case E

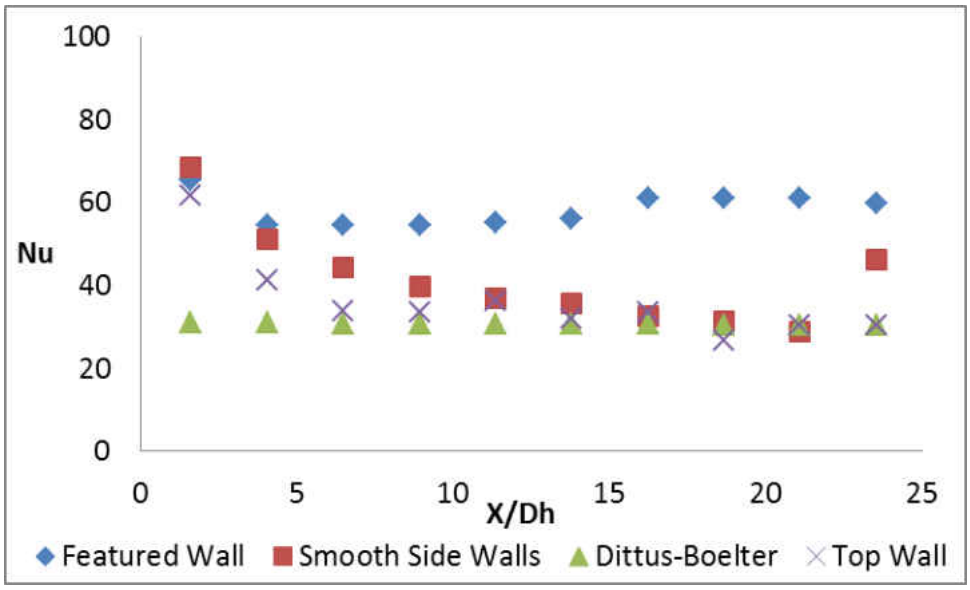

Figure 69: Case E 10,000 Copper Block Nusselt Number

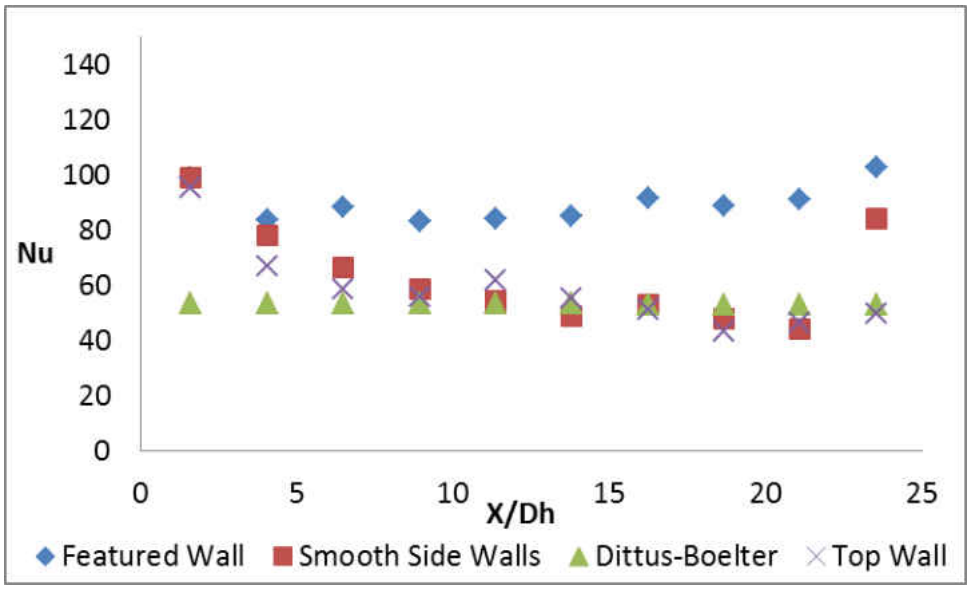

Figure 70: Case E 20,000 Copper Block Nusselt Number

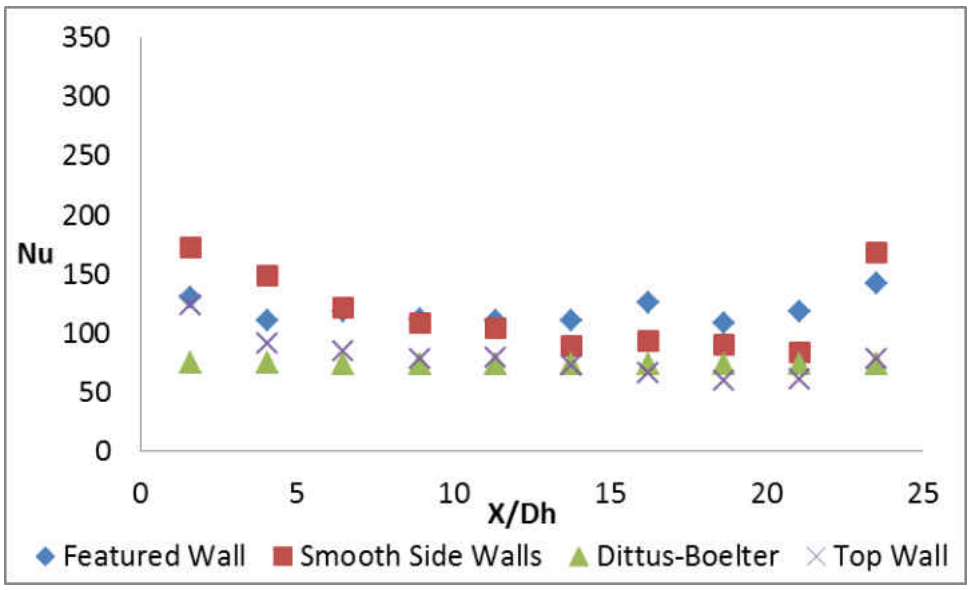

Figure 71: Case E 30,000 Copper Block Nusselt Number

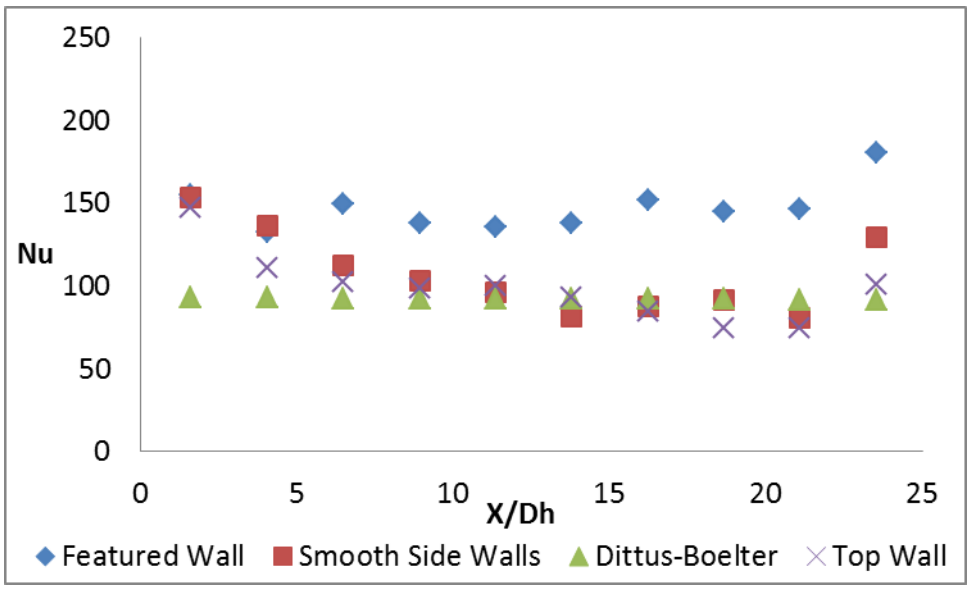

Figure 72: Case E 40,000 Copper Block Nusselt Number

Table 21: Overall Augmentations Case E Copper-Block

Nominal Reynolds Number	10,000	20,000	30,000	40,000
Actual Reynolds Number	9530	19050	28700	37900
$\frac{Nu}{Nu_{DB}}$	1.37	1.21	1.16	1.17

Case F

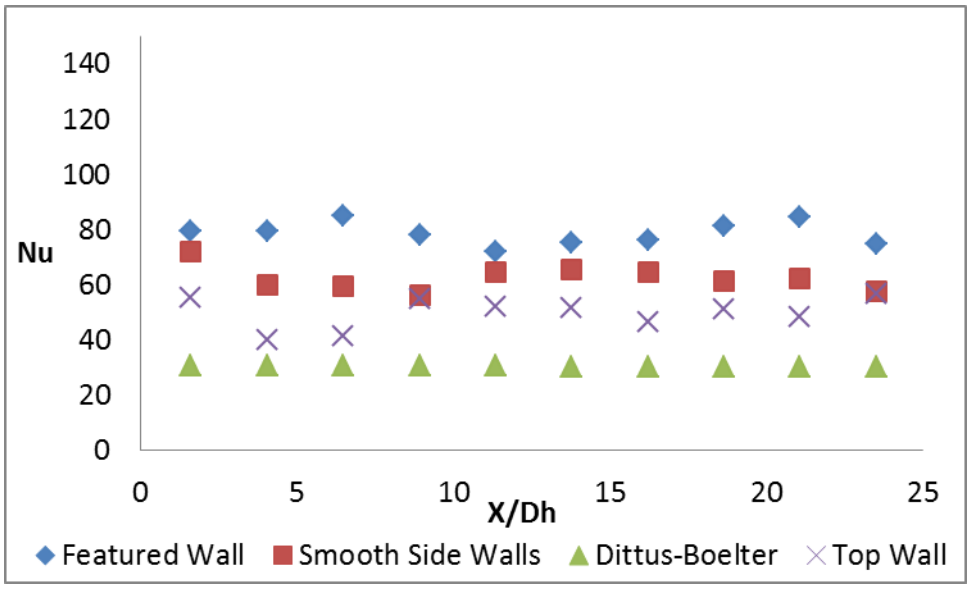

Figure 73: Case F 10,000 Copper Block Nusselt Number

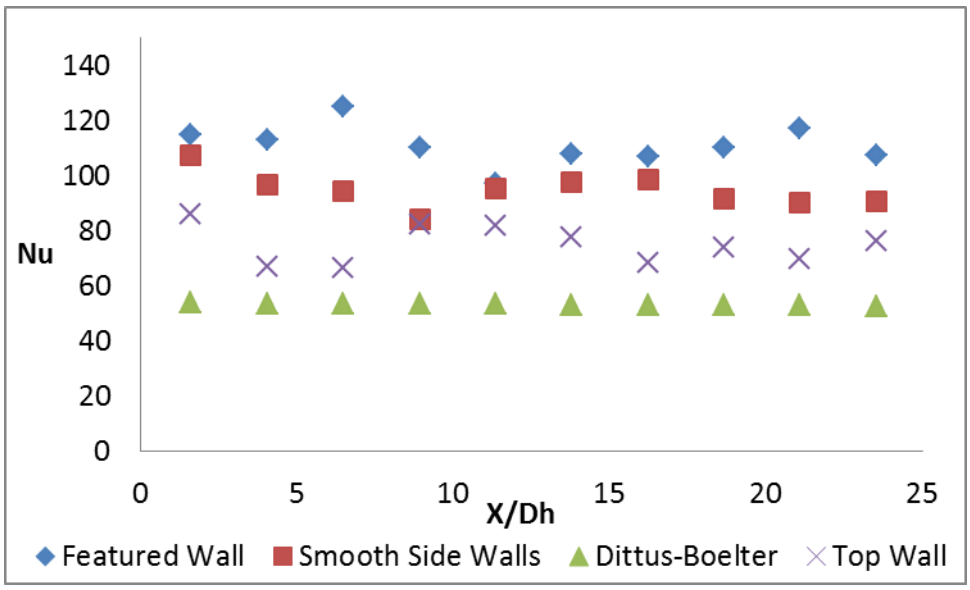

Figure 74: Case F 20,000 Copper Block Nusselt Number

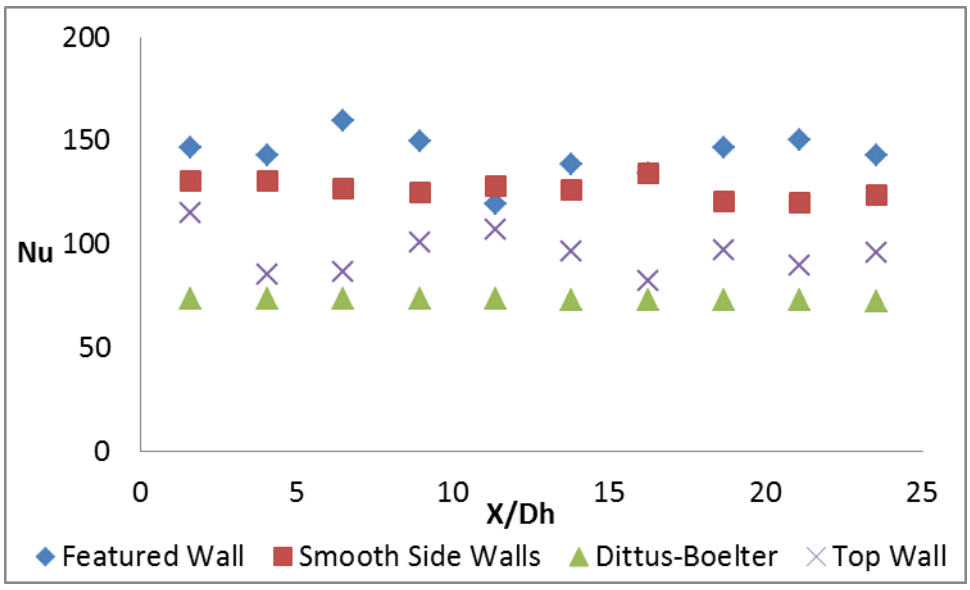

Figure 75: Case F 30,000 Copper Block Nusselt Number

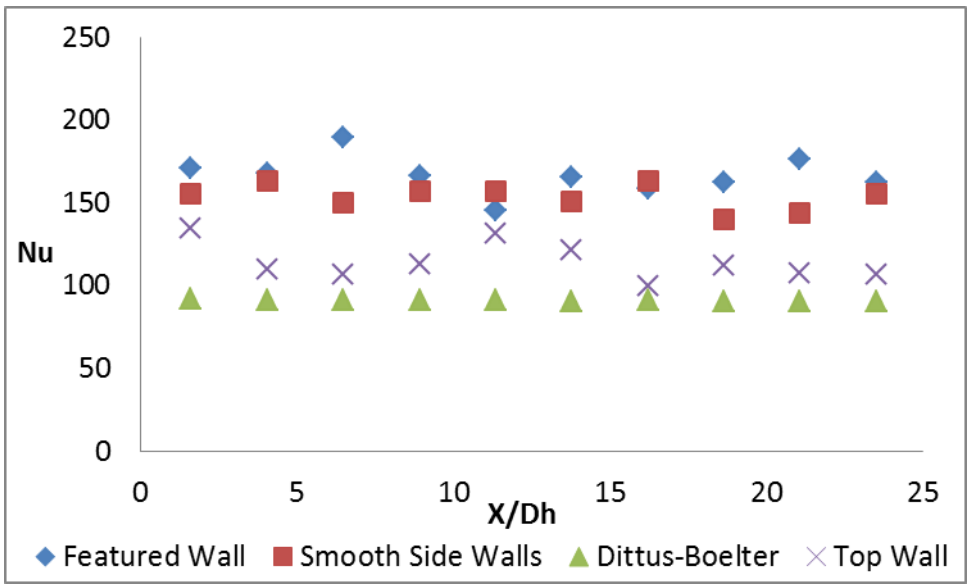

Figure 76: Case F 40,000 Copper Block Nusselt Number

Table 22: Overall Augmentations Case F Copper-Block

Nominal Reynolds Number	10,000	20,000	30,000	40,000
Actual Reynolds Number	9500	19000	28500	37400
$\frac{Nu}{Nu_{DB}}$	2.09	1.74	1.65	1.57

Copper-Block Thermal Performances

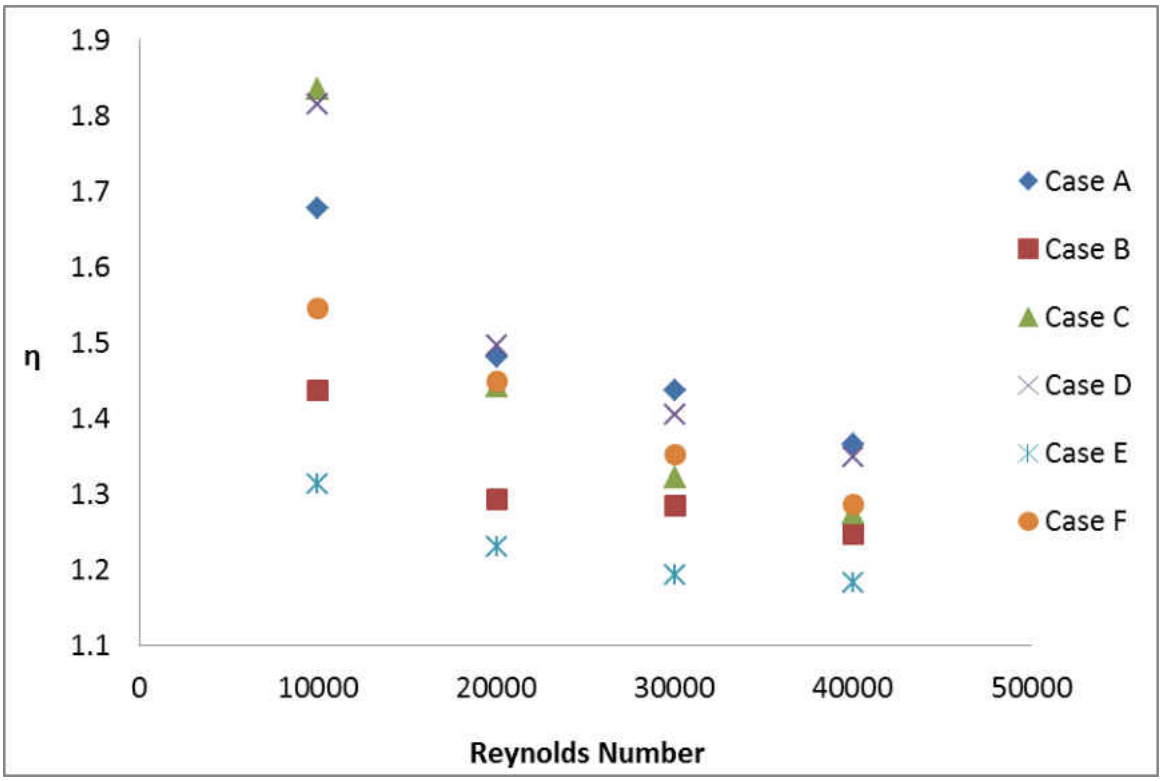

Figure 77: Thermal Performance Copper Block

Table 23: Thermal Performance (η) Values Copper-Block Setup

	Case A	Case B	Case C	Case D	Case E	Case F
10000	1.68	1.44	1.83	1.81	1.31	1.54
20000	1.48	1.29	1.44	1.50	1.23	1.45
30000	1.44	1.28	1.32	1.40	1.19	1.35
40000	1.37	1.25	1.27	1.35	1.18	1.29

Transient TLC

Baseline

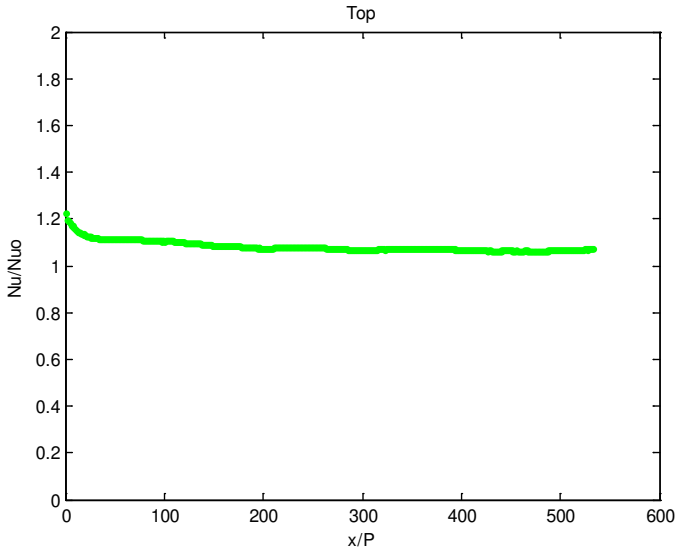

Figure 78: SW TLC Streamwise Averaged Nu/Nuo Top 10,000 Re

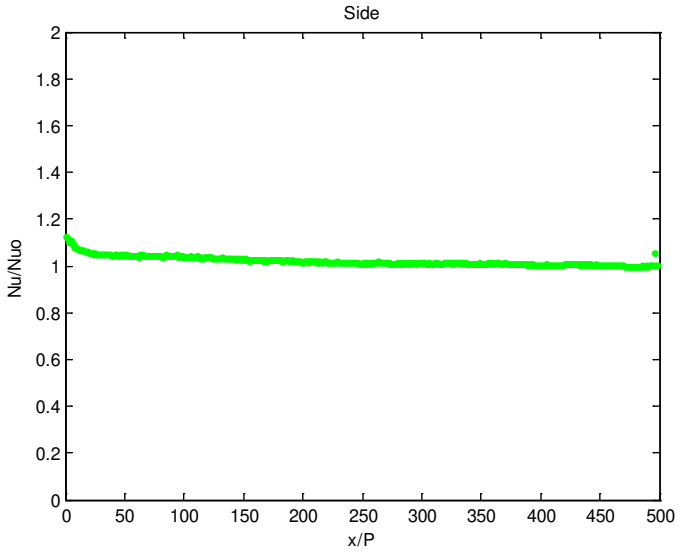

Figure 79: SW TLC Streamwise Averaged Nu/Nuo Side 10,000 Re

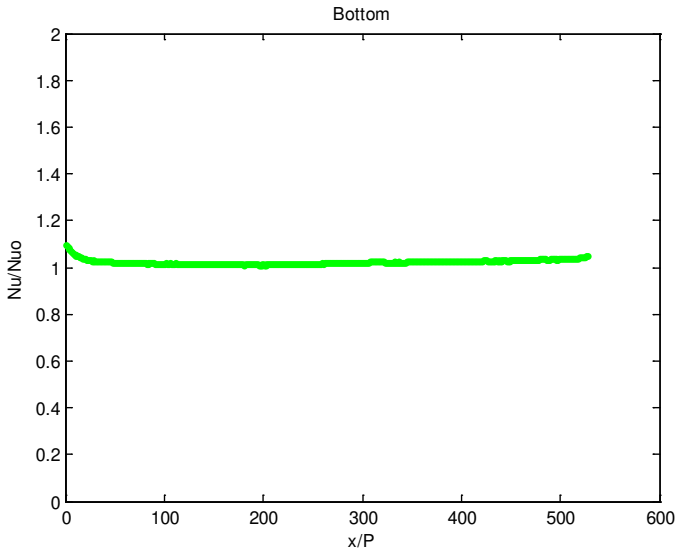

Figure 80: SW TLC Streamwise Averaged Nu/Nuo Bottom 10,000 Re

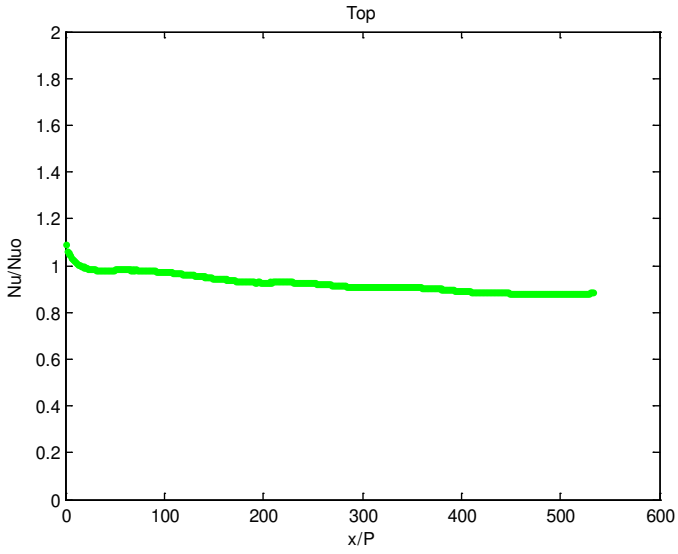

Figure 81: SW TLC Streamwise Averaged Nu/Nuo Top 20,000 Re

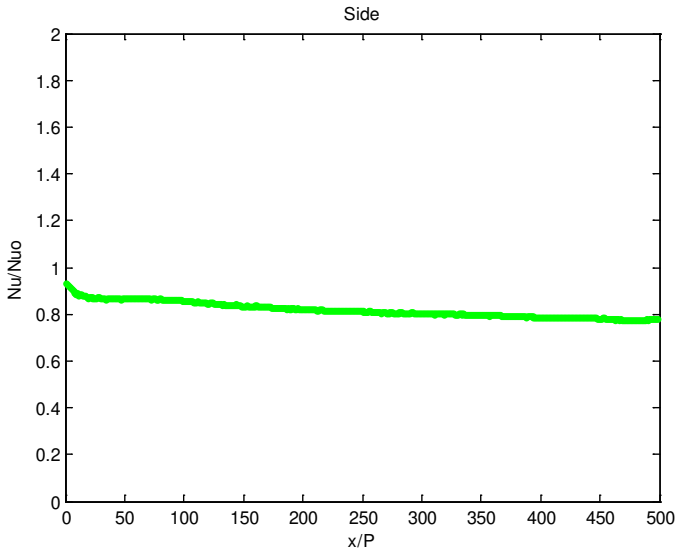

Figure 82: SW TLC Streamwise Averaged Nu/Nuo Side 20,000 Re

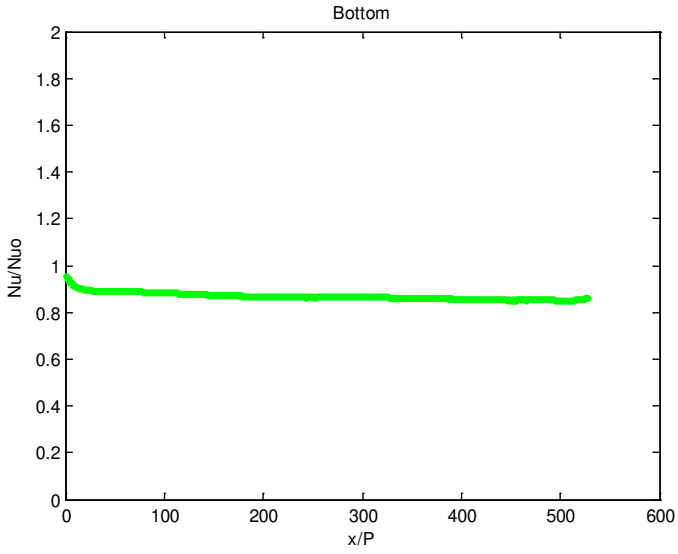

Figure 83: SW TLC Streamwise Averaged Nu/Nuo Bottom 20,000 Re

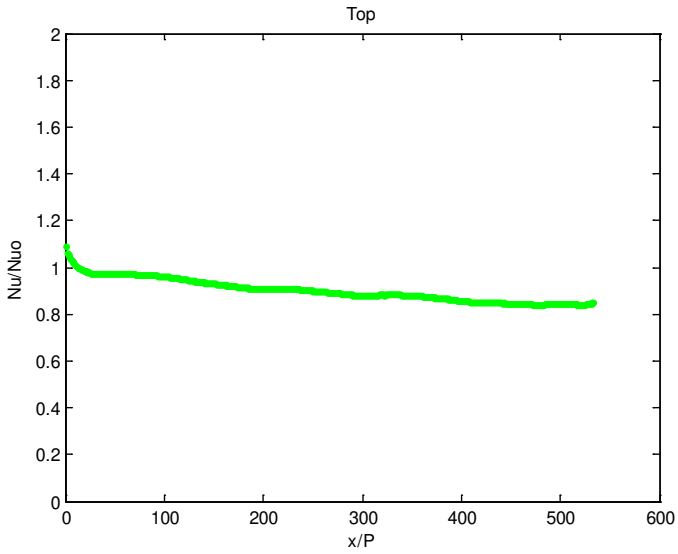

Figure 84: SW TLC Streamwise Averaged Nu/Nuo Top 30,000 Re

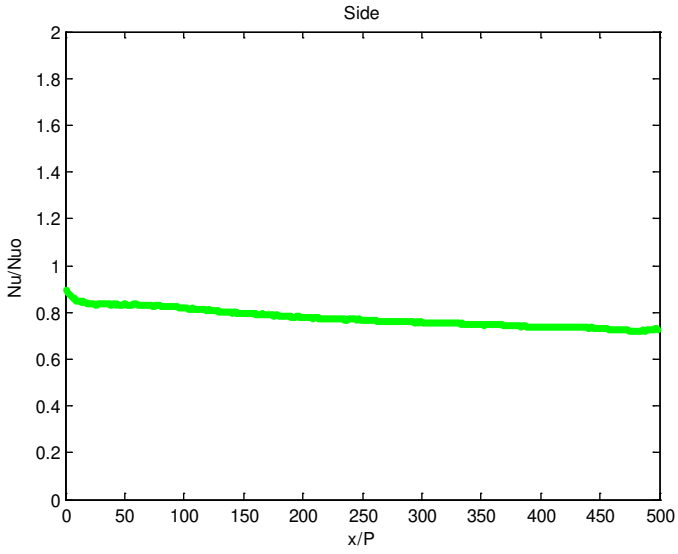

Figure 85: SW TLC Streamwise Averaged Nu/Nuo Side 30,000 Re

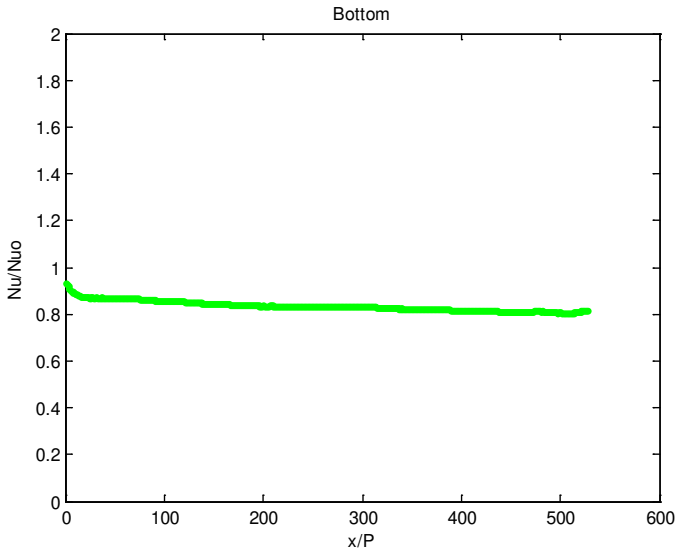

Figure 86: SW TLC Streamwise Averaged Nu/Nuo Bottom 30,000 Re

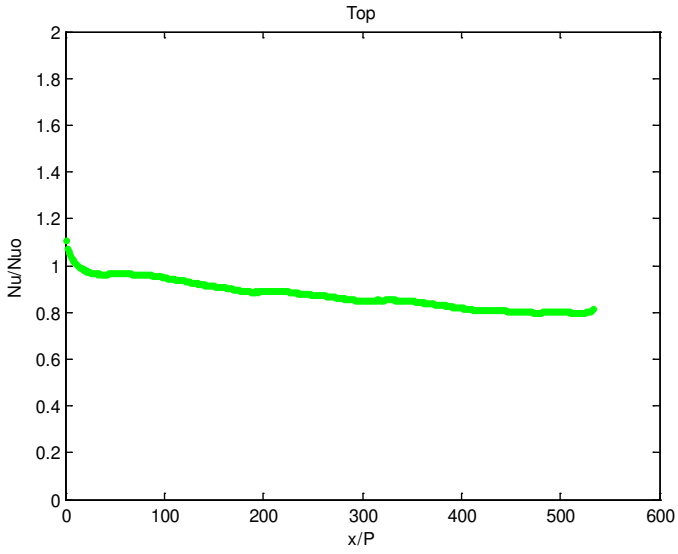

Figure 87: SW TLC Streamwise Averaged Nu/Nuo Top 40,000 Re

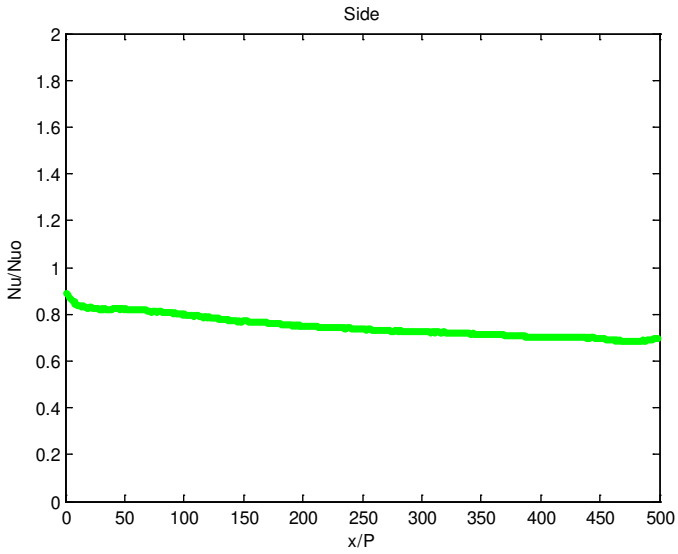

Figure 88: SW TLC Streamwise Averaged Nu/Nuo Side 40,000 Re

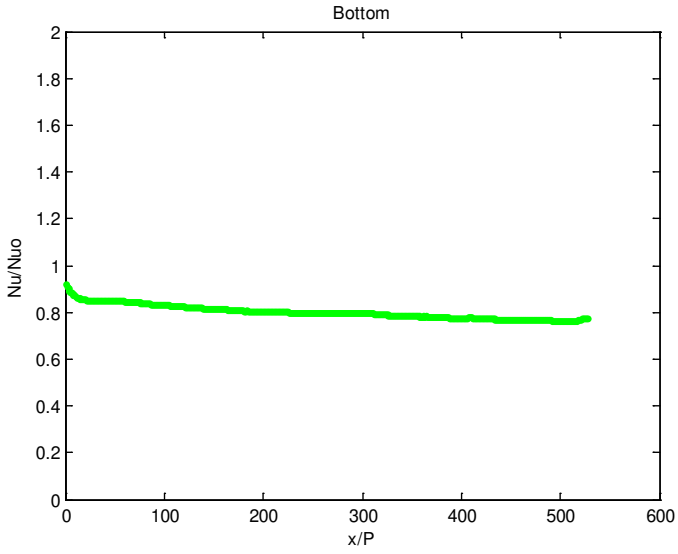

Figure 89: SW TLC Streamwise Averaged Nu/Nuo Bottom 40,000 Re

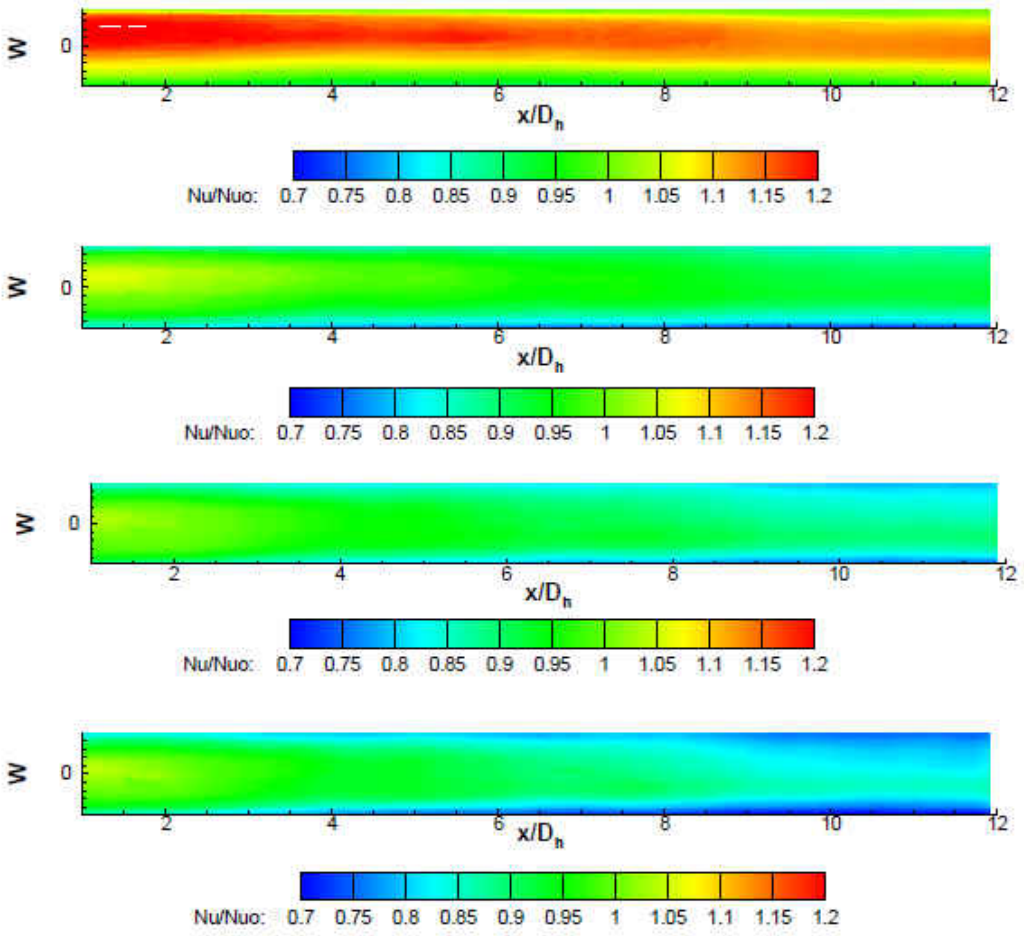

Figure 90: SW Local Nusselt Number Augmentations Top Wall for 10k, 20k, 30k, 40k Re (ordered low-high)

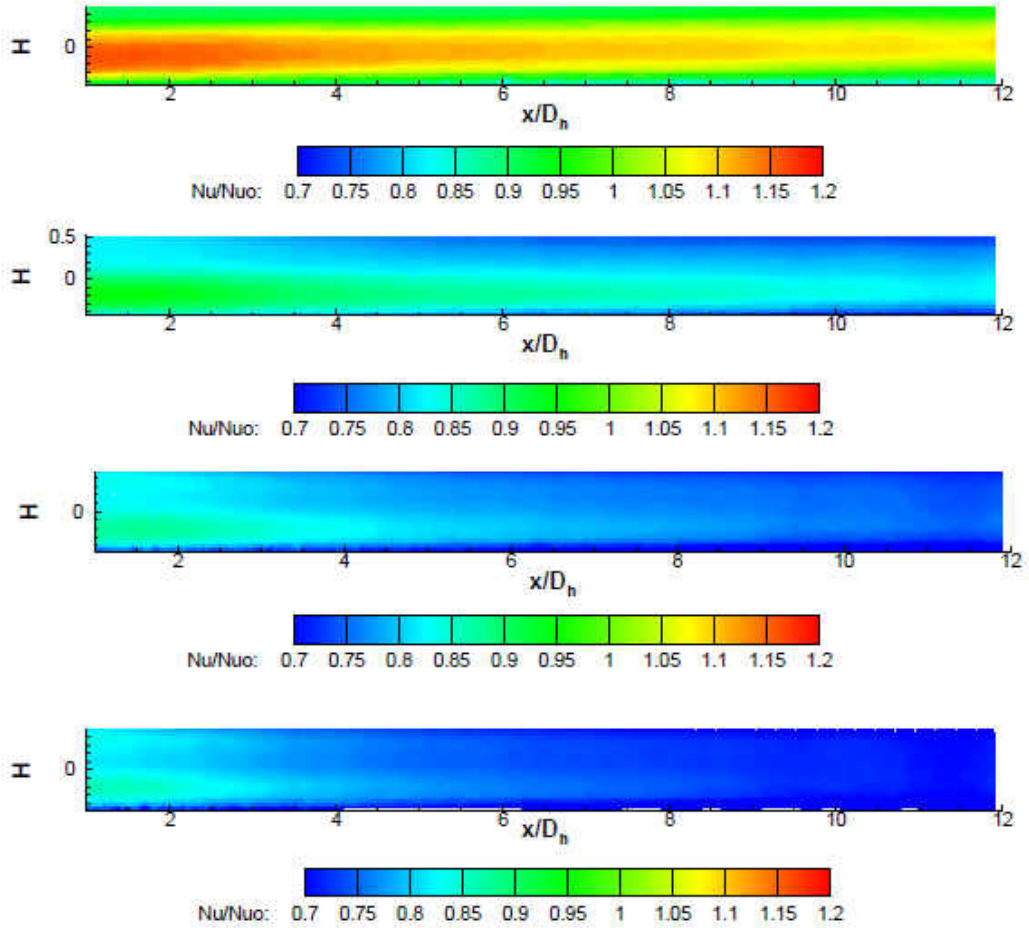

Figure 91: SW Local Nusselt Number Augmentations Side Wall for 10k, 20k, 30k, 40k Re (ordered low-high)

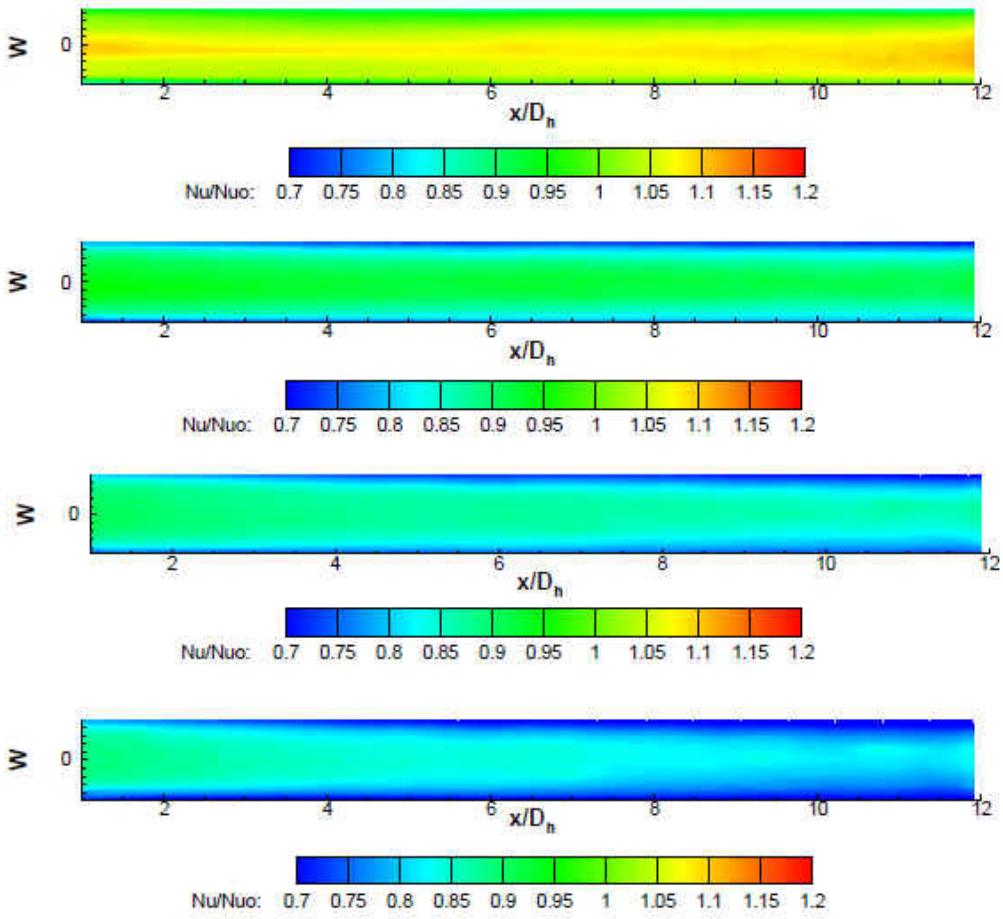

Figure 92: SW Local Nusselt Number Augmentations Bottom Wall for 10k, 20k, 30k, 40k Re (ordered low-high)

Table 24: Overall Augmentations SW TLC

Nominal Reynolds Number	10,000	20,000	30,000	40,000
Actual Reynolds Number	9500	19000	28500	37400
$\frac{Nu}{Nu_{DB}}$	1.07	0.94	0.93	0.91

Case A

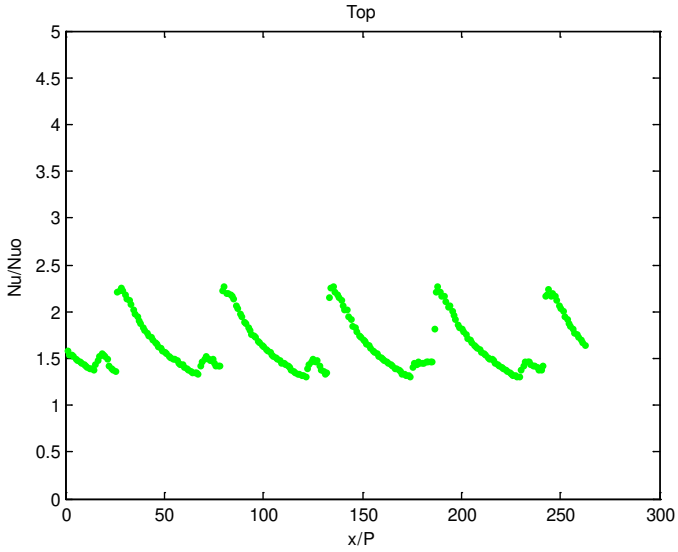

Figure 93: Case A TLC Streamwise Averaged Nu/Nuo Top 10,000 Re

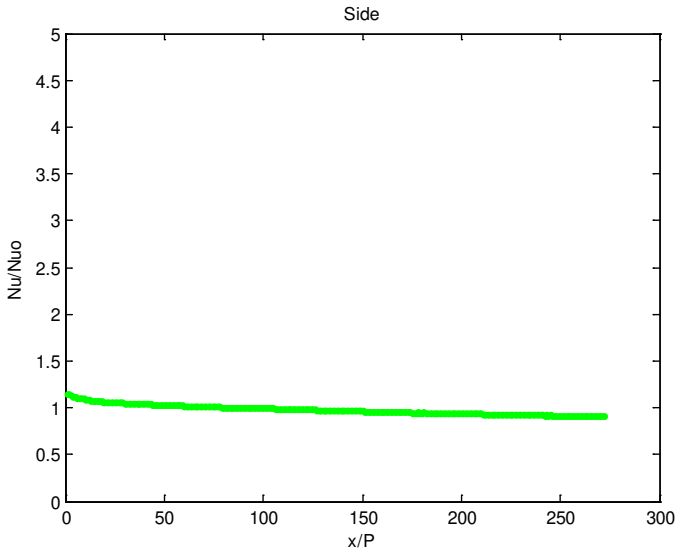

Figure 94: Case A TLC Streamwise Averaged Nu/Nuo Side 10,000 Re

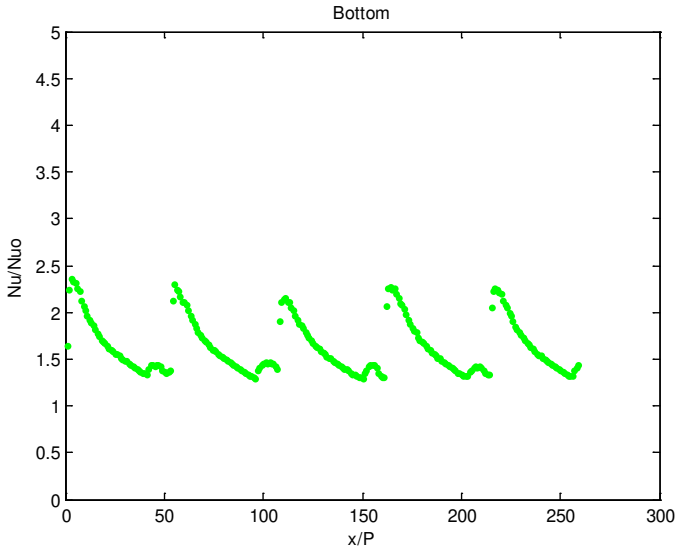

Figure 95: Case A TLC Streamwise Averaged Nu/Nuo Bottom 10,000 Re

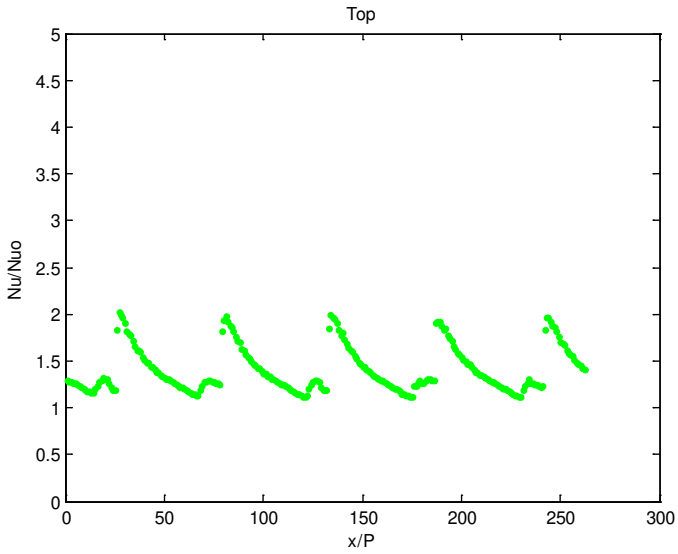

Figure 96: Case A TLC Streamwise Averaged Nu/Nuo Top 20,000 Re

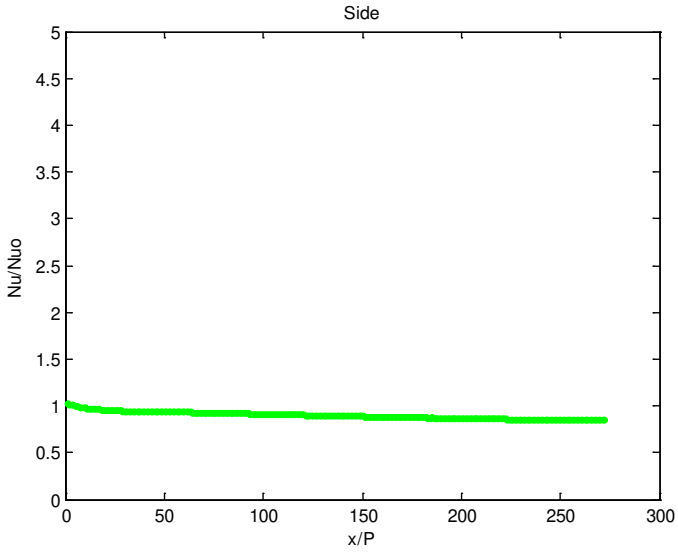

Figure 97: Case A TLC Streamwise Averaged Nu/Nuo Side 20,000 Re

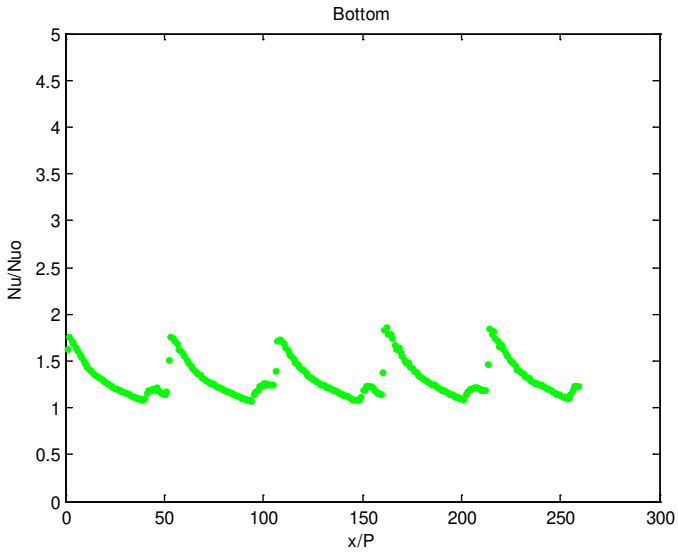

Figure 98: Case A TLC Streamwise Averaged Nu/Nuo Bottom 20,000 Re

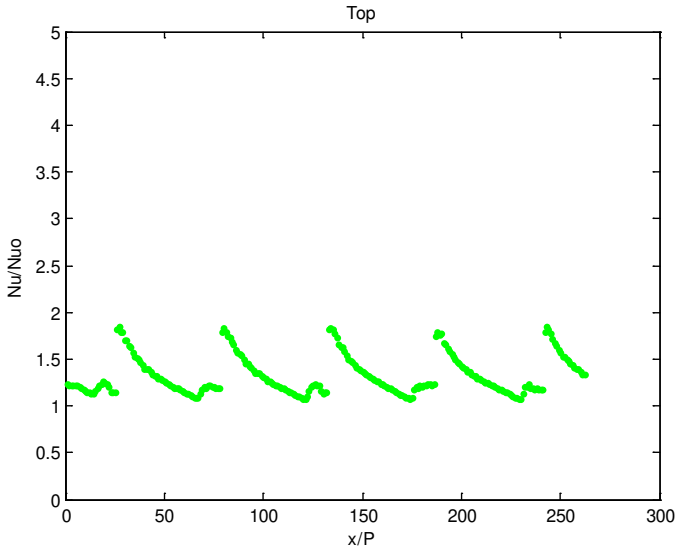

Figure 99: Case A TLC Streamwise Averaged Nu/Nuo Top 30,000 Re

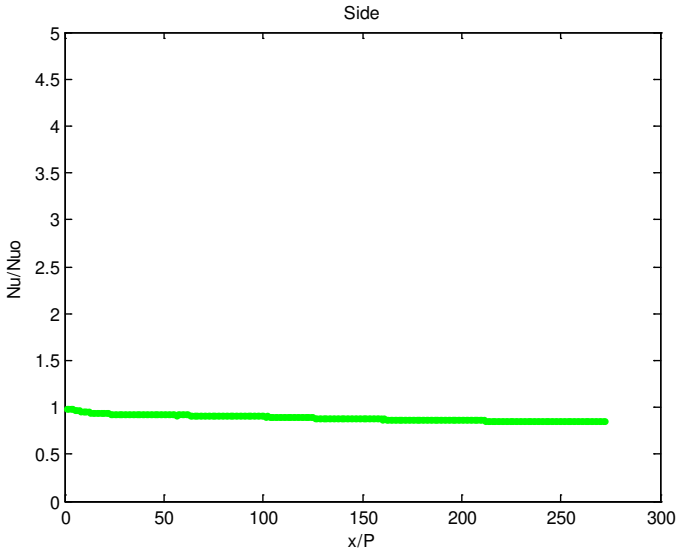

Figure 100: Case A TLC Streamwise Averaged Nu/Nuo Side 30,000 Re

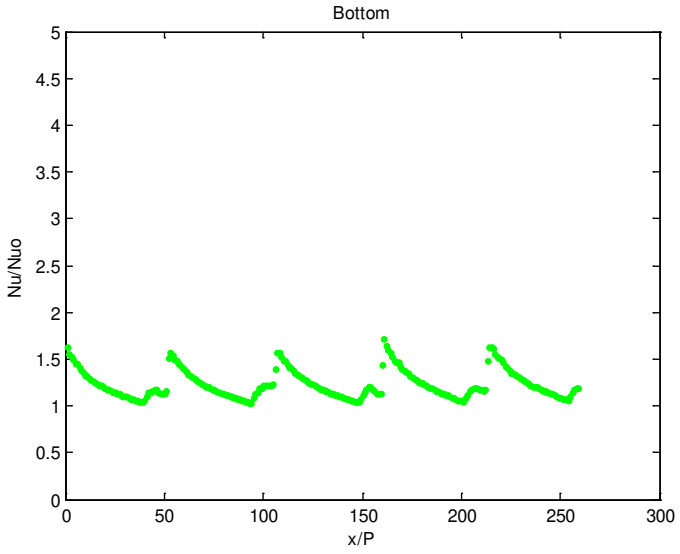

Figure 101: Case A TLC Streamwise Averaged Nu/Nuo Bottom 30,000 Re

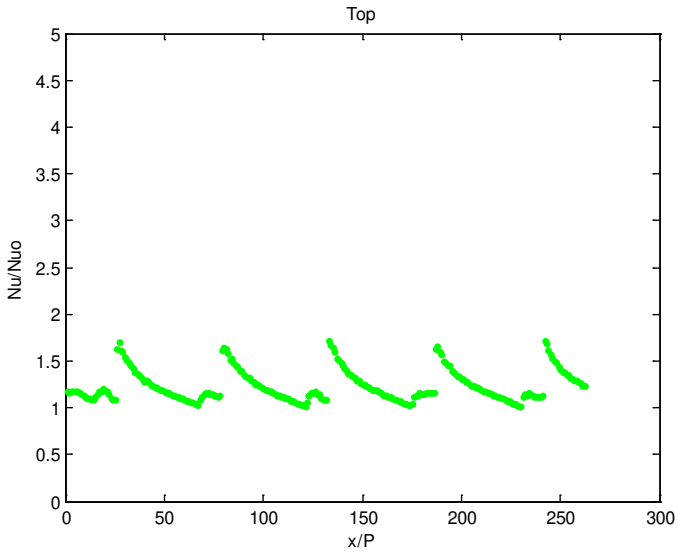

Figure 102: Case A TLC Streamwise Averaged Nu/Nuo Top 40,000 Re

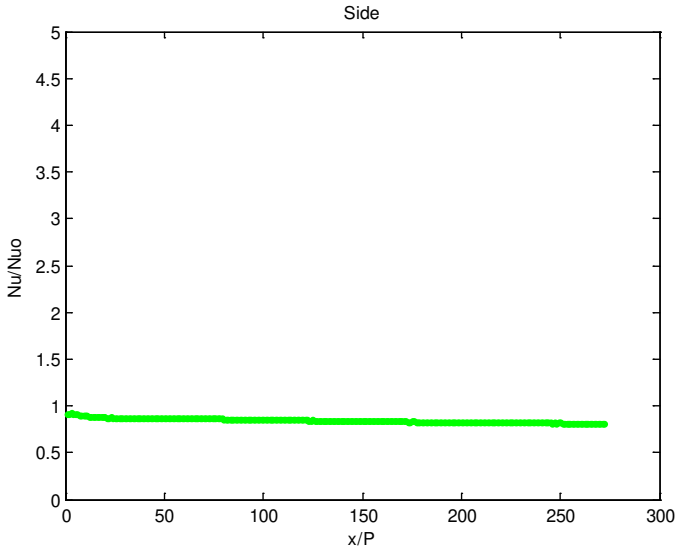

Figure 103: Case A TLC Streamwise Averaged Nu/Nuo Side 40,000 Re

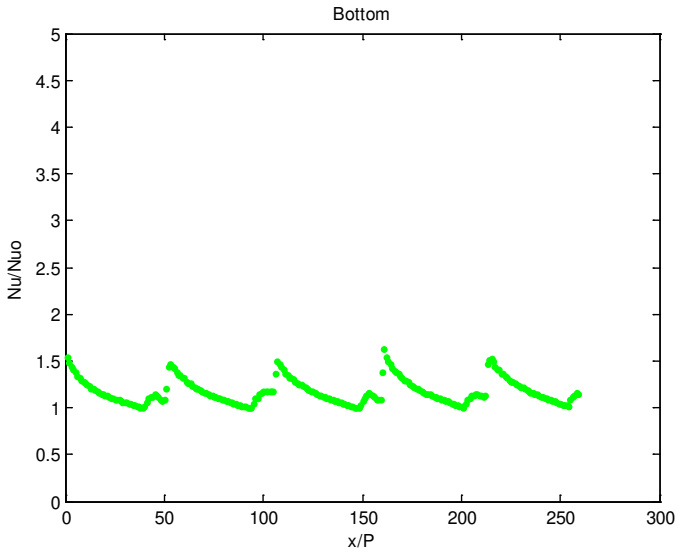

Figure 104: Case A TLC Streamwise Averaged Nu/Nuo Bottom 40,000 Re

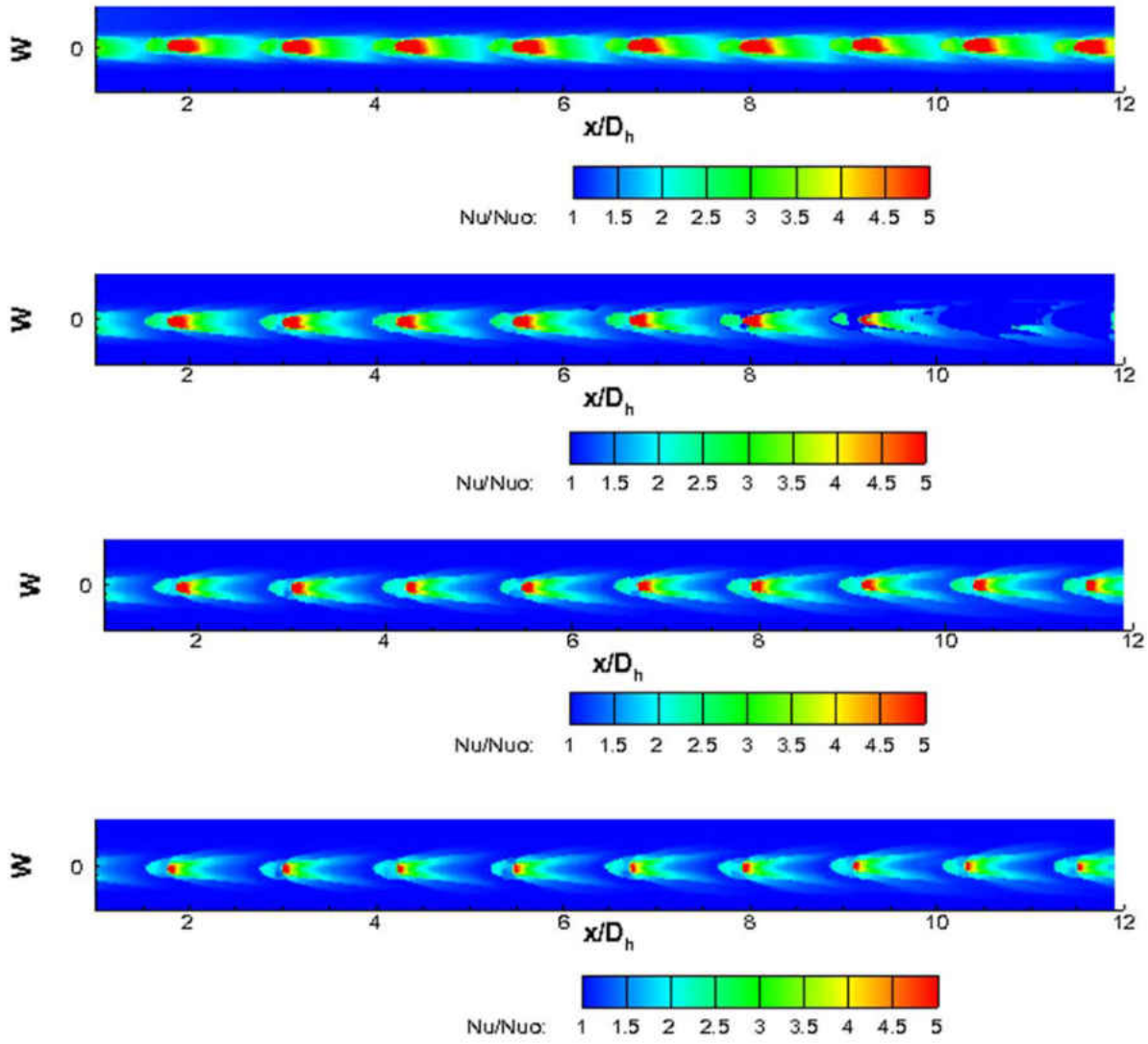

Figure 105: Case A Local Nusselt Number Augmentations Top Wall for 10k, 20k, 30k, 40k Re (ordered low-high)

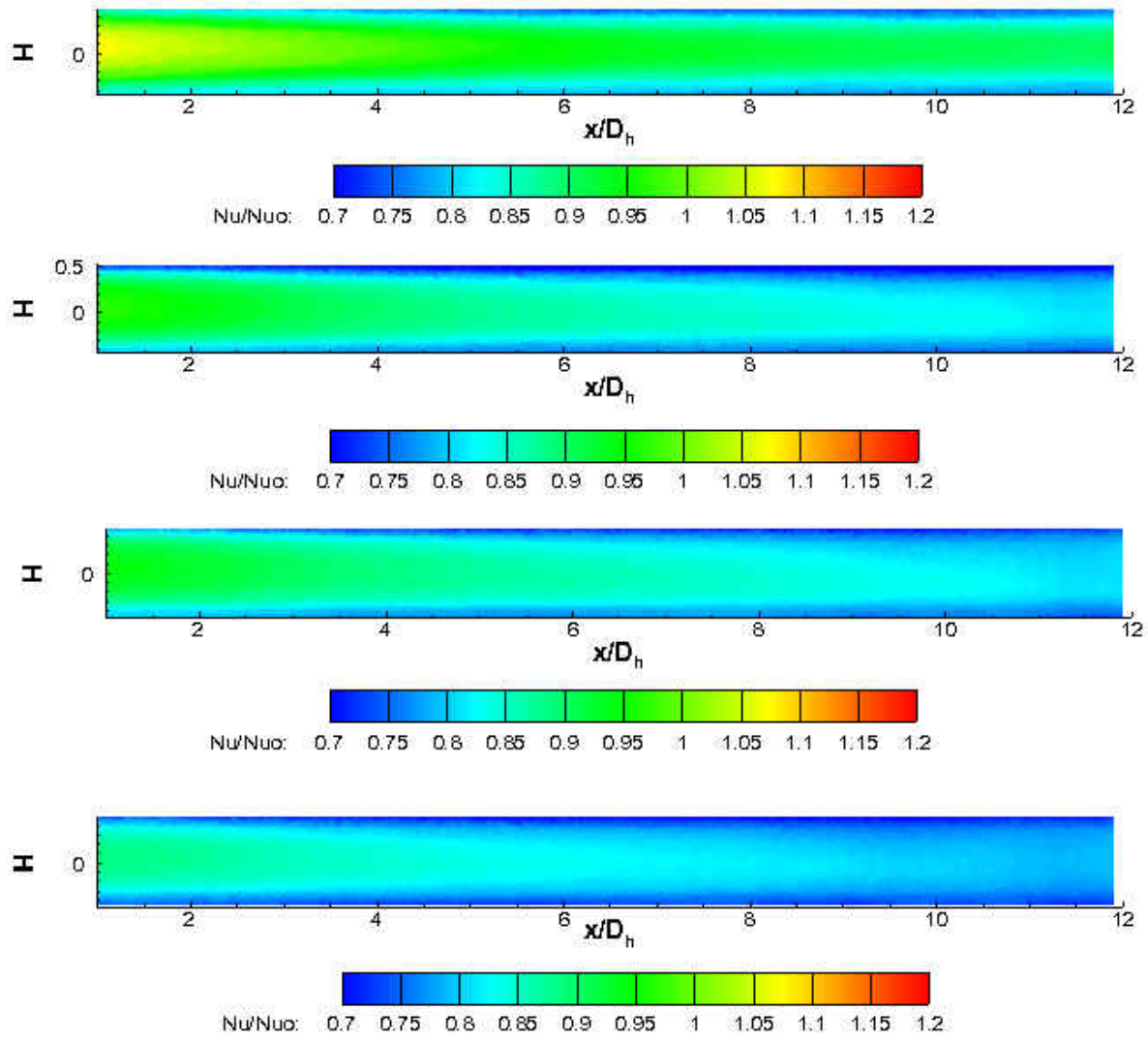

Figure 106: Case A Local Nusselt Number Augmentations Side Wall for 10k, 20k, 30k, 40k Re (ordered low-high)

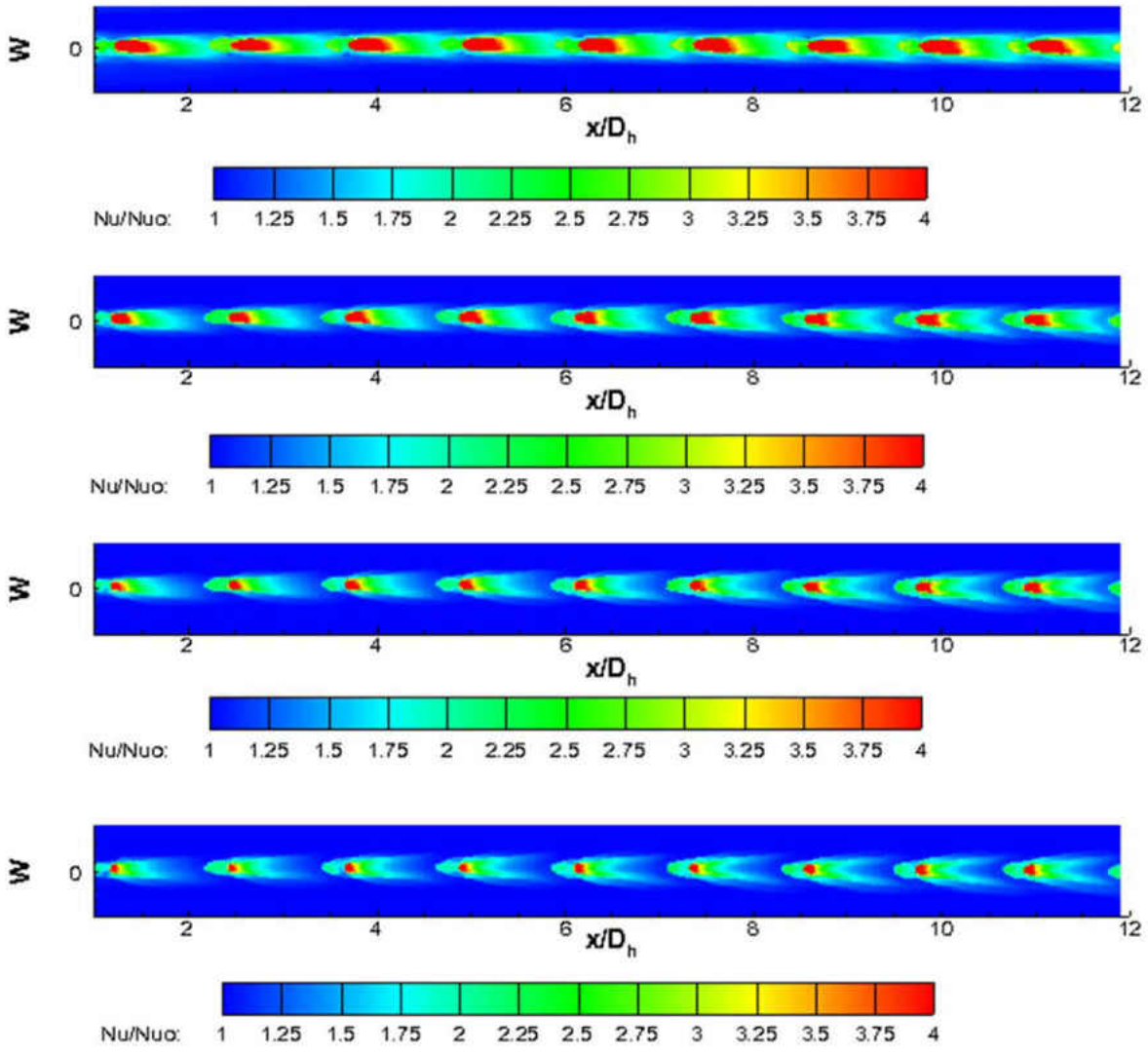

Figure 107: Case A Local Nusselt Number Augmentations Bottom Wall for 10k, 20k, 30k, 40k Re (ordered low-high)

Table 25: Overall Augmentations Case A TLC

Nominal Reynolds Number	10,000	20,000	30,000	40,000
Actual Reynolds Number	10230	20400	29870	40000
$\frac{Nu}{Nu_{DB}}$	1.65	1.37	1.28	1.21

Case B

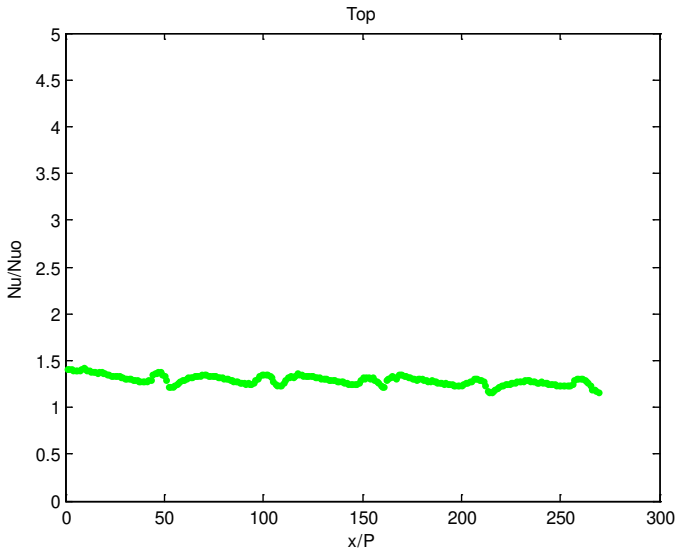

Figure 108: Case B TLC Streamwise Averaged Nu/Nuo Top 10,000 Re

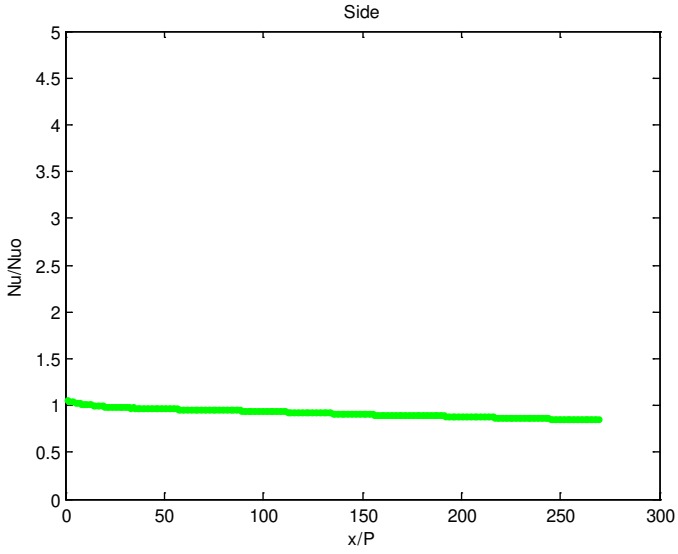

Figure 109: Case B TLC Streamwise Averaged Nu/Nuo Side 10,000 Re

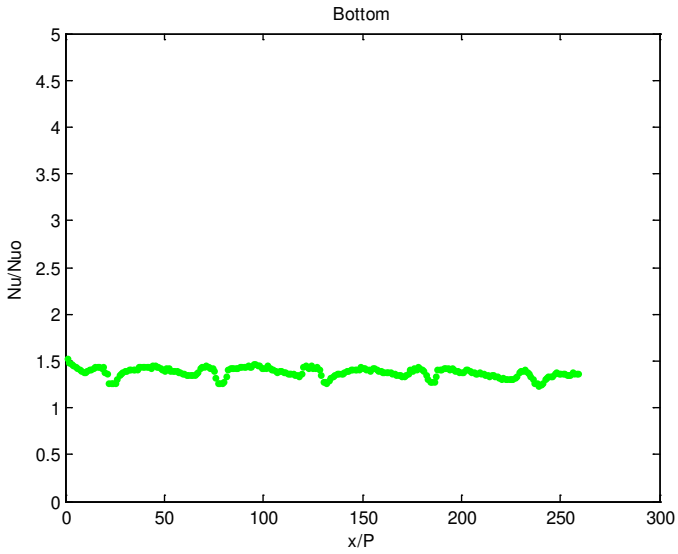

Figure 110: Case B TLC Streamwise Averaged Nu/Nuo Bottom 10,000 Re

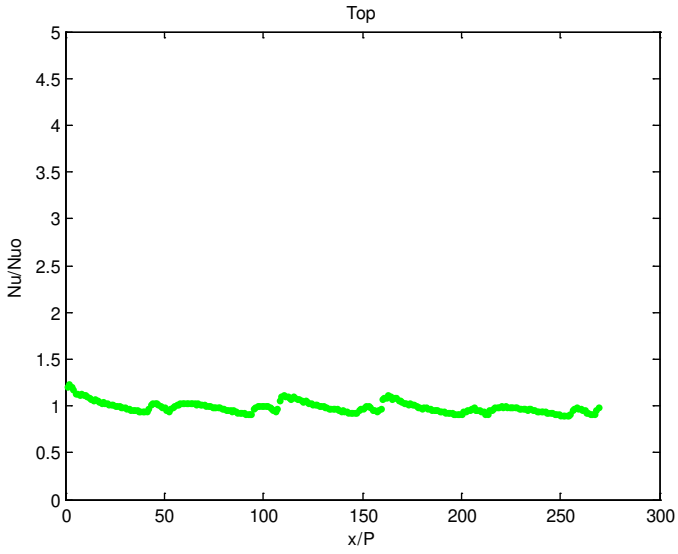

Figure 111: Case B TLC Streamwise Averaged Nu/Nuo Top 20,000 Re

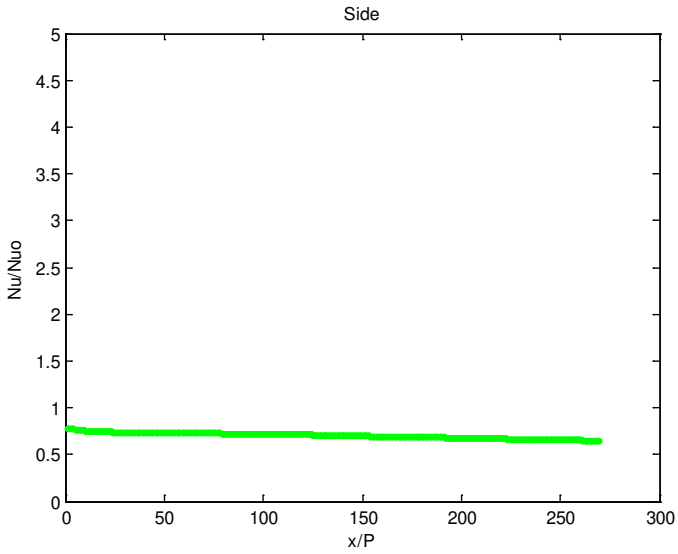

Figure 112: Case B TLC Streamwise Averaged Nu/Nuo Side 20,000 Re

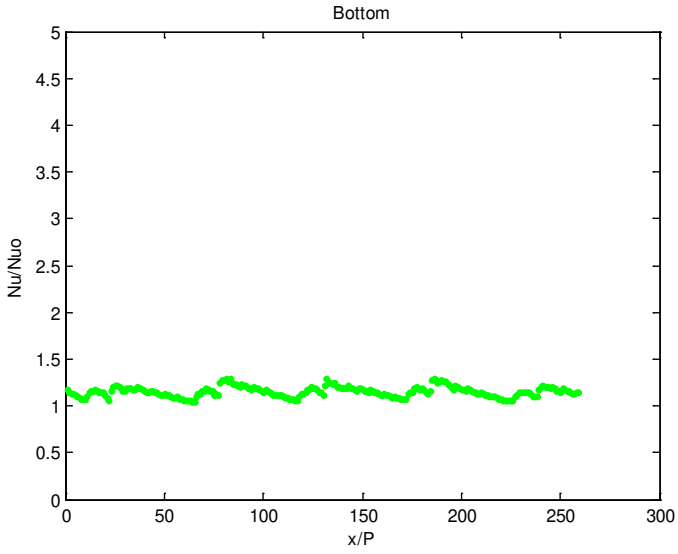

Figure 113: Case B TLC Streamwise Averaged Nu/Nuo Bottom 20,000 Re

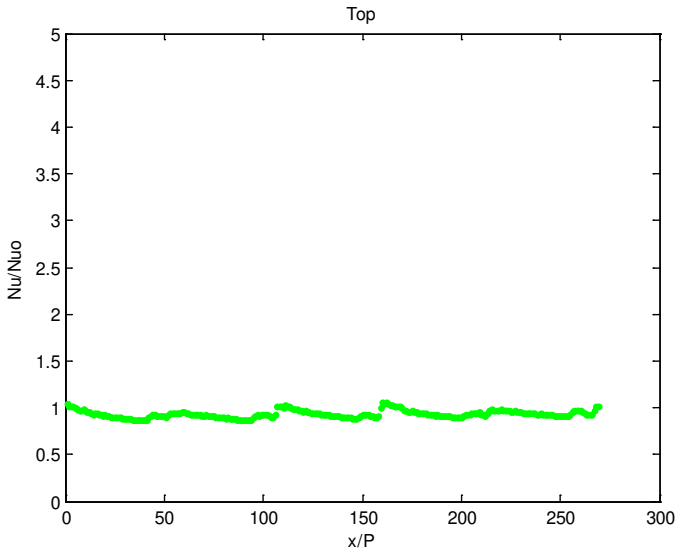

Figure 114: Case B TLC Streamwise Averaged Nu/Nuo Top 30,000 Re

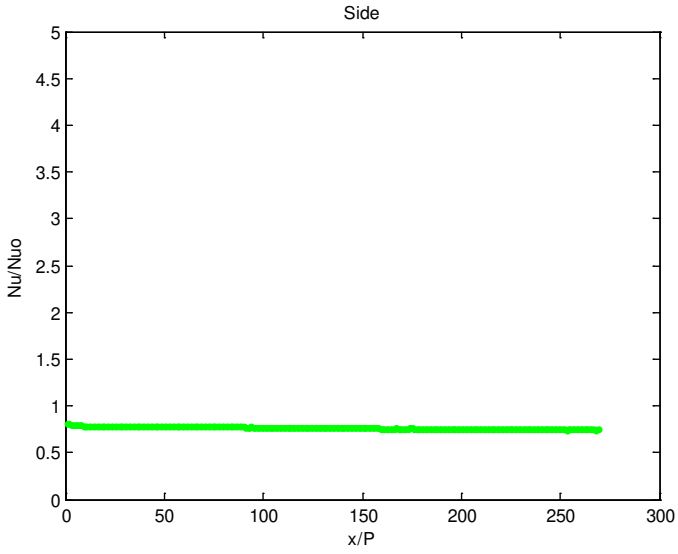

Figure 115: Case B TLC Streamwise Averaged Nu/Nuo Side 30,000 Re

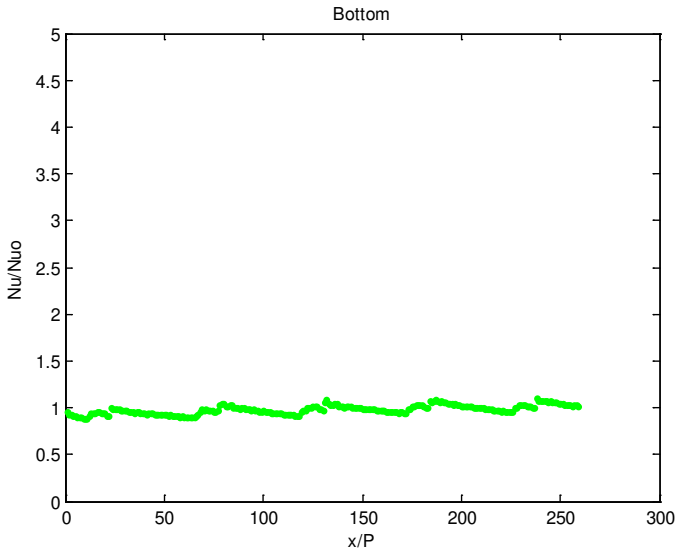

Figure 116: Case B TLC Streamwise Averaged Nu/Nuo Bottom 30,000 Re

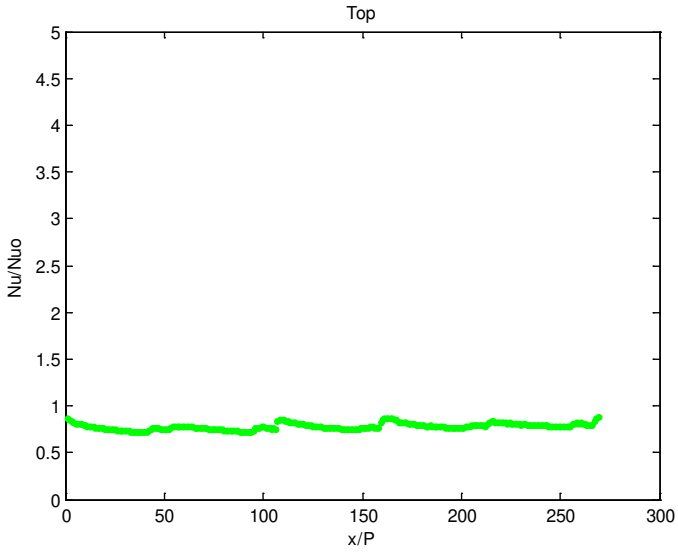

Figure 117: Case B TLC Streamwise Averaged Nu/Nuo Top 40,000 Re

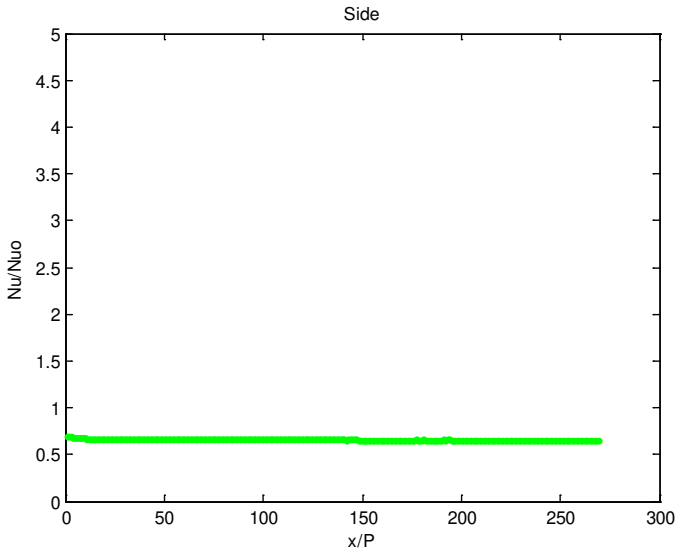

Figure 118: Case B TLC Streamwise Averaged Nu/Nuo Side 40,000 Re

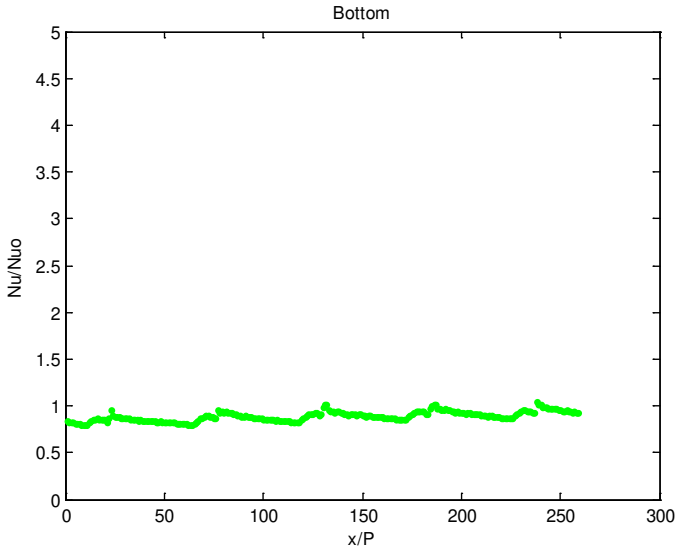

Figure 119: Case B TLC Streamwise Averaged Nu/Nuo Bottom 40,000 Re

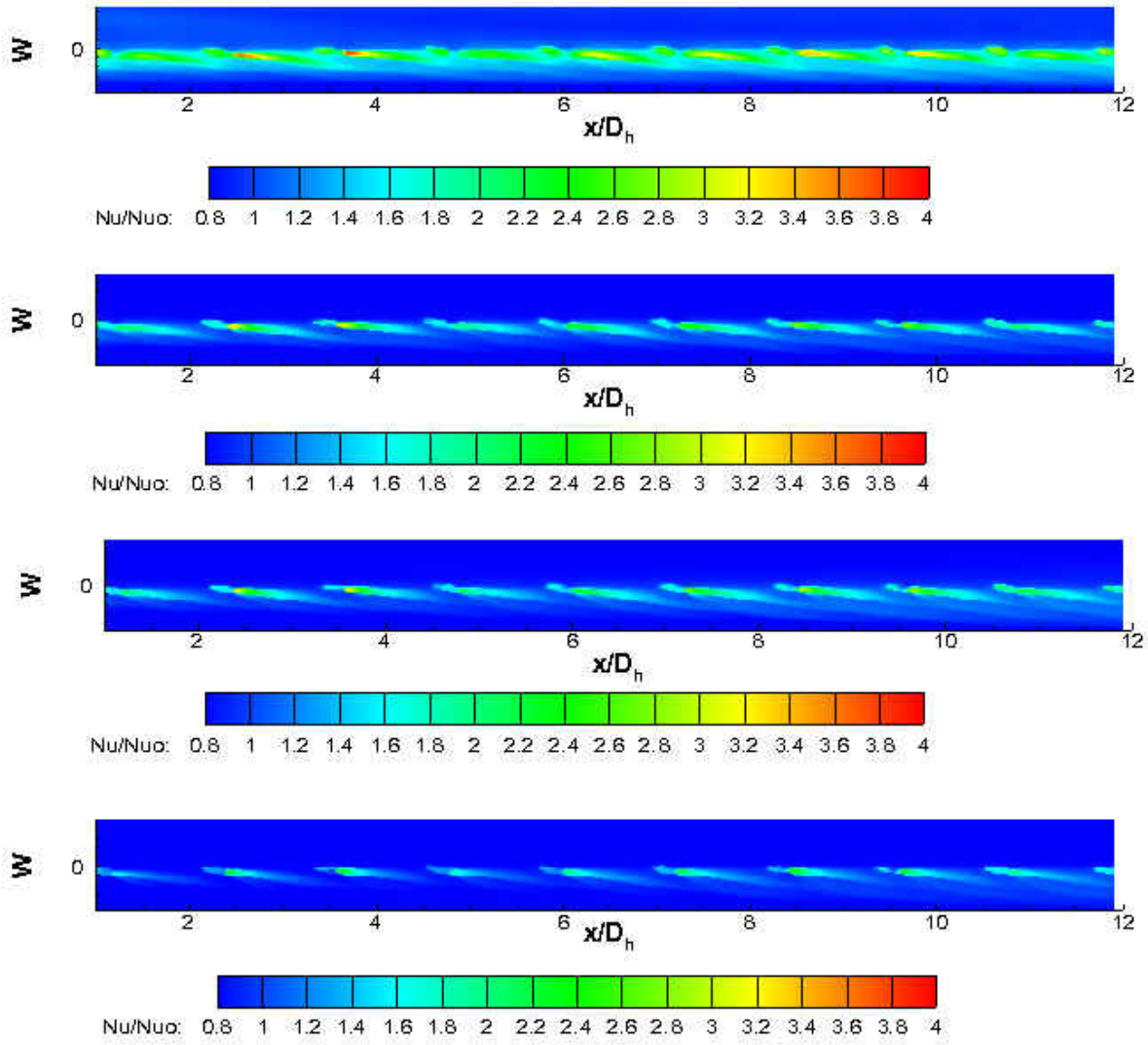

Figure 120: Case B Local Nusselt Number Augmentations Top Wall for 10k, 20k, 30k, 40k Re (ordered low-high)

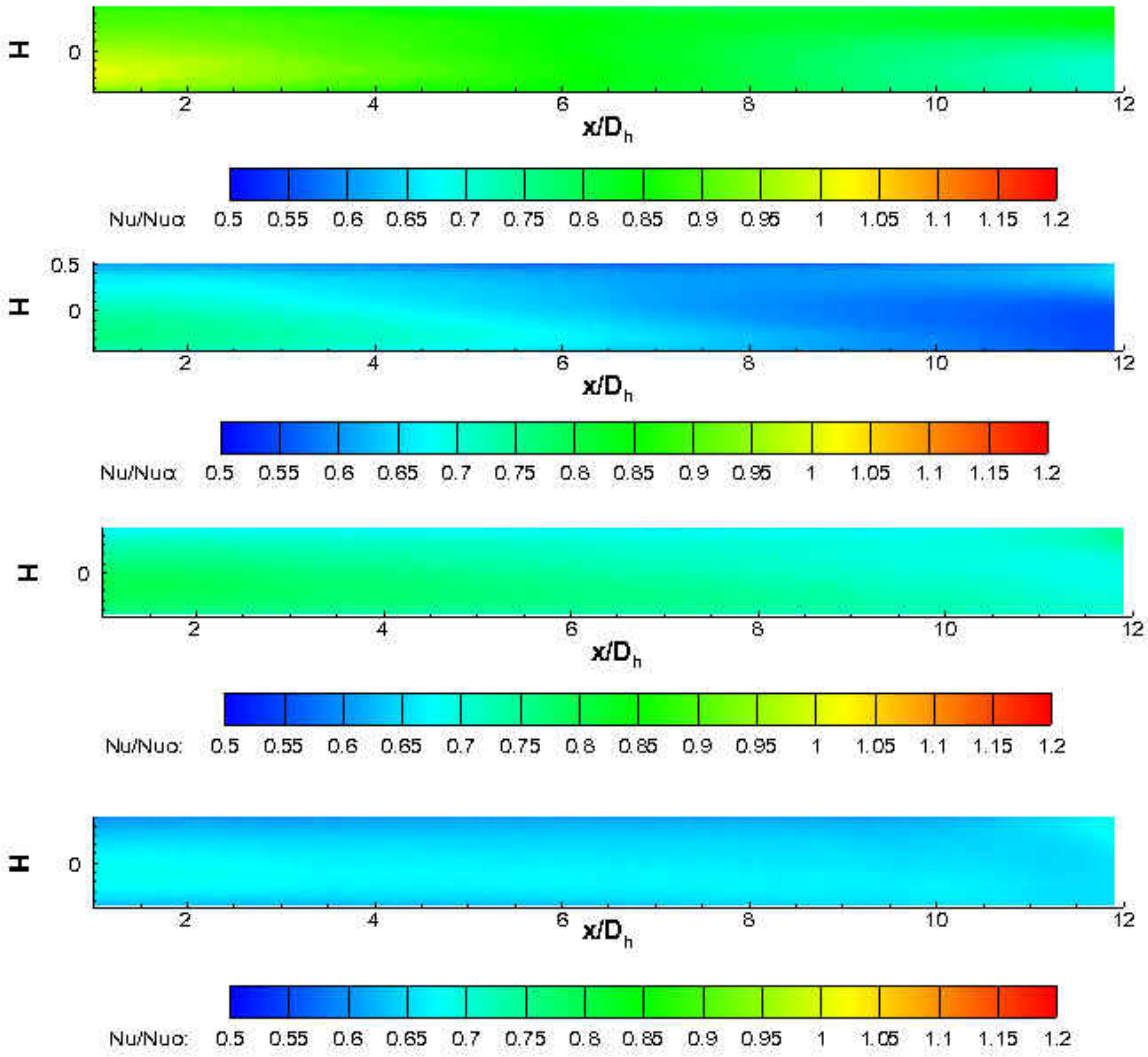

Figure 121: Case B Local Nusselt Number Augmentations Side Wall for 10k, 20k, 30k, 40k Re (ordered low-high)

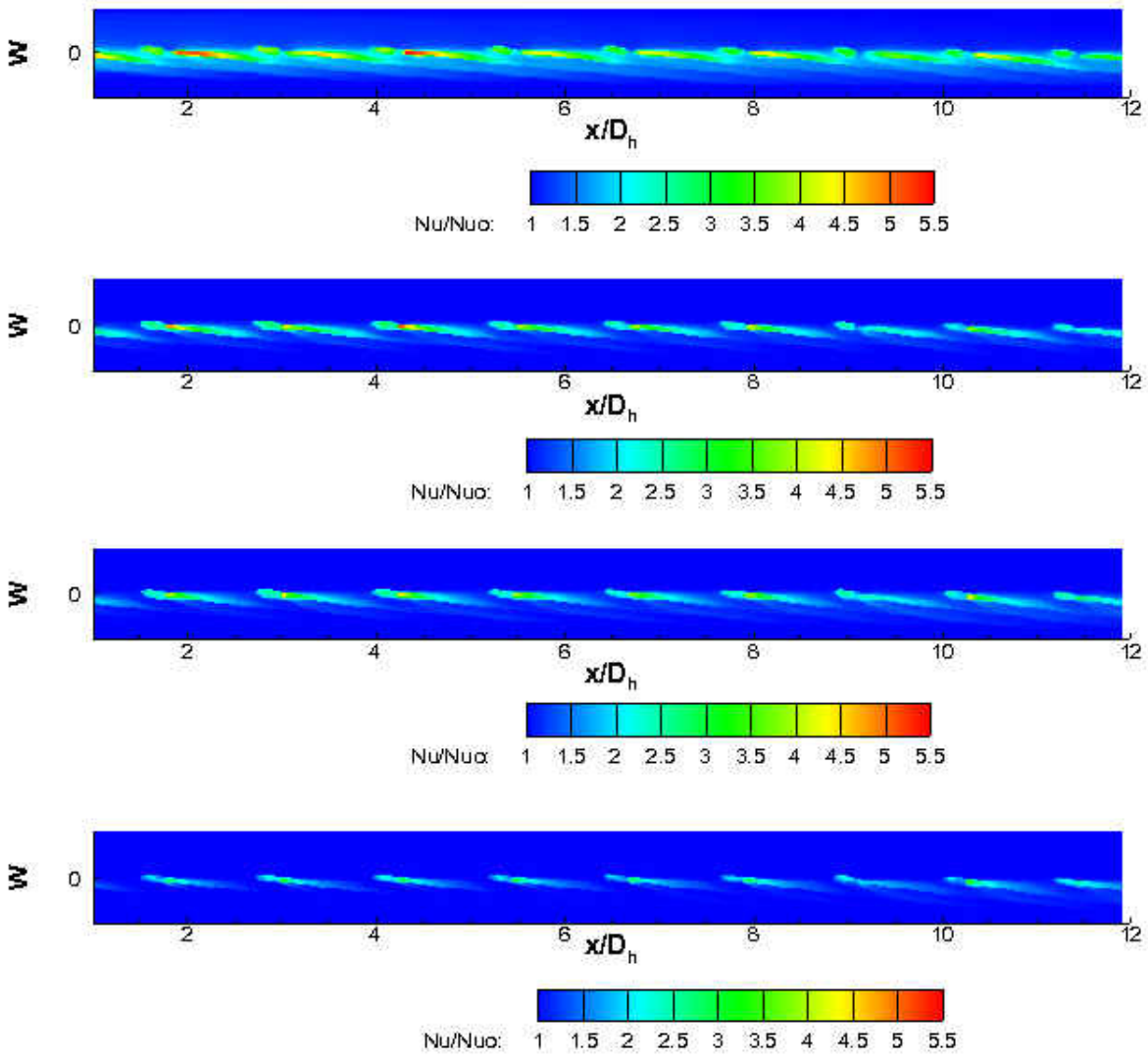

Figure 122: Case B Local Nusselt Number Augmentations Bottom Wall for 10k, 20k, 30k, 40k Re (ordered low-high)

Table 26: Overall Augmentations Case B TLC

Nominal Reynolds Number	10,000	20,000	30,000	40,000
Actual Reynolds Number	10190	20150	30000	39870
$\frac{Nu}{Nu_{DB}}$	1.34	1.07	0.96	0.84

Case C

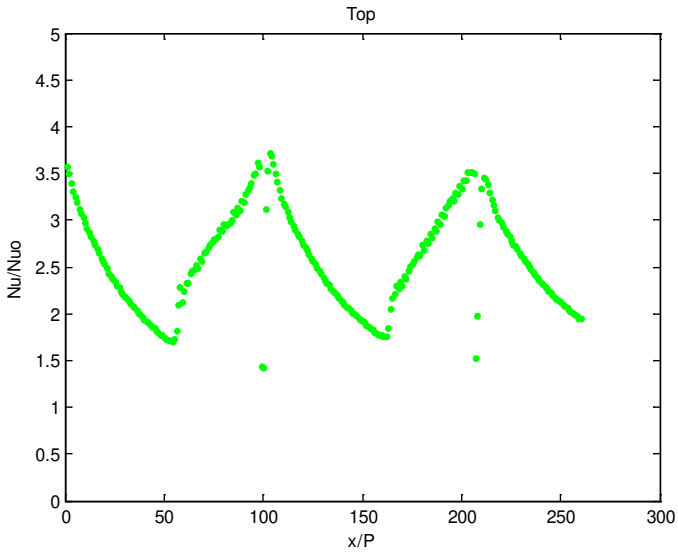

Figure 123: Case C TLC Streamwise Averaged Nu/Nuo Top 10,000 Re

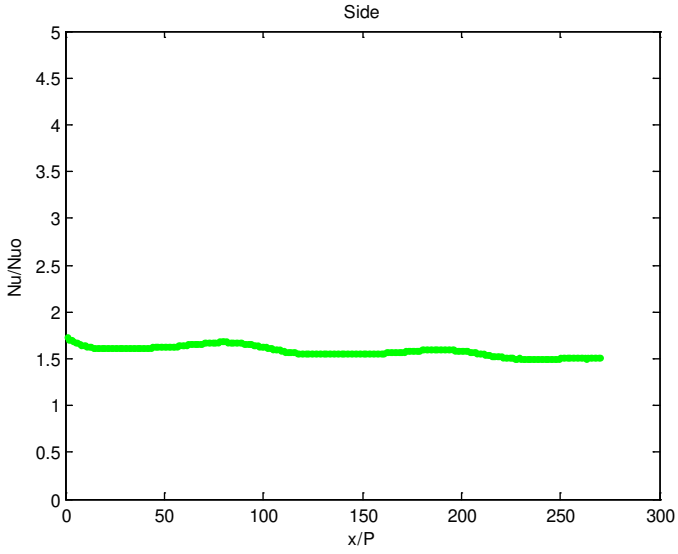

Figure 124: Case C TLC Streamwise Averaged Nu/Nuo Side 10,000 Re

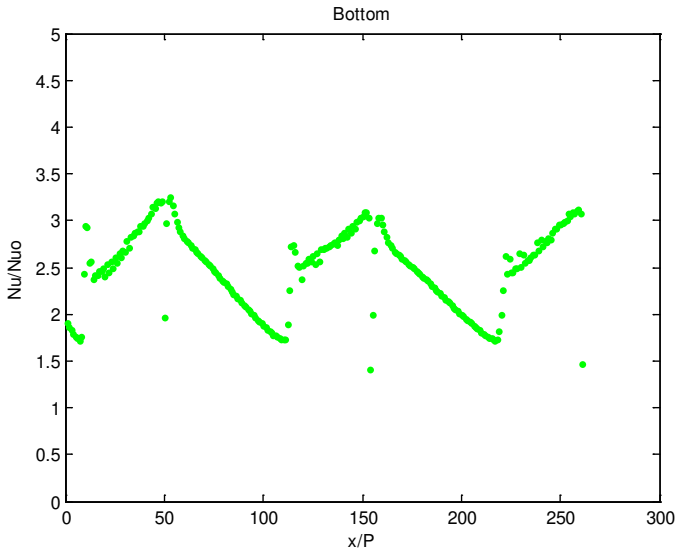

Figure 125: Case C TLC Streamwise Averaged Nu/Nuo Bottom 10,000 Re

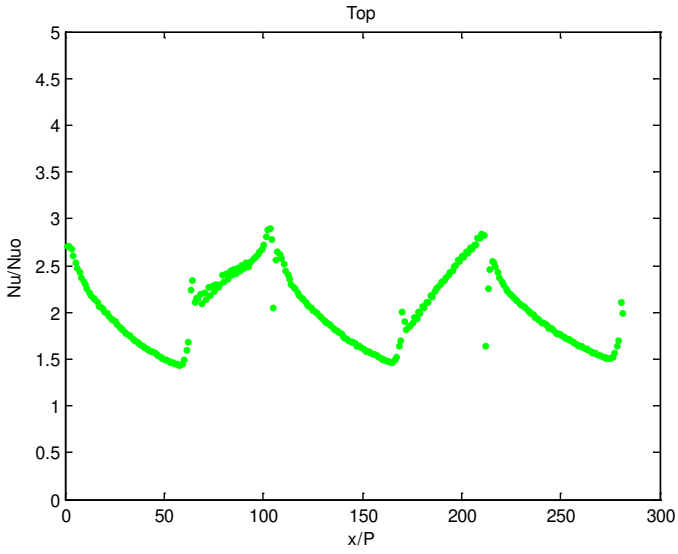

Figure 126: Case C TLC Streamwise Averaged Nu/Nuo Top 20,000 Re

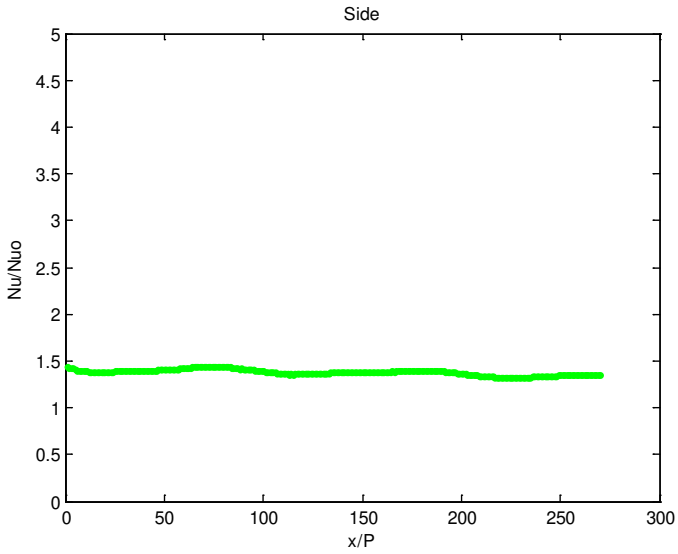

Figure 127: Case C TLC Streamwise Averaged Nu/Nuo Side 20,000 Re

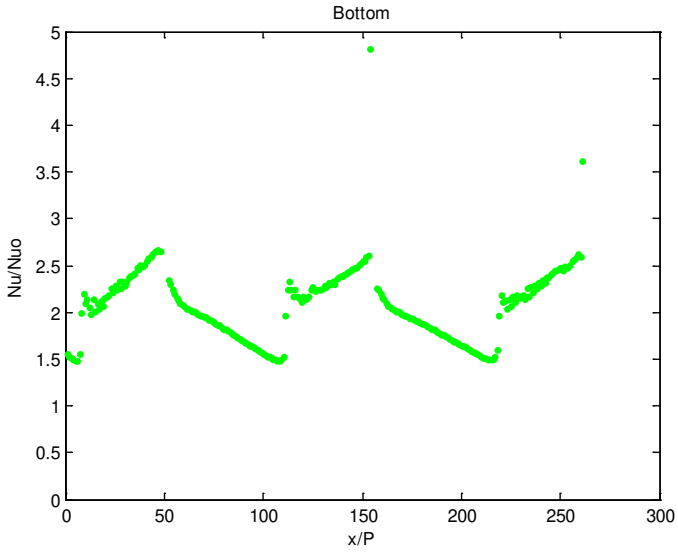

Figure 128: Case C TLC Streamwise Averaged Nu/Nuo Bottom 20,000 Re

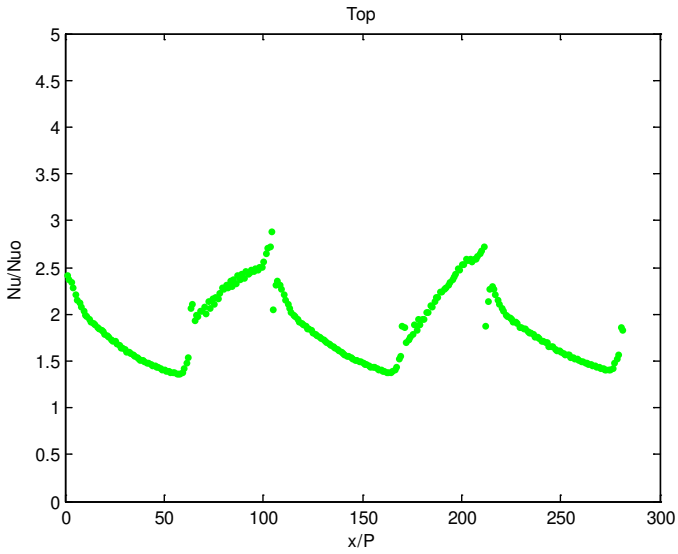

Figure 129: Case C TLC Streamwise Averaged Nu/Nuo Top 30,000 Re

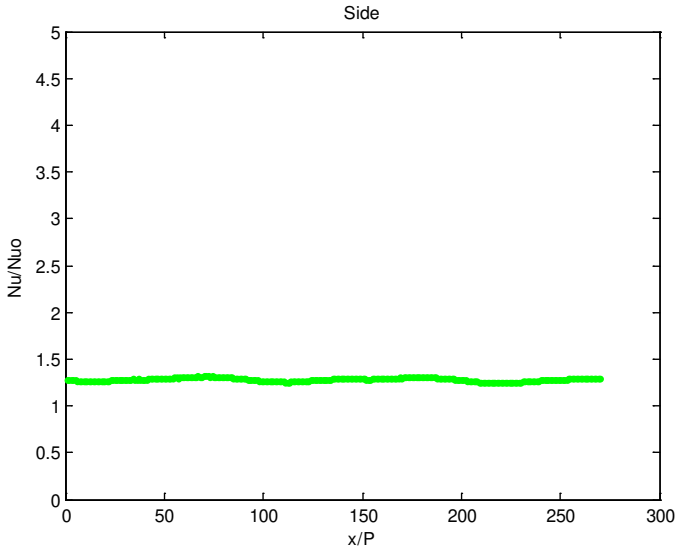

Figure 130: Case C TLC Streamwise Averaged Nu/Nuo Side 30,000 Re

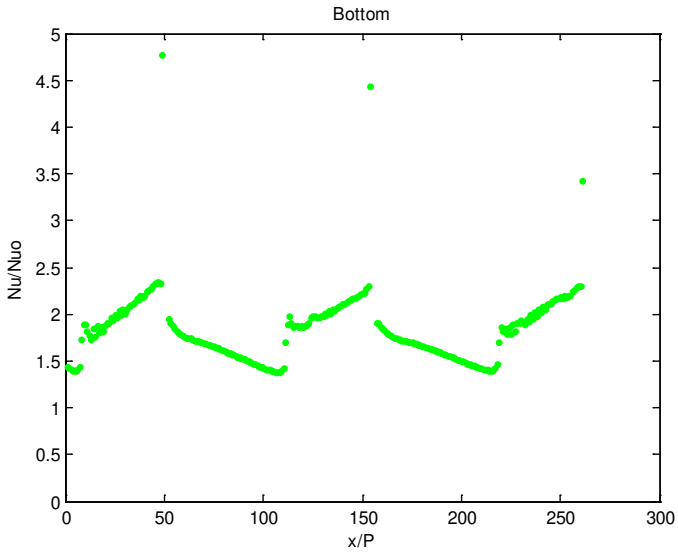

Figure 131: Case C TLC Streamwise Averaged Nu/Nuo Bottom 30,000 Re

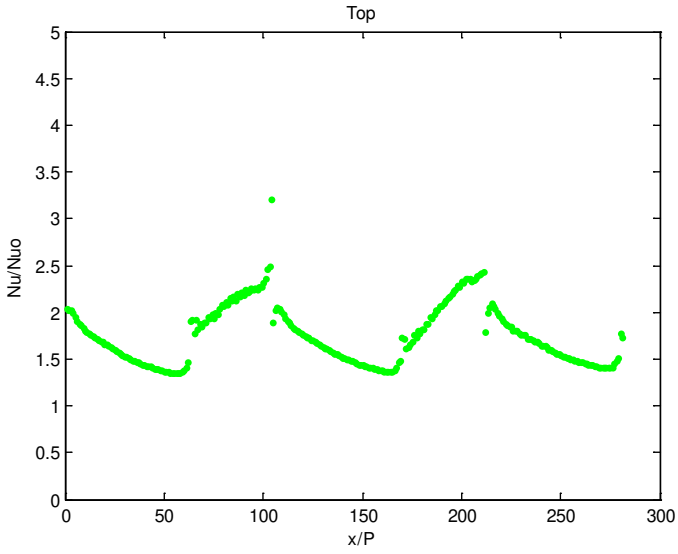

Figure 132: Case C TLC Streamwise Averaged Nu/Nuo Top 40,000 Re

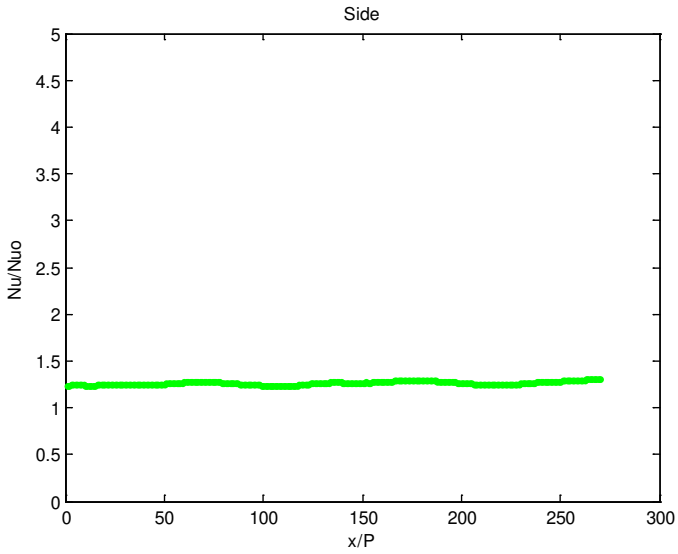

Figure 133: Case C TLC Streamwise Averaged Nu/Nuo Side 40,000 Re

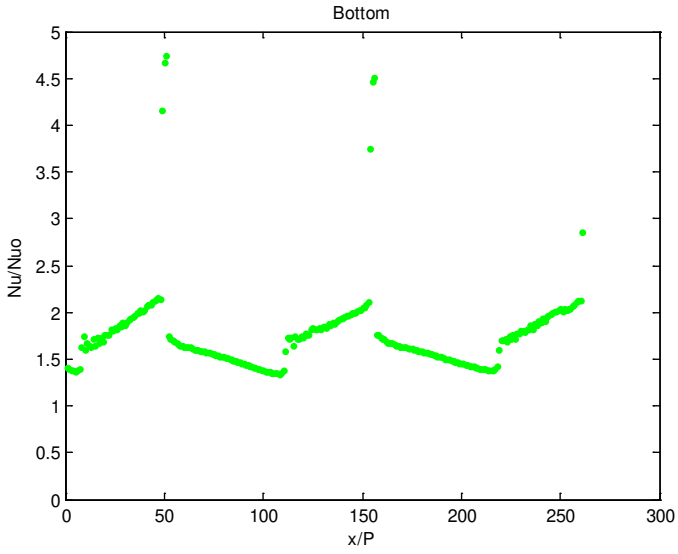

Figure 134: Case C TLC Streamwise Averaged Nu/Nuo Bottom 40,000 Re

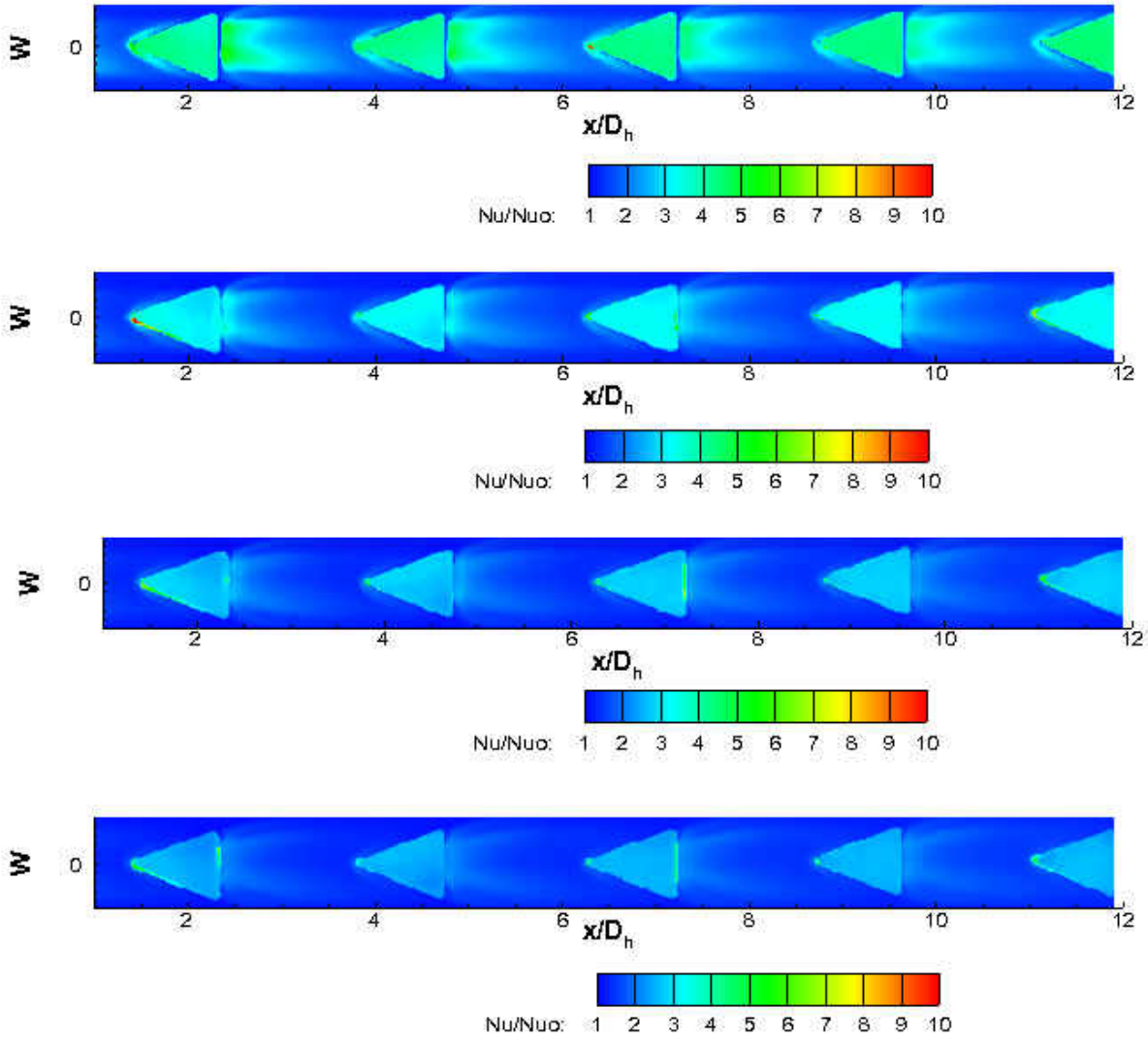

Figure 135: Case C Local Nusselt Number Augmentations Top Wall for 10k, 20k, 30k, 40k Re (ordered low-high)

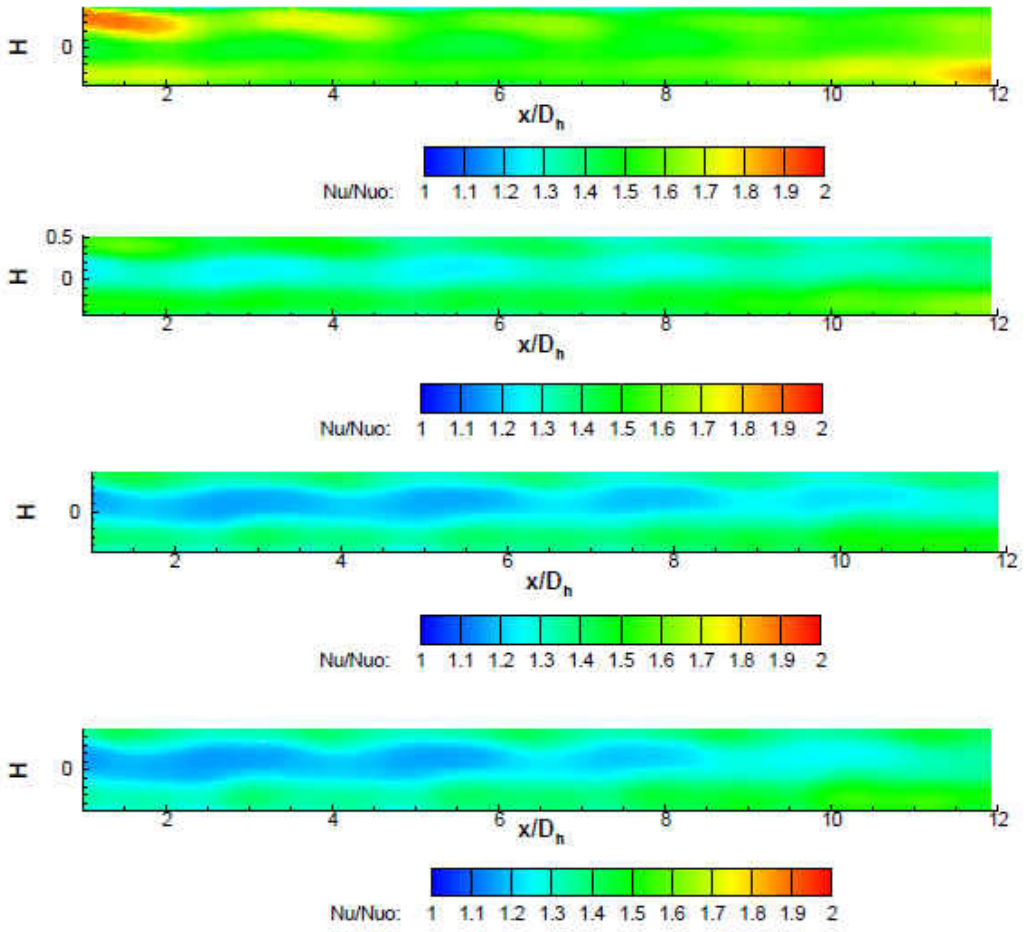

Figure 136: Case C Local Nusselt Number Augmentations Side Wall for 10k, 20k, 30k, 40k Re (ordered low-high)

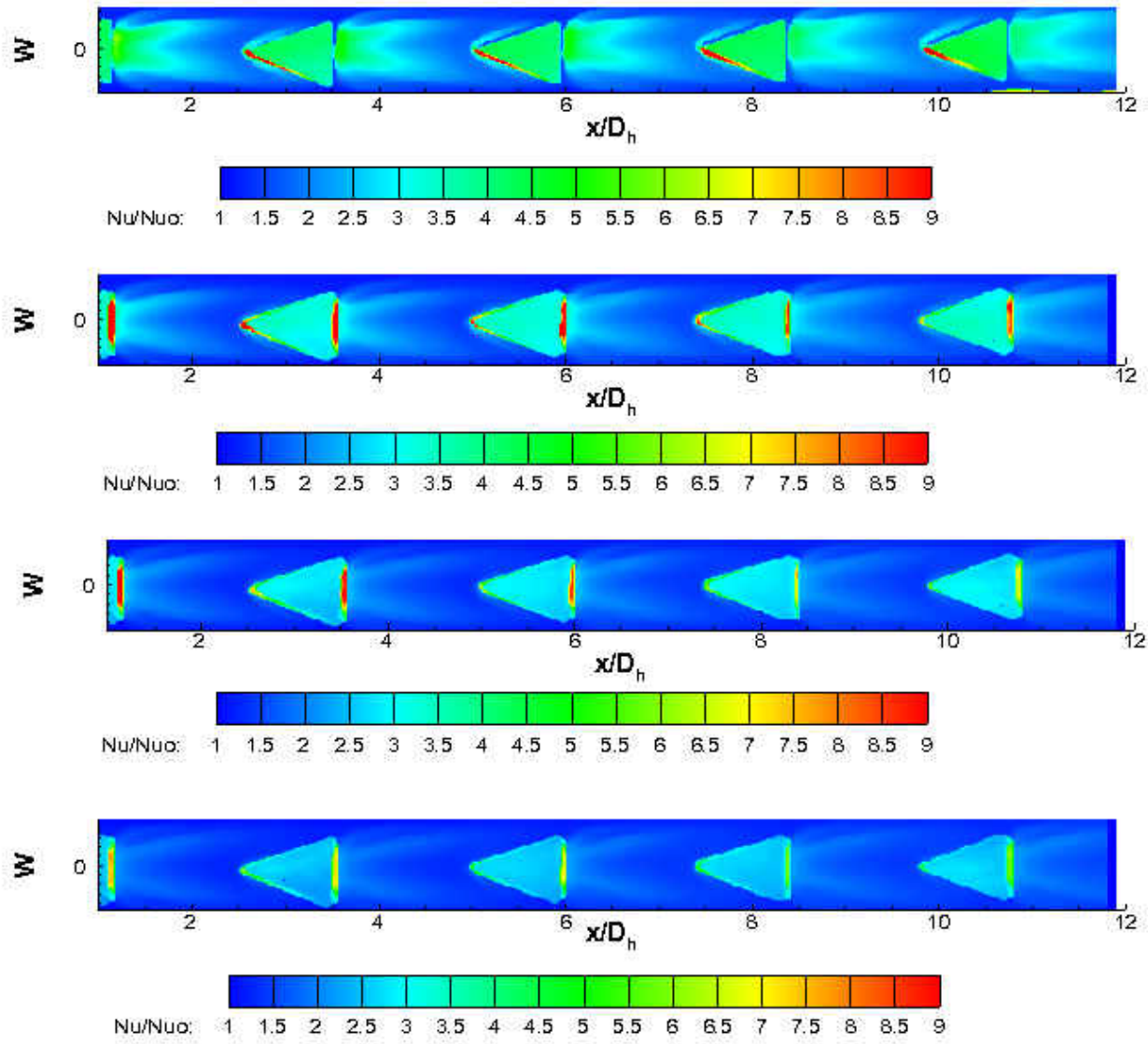

Figure 137: Case C Local Nusselt Number Augmentations Bottom Wall for 10k, 20k, 30k, 40k Re (ordered low-high)

Table 27: Overall Augmentations Case C TLC

Nominal Reynolds Number	10,000	20,000	30,000	40,000
Actual Reynolds Number	10300	19920	29750	39850
$\frac{Nu}{Nu_{DB}}$	2.59	2.09	1.89	1.76

Case D

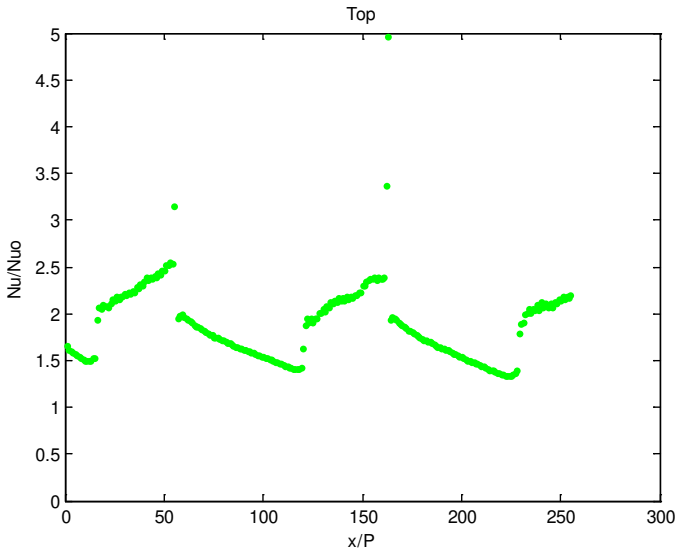

Figure 138: Case D TLC Streamwise Averaged Nu/Nuo Top 10,000 Re

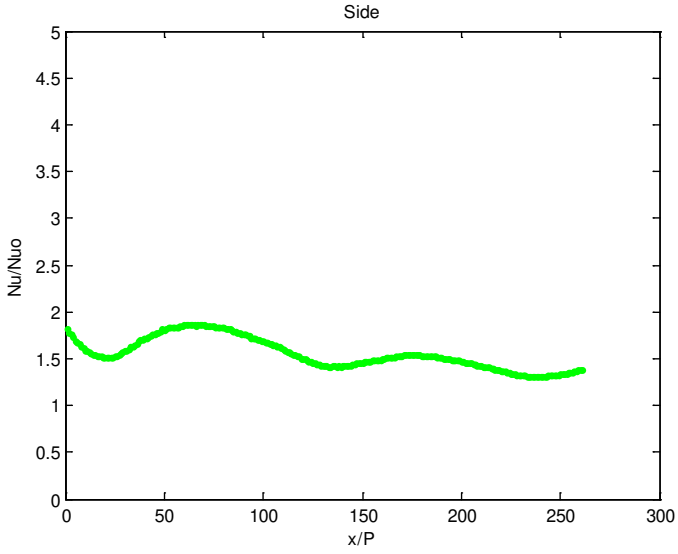

Figure 139: Case D TLC Streamwise Averaged Nu/Nuo Side 10,000 Re

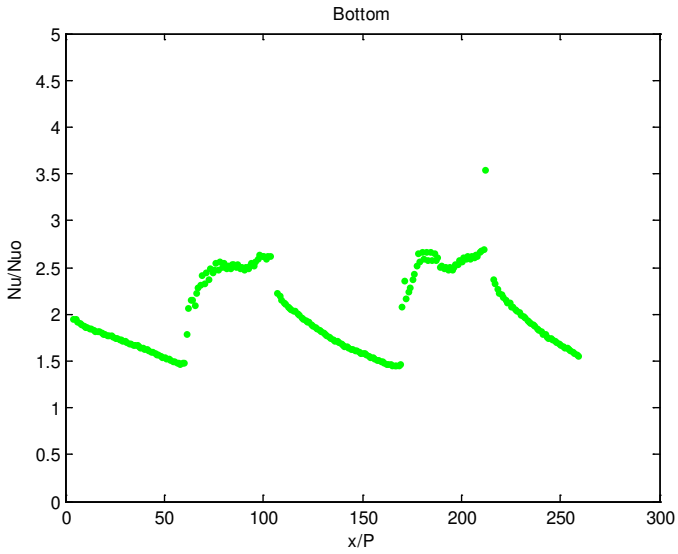

Figure 140: Case D TLC Streamwise Averaged Nu/Nuo Bottom 10,000 Re

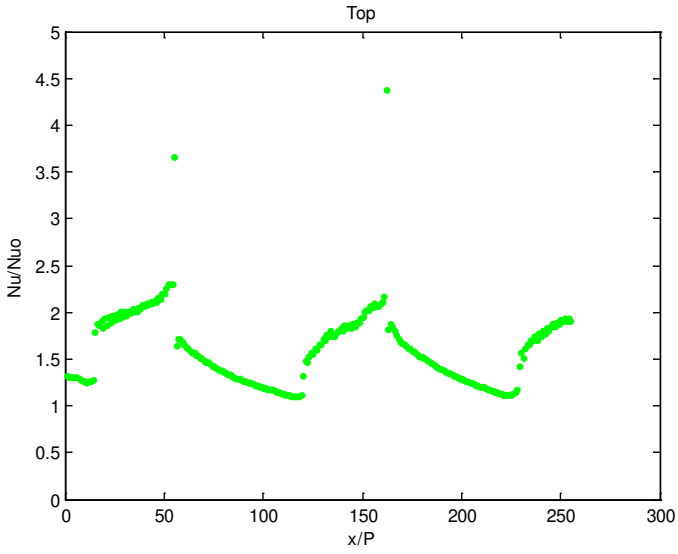

Figure 141: Case D TLC Streamwise Averaged Nu/Nuo Top 20,000 Re

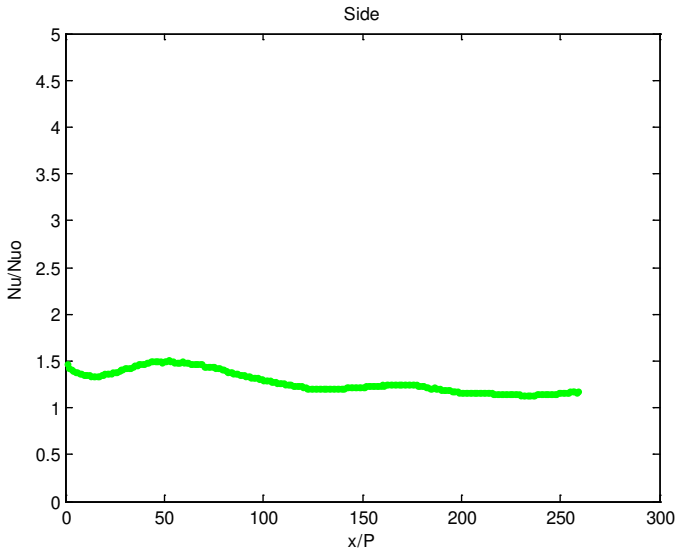

Figure 142: Case D TLC Streamwise Averaged Nu/Nuo Side 20,000 Re

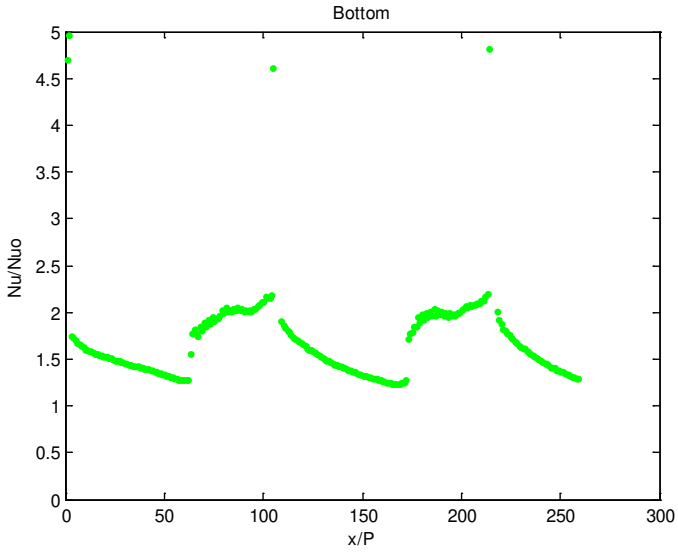

Figure 143: Case D TLC Streamwise Averaged Nu/Nuo Bottom 20,000 Re

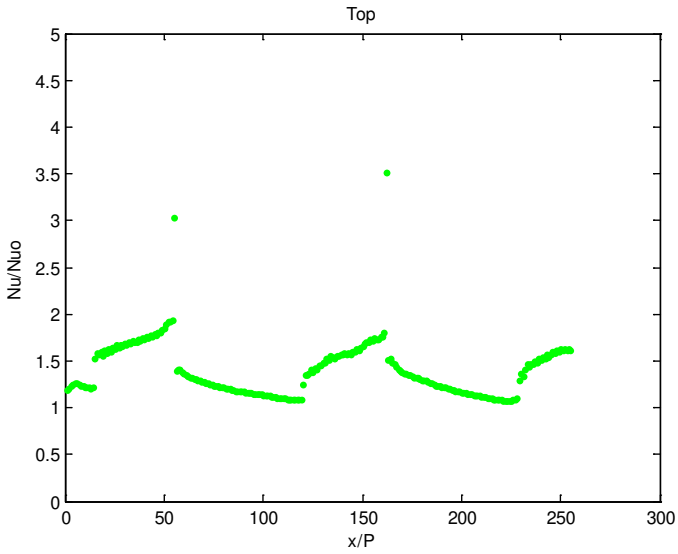

Figure 144: Case D TLC Streamwise Averaged Nu/Nuo Top 30,000 Re

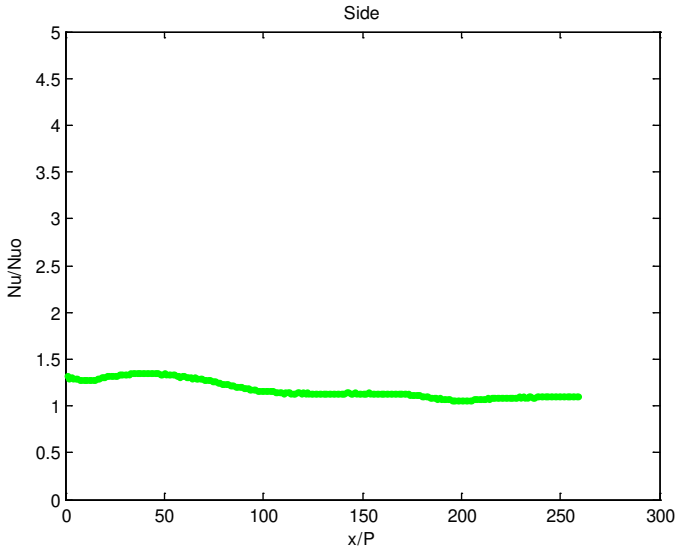

Figure 145: Case D TLC Streamwise Averaged Nu/Nuo Side 30,000 Re

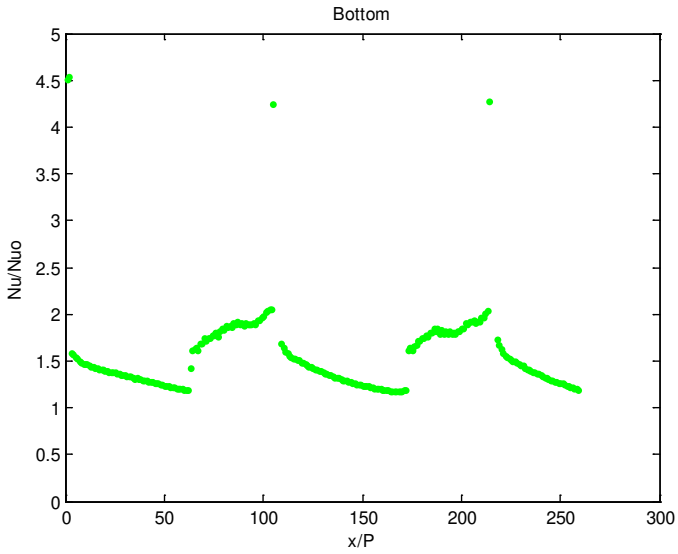

Figure 146: Case D TLC Streamwise Averaged Nu/Nuo Bottom 30,000 Re

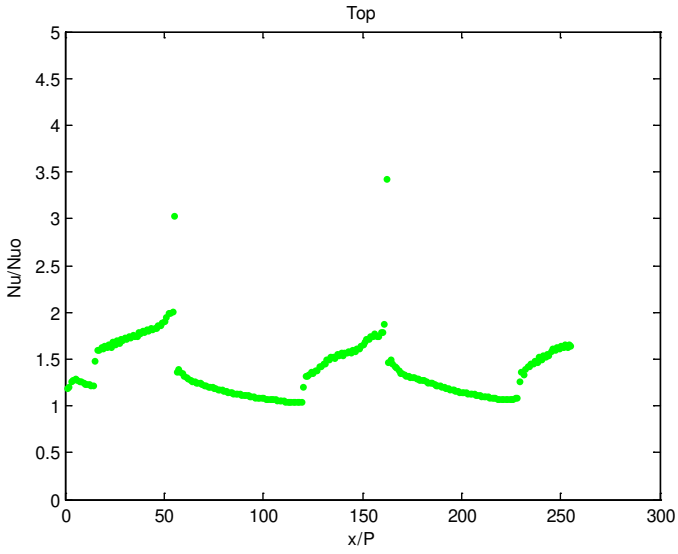

Figure 147: Case D TLC Streamwise Averaged Nu/Nuo Top 40,000 Re

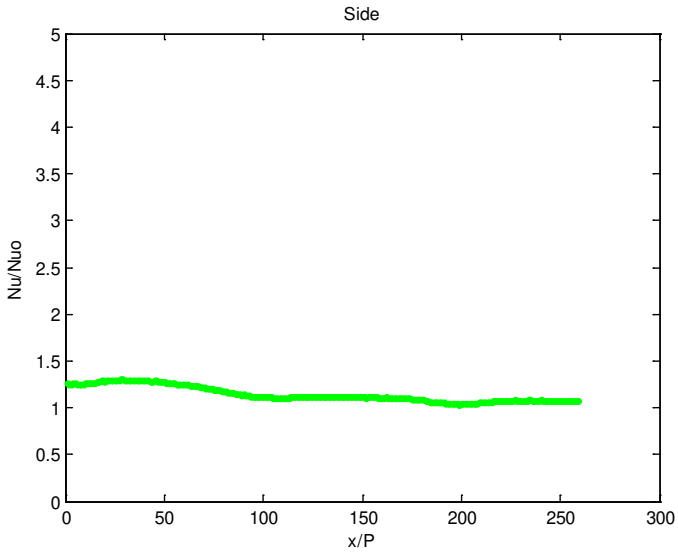

Figure 148: Case D TLC Streamwise Averaged Nu/Nuo Side 40,000 Re

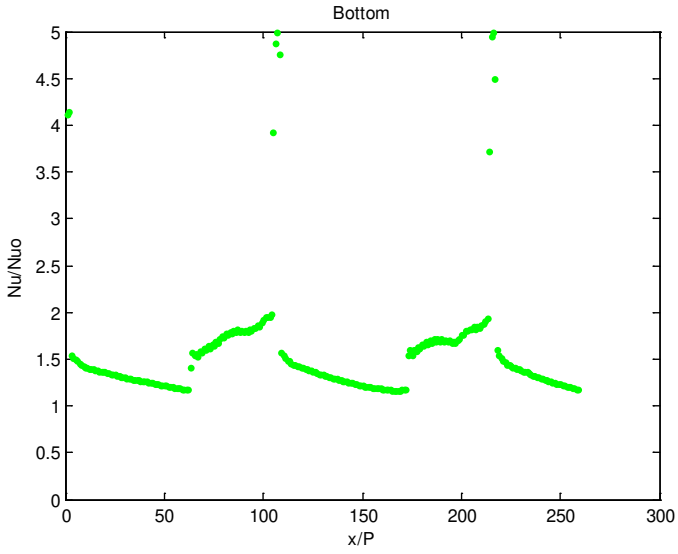

Figure 149: Case D TLC Streamwise Averaged Nu/Nuo Bottom 40,000 Re

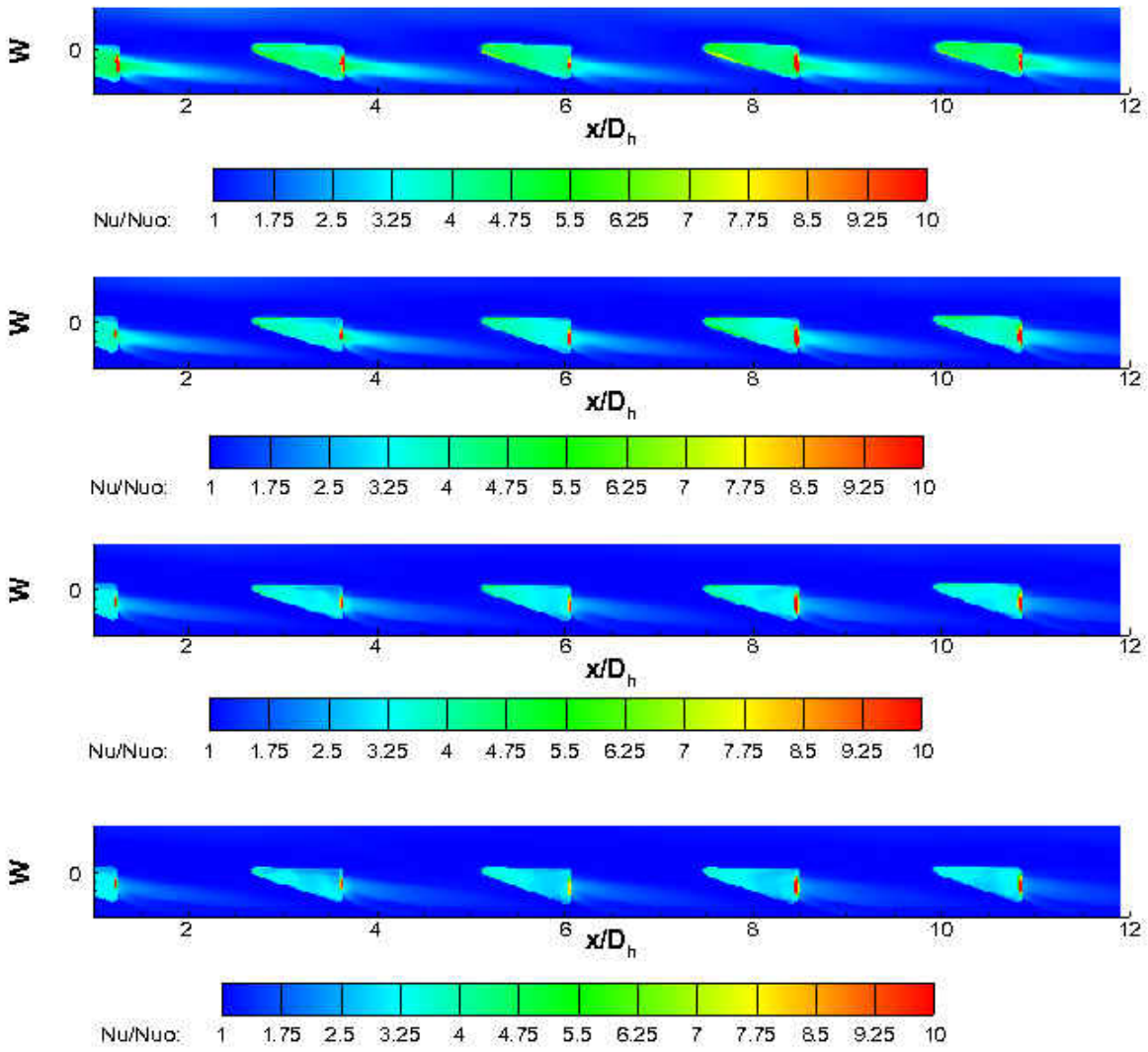

Figure 150: Case D Local Nusselt Number Augmentations Top Wall for 10k, 20k, 30k, 40k Re (ordered low-high)

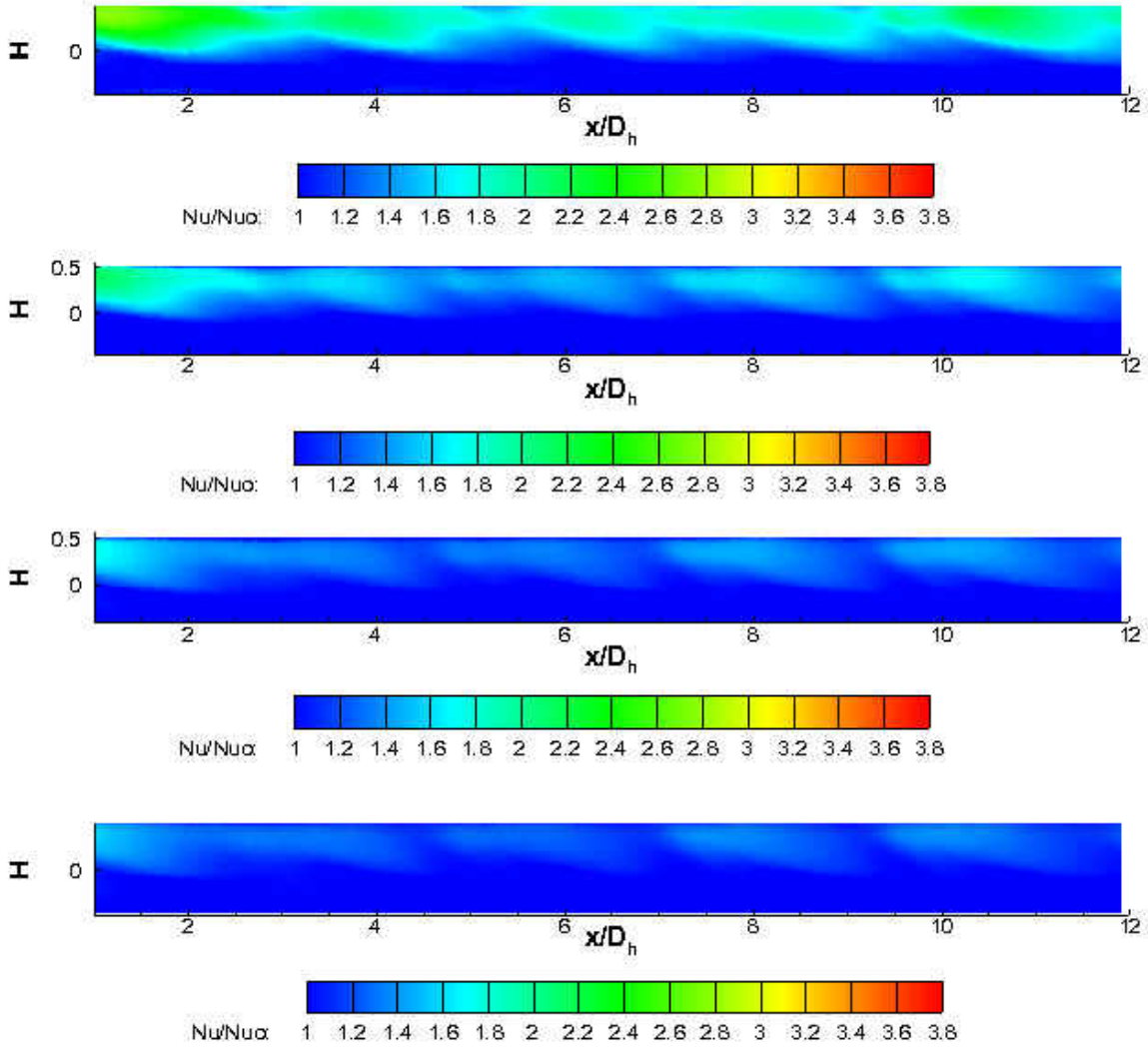

Figure 151: Case D Local Nusselt Number Augmentations Side Wall for 10k, 20k, 30k, 40k Re (ordered low-high)

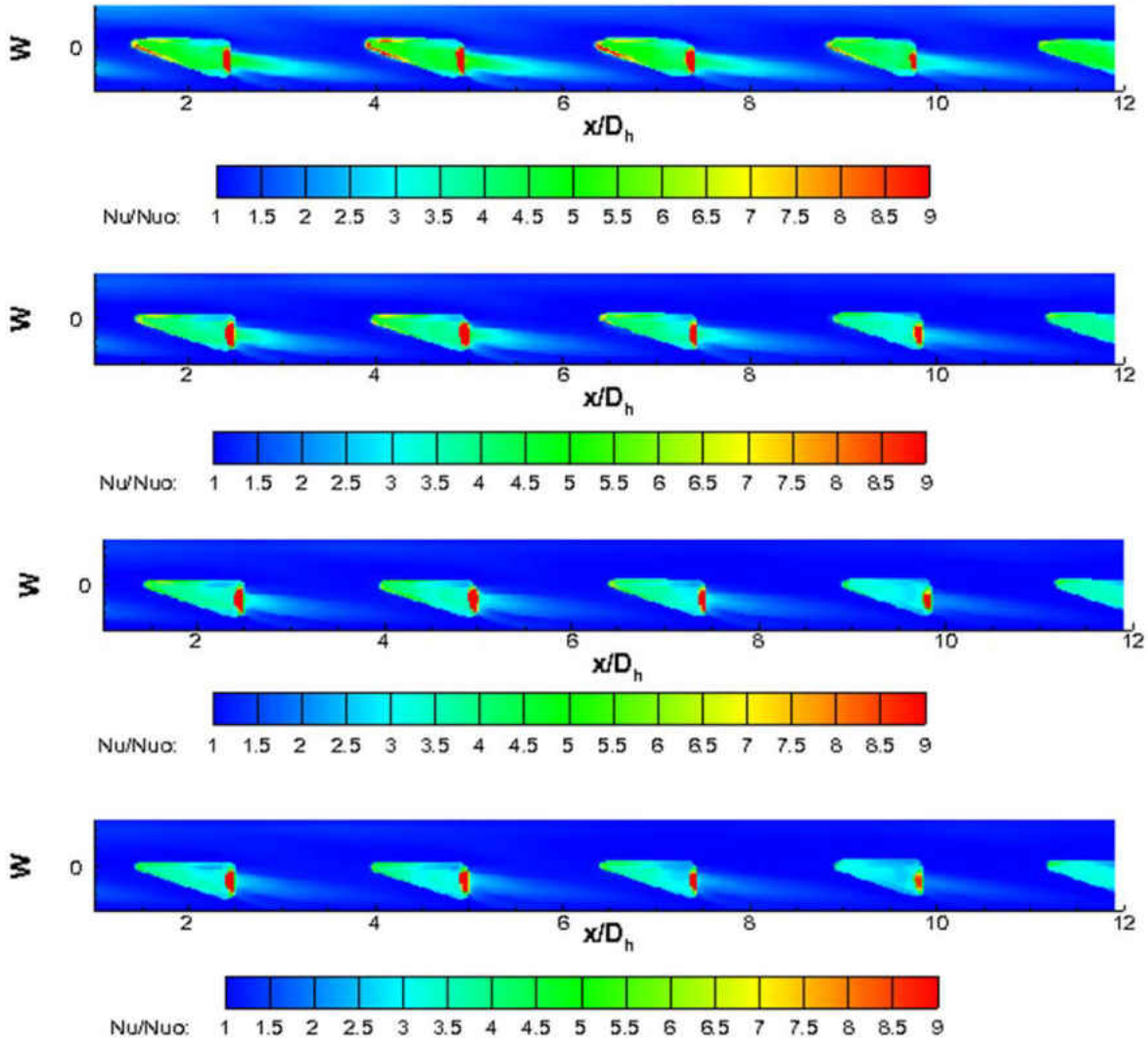

Figure 152: Case D Local Nusselt Number Augmentations Bottom Wall for 10k, 20k, 30k, 40k Re (ordered low-high)

Table 28: Overall Augmentations Case D TLC

Nominal Reynolds Number	10,000	20,000	30,000	40,000
Actual Reynolds Number	10260	20110	30100	39850
$\frac{Nu}{Nu_{DB}}$	1.98	1.65	1.49	1.44

Case E

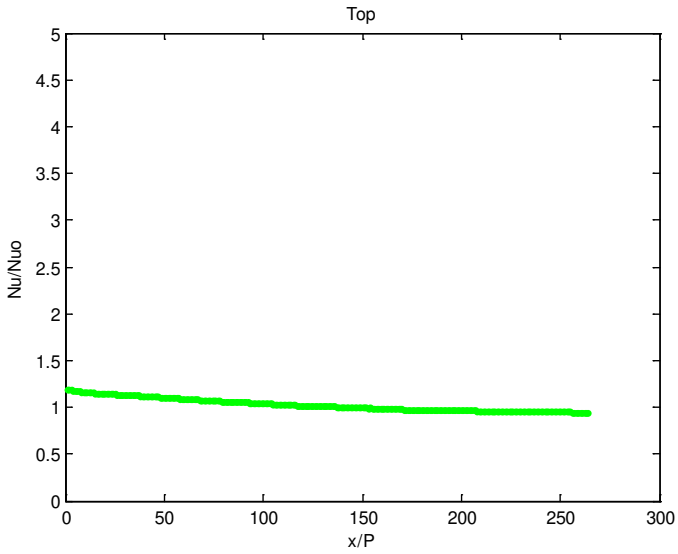

Figure 153: Case E TLC Streamwise Averaged Nu/Nuo Top 10,000 Re

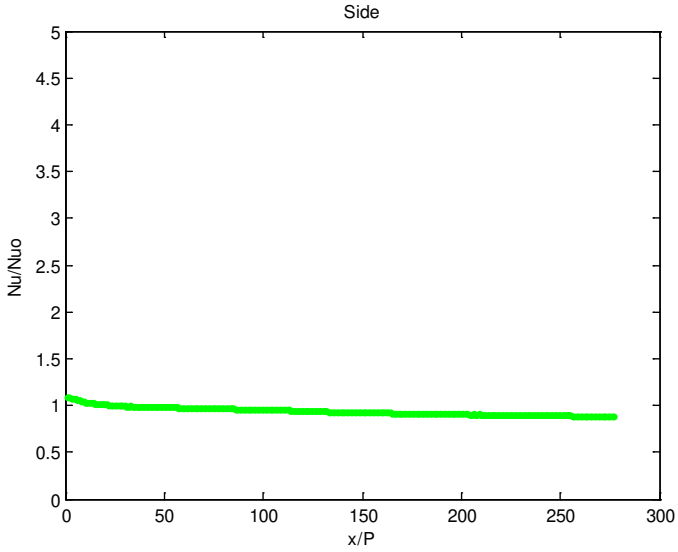

Figure 154: Case E TLC Streamwise Averaged Nu/Nuo Side 10,000 Re

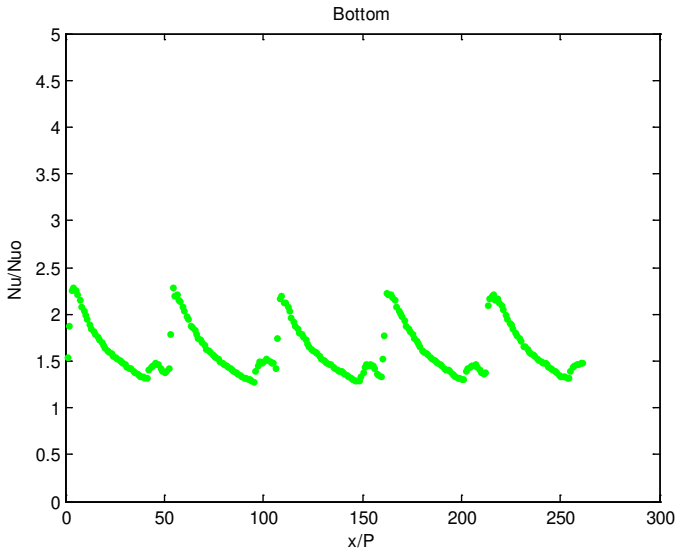

Figure 155: Case E TLC Streamwise Averaged Nu/Nuo Bottom 10,000 Re

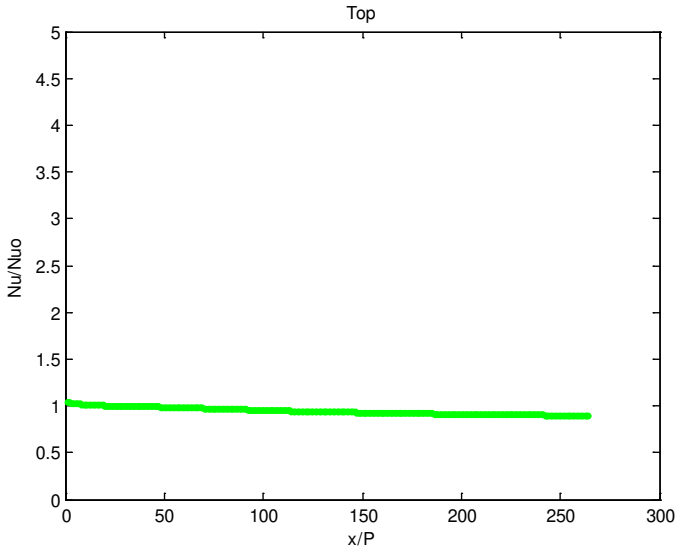

Figure 156: Case E TLC Streamwise Averaged Nu/Nuo Top 20,000 Re

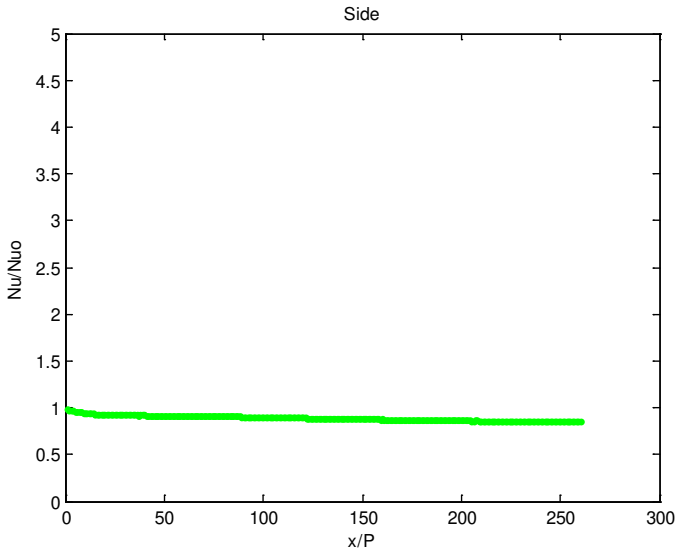

Figure 157: Case E TLC Streamwise Averaged Nu/Nuo Side 20,000 Re

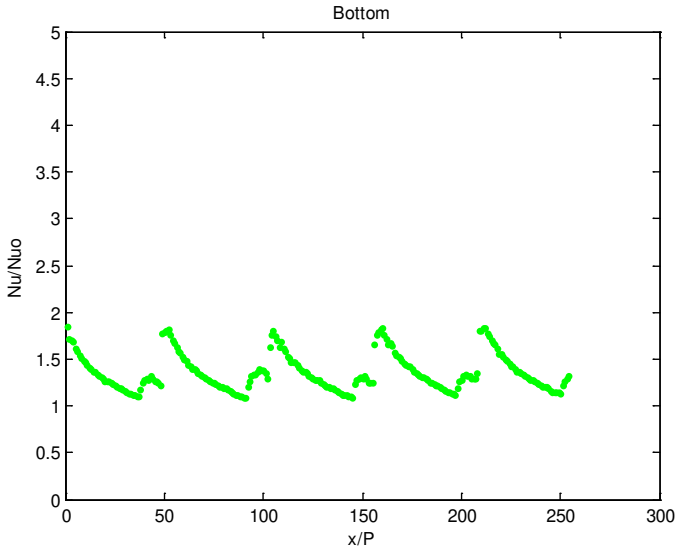

Figure 158: Case E TLC Streamwise Averaged Nu/Nuo Bottom 20,000 Re

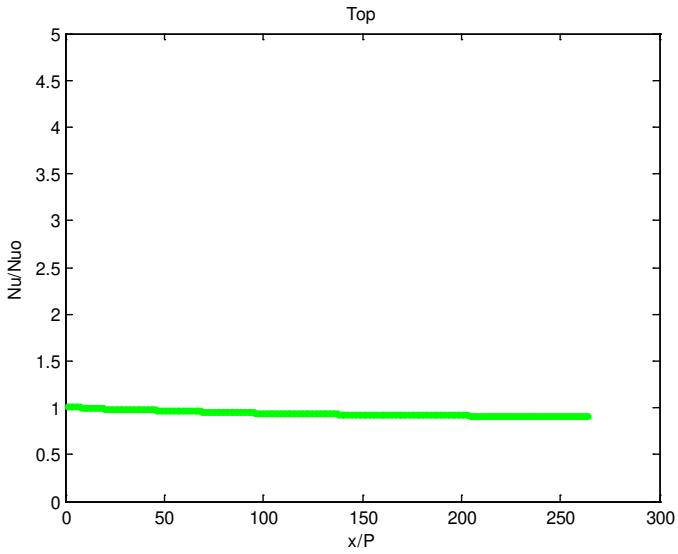

Figure 159: Case E TLC Streamwise Averaged Nu/Nuo Top 30,000 Re

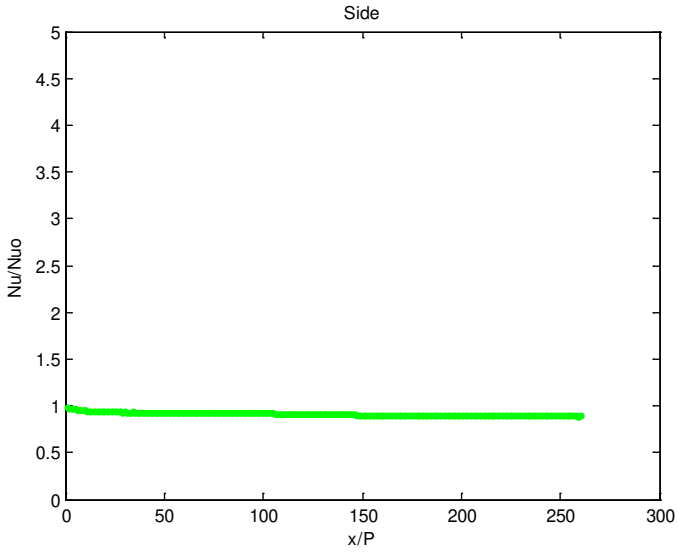

Figure 160: Case E TLC Streamwise Averaged Nu/Nuo Side 30,000 Re

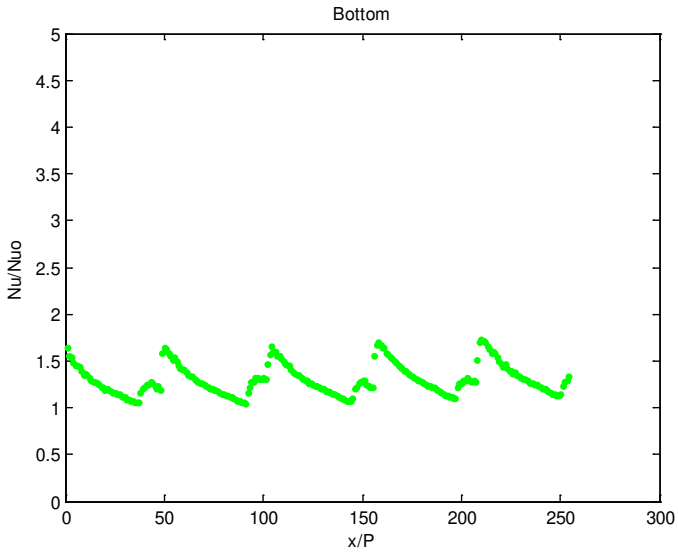

Figure 161: Case E TLC Streamwise Averaged Nu/Nuo Bottom 30,000 Re

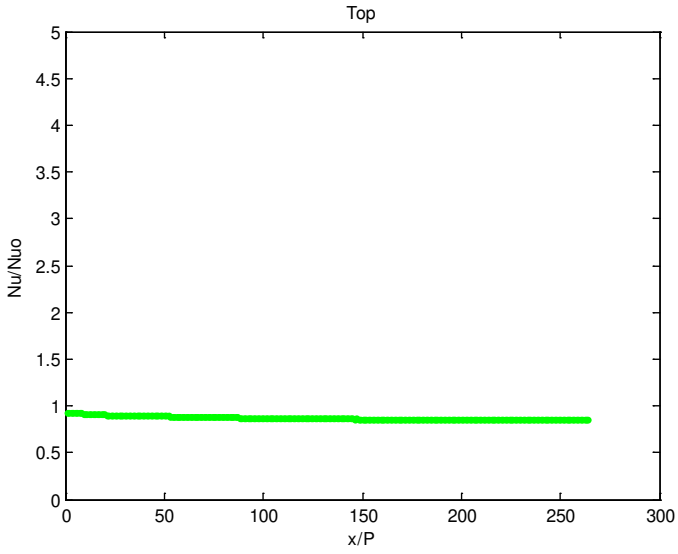

Figure 162: Case E TLC Streamwise Averaged Nu/Nuo Top 40,000 Re

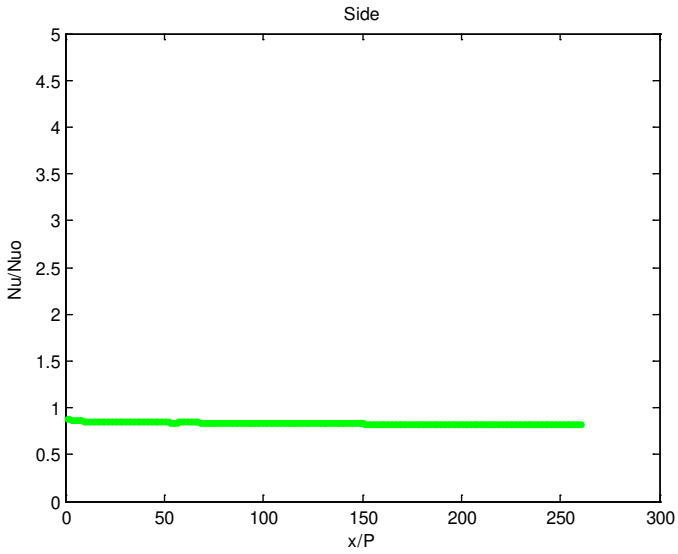

Figure 163: Case E TLC Streamwise Averaged Nu/Nuo Side 40,000 Re

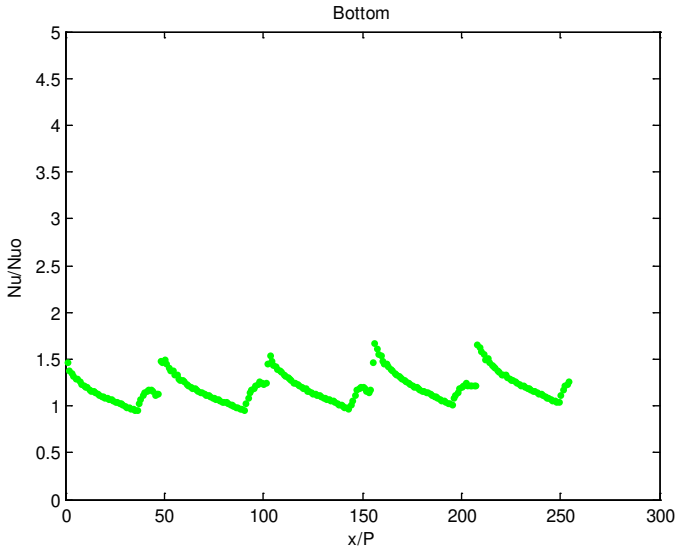

Figure 164: Case E TLC Streamwise Averaged Nu/Nuo Bottom 40,000 Re

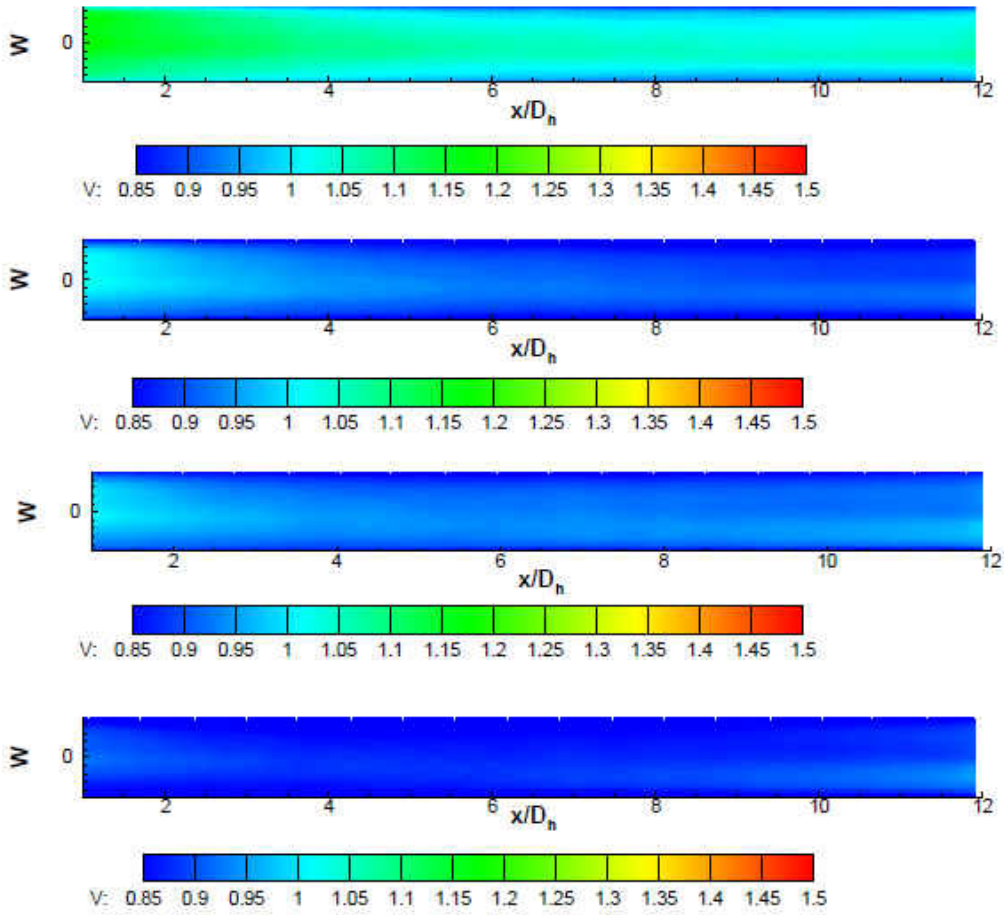

Figure 165: Case E Local Nusselt Number Augmentations Top Wall for 10k, 20k, 30k, 40k Re (ordered low-high)

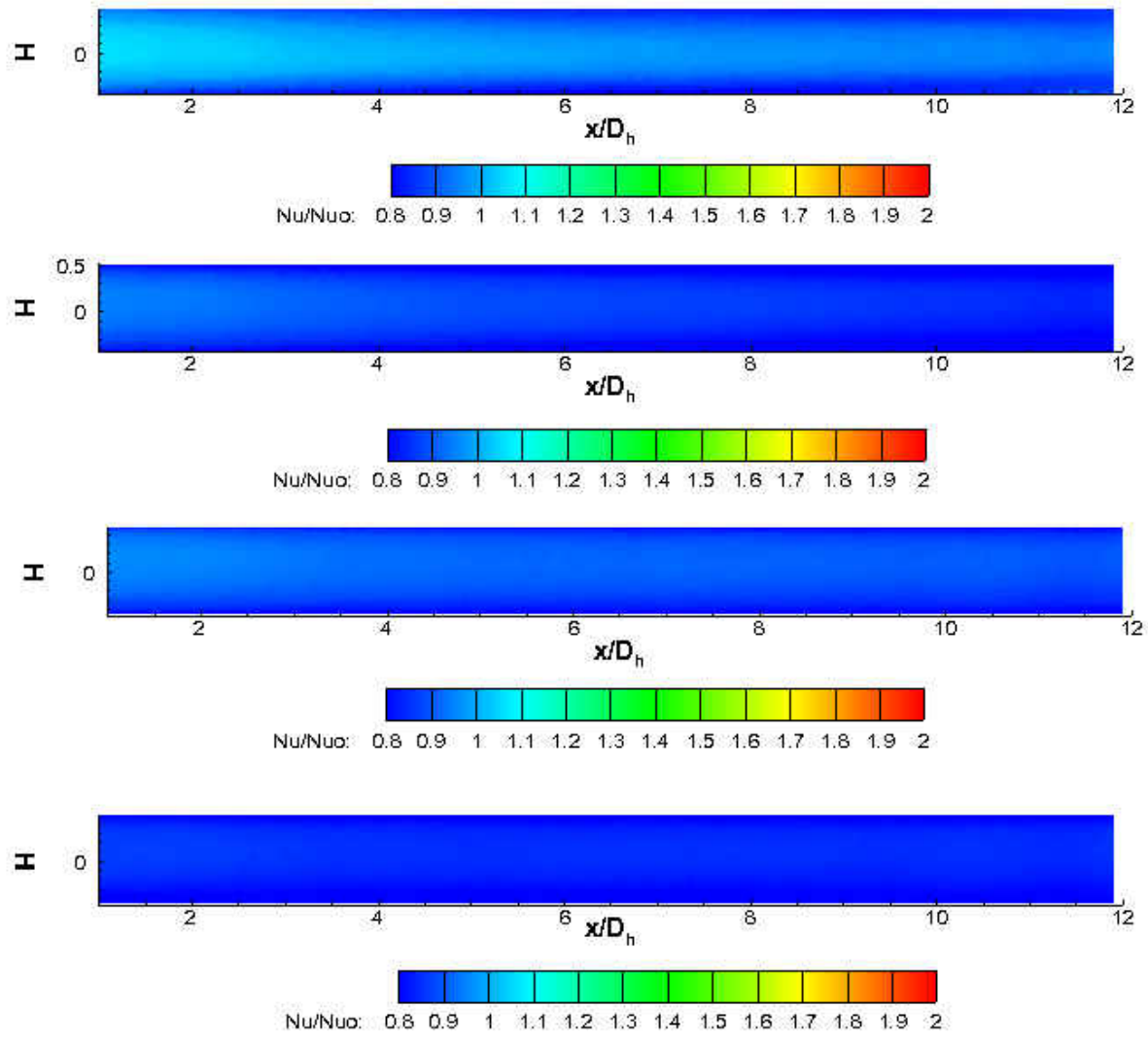

Figure 166: Case E Local Nusselt Number Augmentations Side Wall for 10k, 20k, 30k, 40k Re (ordered low-high)

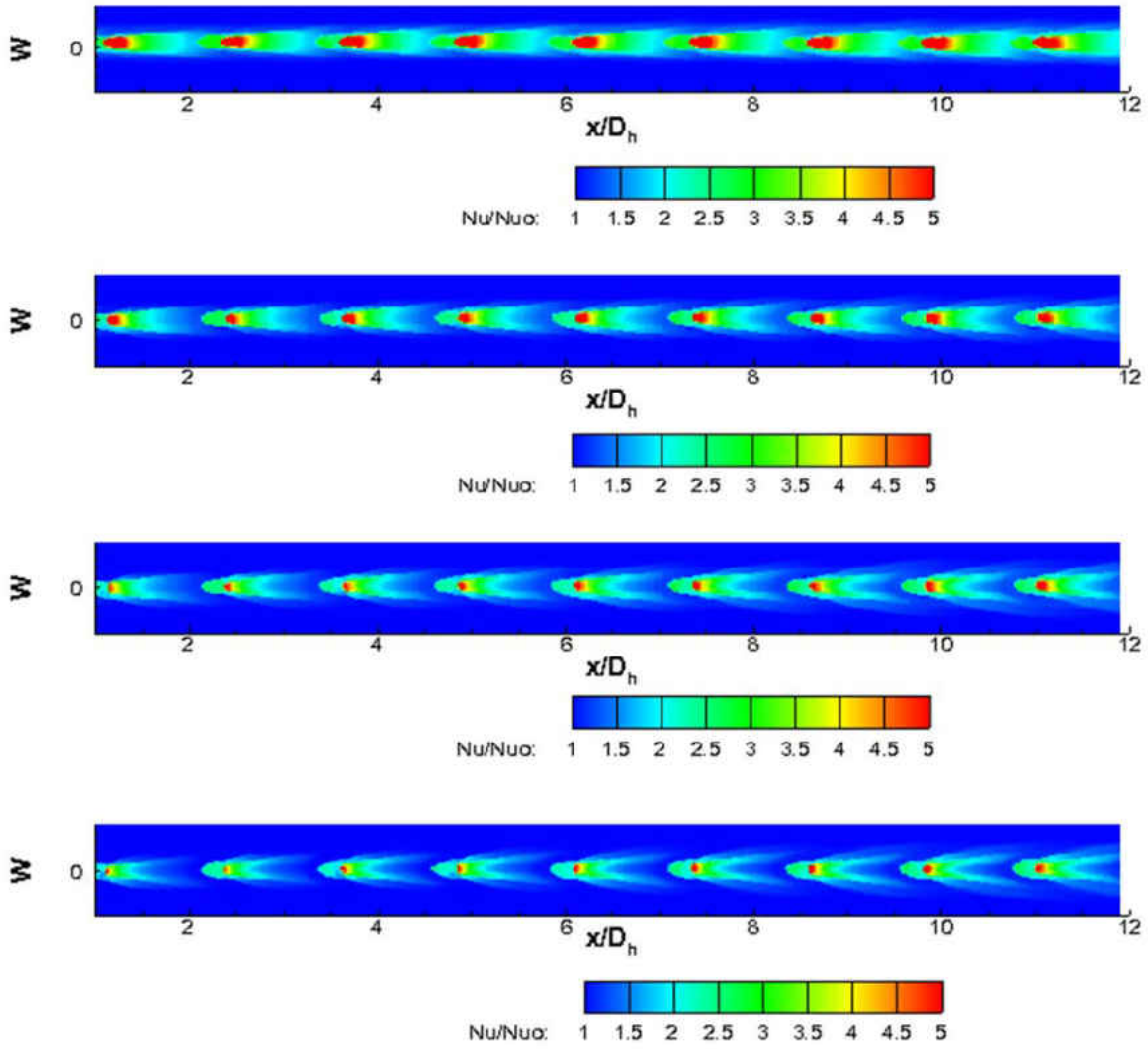

Figure 167: Case E Local Nusselt Number Augmentations Bottom Wall for 10k, 20k, 30k, 40k Re (ordered low-high)

Table 29: Overall Augmentations Case E TLC

Nominal Reynolds Number	10,000	20,000	30,000	40,000
Actual Reynolds Number	10236	19954	29930	40100
$\frac{Nu}{Nu_{DB}}$	1.33	1.16	1.13	1.04

Case F

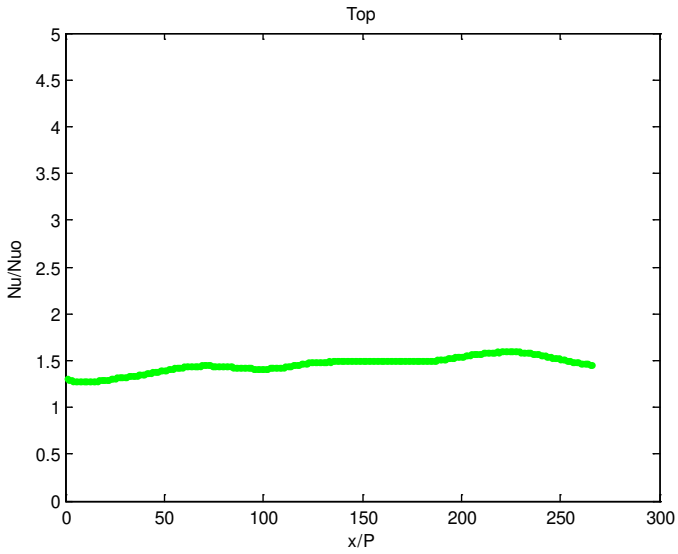

Figure 168: Case F TLC Streamwise Averaged Nu/Nuo Top 10,000 Re

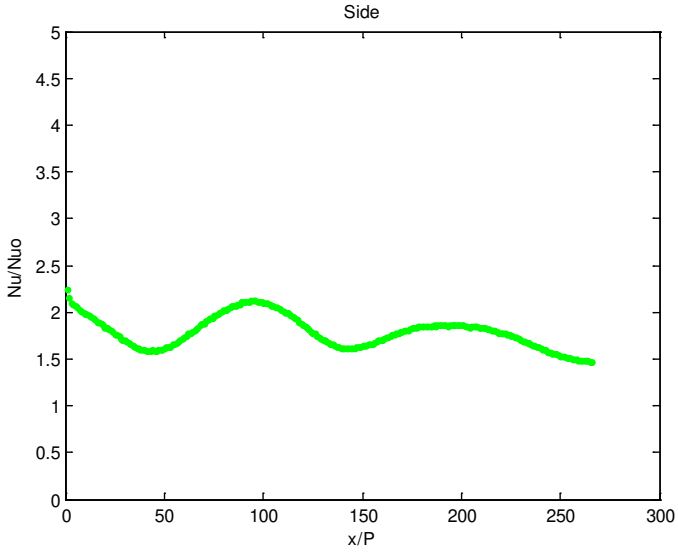

Figure 169: Case F TLC Streamwise Averaged Nu/Nuo Side 10,000 Re

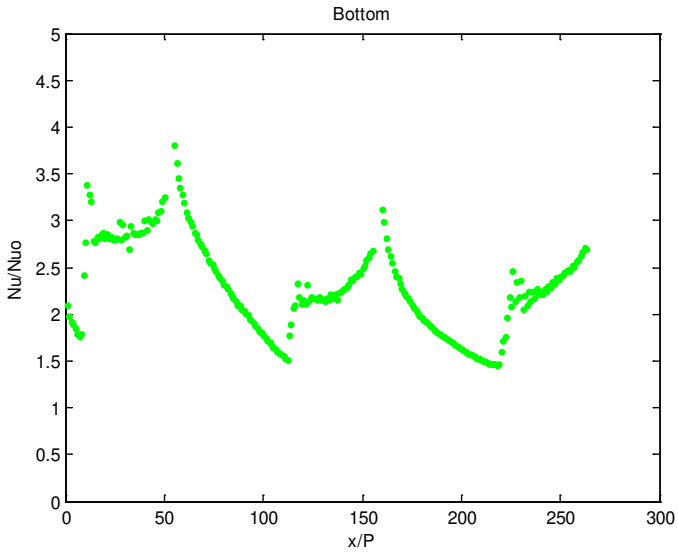

Figure 170: Case F TLC Streamwise Averaged Nu/Nuo Bottom 10,000 Re

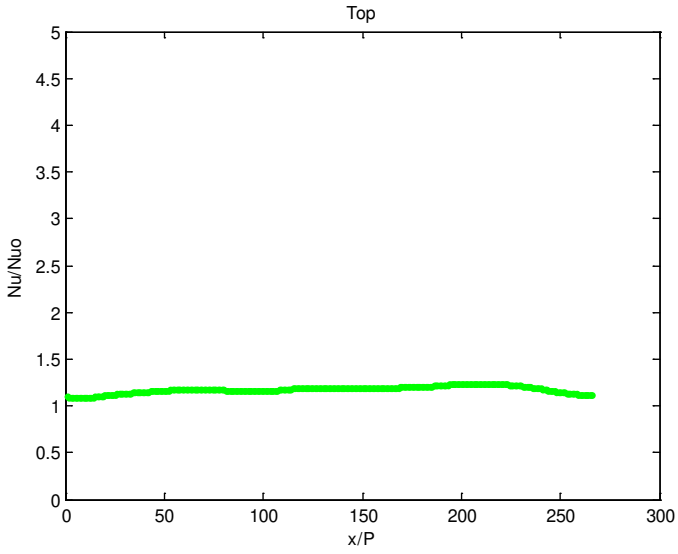

Figure 171: Case F TLC Streamwise Averaged Nu/Nuo Top 20,000 Re

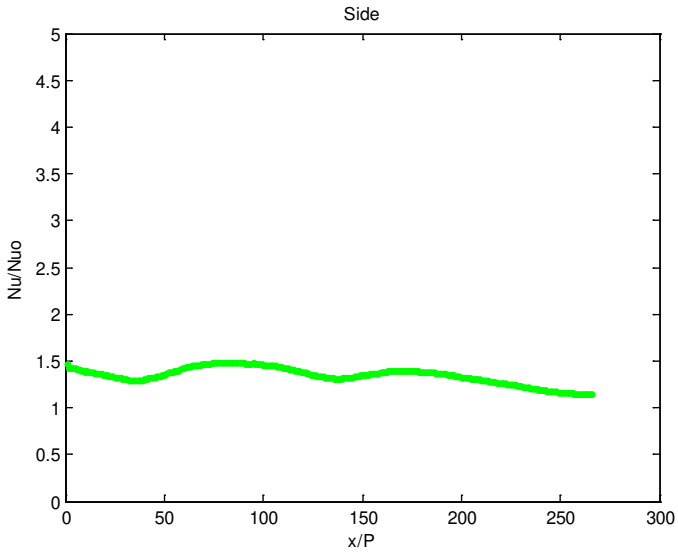

Figure 172: Case F TLC Streamwise Averaged Nu/Nuo Side 20,000 Re

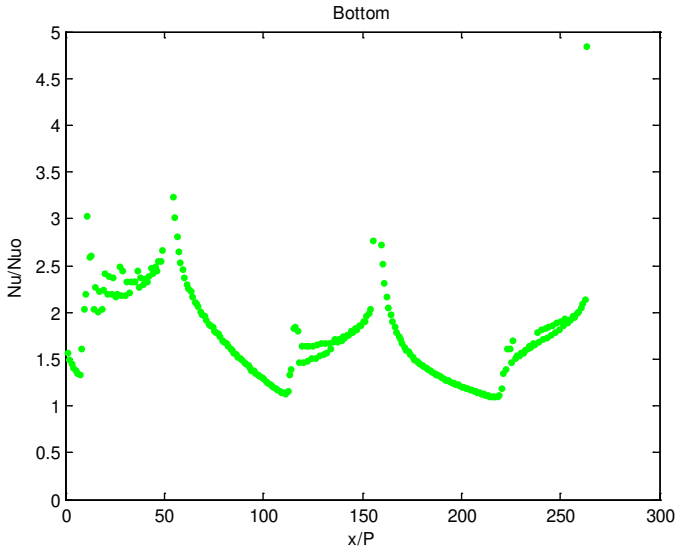

Figure 173: Case F TLC Streamwise Averaged Nu/Nuo Bottom 20,000 Re

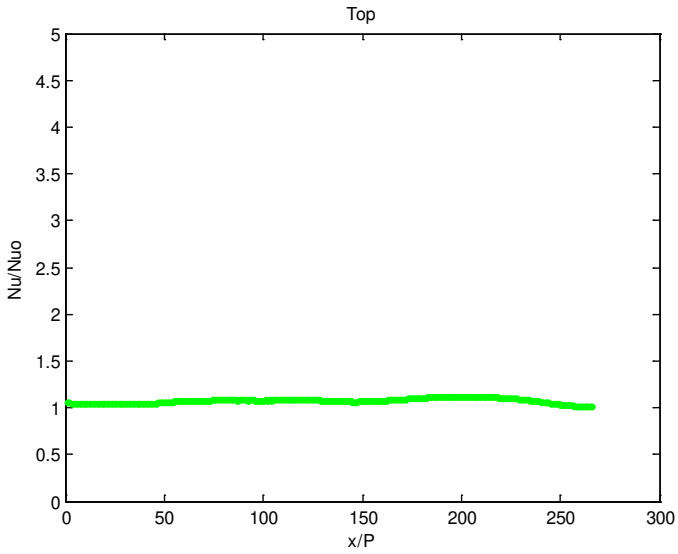

Figure 174: Case F TLC Streamwise Averaged Nu/Nuo Top 30,000 Re

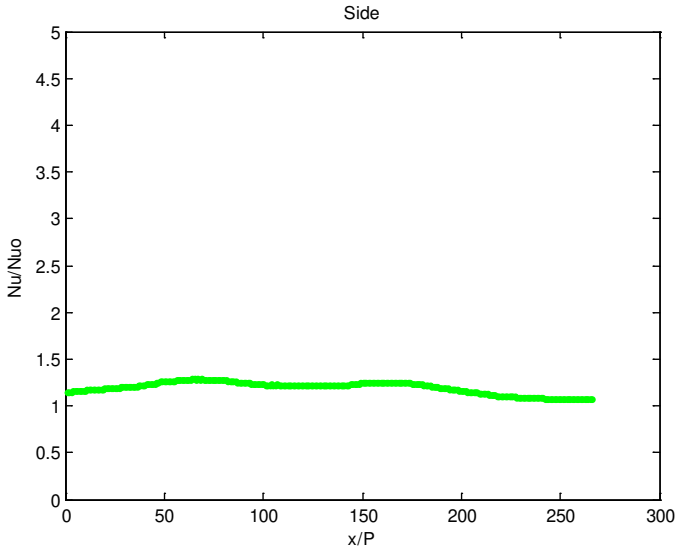

Figure 175: Case F TLC Streamwise Averaged Nu/Nuo Side 30,000 Re

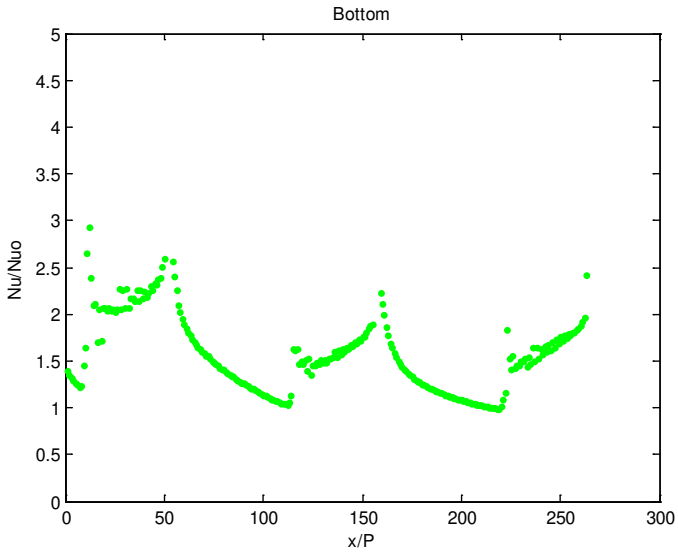

Figure 176: Case F TLC Streamwise Averaged Nu/Nuo Bottom 30,000 Re

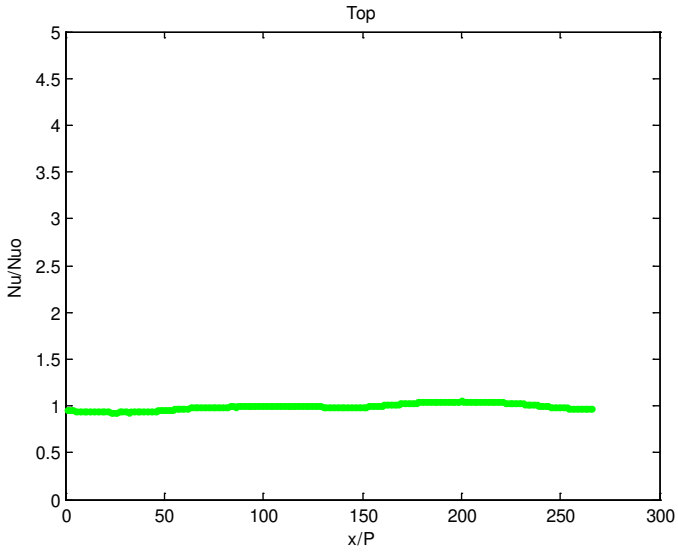

Figure 177: Case F TLC Streamwise Averaged Nu/Nuo Top 40,000 Re

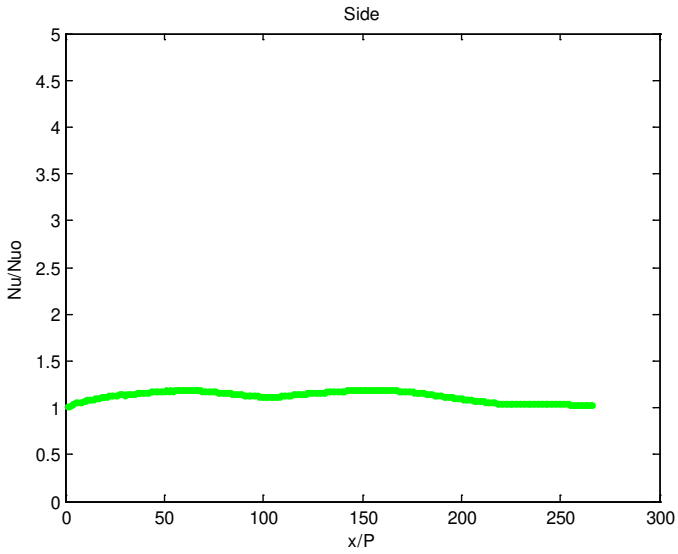

Figure 178: Case F TLC Streamwise Averaged Nu/Nuo Side 40,000 Re

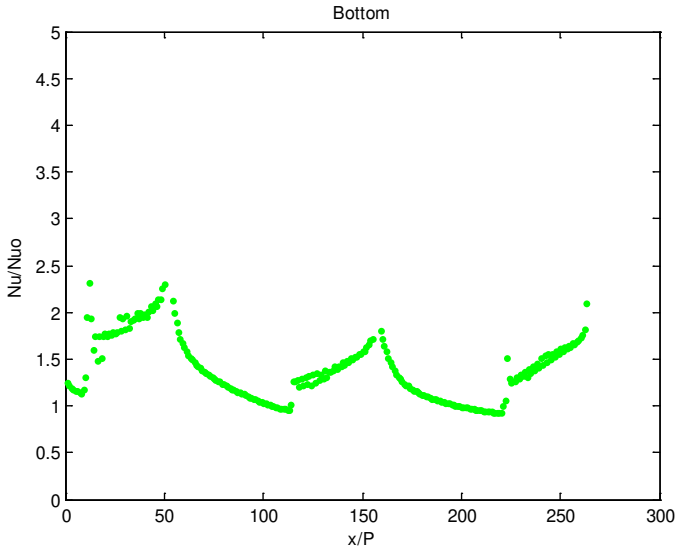

Figure 179: Case F TLC Streamwise Averaged Nu/Nuo Bottom 40,000 Re

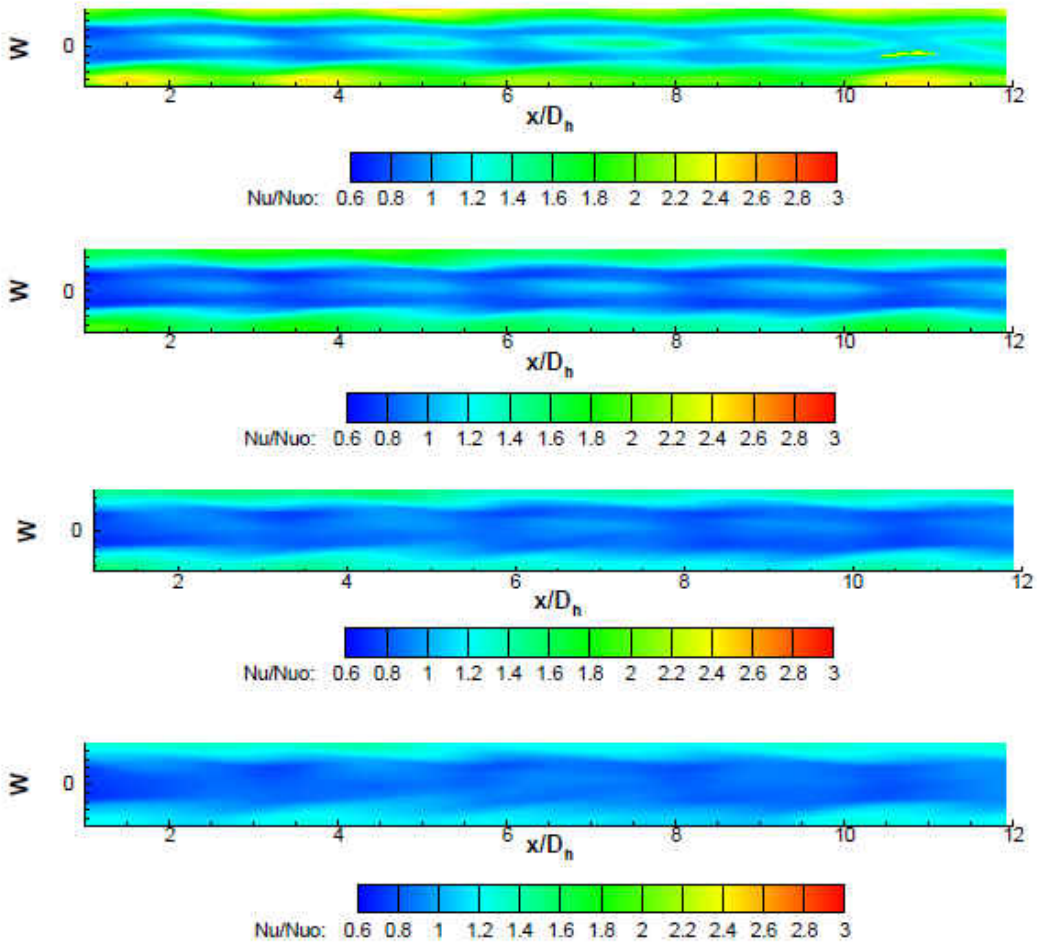

Figure 180: Case F Local Nusselt Number Augmentations Top Wall for 10k, 20k, 30k, 40k Re (ordered low-high)

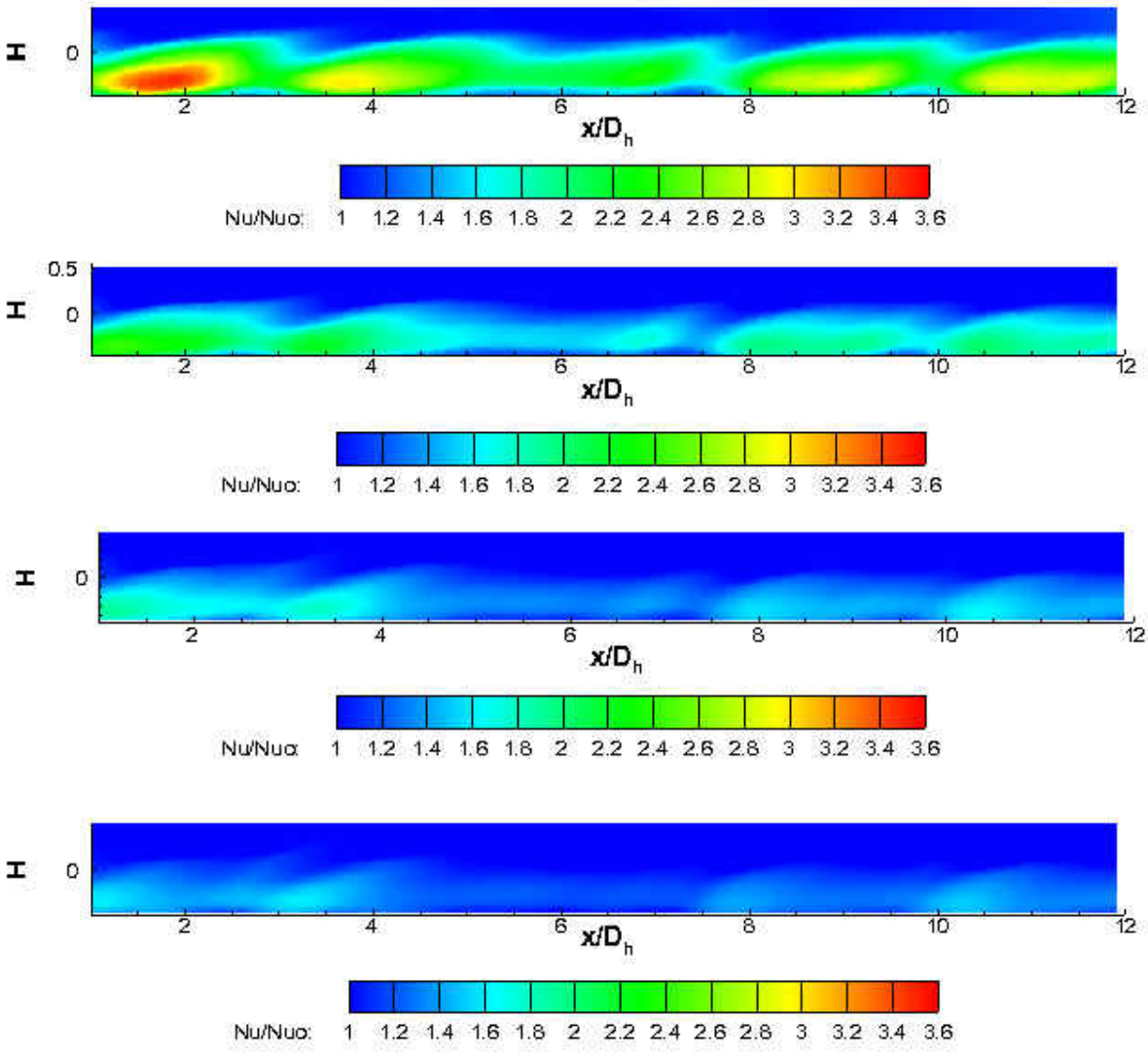

Figure 181: Case F Local Nusselt Number Augmentations Side Wall for 10k, 20k, 30k, 40k Re (ordered low-high)

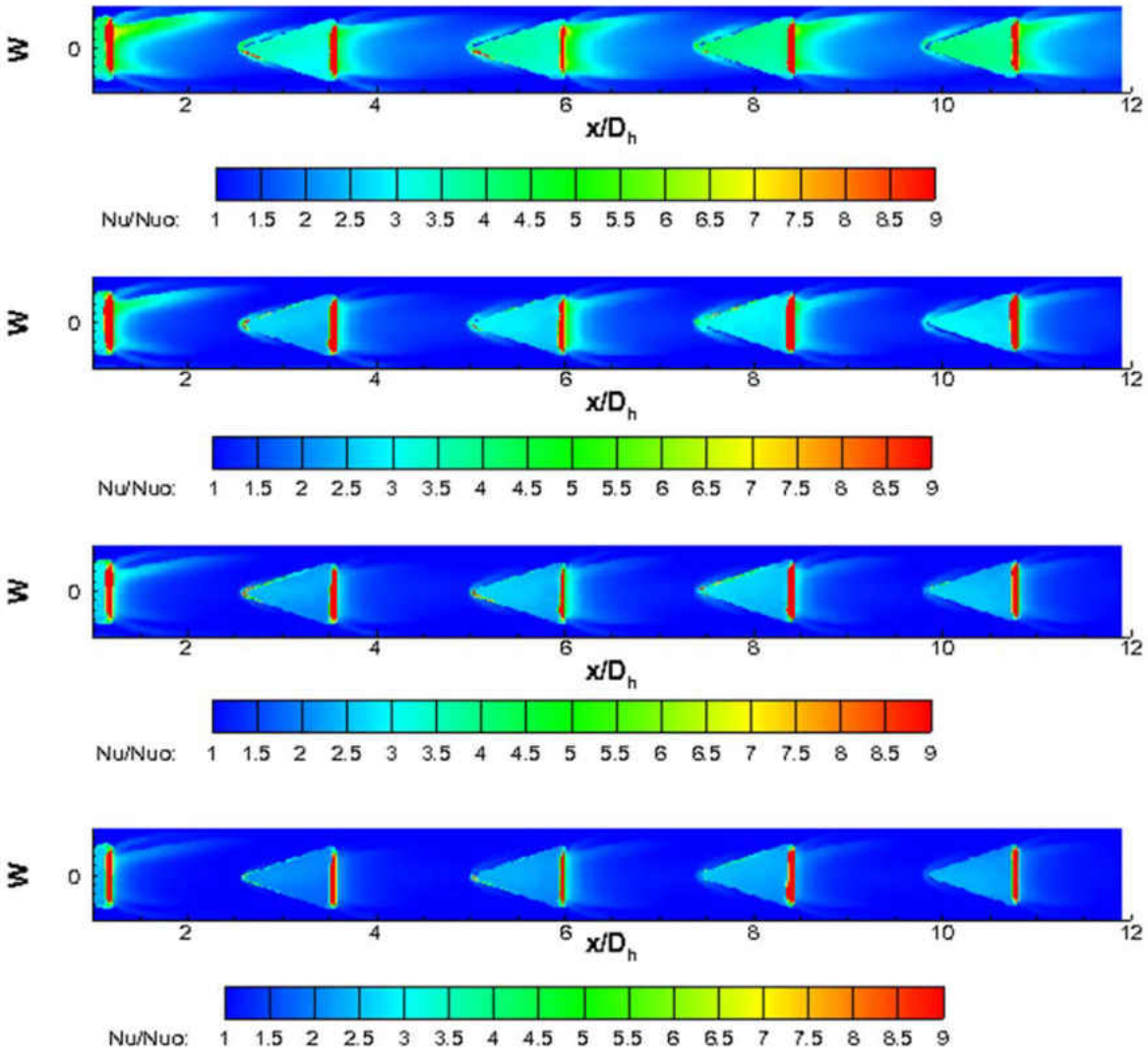

Figure 182: Case F Local Nusselt Number Augmentations Bottom Wall for 10k, 20k, 30k, 40k Re (ordered low-high)

Nominal Reynolds Number	10,000	20,000	30,000	40,000
Actual Reynolds Number	10260	20260	30000	39950
$\frac{Nu}{Nu_{DB}}$	2.03	1.61	1.42	1.27

Transient TLC Thermal Performances

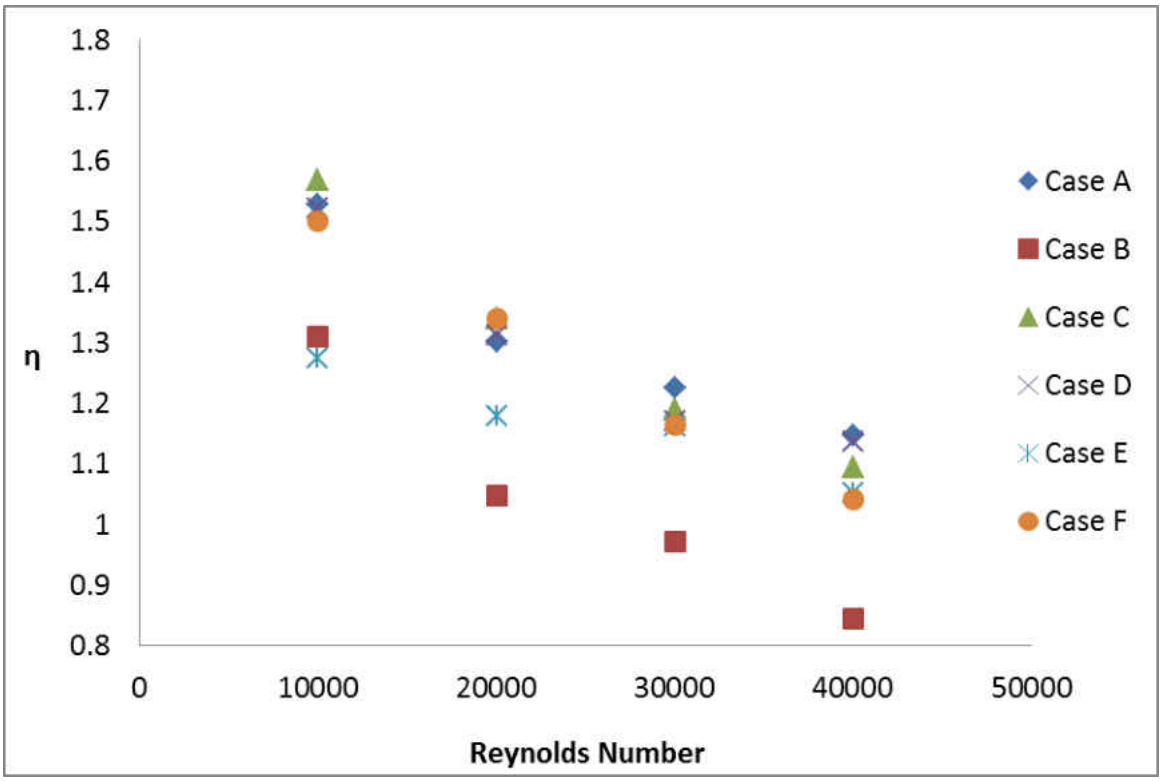

Figure 183: Thermal Performance TLC

Table 30: Thermal Performance (η) Values TLC Setup

	Case A	Case B	Case C	Case D	Case E	Case F
10000	1.53	1.31	1.57	1.52	1.27	1.50
20000	1.30	1.05	1.34	1.31	1.18	1.34
30000	1.23	0.97	1.19	1.17	1.16	1.16
40000	1.15	0.85	1.09	1.14	1.05	1.04

CFD

Case A

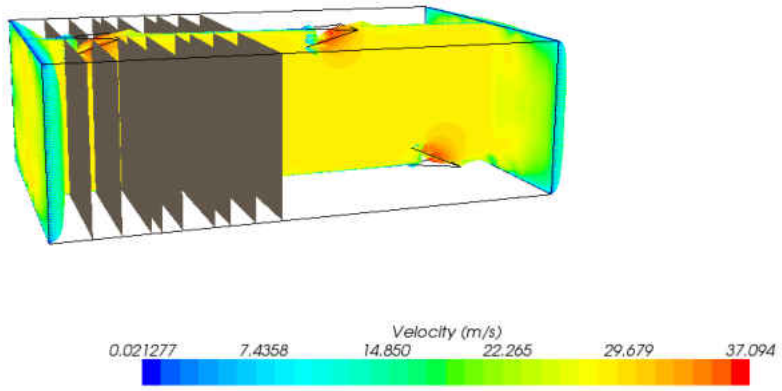

Figure 184: Streamwise Plane Cuts Case A

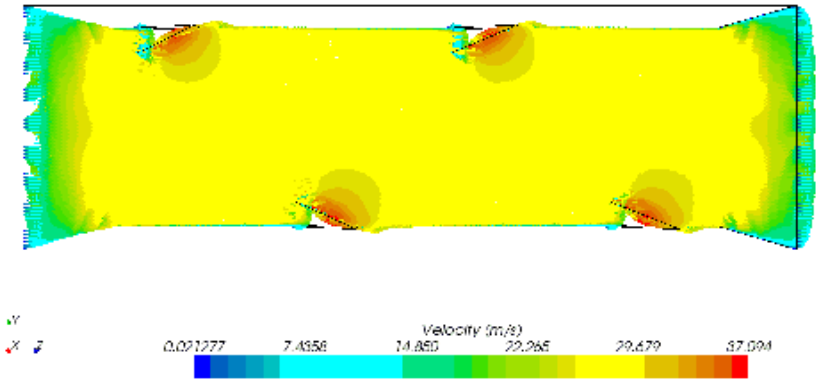

Figure 185: Centerline Velocity Case A

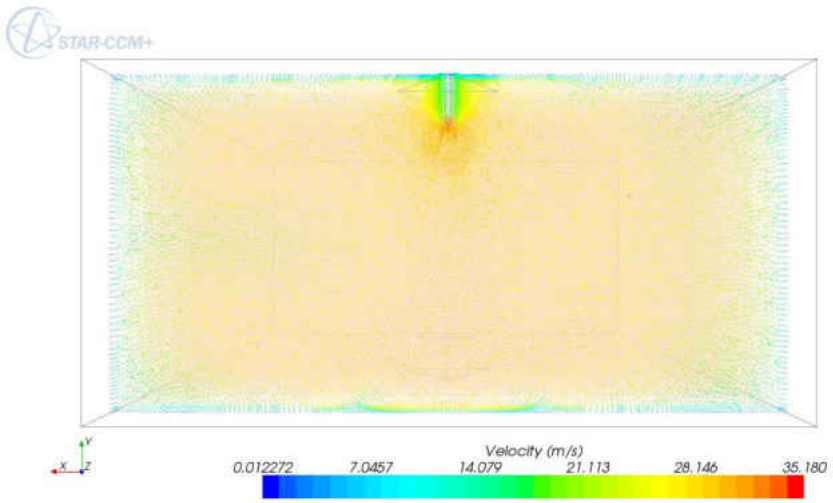

Figure 186: Velocity at Wedge Tip Case A

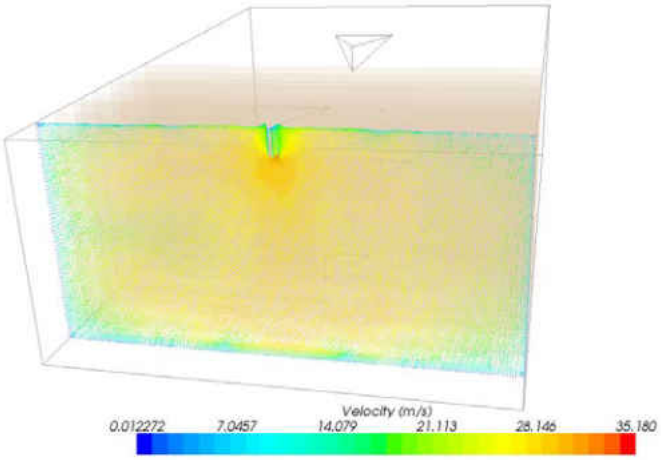

Figure 187: Case A Velocity Plane 1

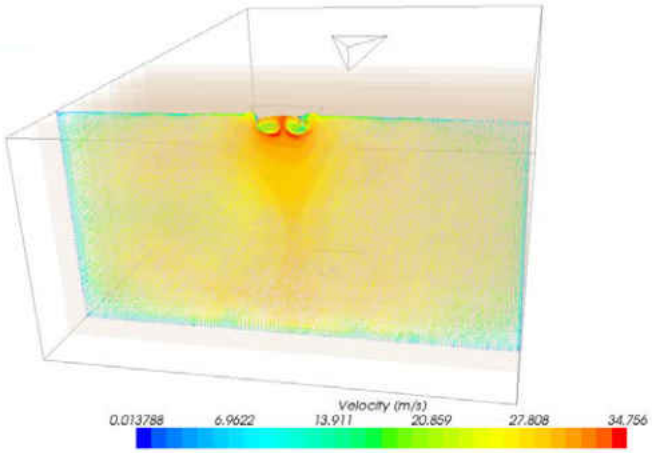

Figure 188: Case A Velocity Plane 2

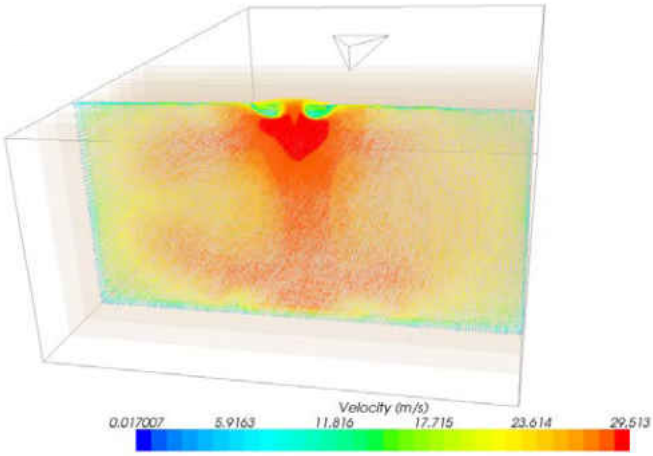

Figure 189: Case A Velocity Plane 3

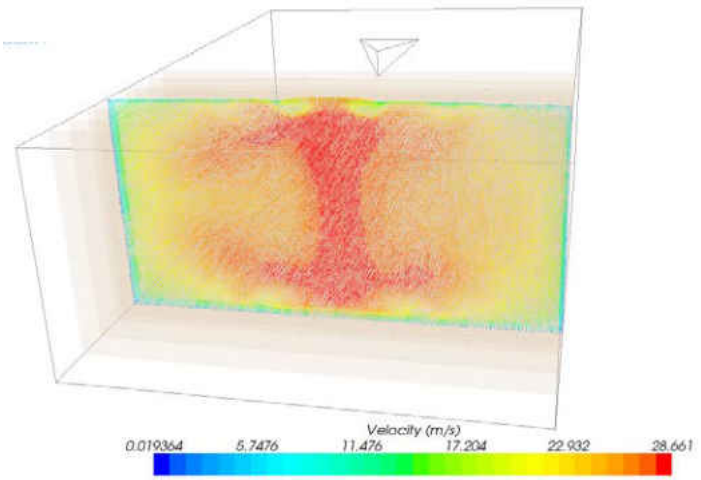

Figure 190: Case A Velocity Plane 4

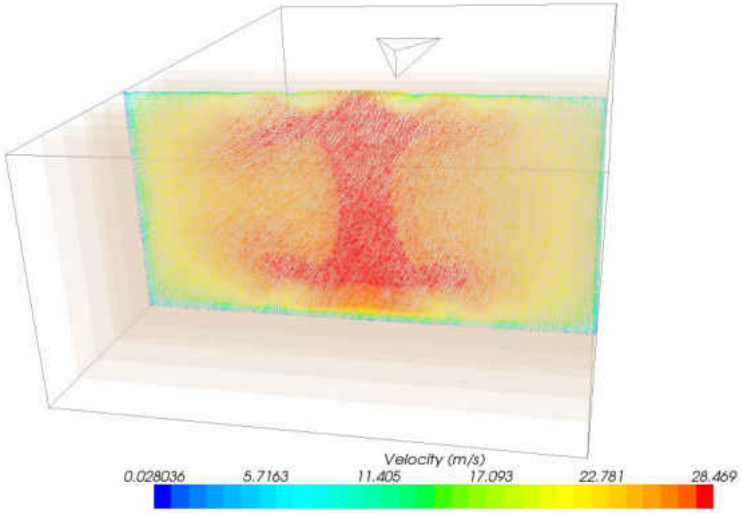

Figure 191: Case A Velocity Plane 5

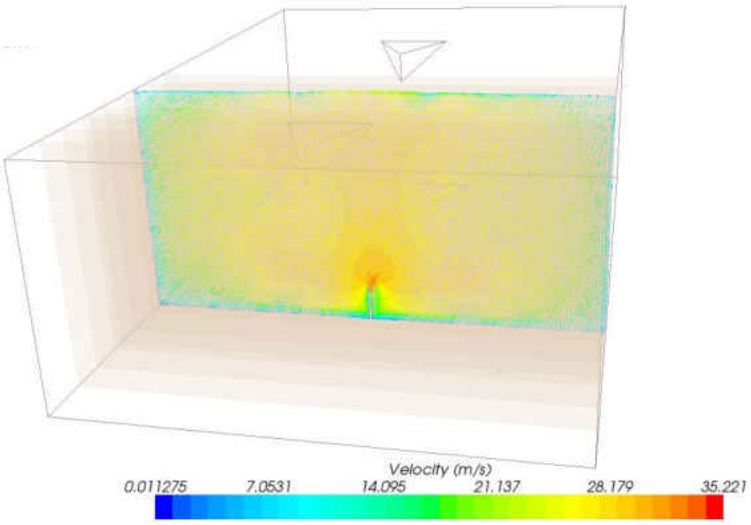

Figure 192: Case A Velocity Plane 6

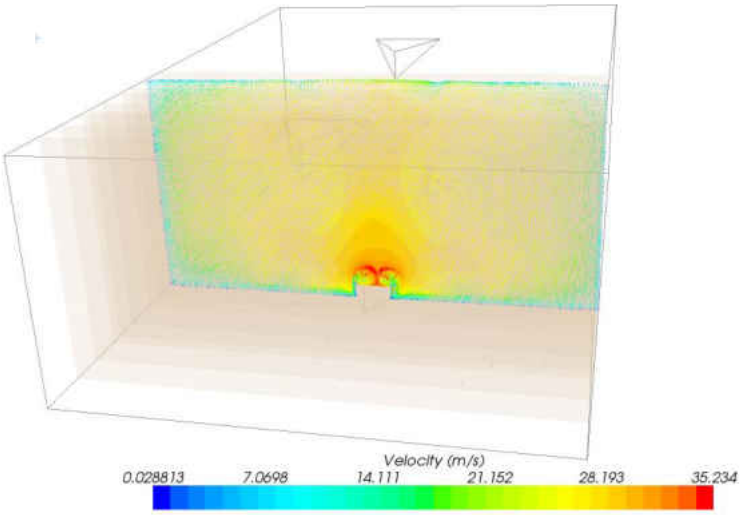

Figure 193: Case A Velocity Plane 7

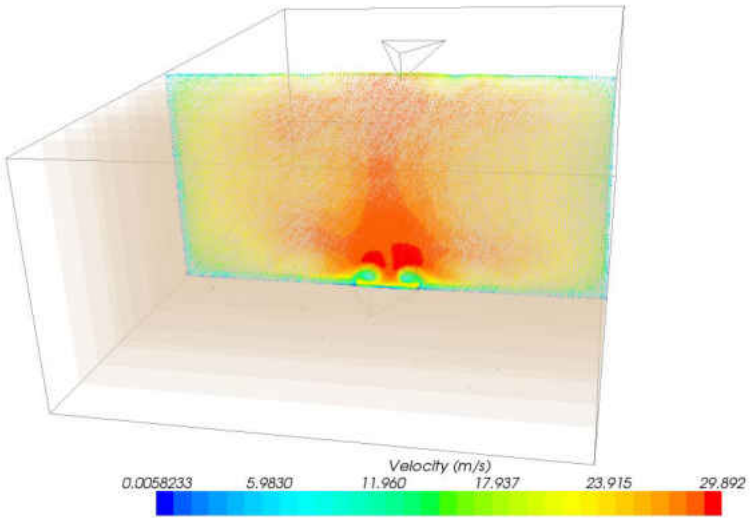

Figure 194: Case A Velocity Plane 8

Case B

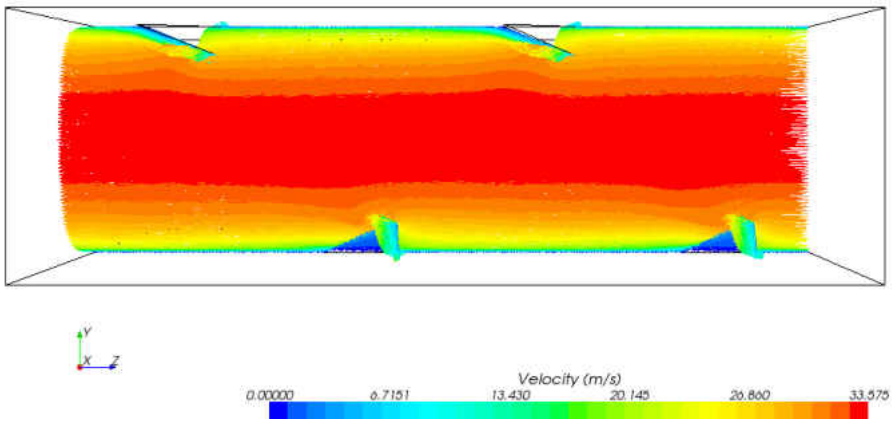

Figure 195: Centerline Velocity Case B

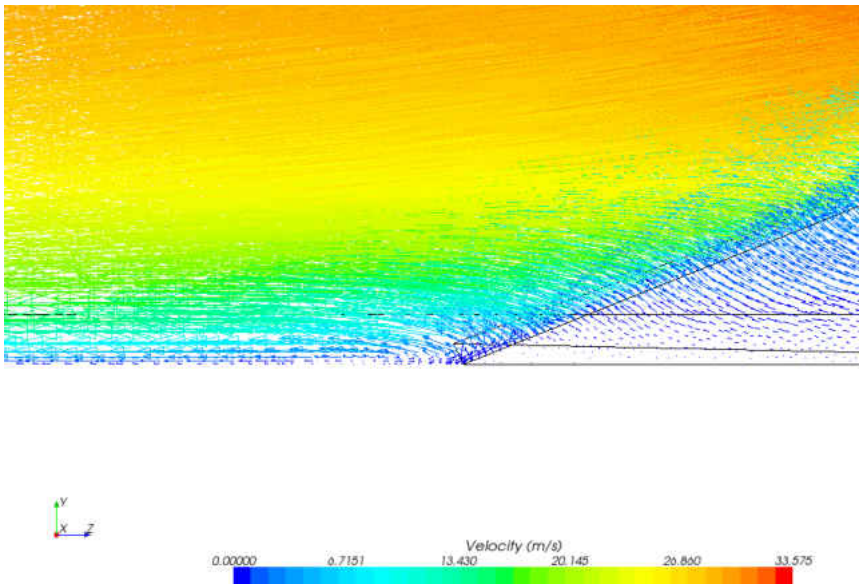

Figure 196: Recirculation at Wedge Tail

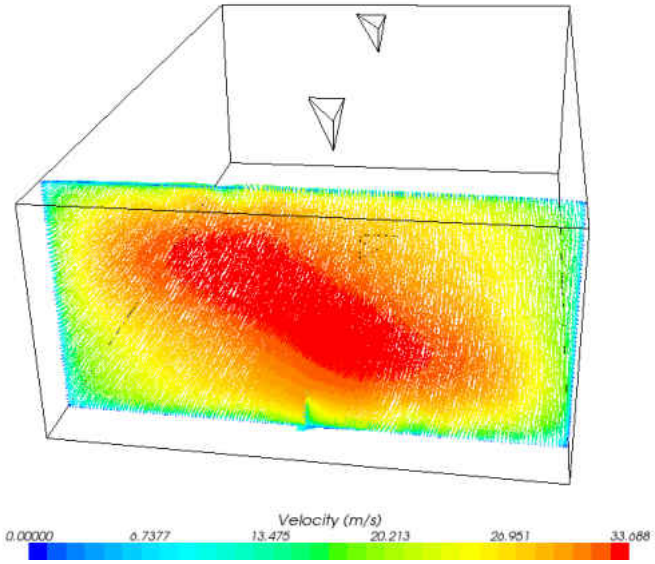

Figure 197: Case B Velocity Plan 1

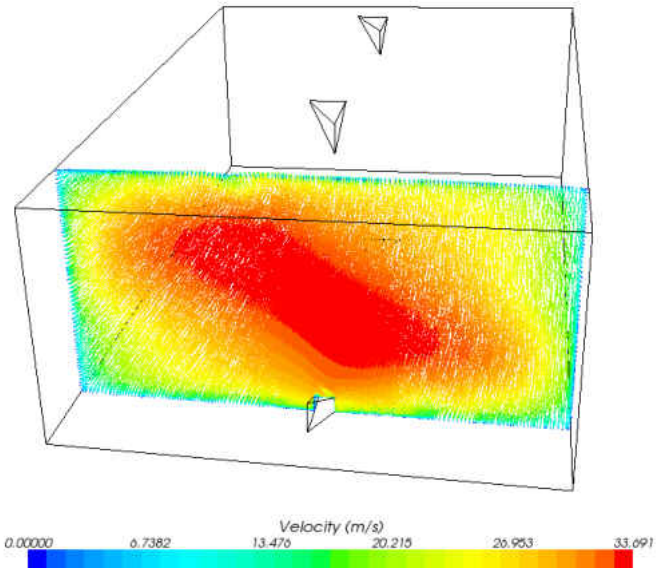

Figure 198: Case B Velocity Plan 2

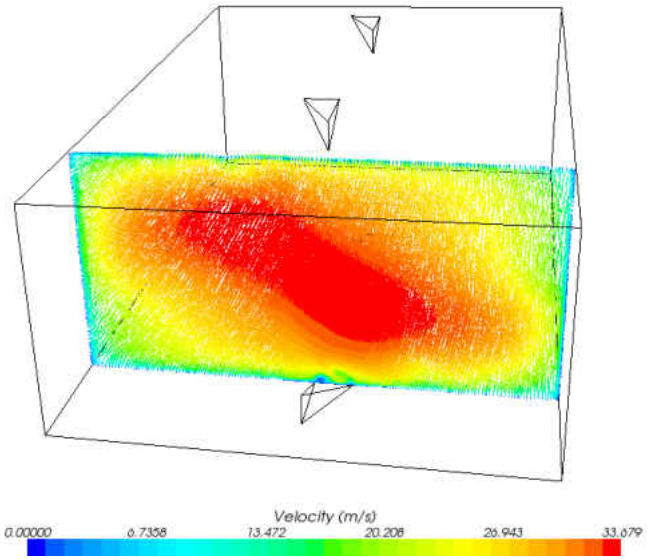

Figure 199: Case B Velocity Plan 3

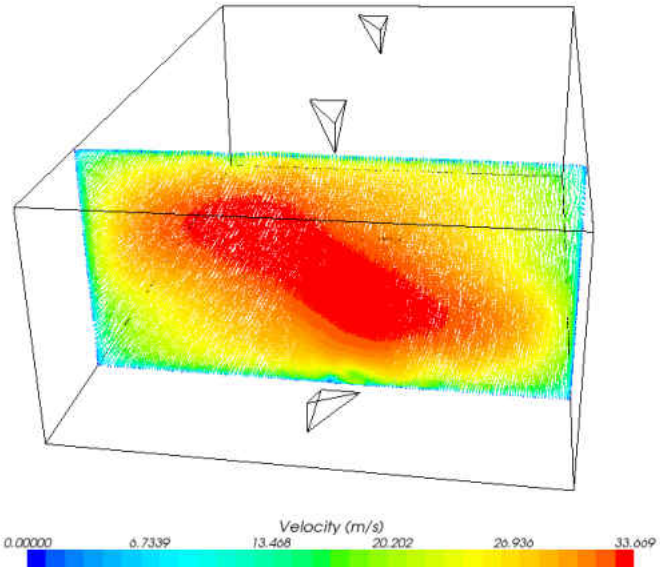

Figure 200: Case B Velocity Plan 4

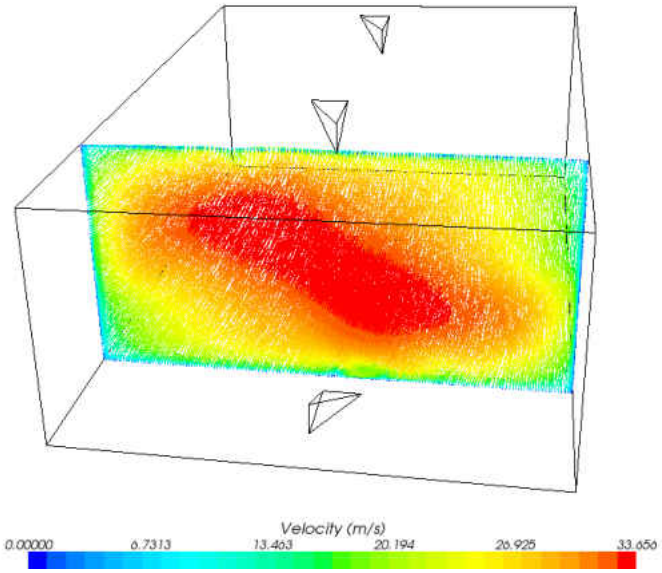

Figure 201: Case B Velocity Plan 5

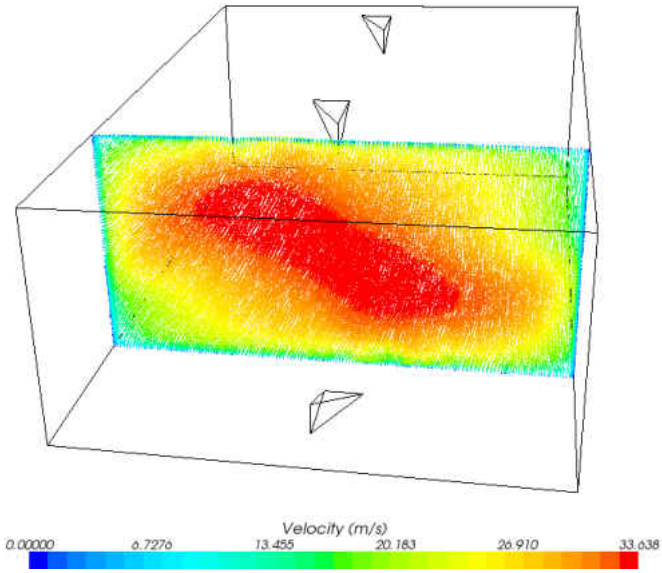

Figure 202: Case B Velocity Plan 6

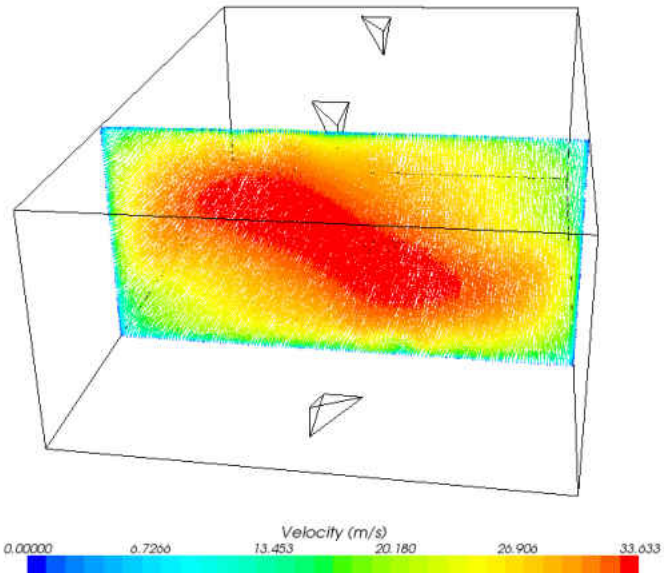

Figure 203: Case B Velocity Plan 7

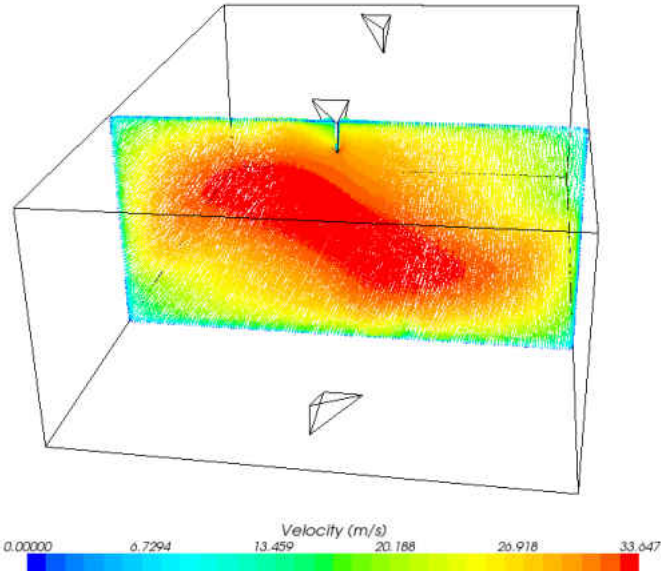

Figure 204: Case B Velocity Plan 8

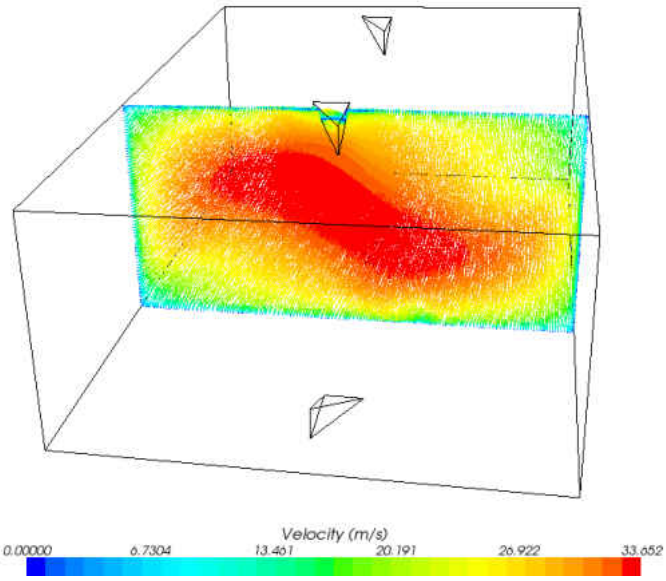

Figure 205: Case B Velocity Plan 9

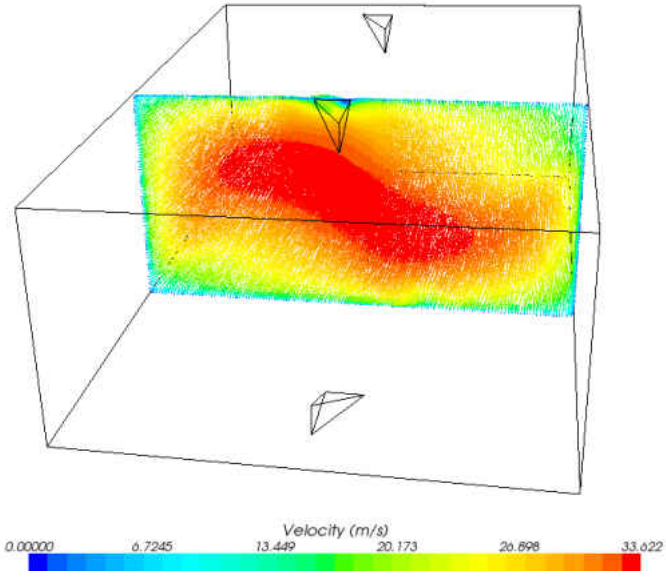

Figure 206: Case B Velocity Plan 10

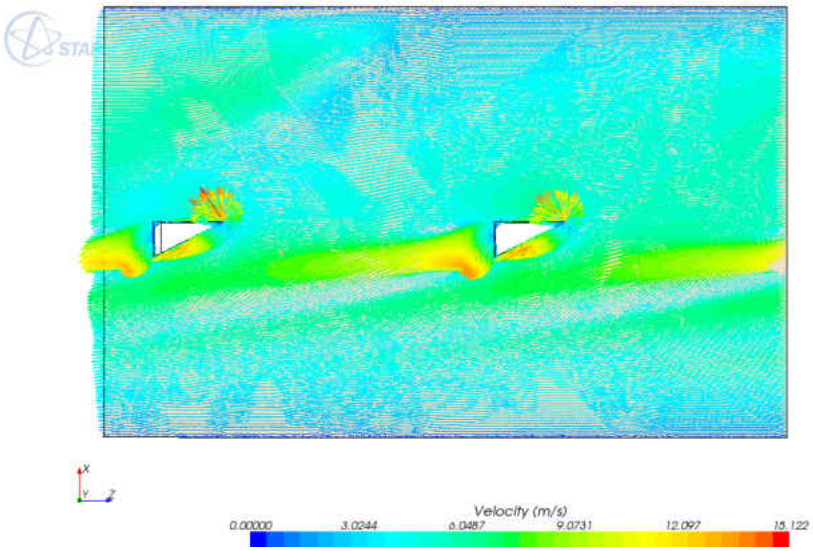

Figure 207: Bottom Surface Velocity Case B

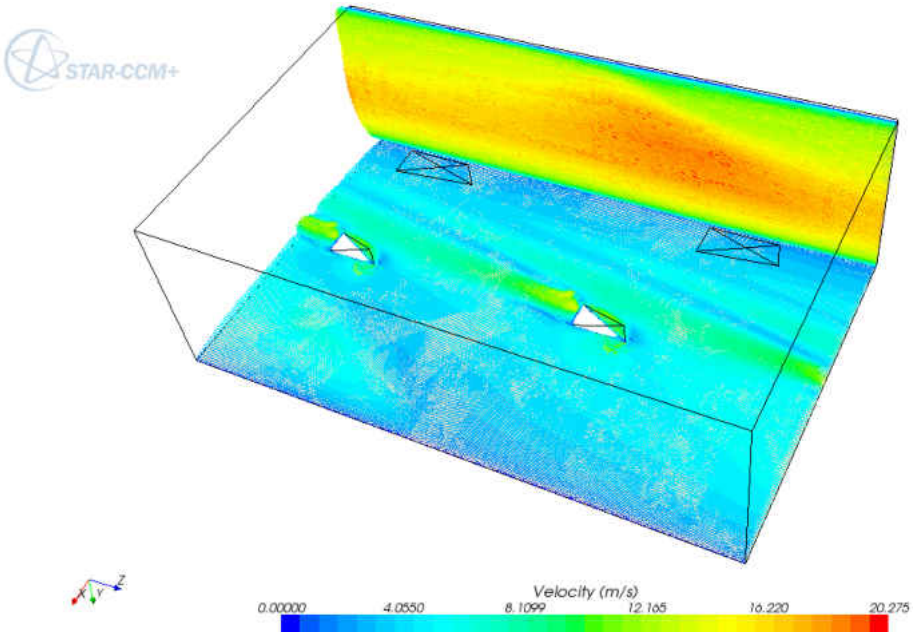

Figure 208: Side Wall Interaction Case B

Case C

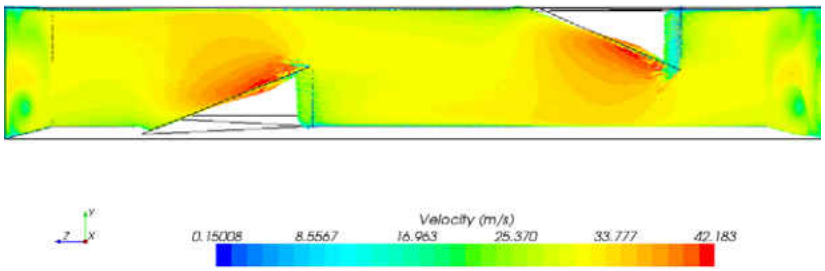

Figure 209: Centerline Velocity Case C

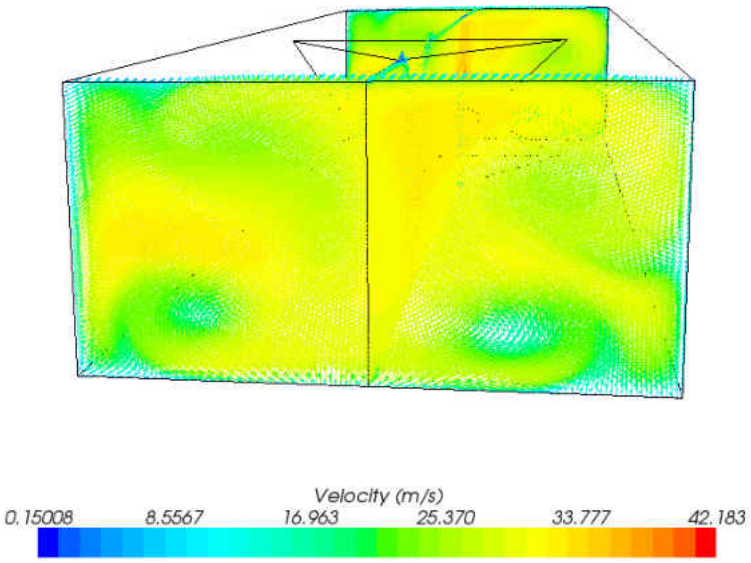

Figure 210: Case C Velocity Plane 1

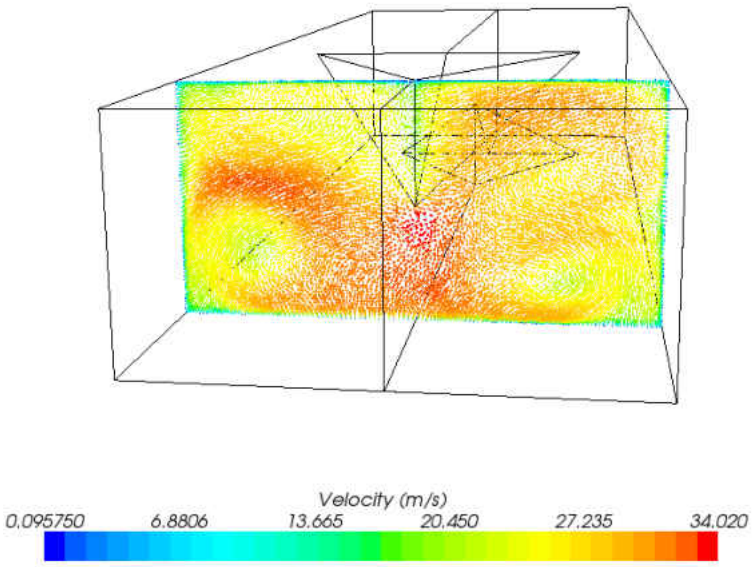

Figure 211: Case C Velocity Plane 2

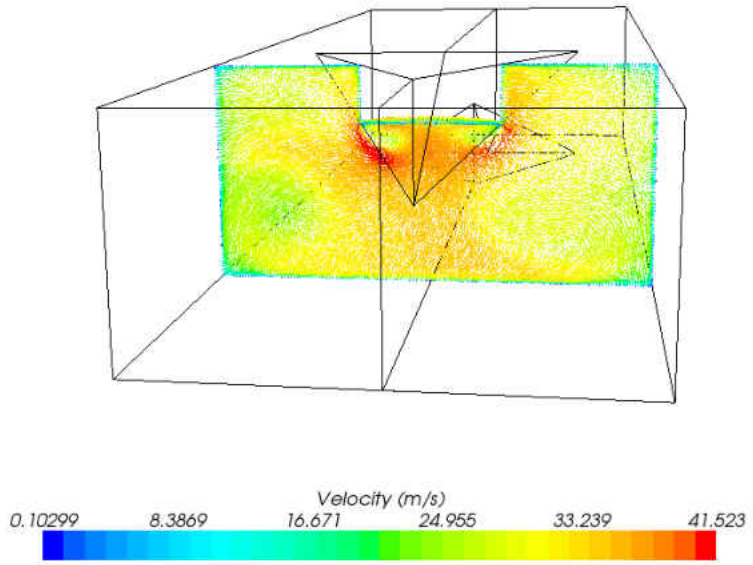

Figure 212: Case C Velocity Plane 3

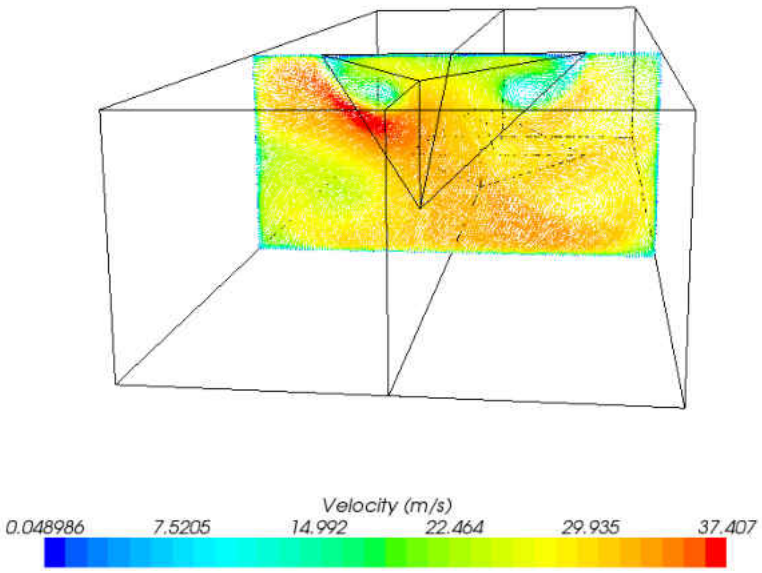

Figure 213: Case C Velocity Plane 4

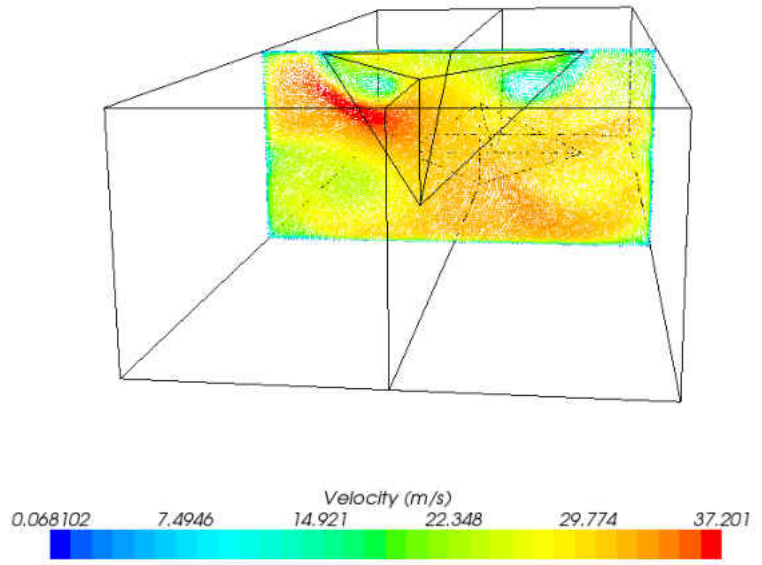

Figure 214: Case C Velocity Plane 5

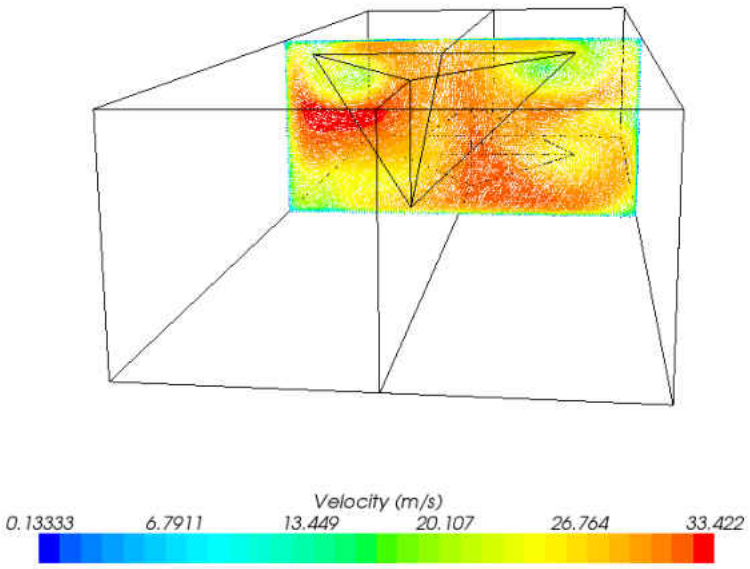

Figure 215: Case C Velocity Plane 6

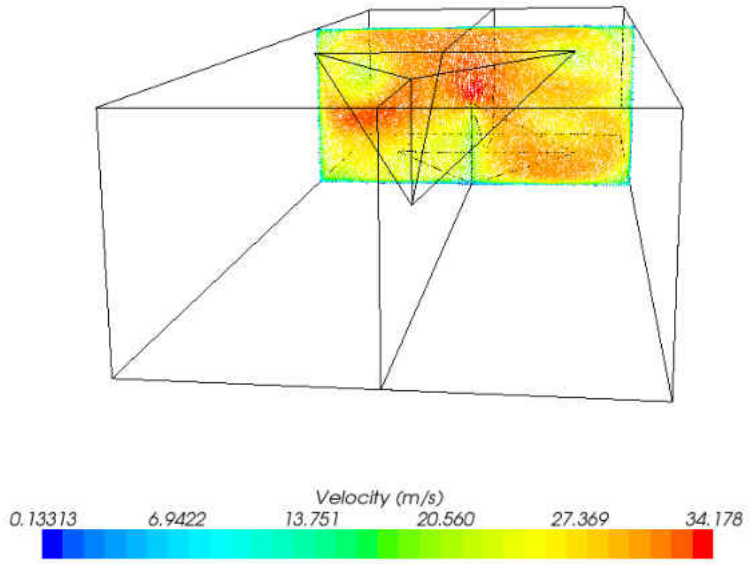

Figure 216: Case C Velocity Plane 7

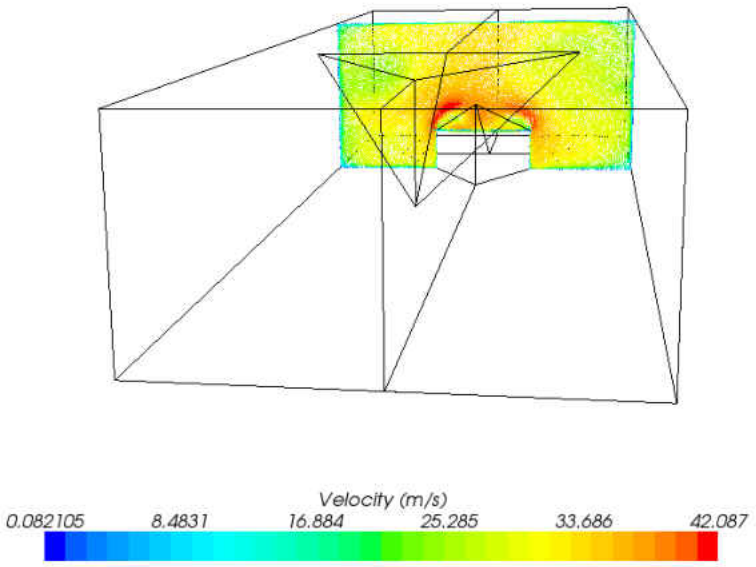

Figure 217: Case C Velocity Plane 8

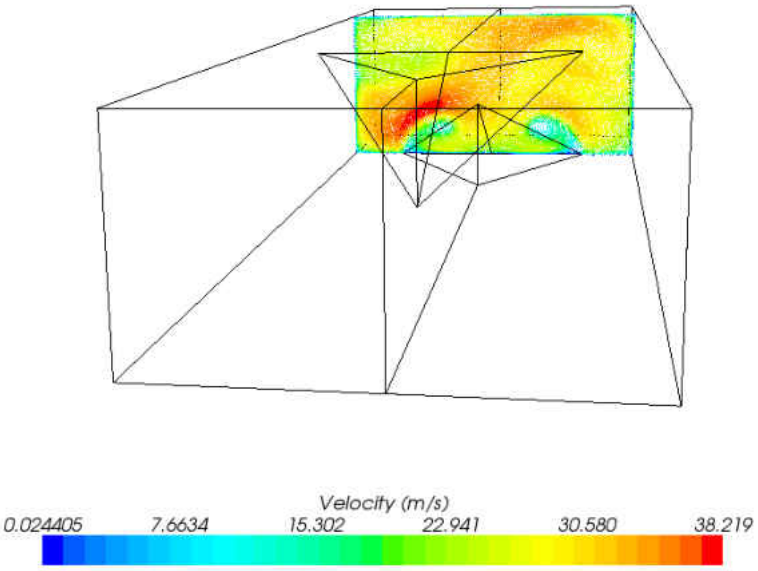

Figure 218: Case C Velocity Plane 9

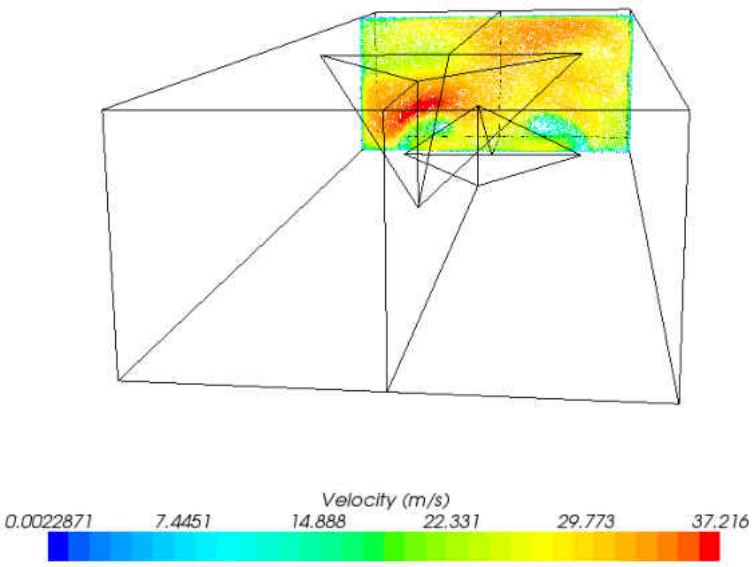

Figure 219: Case C Velocity Plane 10

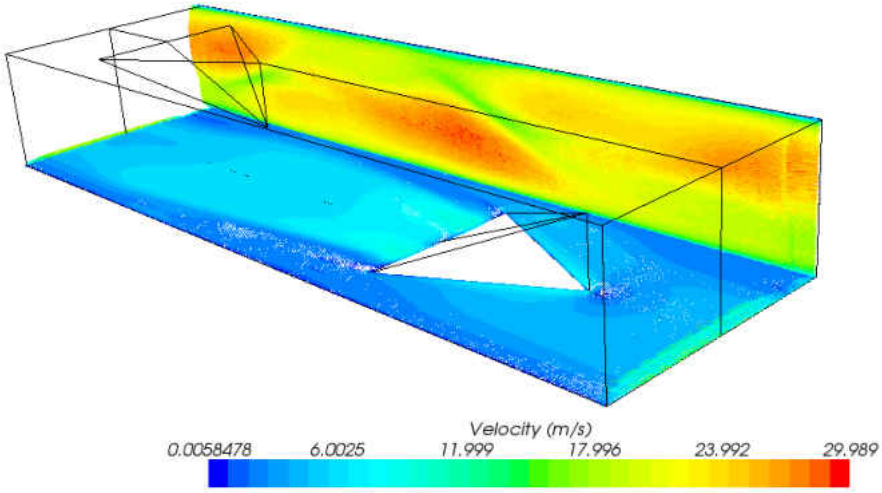

Figure 220: Side Wall Interaction Case C

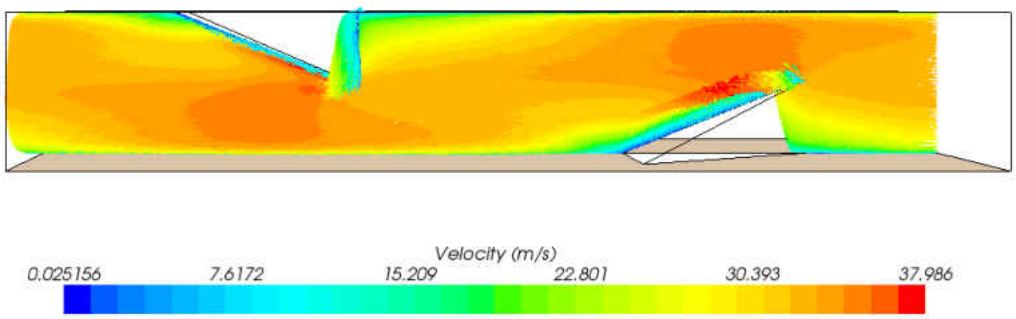

Figure 221: Centerline Velocity Case D

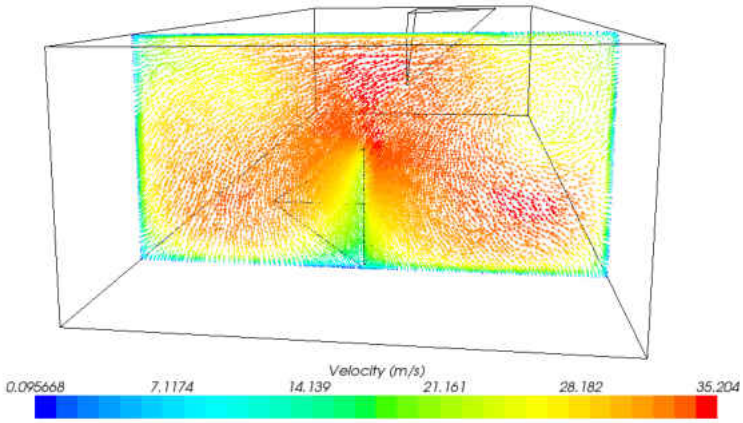

Figure 222: Case D Velocity Plane 1

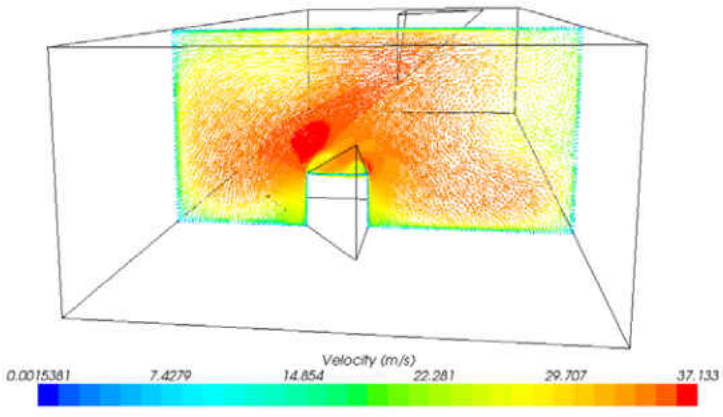

Figure 223: Case D Velocity Plane 2

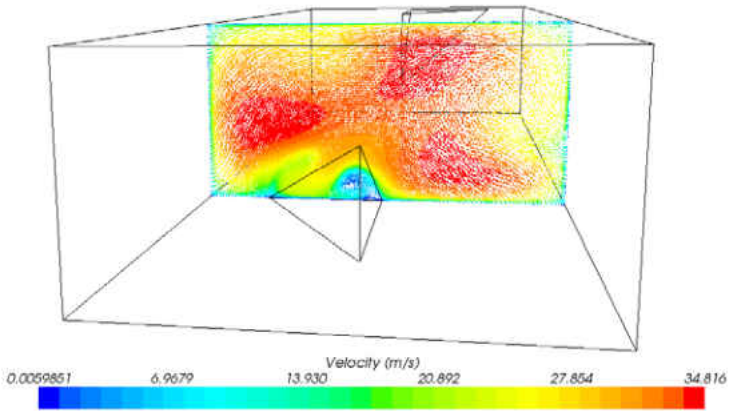

Figure 224: Case D Velocity Plane 3

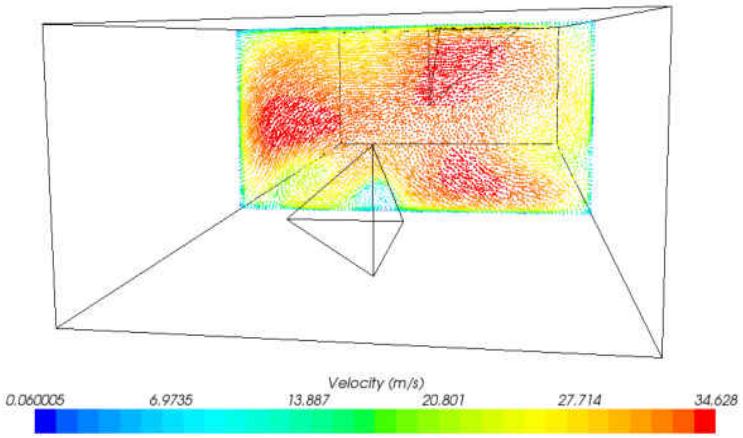

Figure 225: Case D Velocity Plane 4

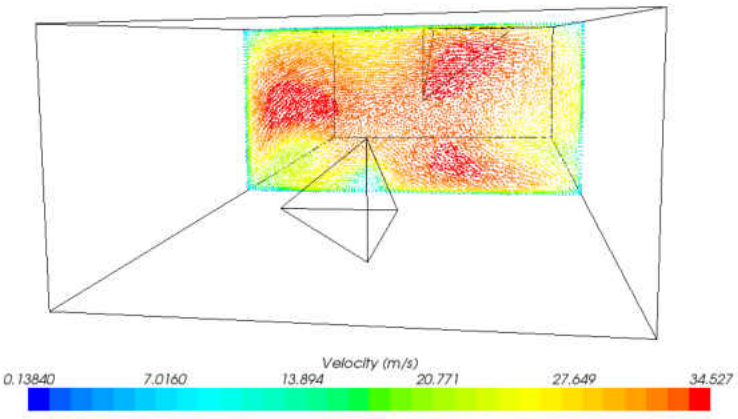

Figure 226: Case D Velocity Plane 5

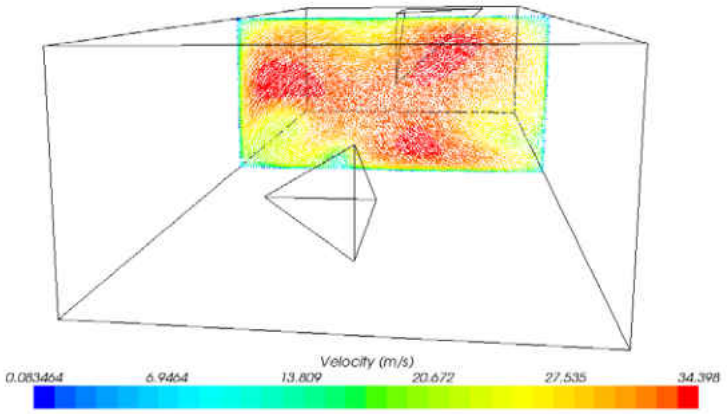

Figure 227: Case D Velocity Plane 6

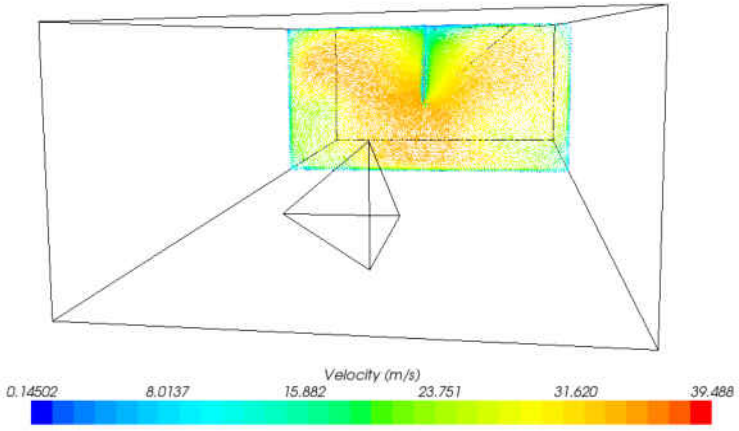

Figure 228: Case D Velocity Plane 7

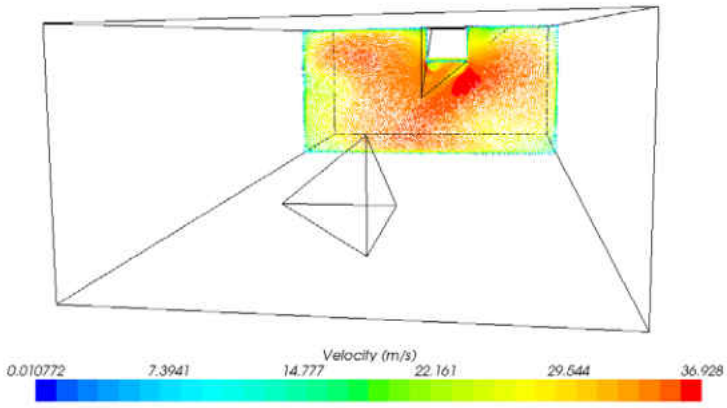

Figure 229: Case D Velocity Plane 8

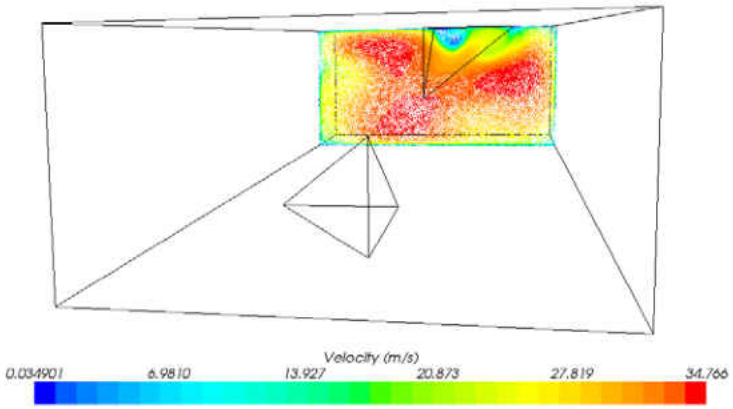

Figure 230: Case D Velocity Plane 9

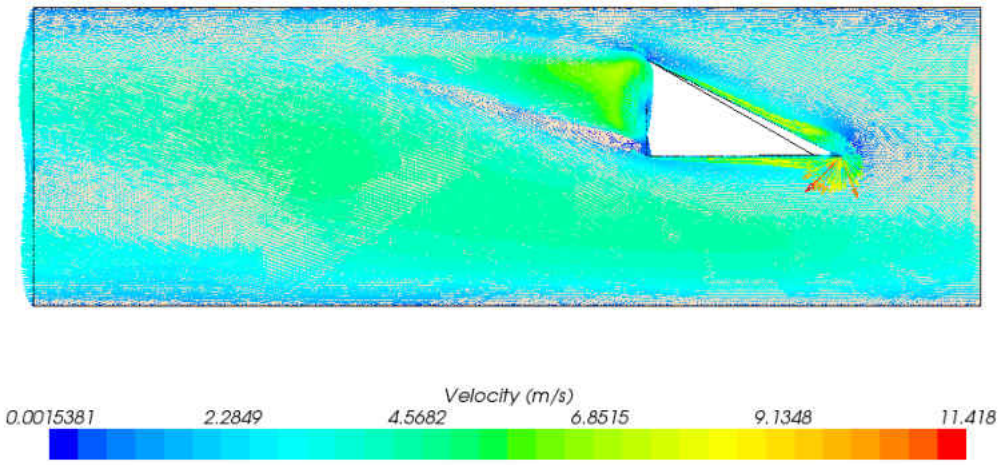

Figure 231: Bottom Wall Velocity Case D

Case E

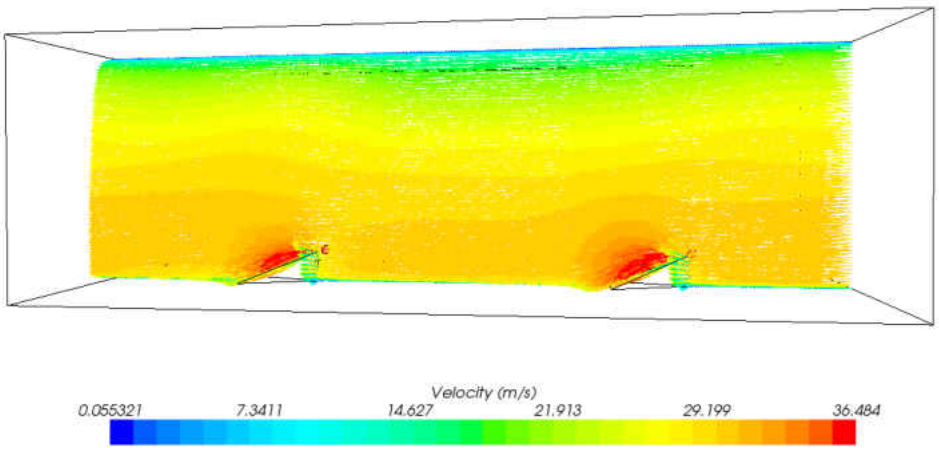

Figure 232: Centerline Velocity Case E

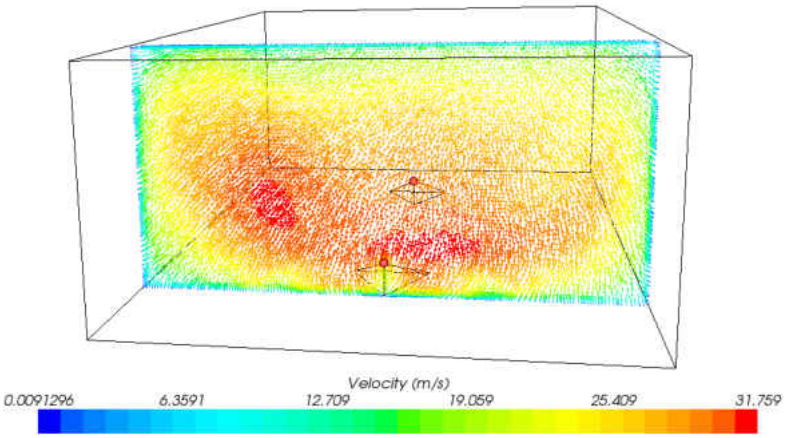

Figure 233: Case E Velocity Plane 1

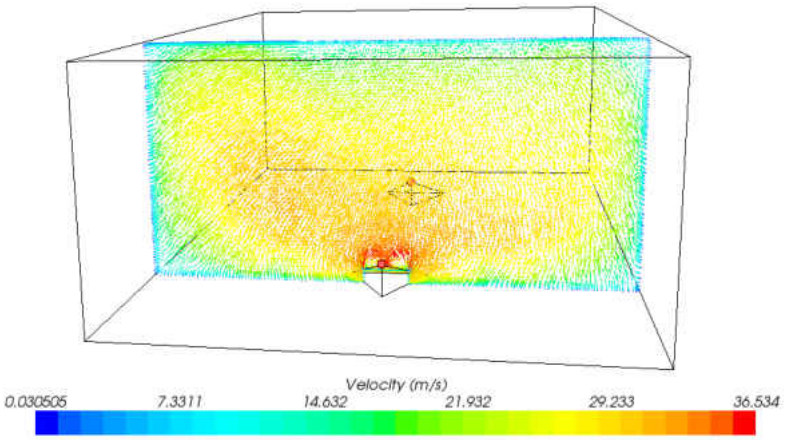

Figure 234: Case E Velocity Plane 2

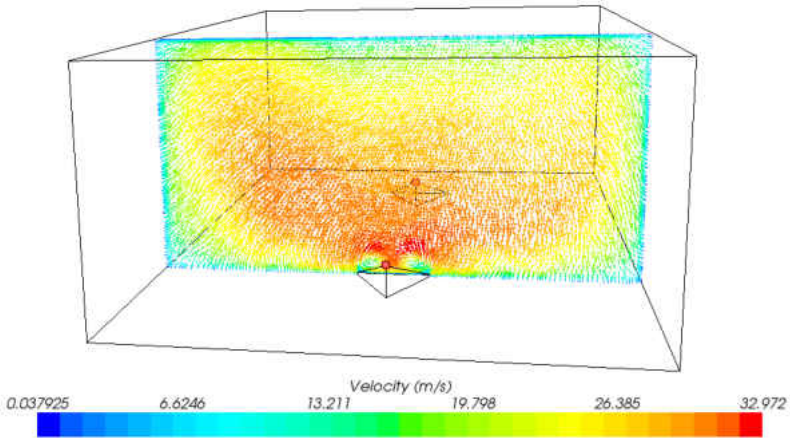

Figure 235: Case E Velocity Plane 3

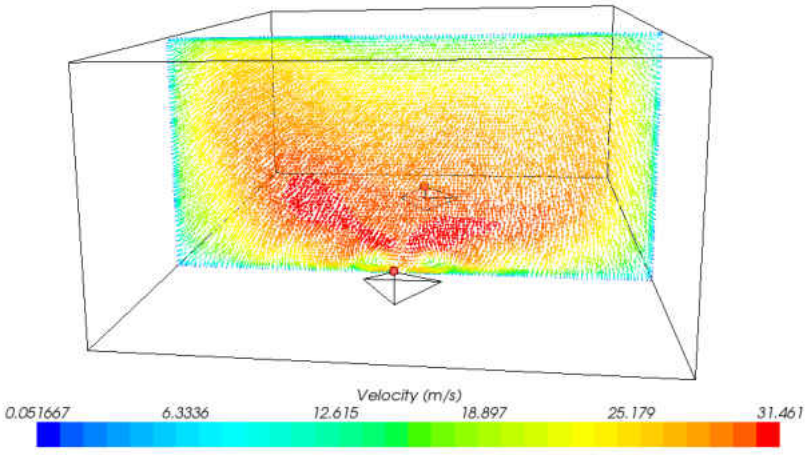

Figure 236: Case E Velocity Plane 4

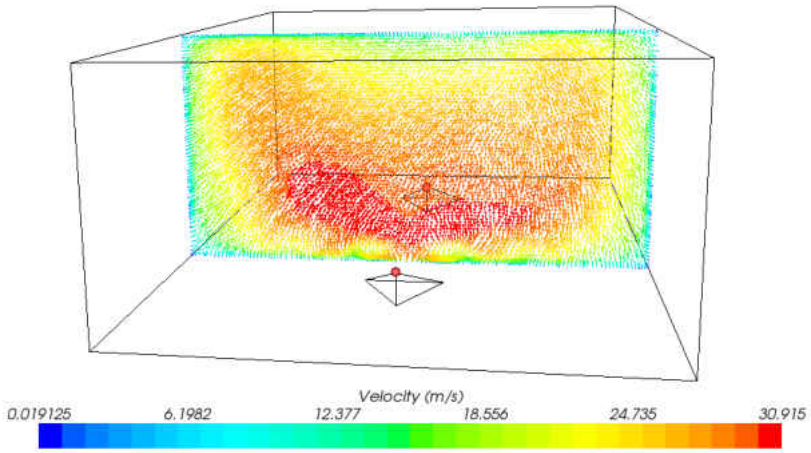

Figure 237: Case E Velocity Plane 5

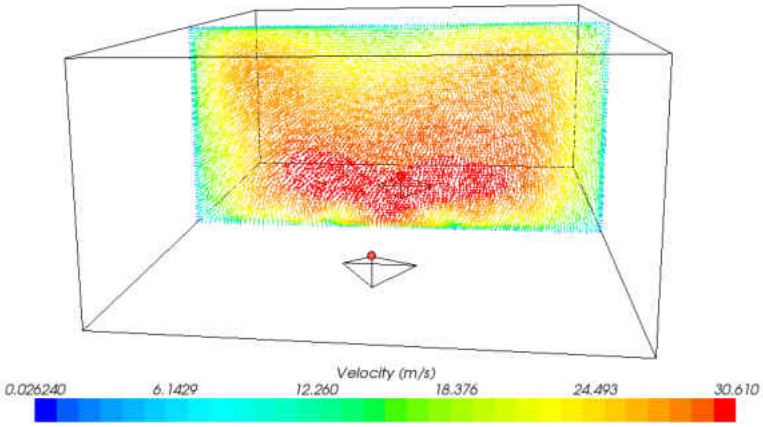

Figure 238: Case E Velocity Plane 6

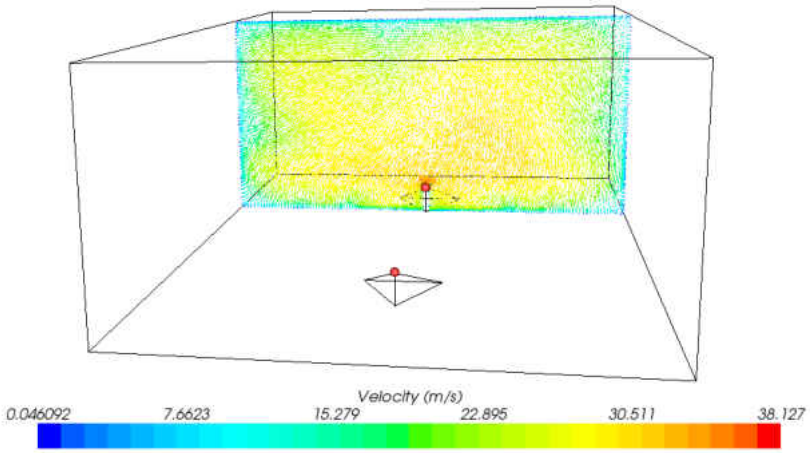

Figure 239: Case E Velocity Plane 7

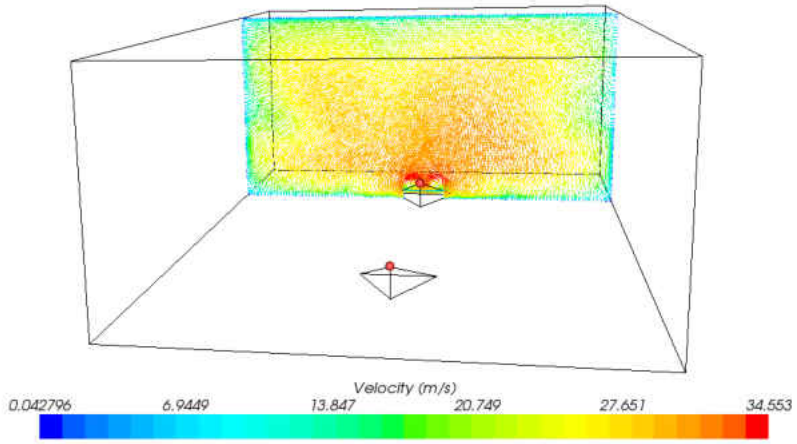

Figure 240: Case E Velocity Plane 8

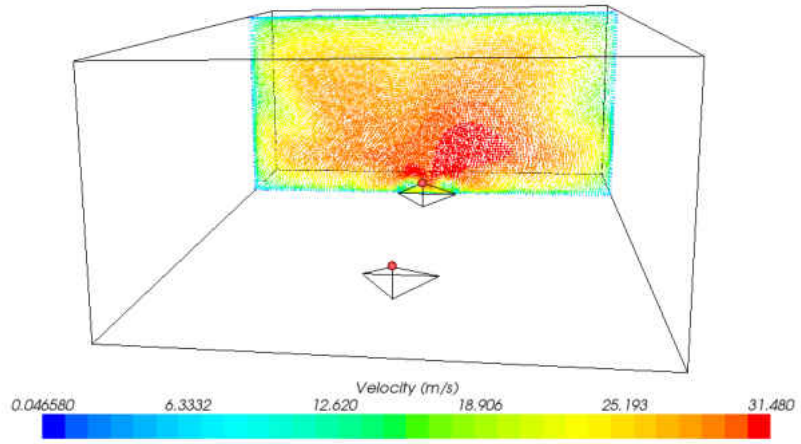

Figure 241: Case E Velocity Plane 9

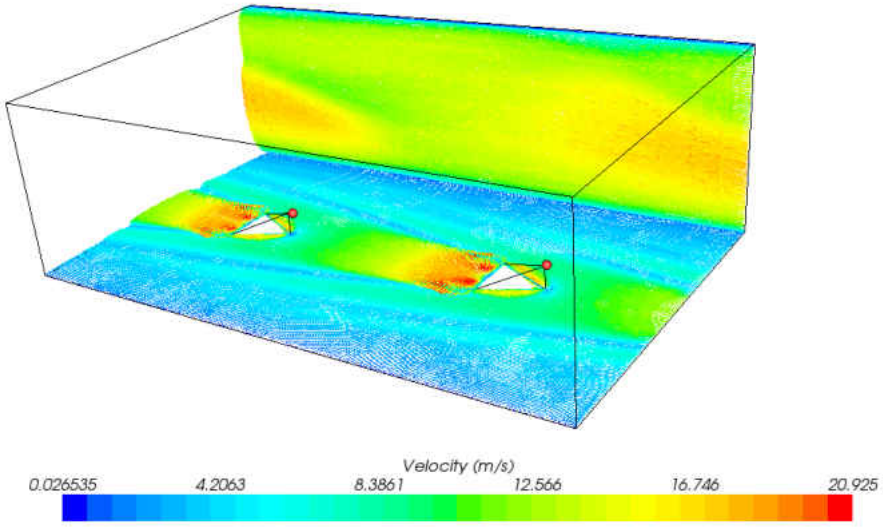

Figure 242: Side Wall Interaction Case E

Case F

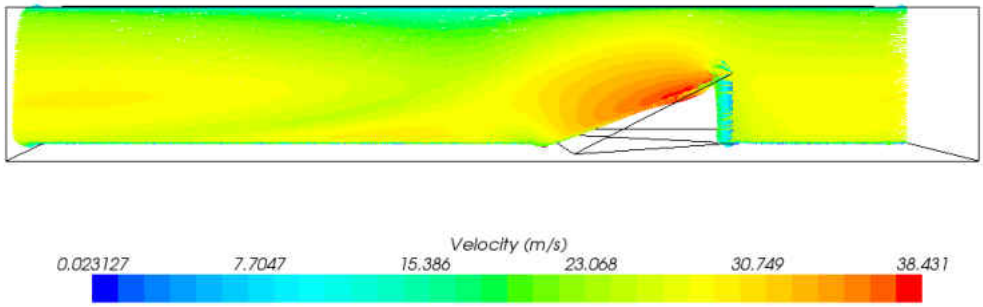

Figure 243: Centerline Velocity Case F

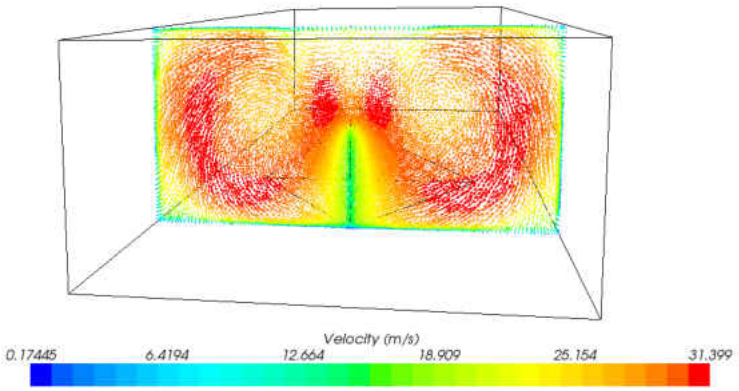

Figure 244: Case F Velocity Plane 1

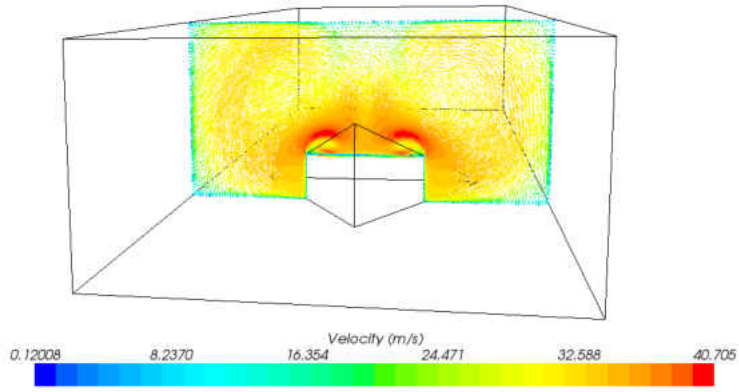

Figure 245: Case F Velocity Plane 2

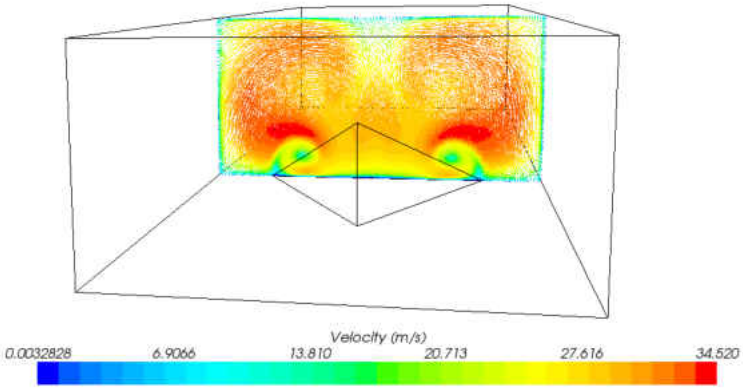

Figure 246: Case F Velocity Plane 3

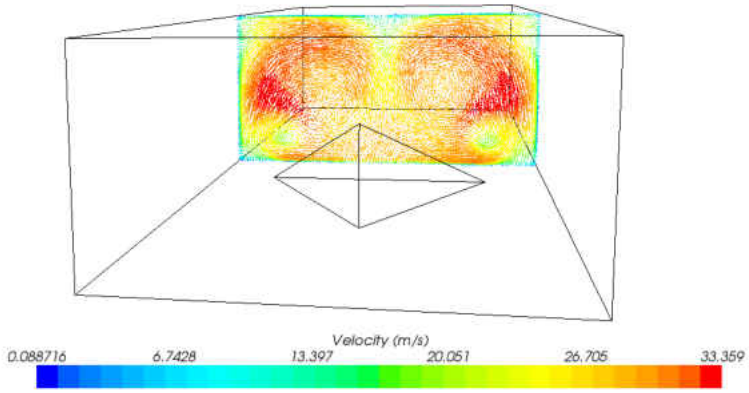

Figure 247: Case F Velocity Plane 4

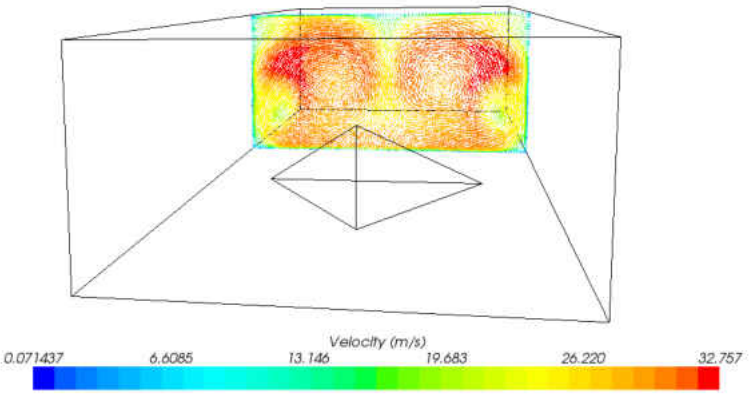

Figure 248: Case F Velocity Plane 5

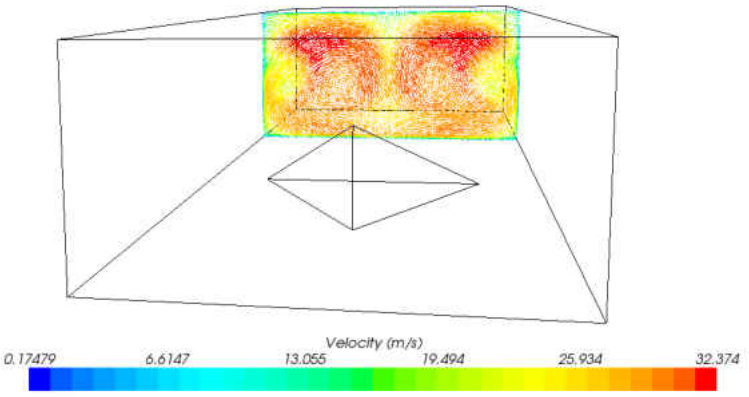

Figure 249: Case F Velocity Plane 6

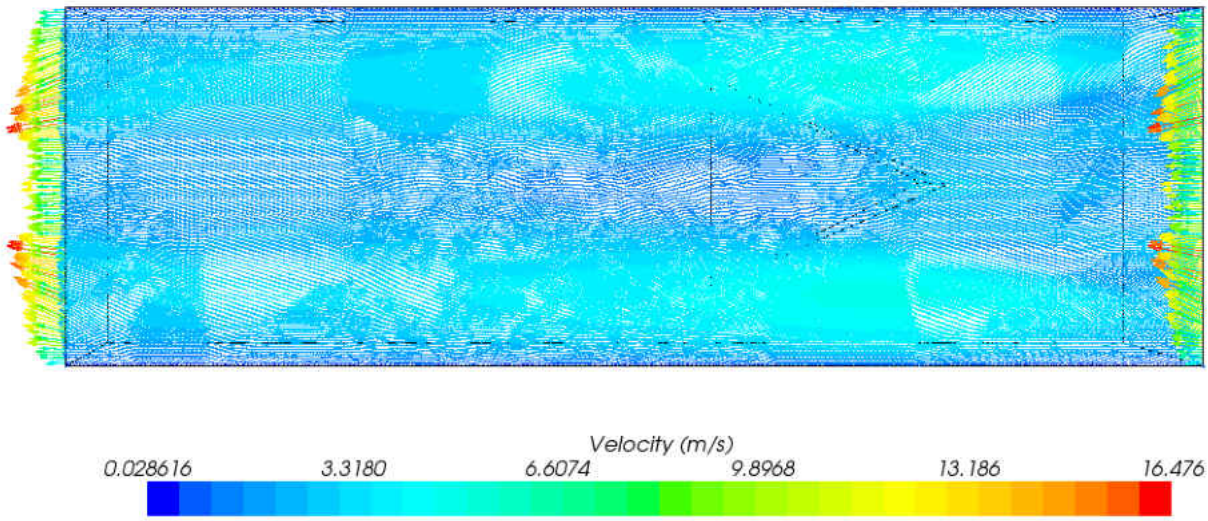

Figure 250: Top Wall Velocity Case F

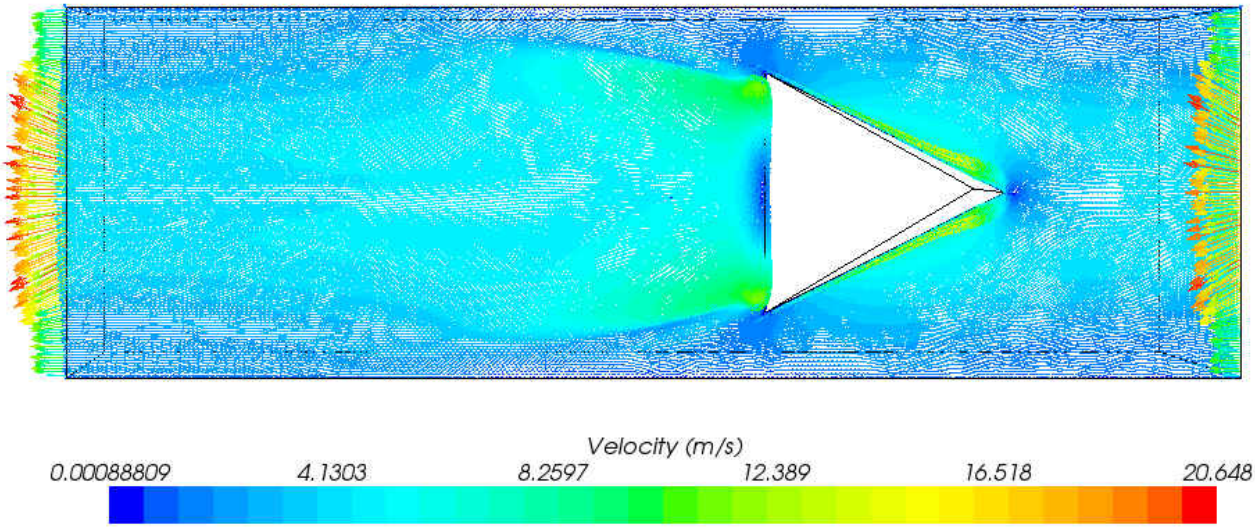

Figure 251: Bottom Wall Velocity Case F

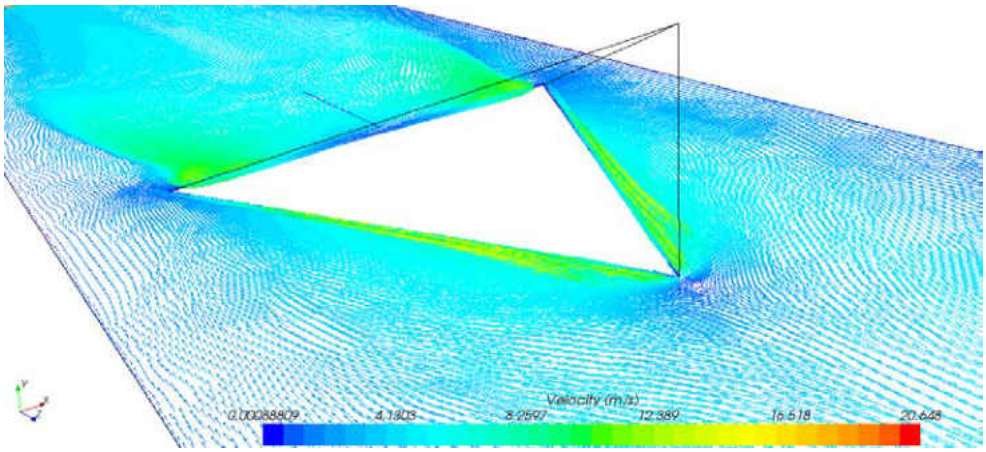

Figure 252: Bottom Wall Velocity Case F (Around Wedge)

CHAPTER 4: DISCUSSION

Friction Factor

The results for the friction factors determined in the acrylic channel for all seven cases (when including the baseline), have been shown in the figures as experimental friction factor (f) versus the Blasius correlation (f_o) in Chapter 3 - Friction Factor. The values for each case are shown in the tables below the figures. The figures show the nominal Reynolds numbers, where the actual Reynolds numbers tested may be located in each case table.

The first case friction factors, the validation baseline case, show a similar trend in relation to increasing Reynolds number to the Blasius correlation. The values, however, are approximately 10% lower, with the largest difference at the 20,000 Reynolds number at 13.5% less than Blasius, seen in Table 9. The offset present results from the uncertainty of the experiment including Reynolds number, bias in the Scanivalve, and uncertainty in the flow measurement devices. Results remain within the uncertainty of the experiment as described in Chapter 2 – Uncertainty.

Results for experimental friction factors and Blasius friction factors for Case A are shown in Figure 43. The values for the actual Reynolds number tested and friction factor augmentation are in Table 10. The friction factor augmentation shows a decreasing trend with increasing Reynolds numbers, as expected, following the increase in pressure drop and Equation 2 above. The results for the small full wedge, 2 wall case, also show minimal increase in pressure drop over the smooth pipe Blasius correlation. This minimal increase is not surprising, as the features e/H was near a

surface roughness feature. There is a comparison though to the same feature on one wall, for Case E, where the at the 10,000 Reynolds number case, the one and two wall setups have similar pressure drop, but at the 20,000, 30,000, and 40,000 Reynolds number cases, the friction augmentations are approximately 10% less than Case A.

Results for Case B, friction factor experimental versus baseline correlation are displayed in Figure 44. The friction factor augmentation still decreases with Reynolds number, however it decreases more rapidly than the full wedge case; the small full wedge case stayed near 20% increase in friction over the smooth wall channel where the half wedge case drops from 10% increase over the smooth wall to 0%. The values for the friction augmentations for Case B are in Table 11.

Friction factor augmentation results as determined for Case C are shown in Table 12 and Figure 44. The decrease in friction factor shows a large drop in friction augmentation between the 10,000 and 20,000 Reynolds number and, similarly to Case A, there is a more steady trend in friction factor trend from 20,000 to 40,000 Reynolds numbers. Friction augmentation for Case C in comparison to the smaller full wedge Case A, is ~3.5 times higher at all four Reynolds numbers. The large increase in friction factor augmentation is caused by the increased blockage in the channel, contributing to a much higher pressure drop over the length of the channel.

Friction factor augmentations for Case D are more than double the friction factor augmentations shown for Case B, the smaller half wedge case on 2-walls but almost half the friction augmentation of the larger full wedge Case C. This half wedge feature does have the same channel height blockage as the full wedge Case C, however, as a half shape wedge, the pressure loss over the length of the channel is significantly less.

This reduction in friction augmentation for the half wedge case could offset Case D from Case C in overall thermal performance, dependent on the Nusselt number augmentations.

Friction augmentation for the one wall small symmetrical wedge Case E, results in lower values for the three higher Reynolds numbers, as discussed above with Case A. However, at the lowest Reynolds number, 10,000, both cases resulted in similar frictional losses. Better visualization of how the flow acts at this Reynolds number may help support this conclusion.

The final case, the one wall large symmetrical wedge Case F, shows a significant reduction in frictional losses from the same feature on two walls. The lesser effect on pressure loss through the channel with the one wall case is as expected, since there are less features and less overall blockage through the channel. The comparison of this case to the large half wedge Case D shows similar frictional losses between the cases. It will be interesting then to review these two cases side by side in thermal performance, where the heat transfer effects on the surrounding smooth walls for each case may contribute to the enhancement of thermal performance of one case over the other.

Segmented Copper Blocks

The smooth-wall validation baseline case for the copper block setup Nusselt numbers are viewed in Figure 50 thru Figure 52, with overall area weighted Nusselt number augmentation values in Table 16. From the figures, the fully developed region is evident; this region is where the Nusselt numbers are in a linear trend where they overlap (for validation case) the Dittus-Boelter correlation. This fully developed area is in

the range from x/D_h~10 to x/D_h~20. For each Reynolds number on the SW case, the Nusselt number values in the fully developed overlap so that augmentations are all ~1. The match to Dittus-Boelter validates the copper block test section, unquestionably within the uncertainty of the experiment.

In reviewing data shown in Chapter 3 for Case A with the copper-clock setup, the Nusselt number values are plotted by averaging the featured walls (top and bottom) together and the side walls together. The combination allows for easier viewing of the data on the plot, however, when each wall is plotted separately, Nusselt number values for each location on the top wall lie on the values for the bottom wall (within uncertainty of the experiment), since the two walls for this case are both featured. This match in Nusselt number values at the locations between the top and bottom wall is expected; the walls contain identical features. This concept is the same for the smooth side wall Nusselt number values as well.

From these results for Case A, there is a clear distinction between developing section and fully developed section of the channel at all four Reynolds numbers. There is also a slight drop in Nusselt number visible at the end of the channel section. This drop may be due to added heat loss, since there are no surrounding copper blocks at the exit, or from exit flow effects propagating back into the copper block section.
The large offset between Nusselt numbers for the featured walls and the surrounding smooth side walls shows the added increase in heat transfer to the walls that contain the wedge features and imply the features do not contribute to as much of an increase on the surrounding smooth walls. Nusselt number augmentations for the side walls for both the 10,000 and 20,000 Reynolds number cases do show an increase in heat

transfer from the Dittus-Boelter smooth pipe correlation of 30% and 10%, respectively. In other words, the side walls benefitted from the vortices created by the wedges. The overall area weighted Nusselt numbers for each Reynolds number for Case A are shown in Table 17. Although the side walls of the 30,000 and 40,000 Reynolds number cases saw no improvement from the smooth wall correlation, the overall heat transfer augmentation showed improvements around 45%. The overall heat transfer augmentation also shows a decreasing trend with increasing Reynolds number. The reason the improvement drops with increasing flow rate, in addition to the side walls not showing improvement at the 30,000 and 40,000 Reynolds numbers discussed above, can be contributed to the increase in free-stream flow turbulence. As the flow becomes more turbulent, the flow interactions between the vortices created by the shape of the wedge, shown in Figure 9, and the turbulent free-stream flow are less significant because of the increased free-stream turbulence, diminishing the effect the wedge features have on the heat transfer augmentation.

Results for the Nusselt number augmentation of the featured and smooth side walls for all four Reynolds numbers for Case B are in Figure 57 thru Figure 60. For the 10,000 Reynolds number case, an overlap in the fully developed region for the smooth side walls and the featured walls is evident. The small half wedge 2-wall design at a 10,000 Reynolds number shows similar improvement in heat transfer for the smooth side walls as in the featured walls. This improvement is approximately 20% above the Dittus-Boelter correlation. However, for the remainder of Reynolds numbers tested, the offset between Nusselt numbers from the featured walls and side walls begins to increase. Overall heat transfer augmentations are noted in Table 18. The overall heat

transfer augmentation again decreases with increasing Reynolds number, following the same trend as Case A, the small full wedge 2-wall setup. Improvements in heat transfer range from 24% at 40,000 Reynolds number to 47% at 10,000 Reynolds number. Although the smooth side wall shows similar heat transfer to the featured wall, where Case A did not show this, the overall heat transfer improvement is significantly less than the small full wedge 2-wall case. The minimal offset between the smooth side walls and the featured bottom walls in Case B, then, is due to the features not contributing as much to heat transfer on the featured walls, rather than an improvement of heat transfer in the side walls when compared to the full wedge Case A.

The Nusselt number results for wedge design Case C, where Case A is upscaled four times, for all four Reynolds numbers are shown in Figure 61 to Figure 64. The Nusselt numbers for the featured walls are 20% to 30% higher than the smooth side walls for all four Reynolds numbers. The overall heat transfer augmentations for Case C are nearly double the augmentation seen for Case A at the 10,000 Reynolds number and 50% higher than Case A at the 40,000 Reynolds number. Actual Reynolds numbers and Nusselt number augmentation value are found in Table 19.

Results for copper block setup Case D, Nusselt numbers, are shown in Figure 65 to Figure 68for all Reynolds number tested. The offset between smooth side walls and the featured top and bottom walls is again minimal, as seen with the first set of half wedges tested for 2-walls. Also similar to the wedges in Case B, the wedges in Case D result in a smaller overall heat transfer augmentation than the full size wedges of the same size on 2-walls. Again, the half wedge shapes contribute less to the featured wall in terms of heat transfer improvement, when compared to the large full wedge 2-wall

Case C. Overall Nusselt number augmentations for the copper block Case D are in Table 20. The overall heat transfer augmentations of Case D are approximately 1.5 times higher than the Nusselt number augmentations of the ¼ sized Case B wedges.

For the first one wall case, using the small full wedges tested in Case A for 1-wall Case E, the figures for Nusselt numbers in the channel split the top and bottom wall, which before were averaged for the two feature wall cases. They were left separated for the one wall cases to view the effect of the feature on the bottom wall to the opposite smooth top wall. For this case, however, it is visible there is no effect of the small wedge features onto either the smooth side walls or the opposite non-featured top wall. The contribution to the overall Nusselt number augmentations, then are primarily from the bottom featured wall. These overall Nusselt number augmentation values range from 37% improvement above the baseline to 17% improvement above the baseline. This is approximately 30% lower than the two wall case at the lowest Reynolds number and roughly 20% lower than the two wall case at the 40,000 Reynolds number.

The last case, the large full wedge on one wall Case F shows improvements from the baseline on all four walls, including the opposite smooth top wall. The size of this feature contributed to the improvements in heat transfer on the non-featured walls as well as the bottom featured wall. These findings are supported in the results from the transient TLC results reviewed in the section below. The overall Nusselt number augmentations however did not exceed those from the 2-wall case as expected with less features and less overall channel blockage. Case F resulted in overall Nusselt number augmentations 50% lower than Case C at the 10,000 Reynolds number and 30% lower than Case C at the highest Reynolds number tested.

Comparing thermal performance for all the copper block tests, at constant pumping power, is shown in Figure 77 and Table 23. At the lowest Reynolds number, the full wedges on 2-walls outperform the half wedges for both sized cases. However, as Reynolds number increases, the thermal performances of the large half wedges exceed (~5% to 8%) the thermal performances of the large full wedges on two walls. Comparing the smaller wedge two wall cases, the symmetrical wedge (Case A) has higher thermal performance values at all Reynolds numbers when compared to Case B. Consistently, the worst performing case with respect to thermal performance at constant pumping power for the two-walled cases is the smaller half wedge, Case B.

At 20,000, 30,000 and 40,000 Reynolds numbers, cases B and E have thermal performance values that vary at a maximum of 3.5%. Since this variation is less than the uncertainty, these cases can be stated to have the same thermal performance at constant pumping power at the three higher Reynolds numbers.

Comparing the one wall cases to the two wall cases, the small full wedge on one wall had thermal performance values that were lower than Case B, making this case the worst performing case out of all cases tested. The large full wedge on one wall (Case F) however, showed similar results to the same wedge on two walls, Case C for the three higher Reynolds numbers. The lowest Reynolds number still resulted in higher performance from Case C over Case F by 20%. The one wall case could have resulted in similar performance because of the lower frictional losses. With frictional losses similar to the half wedge Case D, it was interesting to see that the half wedge shapes outperformed both the two wall and one wall full large wedges (Case C and F) at the 20,000, 30,000, and 40,000 Reynolds numbers, although only by approximately 5%.

Transient TLC

The results from the transient TLC experiments are displayed in three ways: the streamwise averaged Nusselt number augmentations for each wall, the local Nusselt number augmentations for each wall, and finally the overall Nusselt number augmentations for each case. The streamwise averaged Nusselt number augmentations are plot versus the distance x, shown per the pixel number. The baseline plots shown the entire viewing window in the streamwise averaged plots, where the remaining cases are zoomed in to the first half of the viewing window. Local plots are shown with W or H on the left axis (representing either the width or height of the channel) versus the normalized distance x/D_h.

For the baseline validation, all Nusselt number augmentations should be equal to one, within the uncertainty of the experiment. For the SW validation, the 10,000 Reynolds number streamwise averages show values just above or below one, depending on the wall. For the 20,000, 30,000, and 40,000 cases, the trends decrease along the length of the channel. This decrease could be due to improper measurement of the bulk temperature in the channel. However, the overall Nusselt number augmentation values for all four Reynolds numbers fall within 10% of the Dittus-Boelter smooth pipe solution. Reviewing local plots for the SW, ideally should all appear as one color, there are some ‘streaks’ viewed which could have occurred from the bulk temperature calculation, not allowing enough time for the test, or uneven heating at the inlet from the mesh heaters.

Case A, viewing streamwise Nusselt number augmentation values on the side wall, a decrease with increasing Reynolds number is observed; minimizing heat transfer

contribution on the side walls as the turbulence in the main flow increases. On the top and bottom streamwise average plots, peaks in augmentation values are clearly visible. These peaks occur at the location of the wedges; on the local plots, the highest areas of heat transfer are immediately following the wedge, and decreasing thereafter until the following wedge. This idea is shown by the large jump in Nusselt number augmentation on the streamwise averaged plots followed by a shallower-sloped decrease. From the local plots of the top and bottom walls, it is also evident how far out the improvements in heat transfer reaches, i.e. the increased heat transfer is minimal (if any) as the flow progresses out toward the side walls. This supports the copper results, in that there was very little to no improvement observed on the side walls for Case A. Also visible from the local data, is the decrease of Nusselt number augmentation on all walls as the Reynolds number increases. This is as expected, as the free-stream turbulence in the channel increases; the overall Nusselt number augmentation should decrease, as there is less contribution from the included features. A comparison of the overall Nusselt number augmentations obtained in the TLC tests to the results obtained in the copper block test are shown in Chapter 5.

The streamwise average results are quite different for the half wedge feature of the same size and setup for Case B. Viewing the local Nusselt number augmentation results however, the highest augmentations are shown at the base of the wedge and continue toward the side wall as seen with the full wedge. The streamwise results do not show the jump with the decreasing slope at the wedge locations as seem with the full wedge, because of the way the data is averaged. Since Case B wedge results are limited to half of the channel for each featured wall as viewed in the local results, and

results from the opposite featured wall do not progress around to the other side because of the free-stream turbulence, the half of the channel wall with no heat transfer is averaged into the x-location for the streamwise averages. Therefore, the peak is less obvious then viewed in Case A. Side wall streamwise augmentations are also lower than 1, which could be contributed to the issues with running the TLC tests as described previously, and outlined in Chapter 6. The overall augmentations then, show results less than one at the 30,000 and 40,000 Reynolds number as well, with only 7% improvement in heat transfer on the 20,000 case and 34% for the 10,000 Reynolds number case.

The first of the large wedge cases, Case C, which consisted of symmetrical wedges staggered on two walls shows peaks on all three walls in the streamwise averaged plots for all four Reynolds numbers, decreasing with increasing Reynolds number. It is more easily visible on the large wedge local Nusselt number augmentation plots where the wedge is located, as well as the increases in heat transfer following the wedge. The local plot is similar to the results obtained from Henze and von Wolfersdorf, shown in Figure 9 (Henze & von Wolfersdorf, Influence of Approach Flow Conditions on Heat Transfer Behind Vortex Generators, 2011). The highest areas of heat transfer are shown at the tip of the wedge and at the base of the wedge, then spans out toward the side walls. The secondary flows created from the wedges are pushed into the side walls, where it added improvement in heat transfer also travels up the side walls from both featured walls, visible in Figure 136. Viewing again the streamwise averaged plots, at the peak locations in augmentation following the wedge features on the top and bottom walls at all four Reynolds numbers show points that do not lie in near the plot. On the bottom wall streamwise averaged plots, there are a few points of very high

Nusselt number augmentations (above 3) on the 20,000, 30,000, and 40,000 Reynolds number cases and low augmentations at the location immediately after the wedge in the 10,000 case and on the top wall at 10,000 and 20,000 Reynolds numbers the points like further below . This variation from the trend could have resulted from improper masking. When the mask created for the wedge lumped capacitance calculation covers too much, the augmentation is too high, where the mask doesn't cover the entire feature, the augmentation is too low. For the side wall streamwise average plots, higher augmentation 'peaks' are seen, corresponding to the locations where the secondary flow from the wedge features is projected toward the side wall. Further studies into the flow structures from this setup may help support these findings. Overall augmentations range from 159% over the baseline at the lowest Reynolds number to 76% over baseline at the highest Reynolds number tested.

For the large half wedge Case D, results are similar to the full wedge, in terms of trends for the streamwise average plots. The peaks again in streamwise averaged Nusselt numbers are located at the base of the wedge location and decrease until the following wedge on the same wall. The peaks from the half wedge case are less prominent, where the rise in augmentation is faster, before the 'peak' location following the base of the wedge occurs. This higher augmentation over a longer distance downstream could be a result of the continuation of the secondary flows around the channel from the opposite wall. This data is supported by the local Nusselt number augmentation data, where an increase in heat transfer on each of the featured walls is seen towards the side wall on the non-featured half of the channel (the top of the images for Figure 150 and Figure 152. The vortices from the bottom featured wall travel

into the side wall and mixing continues upward toward the top featured wall and vice-versa. The effects of course, die down with increase in Reynolds number, visible on all three walls in both the local and streamwise plots. Again, the highest areas of heat transfer are found at the tip and base of the wedges. The increased heat transfer following the wedge features does not look the same as the full wedges, in a sense that if the full wedge local data plot were cut down the mid-plane for the features walls (W=0 on the plots) that it would match that of the half-wedge local data, but this is not the case. From the local Nusselt number augmentation plots, the increased heat transfer from the half wedge shifts more toward the side wall. This angle toward the side wall could also be due to the flow from the opposite featured wall, traveling down the side and pushing the flow toward the right and from the free stream flow along the flat side of the wedge spreading into the wake region. Further studies into the flow structures are needed to support these conjectures, concluded from the local Nusselt number augmentation results. Overall augmentations range from 98% above the baseline at the 10,000 Reynolds number to only 44% at the 40,000 Reynolds number.

The first one wall feature Case E, which consisted of the small full wedge features on the bottom wall, was the worst performing case for the copper-block setup. This is consistent with the results seen from the TLC tests. On the top and side walls, little improvement is seen with both the streamwise average and local Nusselt number augmentation plots for the 10,000 Reynolds number case. Where no improvement is seen from the streamwise averaged plots for the remainder of the top wall and side wall cases. The peaks on the bottom wall for Case E match locations and peaks from the bottom wall on Case A for the streamwise averaged Nusselt number plots. Reviewing

the local data plots, Nusselt number augmentations follow the trends shown in the streamwise plots, and in the copper data. The top wall lowest Reynolds number case shows 20% to 5% improvement, and local augmentations decrease with increasing Reynolds number. The side wall also shows small improvement at the 10,000 Reynolds number case, approximately 5% to 10%, also decreasing locally with increasing Reynolds number. The bottom wall local Nusselt number augmentation data for the one wall case agrees with the bottom wall local data from the two wall case. Overall augmentations for the one wall case range from 33% at the 10,000 Reynolds number to 4% at the 40,000 Reynolds number.

The final one wall Case F is the first large full wedge Case C with features from the top wall removed. Viewing the side wall streamwise averaged plots, the Nusselt numbers show enhancement above the baseline for all four Reynolds numbers. For the top wall streamwise averaged plots, the first three Reynolds numbers show improvements from the baseline, with no improvement seen at the 40,000 Reynolds number case. As with the first one wall case, results on the bottom wall for the streamwise averaged plots concur with the results on the bottom wall for the two wall case. When reviewing the local data, again the bottom wall local Nusselt number augmentation matches that shown for the two wall case. The side wall also shows improvement from where the secondary flows from the wedges on the bottom wall are directed toward the side walls. Viewing the top wall local data, the contribution from the features to the opposite non-featured top wall is observed. Secondary flows caused by the wedge features on the bottom wall impede on the side walls and are pushed upward toward the top wall, as reviewed for the two wall Case C, with better visualization on the

top wall of these effects from the opposite featured wall. The overall Nusselt number augmentations from the TLC for Case F show, at the 10,000 Reynolds number case, a 103% improvement in heat transfer over the baseline to 27% improvement over the baseline for the highest Reynolds number case tested.

Thermal performances from the transient TLC experiments for all six cases are shown in Figure 183 and Table 30. The results for the overall thermal performances in comparison to the copper block results are varied. The worst performing case, in terms of the transient TLC result is Case B, which was only the second worst performing case from the copper block results. Cases A, D, and F are the three highest performing cases for both the copper block and transient TLC thermal performance results, with Case C performing similar with the TLC results. Trends within each case, in terms of thermal performance, are similar to individual case trends for the copper block results. The variation in thermal performance results (more specifically the Nusselt number augmentation results, since the friction results for the thermal performance calculations were constant for both copper and TLC) is observed in the offset of the Nusselt number augmentation results for each case, where the TLC results are consistently lower than the copper block. These discrepancies are further reviewed in Chapter 5.

CFD

Numerical testing was completed using STAR-CCM+ to further support results determined from experimental heat transfer tests with flow visualization. A comparison to the experimental results is in Chapter 5. The results for the numerical testing in Chapter 3 show multiple viewing planes for the velocity vectors. The velocity vectors depict secondary flows where circulation is seen on the planes oriented in the spanwise direction. The centerline planes show areas where there is recirculation after the wedge features. Side wall interaction planes are also shown to determine how or if the secondary flows caused by the wedge features on the bottom and top walls extend out to the side walls.

The first image in Chapter 3 – Case A shows the location of spanwise planes. These planes are set so that they cover one period of wedge features, including the tip of the wedges, the centerline of the wedges, the tail of the wedges, and distances between the wedges. The results are then placed in order of distance down the streamwise direction to show how the flow progresses down the length of the channel. These spanwise plane locations are repeated for all wedge cases. Spanwise results from Case A show secondary flows at the first wedge, seen in the Plane 2 image, that continue after the feature, but dissipate prior to the second wedge (Plane 6). Also visible from the spanwise images is the inability for the secondary flows to travel to the side walls. The streamwise centerline velocity for Case A also shows an area after the wedges where the flow has recirculation and reattaches to the bottom (or top) surface.

Results for Case B velocity planes are in Figure 195 to Figure 208. The first two images, showing the centerline plane in the streamwise direction show the recirculation

following the half wedge shape. The reattachment after the recirculation zone does not appear as dramatic as the full wedge case. The spanwise planes for Case B show the secondary flows dissipate before reaching the next wedge, not traveling as far as the full wedge of the same size. The last two images show the velocity along the bottom wall and the interaction of the flows from the featured wall to the side wall. The flow direction is pointed toward the side wall after the wedge feature, but does not make it across from the free-stream flow.

Case C velocity planes are shown in Figure 209 to Figure 220. From the centerline streamwise plane, the highest velocities follow immediately after the tip of the wedge features, as expected. The first spanwise plane at the inlet of the periodic section shows secondary flows from the previous wedge feature continuing toward the next wedge feature on the opposite wall. From the first and second plane images the spanwise planes also show the ability of these features' secondary flows to extend out to the smooth side walls. At plane 3, the secondary flows of the next wedge feature on the opposite wall are formed, while the rotating flows from the previous wedge are still observed on the bottom sides of the image. This case is the first feature to show the interactions on all four walls at one spanwise plane cut. The flow structures are continued in the same manner for the full period of wedges plotted. The final Case C image shows the direction of the velocity along the featured bottom surface and the interaction with the side wall. This image shows flow from the previous wedge on the same wall extending down to the next wedge and into the side walls.

Numerical results for Case D velocity planes are shown in Figure 221 to Figure 231. The streamwise centerline plane for Case D is similar to Case C, where again the

highest velocities are follow the tip of the wedge. The spanwise planes for Case D, however are very different from those of the same sized full wedge. Clockwise rotation through the channel is observed following the orientation and placement of the half wedge features. The secondary flows extend toward the side wall, but are limited to one side. The bottom wall velocity plane agrees, and shows the clockwise flow direction from the periodic condition.

Case E velocity plane images are in Figure 232 to Figure 242. The centerline streamwise velocity plane for Case E is similar to the two-wall Case A, limited to one side. The spanwise results however, show directional changes (secondary flows) developed off of the wedge features dissipating prior to the following wedge feature. It also appears from the spanwise images that the changes to the flow cause by the features also fails to extend out to the side walls or propagate upward to the non-featured top wall. The side wall interaction image agrees. Comparing the one wall to the two wall case with the same feature, Case A incorporates all four walls better than the one wall Case E.

Results for Case F velocity planes are in Figure 243 to Figure 252. The centerline streamwise velocity plane shows the maximum area of velocity following the wedge tip as well as the recirculation and reattachment zone following the tail of the wedge. At the first spanwise plane at the tip of the wedge feature, the secondary flows fully encompass the channel, as with the 2-wall case of the same feature (Case C). As with the two wall case, Case F shows the continuation of secondary flows from the previous wedge on the same wall, as new vorticies are formed from the next wedge feature. Also visible from the spanwise planes is the side wall interaction and how the

vorticies travel up the side walls to the non-featured top wall. The top wall and bottom wall velocity images agree with the spanwise plane images showing the flows directed toward the side walls off the bottom wall feature and the change in direction of the flow on the top surface. The last image shown for the one wall full wedge feature case shows the velocity directions and intensities around the feature, with the recirculation zone following the tail of the wedge visible.

CHAPTER 5: GENERAL DISCUSSION/CONCLUSIONS

Copper Block Data

A comparison of the two different sizes of the wedge cases (smaller cases A and B to larger cases C and D) supports results found. The large wedges with an e/H=0.52 means the wedges completely penetrate the boundary layer, so increase in heat transfer and resultant increase in friction are found. The smaller wedges with an e/H=0.13 are slightly larger than typical surface roughness features (surface roughness typically less than e/H=0.1), so subsequently there is less heat transfer but less friction increase as well. Despite the 2:1 channel aspect ratio, the smaller sized wedge cases, A and B, had no impact on heat transfer on the surrounding smooth side walls at the higher Reynolds numbers tested. However, some increase in heat transfer on the smooth side walls was observed at the 10,000 Reynolds number, 29% and 22% for Case A and B, respectively. The increase in heat transfer on the smooth side walls for the larger sized wedge cases, C and D, ranged from 50% to 115% higher than the smooth pipe correlation. The large jump in heat transfer improvement on the side walls of the large wedge cases compared to the smaller wedge cases, contributed to the significantly higher overall Nusselt number augmentations (nearly doubled at all four Reynolds numbers). However, quadrupling the parameters, including the blockage as e/D_h, resulted in friction factor augmentations two to four times higher than the friction factor augmentations of the smaller wedge cases. With the calculations of thermal performance, both at constant pumping power and constant pressure ratio, the increase in friction factor for cases C and D resulted in thermal performance values less than or

equal to the smaller wedge cases A and B. Further optimization of the wedge size, spacing, and shape has potential to result in configurations superior in performance to the ones in the current study.

Comparing half-wedge cases B and D to full-wedge cases A and C, the full wedge cases had higher overall Nusselt number augmentations for both sizes, approximately 30% to 50% higher for the large wedges and 20% higher for the smaller wedges. The increase in heat transfer for the full wedges was seen on both the featured walls and smooth side walls. The full wedges have a larger surface area to transfer heat to the flow and are angled to push secondary vortices to both smooth side walls from the top and bottom wall features. The half wedges, however, were arranged in an effort to generate additional secondary flows with continuously rotating flow down the length of the channel, to increase heat transfer on all surfaces with a smaller feature, for minimizing material for cost and weight as well as minimize pressure loss through the length of the channel. These positive effects of cutting the wedge in half are seen in the friction augmentation results. Cutting the wedge in half for cases B and D resulted in friction factor augmentations cut nearly in half for the larger wedge and approximately 20% to 40% less for the smaller wedge. The overall thermal performance results, comparing the half to the full shaped wedges and evaluated at constant pumping power, shows the half-wedges having a higher thermal performance than the full wedge case of the same size for the larger wedge cases, but showing lower thermal performance than the full wedge for the smaller size. Out of all six cases, the large half wedge and the small full wedge cases oriented on two walls are the best cases in terms of thermal performance at constant pumping power, at all four Reynolds numbers tested.

Comparing to the one wall cases, friction augmentations for the Case F were more than double the friction augmentation for Case E and Nusselt number augmentations for Case F were 50%-60% higher than Case E. However, in terms of thermal performance at constant pumping power, the large wedge Case F results exceed the thermal performance results for Case E at all Reynolds numbers tested. The small one wall Case E stands out from all other cases as the worst wedge case setup, in terms of thermal performance. Case F, however, stands out as one of the top three cases, in terms of thermal performance. The added frictional benefit of removing one wall of features helped to increase the thermal performance of this case, even though the heat transfer in terms of Nusselt number augmentation, comparing the same wedge on two walls in Case C, was 1.5 times lower for the one wall with comparable thermal performance at the three higher Reynolds numbers. In terms of application, Case F would succeed over Case C, since there would be less material and machining.

Copper-Block vs. Transient TLC

Results of the averaged wall Nusselt number augmentations from each experimental setup are shown per case, per wall in the following sections to compare the two techniques. The overall averaged Nusselt number augmentations are also shown for each case, where error bars are added for 10% uncertainty. The values for the overall Nusselt numbers can be found in Chapter 3: Results under each case section.

Case A

Nusselt number augmentations for the top, side, and bottom wall for Case A, the small full wedge case on two walls, are shown in Figure 253, Figure 254, and Figure 255. Copper Nusselt numbers are represented by the blue diamonds and TLC results are represented by the red squares. For all walls, the TLC results are lower at all four Reynolds numbers tested. The trends however, in reference to the increasing Reynolds number for each experimental setup are the same. The TLC results are approximately 20% lower than the copper block results for each wall and at all four Reynolds numbers. When reviewing the overall results in Figure 256, the transient TLC technique produced results 9%-16% less than the copper block technique. The error bars then, at 10% for each experiment, overlap showing the results are within the uncertainty of both the experiments. Although the bias is present in reviewing the Nusselt number values, the local plots of the data from Chapter 3 show valuable insight into approximating the flow structures caused by the features.

Results for the top and bottom wall, which have identical features, have the same Nusselt number augmentation values for each experimental setup, as expected. For the side wall, the three highest Reynolds numbers tested for each setup show approximately no heat transfer improvement, however there is a discrepancy in the 10,000 Reynolds number case, where the offset present between the experimental techniques shows some improvement with the copper block test, but no improvement with the transient TLC.

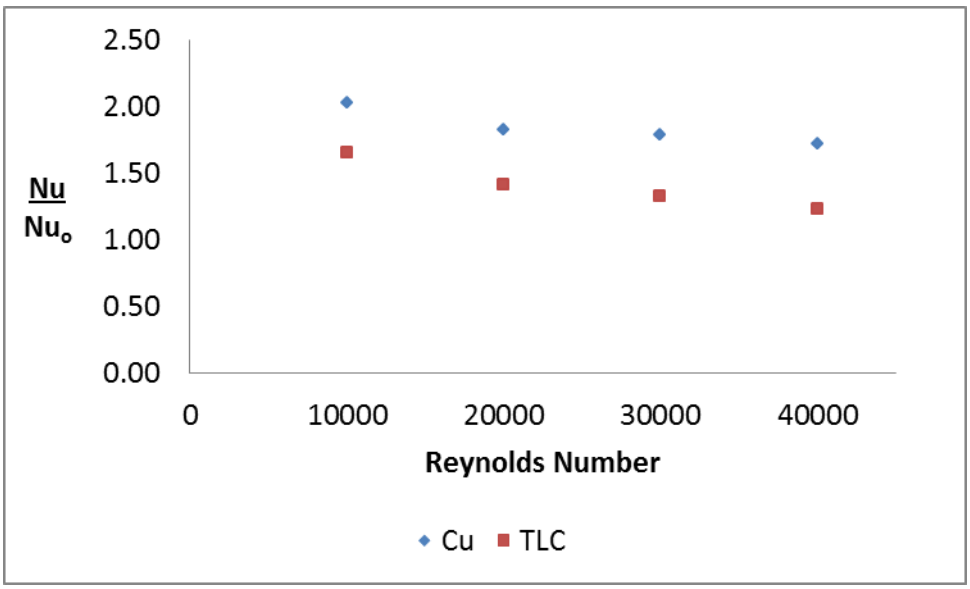

Figure 253: Nusselt Number Augmentation Copper to TLC Comparison Case A Top Wall

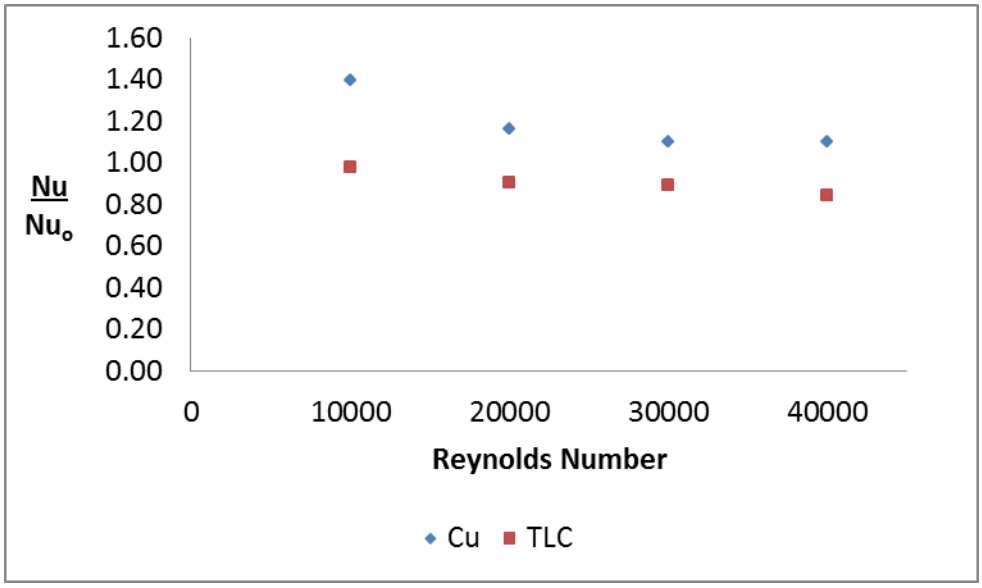

Figure 254: Nusselt Number Augmentation Copper to TLC Comparison Case A Side Wall

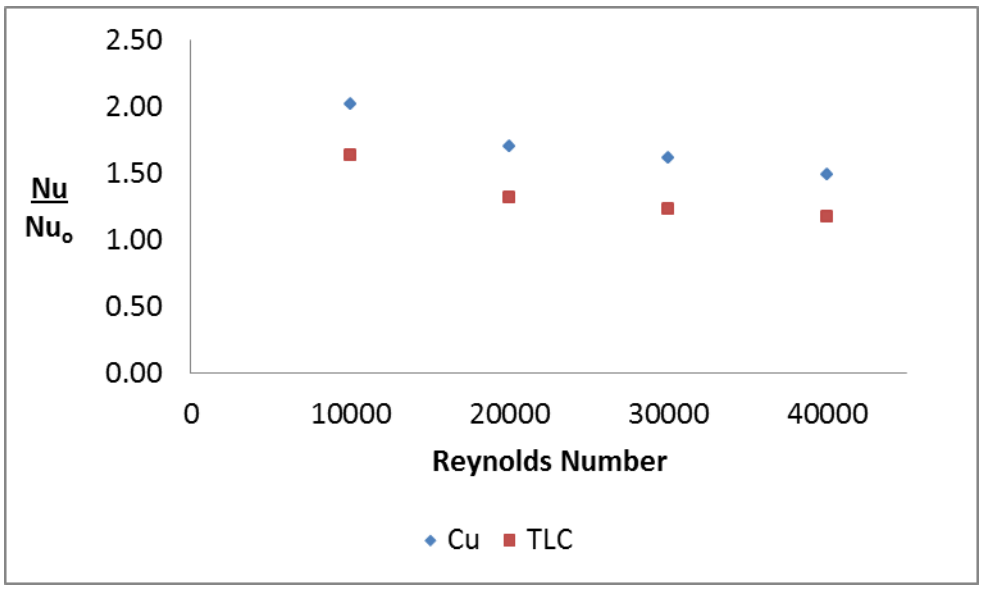

Figure 255: Nusselt Number Augmentation Copper to TLC Comparison Case A Bottom Wall

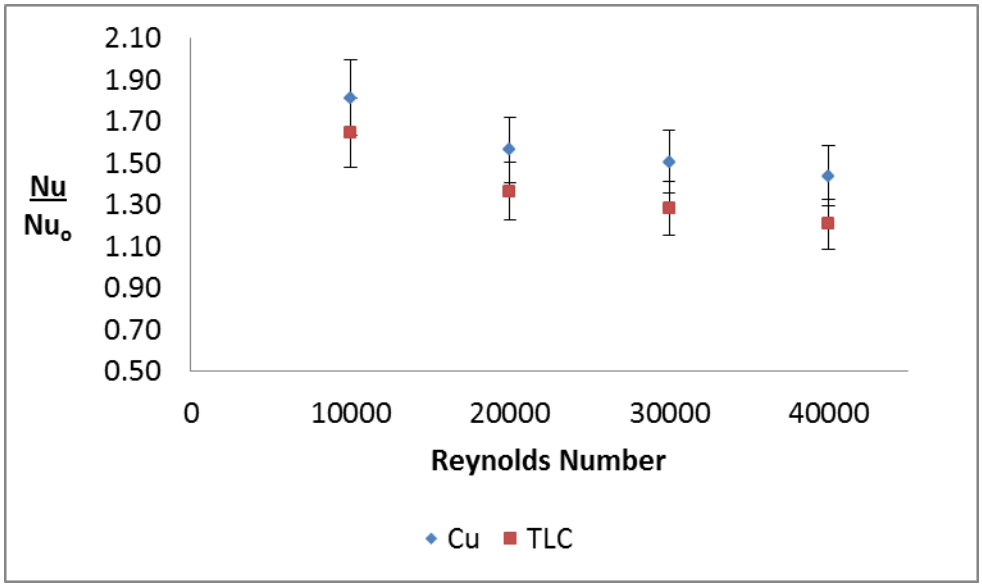

Figure 256: Nusselt Number Augmentation Copper to TLC Comparison Case A Overall

Case B

Wall averaged Nusselt number augmentation results for Case B for each experimental setup are shown in Figure 257, Figure 258, and Figure 259 for the top, side, and bottom wall respectively. As found with Case A, the transient TLC results for Nusselt number augmentations are lower than the copper block results for each wall and all four Reynolds numbers. The offset between the copper block results and the TLC results for the top, side, and bottom walls at the 40,000 Reynolds number are the furthest from the copper block data, where the 10,000 Reynolds number case shows the least offset for all three side walls. The side wall TLC Nusselt number augmentation results are consistently near 30% for all four Reynolds numbers tested. The offset for the top and bottom walls range from approximately 10% to 40%. The larger discrepancies between the copper and TLC results support the difference in thermal performance results, where for the copper Case E showed the worst thermal performance and for the TLC, Case B showed the worst thermal performance.

The overall averaged Nusselt number augmentation results, in Figure 260 also shown with 10% error bars for each experimental setup, continue the trends seen from the individual walls; as the Reynolds number increases, the offset between the copper block results and the TLC results increases. The percent difference of the TLC results to the copper block range from 9% to 32%. Although the TLC is again under-representing the heat transfer enhancement, the local plots shown in Chapter 3 still help predict direction of the flow caused by the small half wedge features. Further investigation into the flow, from CFD results support the trends found in the TLC local Nusselt number augmentation results.

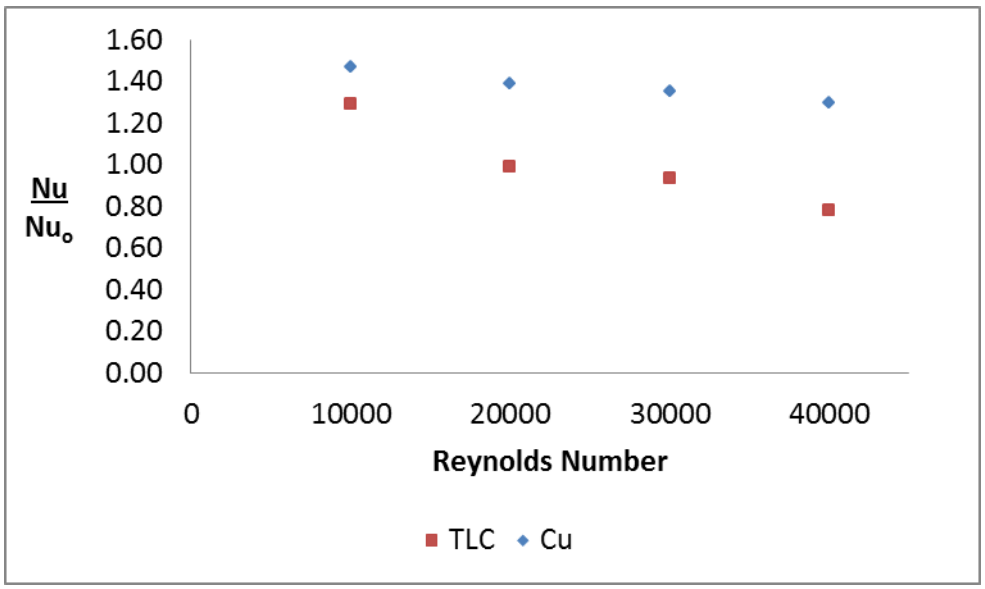

Figure 257: Nusselt Number Augmentation Copper to TLC Comparison Case B Top Wall

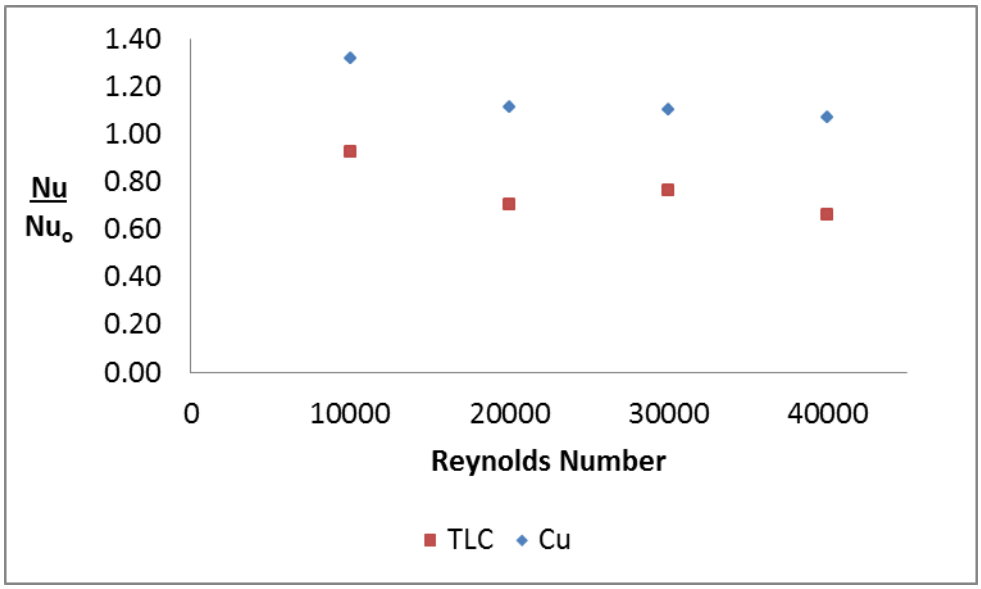

Figure 258: Nusselt Number Augmentation Copper to TLC Comparison Case B Side Wall

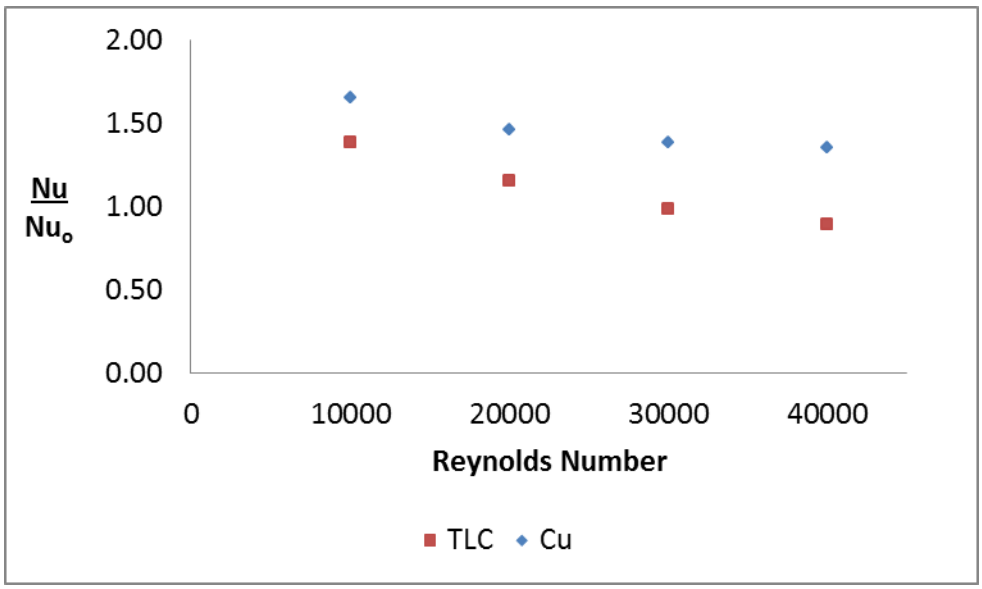

Figure 259: Nusselt Number Augmentation Copper to TLC Comparison Case B Bottom Wall

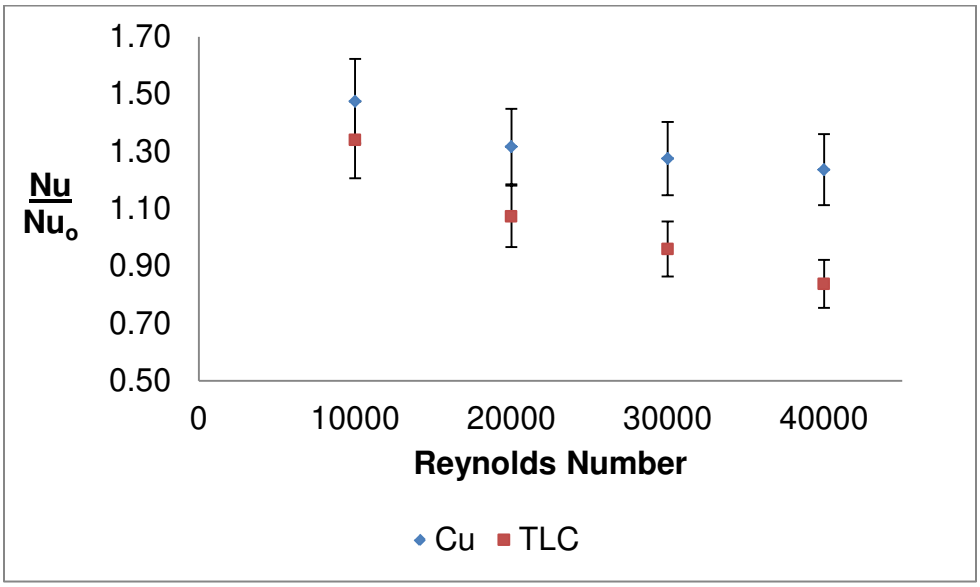

Figure 260: Nusselt Number Augmentation Copper to TLC Comparison Case B Overall

Case C

Wall Nusselt number augmentation results for comparing copper block to TLC show approximately a 30% offset for all four Reynolds numbers on the side wall and the 10,000 Reynolds number on the top wall, but only a 4% to 20% offset on the bottom wall and remaining top wall Reynolds numbers, viewed in Figure 261, Figure 262, and Figure 263. The largest difference for the bottom wall data is at the 10,000 Reynolds number case (20%), all other Reynolds numbers show a difference of less than 15% with similar drop in the offset at these Reynolds numbers for the top wall. The differences between the percent changes for the 10,000 Reynolds number case, and the reason why the bottom wall shows better (as closer to the copper results) than the top and side could be from the mask. As described above, and further outlined in Chapter 6, if the mask for the bottom wall covered too much (as in covering more than the copper feature area), the results for the Nusselt number augmentation would show higher. Furthermore, the 10,000 case would be different from the three remaining cases, because for the 10,000 case the venturi has to be changed to the 1/2”-20, which causes slight movement of the channel, and therefore has a different mask than the remaining Reynolds number cases tested.

The overall averaged Nusselt number augmentation results, shown in Figure 264, show overlap of the 10% error bars for the 10,000, 20,000, 30,000, and 40,00 Reynolds number cases. Results from the transient TLC experiment support the values determined in the copper block setup.

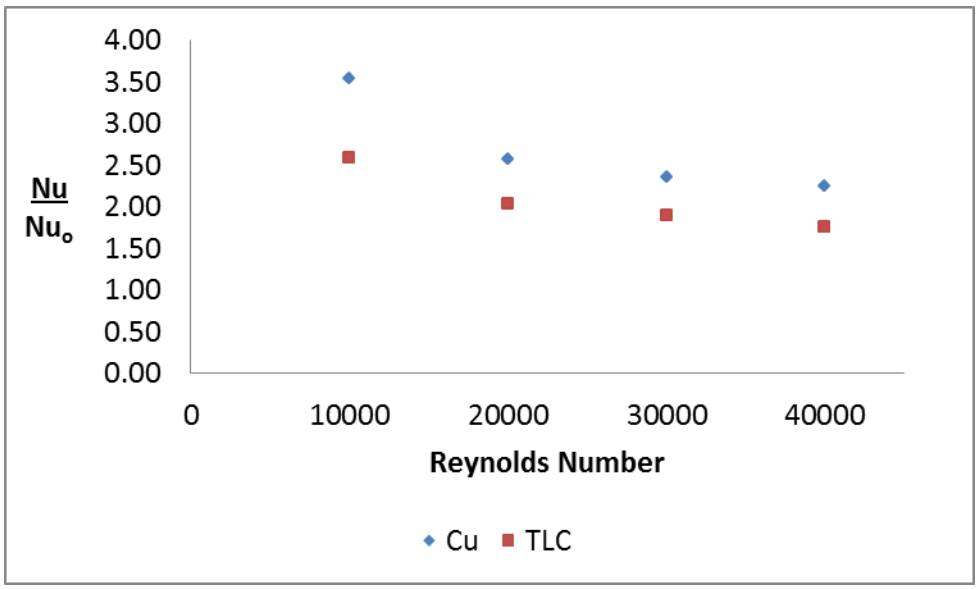

Figure 261: Nusselt Number Augmentation Copper to TLC Comparison Case C Top Wall

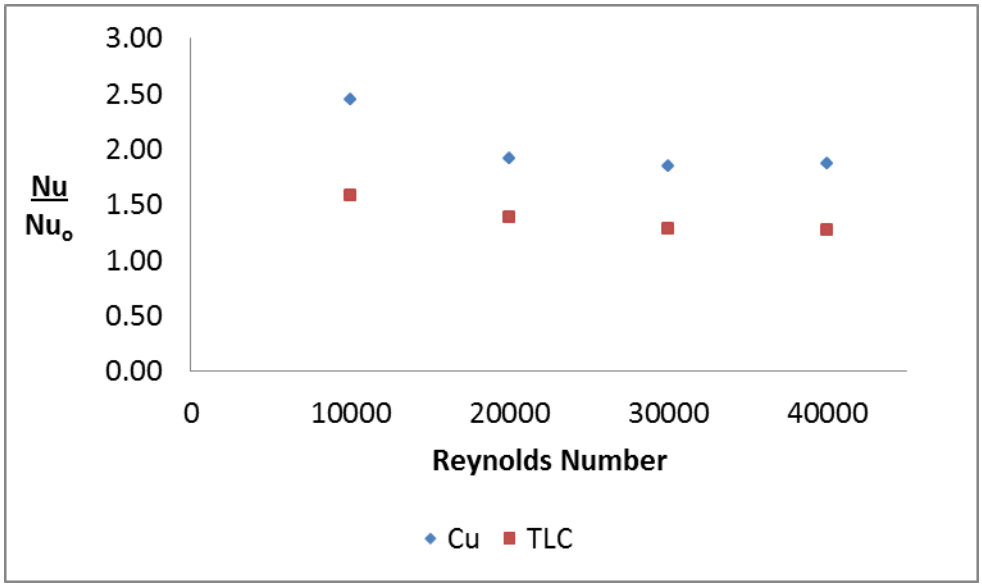

Figure 262: Nusselt Number Augmentation Copper to TLC Comparison Case C Side Wall

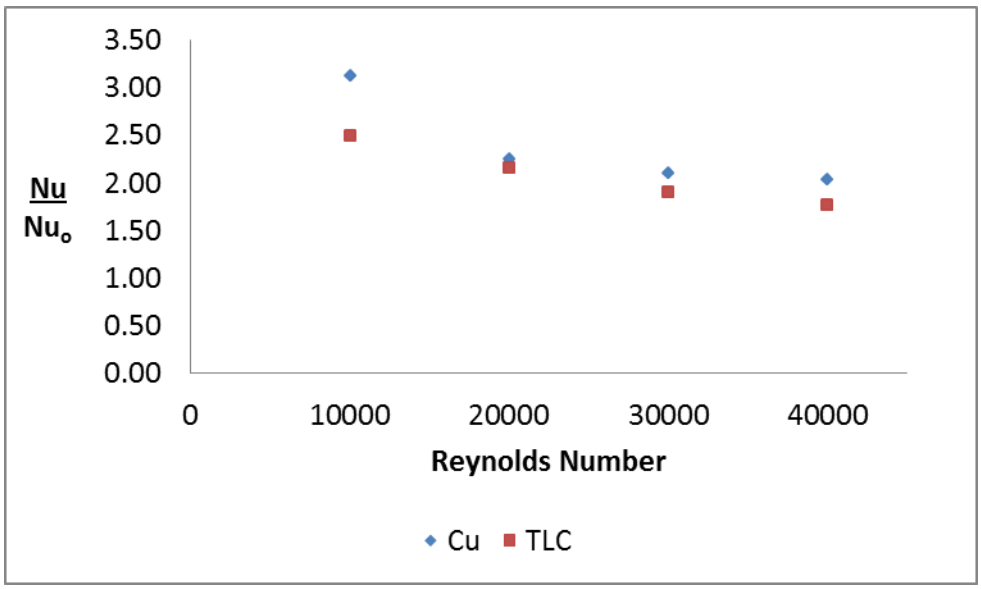

Figure 263: Nusselt Number Augmentation Copper to TLC Comparison Case C Bottom Wall

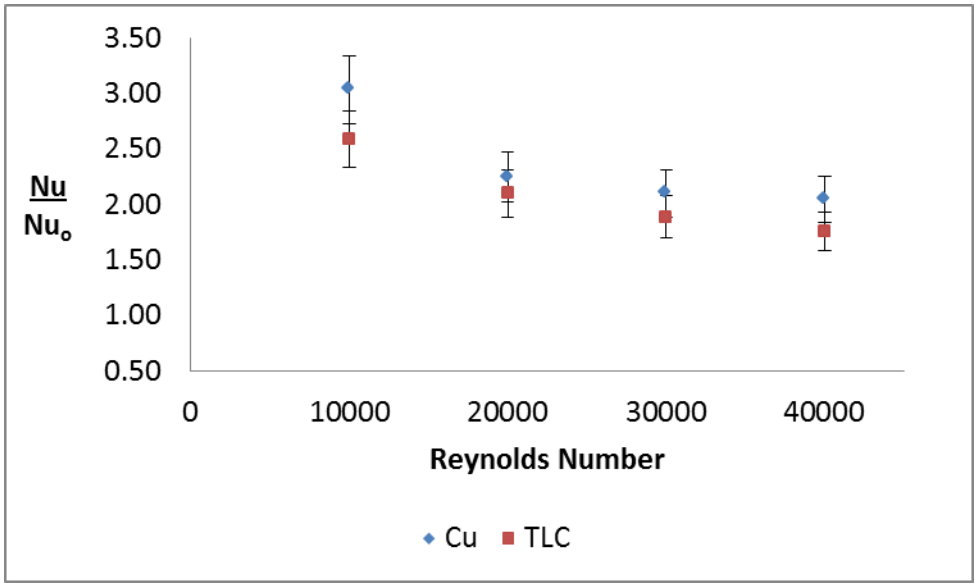

Figure 264: Nusselt Number Augmentation Copper to TLC Comparison Case C Overall

Case D

Similar to the previous case, the differences between the copper block and transient TLC results change, dependent on the wall. For the top wall, the TLC Nusselt number augmentations for all four Reynolds numbers are approximately 18%-23% lower than the copper block; for the side wall, augmentation results for the TLC are 25%-29% lower than the copper block results; for the bottom wall, TLC results are only about 10% lower than the copper block results. The differences again could be in part to the masks. If the values are significantly lower than the copper block, the mask created for the TLC processing was too small, perhaps did not cover the entire copper feature footprint; whereas for the bottom, the mask again may have covered too much, or more than just the copper feature footprint. Side wall results are near consistent for all the cases thus far, within 20% to 30% offset between results for the two experimental techniques. The trends with respect to Nusselt number augmentation as Reynolds number increases, for all three walls between the two experiments are the same and therefore the local results from the TLC help depict the flow characteristics that occurred in the copper block setup, with further studies into the flow from CFD.

The 10% error bars on the overall averaged Nusselt number augmentation plot in Figure 268 overlap at all Reynolds numbers tested, the percent difference between the experimental tests range from 12% to 16%, where trends of the overall averaged augmentation with respect to Nusselt number for all four tests are consistent.

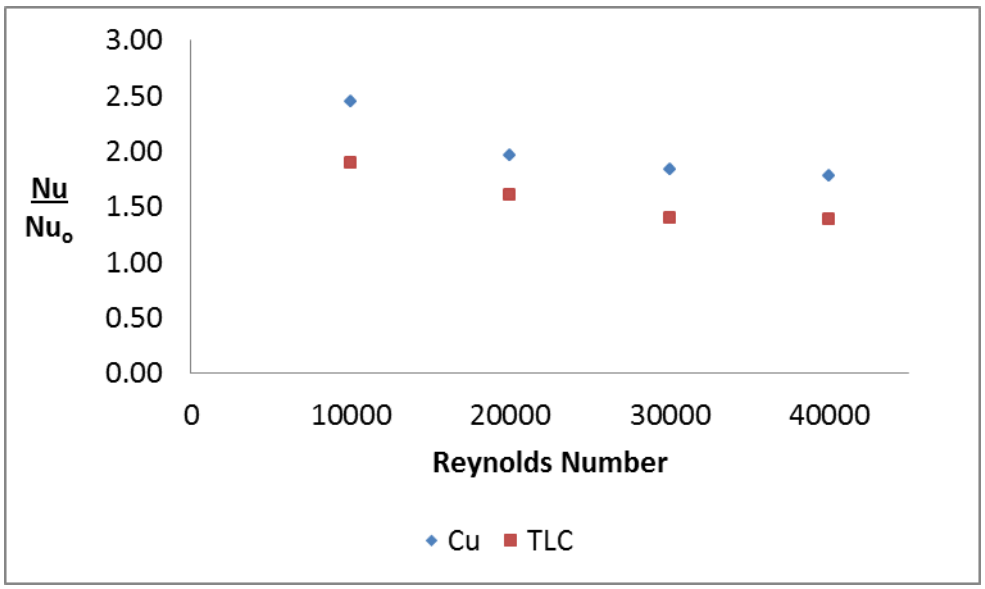

Figure 265: Nusselt Number Augmentation Copper to TLC Comparison Case D Top Wall

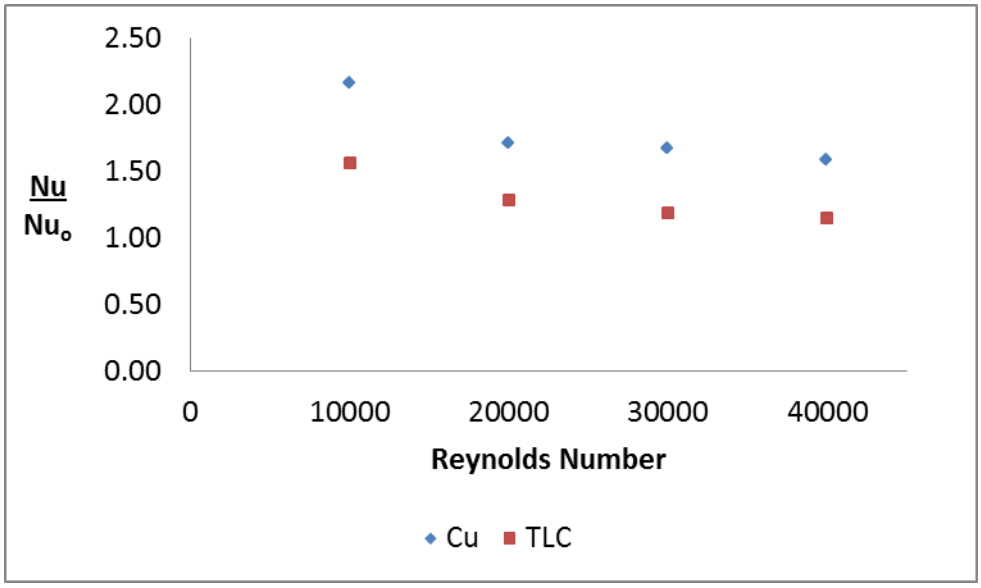

Figure 266: Nusselt Number Augmentation Copper to TLC Comparison Case D Side Wall

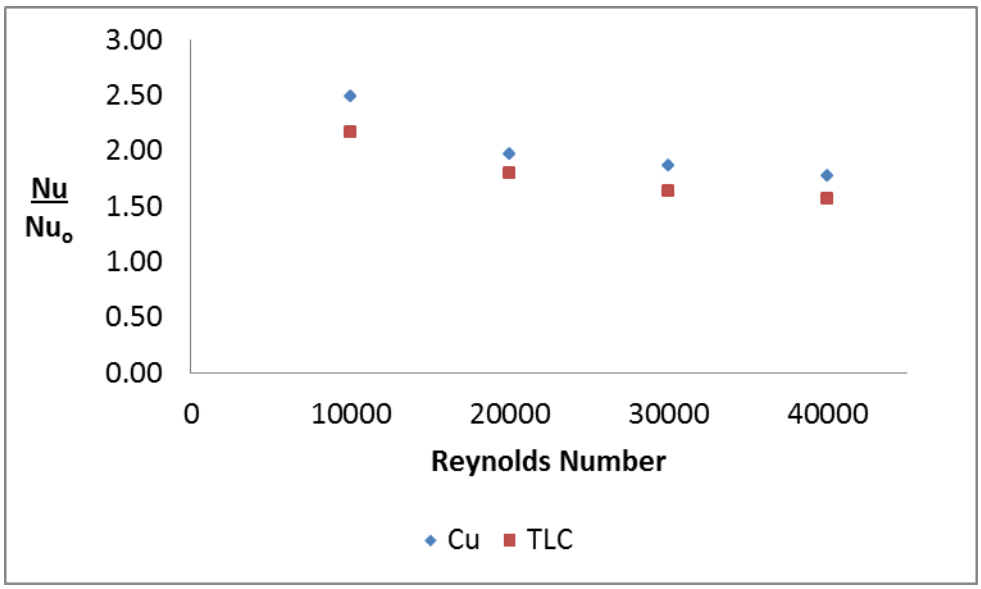

Figure 267: Nusselt Number Augmentation Copper to TLC Comparison Case D Bottom Wall

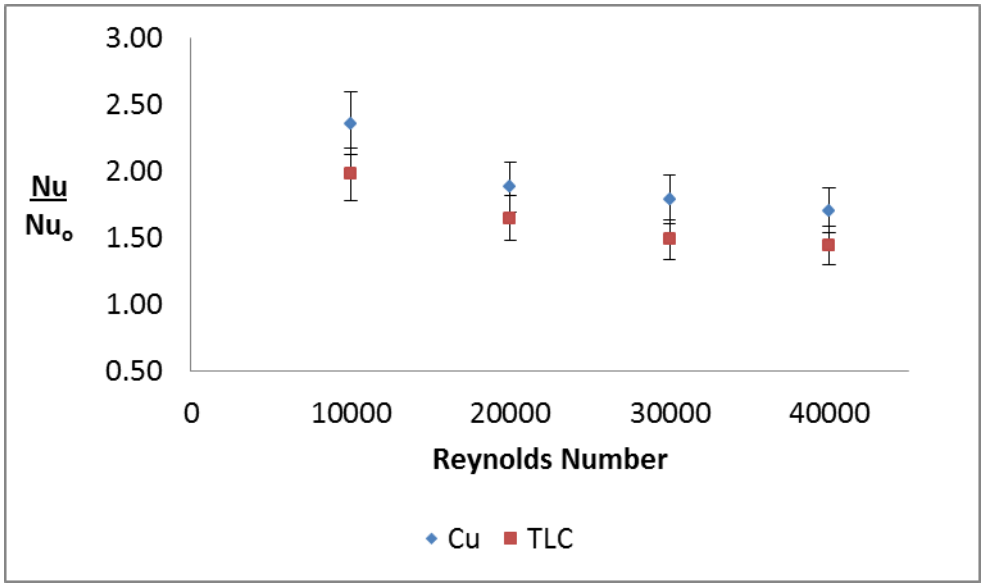

Figure 268: Nusselt Number Augmentation Copper to TLC Comparison Case D Overall

Case E

Case E, the first one wall test, shows variation in the trends for Nusselt number augmentation as a function of Reynolds number between the copper block and TLC tests. In Figure 269, Figure 270, and Figure 271 below, the 30,000 Reynolds number case for the TLC results are much closer to the copper block results than any other Reynolds number tests, for all three walls, with the TLC results from the 40,000 case as the furthest away from copper block results, with the exception of the side wall TLC result at 10,000 which is 4% less than the 40,000 Reynolds number TLC result. Differences between these Reynolds numbers could result from the timing of the test, which is visible in the local Nusselt number augmentation results of the TLC experiment by the ‘streaks’ or areas of higher augmentation that indicate the test may not have been run at either a long enough time, or the voltage was too low to complete the test during the 30 second test duration time.

Although the 40,000 case for the top wall appears to be much larger than the experimental uncertainty, the issue is ultimately with the scale for the plot. The TLC results for the top wall range from only 2% to 9% below the copper block tests, 5% to 18% below copper block results on the side wall, and 14% to 22% on the bottom wall. The overall Nusselt number augmentation results in Figure 272 show the TLC 2% to 11% below the copper block; results for the TLC support the copper block and results are within the uncertainty of the experiment.

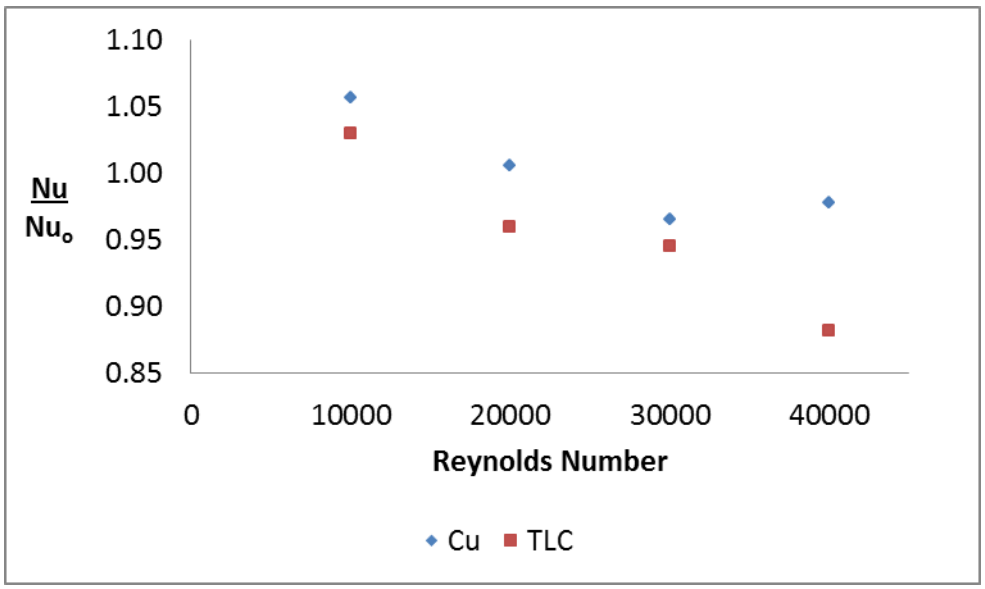

Figure 269: Nusselt Number Augmentation Copper to TLC Comparison Case E Top Wall

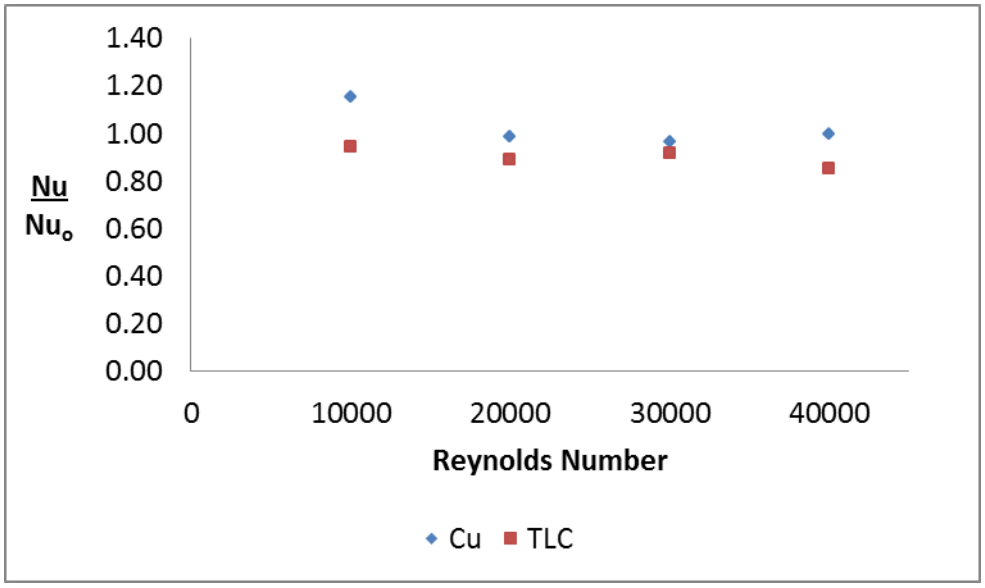

Figure 270: Nusselt Number Augmentation Copper to TLC Comparison Case E Side Wall

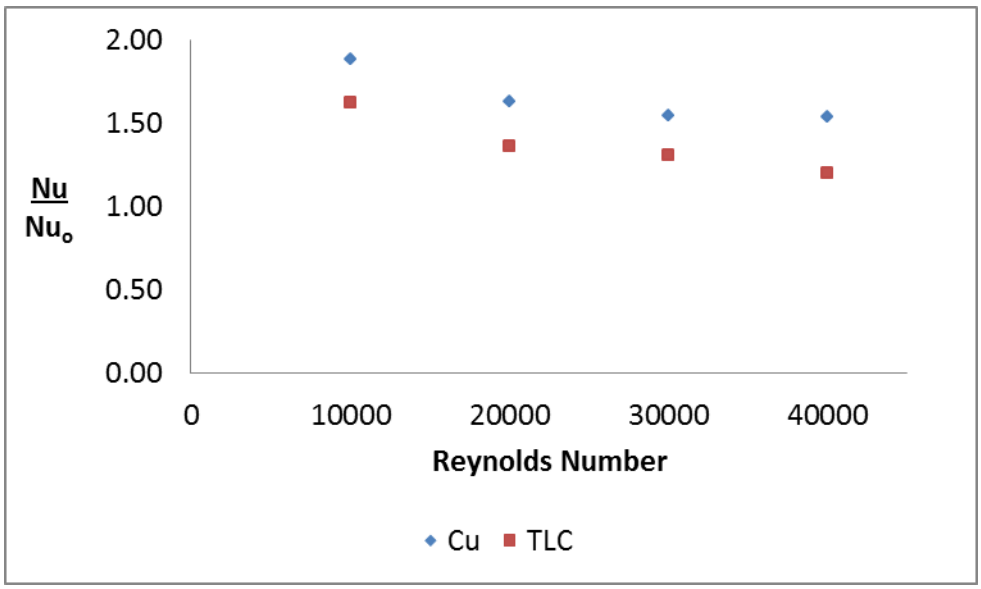

Figure 271: Nusselt Number Augmentation Copper to TLC Comparison Case E Bottom Wall

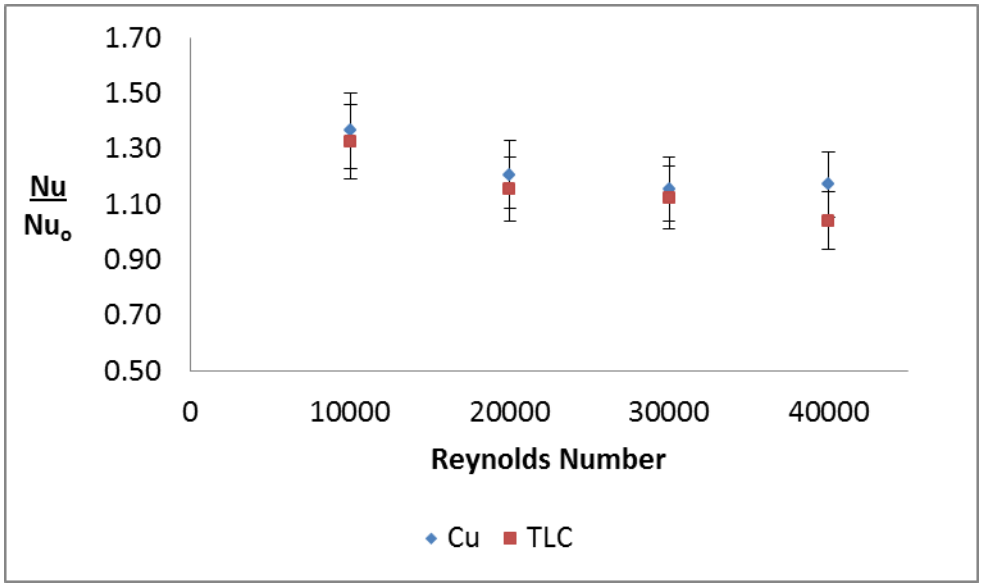

Figure 272: Nusselt Number Augmentation Copper to TLC Comparison Case E Overall

Case F

Comparisons of the Nusselt number augmentations from both experimental setups for all three walls tested are in Figure 273, Figure 274, and Figure 275. As with the other cases, although there is an offset between copper block and TLC Nusselt number augmentation results, the trends of the augmentations as a function of Reynolds number are still consistent between the two test setups. The TLC Nusselt number augmentation results for the top wall are 13% to 21% less than the copper block results, 13% to 33% less than the copper block results for the side wall (where the jump is between the 10,000 and 20,000 Reynolds number cases), and -1% to 12% from the copper block results on the bottom wall. The jump for the side wall is evident in the local Nusselt number augmentation plots as well, where very high heat transfer is shown from where flow from the first wedge location interacts with the side wall at the 10,000 Reynolds number. The top wall results show increase in heat transfer for both experiments at all four Reynolds numbers and with the similar trend in augmentation as a function of Reynolds number; the local TLC results help support the copper block results (this is for all walls) and help to picture the flow interactions that rise from the featured wall around to the opposite smooth top surface.

The overall averaged Nusselt number augmentation results from both the copper block and TLC as a function of Reynolds number are shown in Figure 276. The TLC results are 3% less than the copper block at the 10,000 Reynolds number, 7.5% less at the 20,000 Reynolds number, 13.6% less at the 30,000 Reynolds number, and 19.5% less at the 40,000 Reynolds number case. The error bars then overlap at the first three Reynolds numbers tested and are separated by 1.6% at the 40,000 Reynolds number.

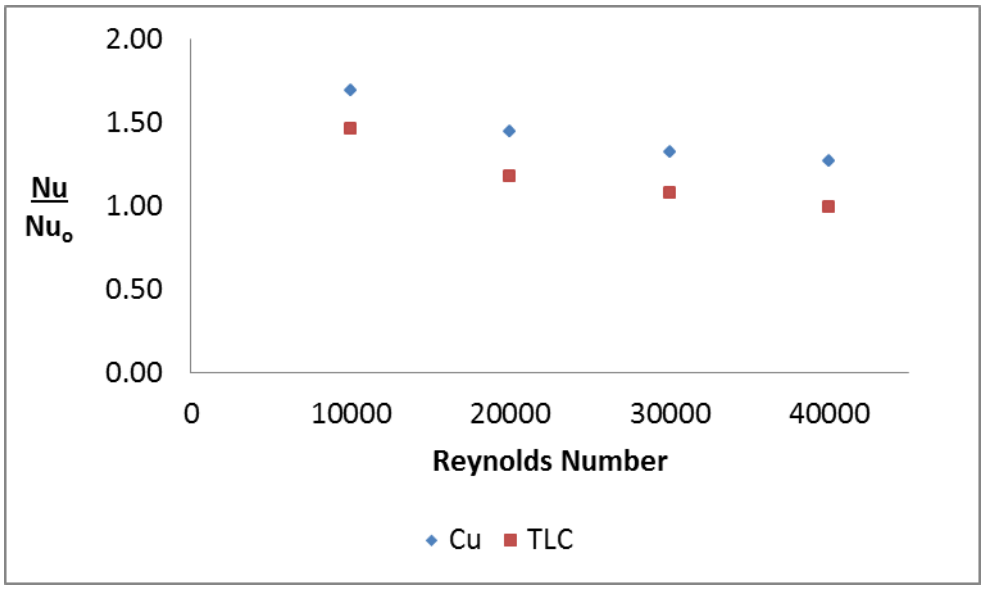

Figure 273: Nusselt Number Augmentation Copper to TLC Comparison Case F Top Wall

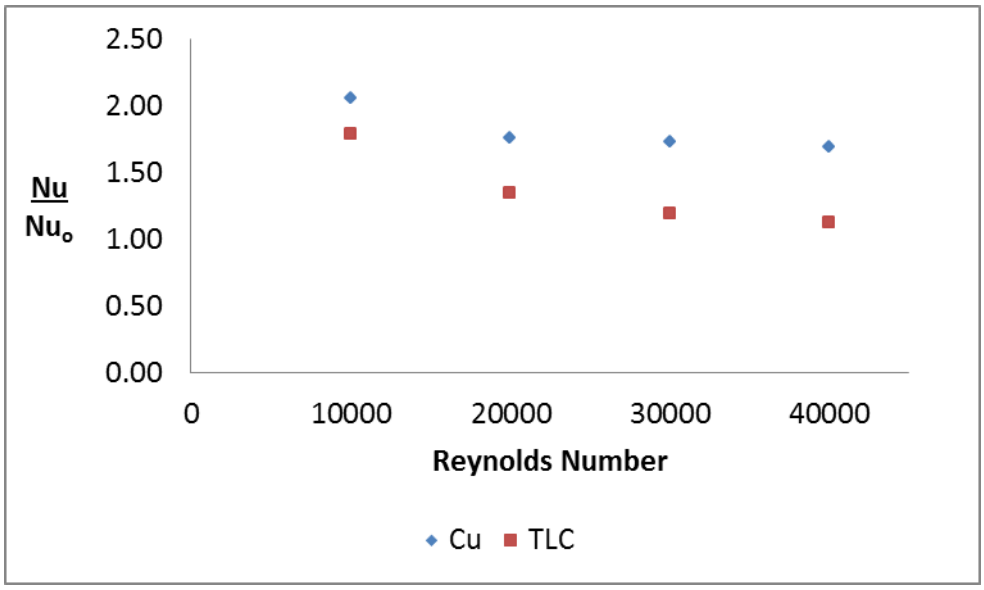

Figure 274: Nusselt Number Augmentation Copper to TLC Comparison Case F Side Wall

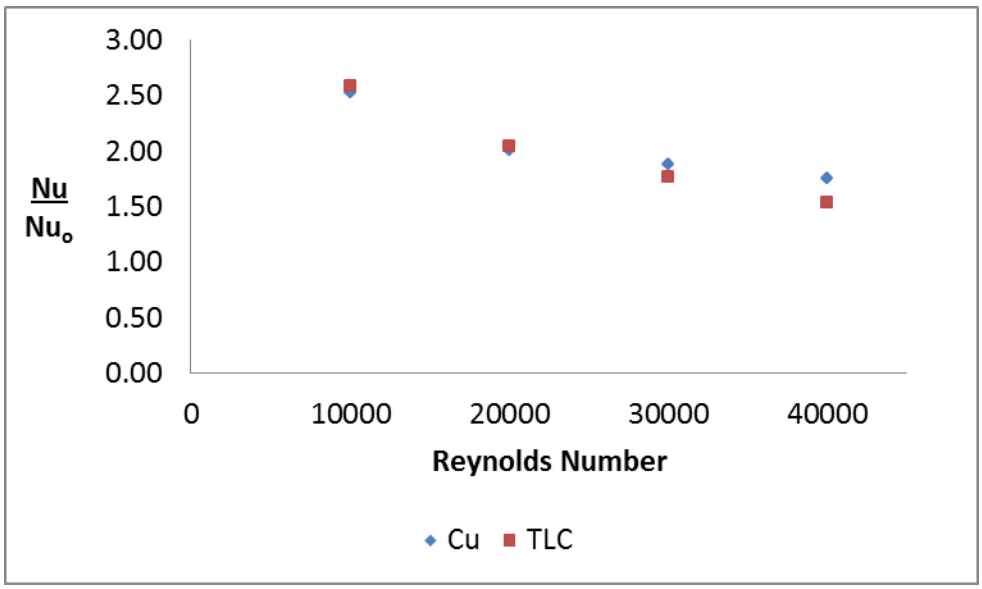

Figure 275: Nusselt Number Augmentation Copper to TLC Comparison Case F Bottom Wall

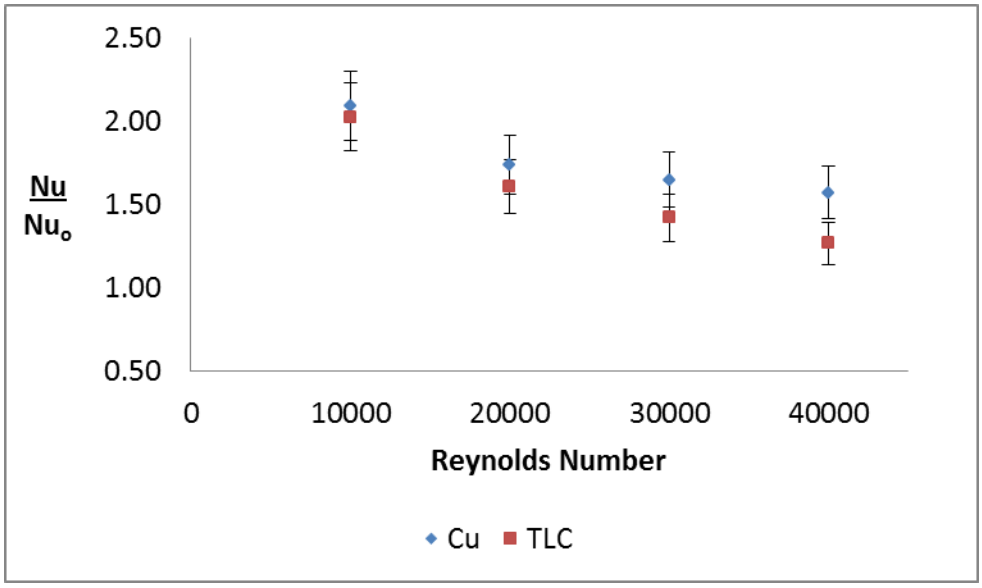

Figure 276: Nusselt Number Augmentation Copper to TLC Comparison Case F Overall

CFD Comparison

Flow visualization using STAR-CCM+ was used to help support conclusions on the flow characteristics developed from the heat transfer experiments, more particularly the local results from TLC and give more insight to the secondary flows developed from the features. The bottom wall, top wall, and side wall interaction velocity planes show consistencies with the local heat transfer results from the transient TLC plots, with respect to intensities. The areas of higher velocity near the wall from the CFD results are areas of higher heat transfer with the TLC results.

Case A velocity results near the bottom wall and the side wall interaction planes agree with the local transient TLC results. The higher velocities follow the wedge features and spread toward the side walls but do not reach the side walls. This result is supported by the secondary flows observed in the spanwise planes discussed in Chapter 4. Vorticities formed by the wedge feature directed toward the side walls are pushed by the free-stream flow in the streamwise direction. The velocity planes agree with the local TLC results that show areas of high heat transfer following the wedge aimed toward the side walls, but dissipate before reaching the smooth side walls.

Velocity results for Case B, observing the bottom wall plane and side wall interaction planes in Figure 207 and Figure 208 also agree with local TLC results in Chapter 3. Similar to the full wedge feature of the same size, Case A, higher velocities are pointed toward the side wall (following the angle of the wedge, but limited to one side with the half wedge) but do not extend all the way out to the side wall. The same angles are also observed in the velocity plane magnitudes as observed with the higher heat transfer in the local TLC results, where the half wedge feature did not mimic the full

wedge results from the centerline of the channel. Also visible in the velocity plane is the higher velocities from the previous wedge feature on the same wall following the direction for the next wedge, developing the angled flow away from the centerline of the channel, where velocities curve around the flat side of the wedge (in the centerline) toward the tail of the wedge following more of the angle from the clockwise shaped right triangle wedge design.

Case C, Figure 220, showing the bottom and side wall velocity planes indicate the secondary flows and higher velocities induced by the wedge features extend out to the side wall, alternating from the top and bottom features and continue in the streamwise direction to build on the following wedges in the channel. The local TLC results also are supported by these flow characteristics, where areas of higher heat transfer on the side wall are alternated from top and bottom, dependent on the location of the wedge feature on the top and bottom walls, and the higher heat transfer on the top and bottom featured walls continues to the next wedge in the streamwise on the same walls, fanned or angled toward the side walls.

Case D velocity directions and magnitudes observed near the bottom (or top) wall surface in Figure 231 are similar to the smaller wedge Case B; however the higher velocities do extend out to the side wall, in the clockwise direction following the wedge angle. The higher velocities angled toward the side wall that reach the side wall in Case D support the local TLC results for the side wall in Figure 151, showing areas of higher heat transfer following a wedge feature, limited to one side (near the top or bottom dependent on the side, since the wedges only point toward one side).

The first one wall wedge, Case E velocity plane showing side wall interaction in Figure 242 is similar to the two-wall Case A of the same size full wedge, similar to local results determined from the TLC results. Similar to the two-wall case, higher velocities, or higher areas of heat transfer in the TLC results are limited to the featured wall, where free-stream flows prevent the flow from continuing toward the side walls. The flow does continue streamwise on the bottom wall to the following wedge feature, consistent with the local TLC results in Figure 167. From the spanwise velocity plots, results support the TLC, where the flow characteristics from the wedge features do not reach the top wall; higher augmentations on the top wall are not achieved.

Case F near wall velocity planes shown in Figure 250 to Figure 252. The two-wall large full wedge Case C showed significant incorporation of all four walls with all tests completed. The one-wall Case F also showed ability to increase heat transfer on all four walls, where experimental results are supported by the flows observed in the CFD results. The spanwise plots show secondary flow created by the wedge features continuing to expand in the streamwise direction and extending out to the side walls. The flows build with the following streamwise wedge features and propagate up to the top non-featured wall, observed in both the spanwise plane cuts and Figure 250. The near top wall velocity plane in this figure shows higher areas of velocity near the side walls, this is duplicated from the local TLC results in Figure 180, where flow effects from the feature continue up to the top wall, not seen with the smaller full wedge one-wall feature Case E.

Comparison to Rib Study

The wedge Nusselt number augmentations of all cases for the current study are comparable to the Nusselt number augmentations of the three rib aspect ratio cases tested by Tran et al. (Tran, Valentino, Ricklick, & Kapat, 2011). Results of the three aspect ratio cases are shown in Figure 277 and Figure 278 below. A1 corresponds to the rib aspect ratio of 1, A3 to rib aspect ratio of 3, and A5 to rib aspect ratio 5. Although the Nusselt number augmentations for the wedge cases are similar to the full rib cases, the friction factor augmentations of the full ribs are 5 to 10 times higher than the wedge cases tested in the current study. With the ability of the wedges to increase heat transfer while resulting in minimal frictional losses, parametric studies of the wedge spacing and size to determine the optimal wedge case design is the next step, continuing the current study.

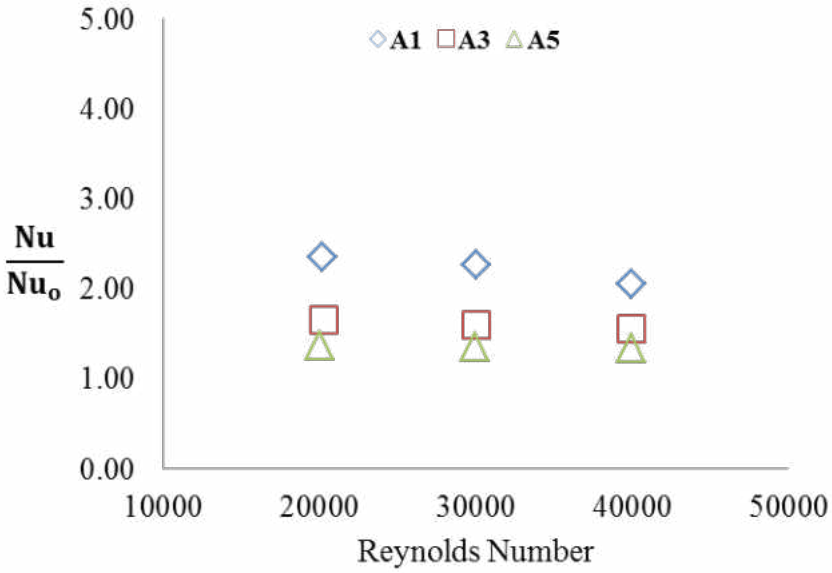

Figure 277: Rib Aspect Ratio Nu Aug Results from (Tran, Valentino, Ricklick, & Kapat, 2011)

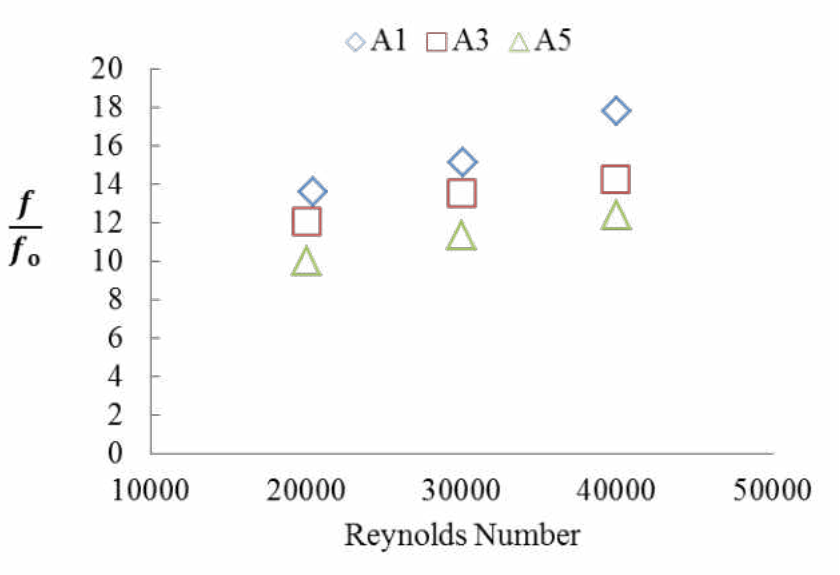

Figure 278: Rib Aspect Ratio Nu Aug Results from (Tran, Valentino, Ricklick, & Kapat, 2011)

CHAPTER 6: FURTHER STUDIES AND RECOMMENDATIONS FROM LESSONS LEARNED

Conclusions from these tests indicate that further studies altering the wedge pitch and size are necessary for determining the optimization. Error associated with the TLC data may also be minimized with the following:

- Calculation of T_{bulk}; only one thermocouple was inserted into the flow in this case at 4 locations along the center of the channel to determine a non-linear curve fit equation to determine T_{bulk} ; adding multiple thermocouples traversed in height and/or width of the channel at each location could reduce the offset in T_{bulk}
- The bulk temperature calculation for the lumped capacitance on wedge areas was not calculated with the same step function (varying T_{bulk}) as with the semi-infinite to save on process time. However, one case run with the varying T_{bulk} and found to have a 4% difference in local heat transfer coefficient. Future cases then should all be processed with the varying T_{bulk} to eliminate this error.
- Test section inlet/heater box; mesh heaters heated flow uneven in the channel and may have caused offset in the heat transfer calculations (seen with the smooth wall where the streak in temperature was shifting toward the bottom of the side wall). This issue may have resulted from creating a heater inlet box larger than the channel, funneling the heated air to the channel and causing uneven distributions.
- Masks; if the masks created for the image did not completely cover the copper piece; the results would turn out numbers too low for the augmentations, if the

masks created for the image covered too much, the results would turn out too high in augmentations. Issues came up with covering the correct size of the wedge, since it was difficult to identify through the black backing, or when being heated or cooled.

- Although the bulk temperature correction factor method presented by Chyu et al. and reviewed in this study showed TLC results closer to the copper block results, it is not applicable in the lumped capacitance areas. Further study re-developing the correction factor for the areas or cases with lumped capacitance would be necessary before applying the correction in each case test.
- As the test section in the TLC experiments starts 10 inches from the inlet, the proper inlet temperature is not calculated properly since there is heat absorbed into the acrylic over the first 10 inches of the channel. It is proposed then to develop a test channel with an insulated starting section, i.e. using Rohacell instead of acrylic at the first 10 inches.

Another issue with the wedges tested in this study for both TLC and Copper block experiments is the alignment. Since the features were designed to be removed for placement on other test rig setups, the wedges were placed onto either the copper blocks or acrylic inserts by measuring and marking their location with a digital micrometer. This placement technique leaves a lot of room for human error, where placement of the wedges could have been shifted. One way to solve this issue would be machining the feature directly to the copper block and acrylic insert; however this would add significant cost in machining to the experiments. Another method could include etching the footprint of the feature into the copper block or acrylic, but again, costs

would be added for materials, as each case would need separate copper block and acrylic smooth wall pieces. The most cost effective way to minimize issues with placement of the wedges could be achieved by machining stencils for each case. The stencils would not have significant cost for either the material or machining. This method then may be applied for further testing.

APPENDIX A: MATLAB AND NLREG CODES

Matlab Codes (In the order as run):

ReadImages

```
%-------------------------------------------------------------------------%
% TRANSIENT TLC
%   Processing Step 1 ()
%   Reading Sequenced Images
%
% LUCKY TRAN & MICHELLE VALENTINO
% Open Publication Project
% Revision 3
% Last Updated 05/12/2010
%-------------------------------------------------------------------------%
% Bitmap Info
%   imread ('filename','BMP')
%   IM(:,:,1) = red data;
%   IM(:,:,2) = green data;
%   IM(:,:,3) = blue data;
%   imwrite ( IM, 'file.bmp', 'BMP' )
%-------------------------------------------------------------------------%

clc
close all
clear all

% Inputs
%Set Working Directory if needed
cd ('E:\Documents\Wedges\TLC\Run 2 8_2011\SW\SW_9-1-11\ASM3_2W_T1_10k');

% Directory Names for Bot,Bot,Bot wall images
directory = 'Top';

%Total Number of Sequenced Images
numimages = 1351;

% Reads File ahead of time to pre-allocate output & oneFile
% Use any arbitrary representative image
fullFileName = fullfile(directory,'ASM3_2W_T1_10k_1_Top_000000.bmp');
oneFile = imread(fullFileName,'BMP');
[h w r] = size(oneFile) ;
output = zeros(h,w,3,numimages);

tic
%READIN loop
    index = 1;
    for i = 0:9
        for j = 0:9
            for k = 0:9
                for l = 0:9
                    bmpfilename =
sprintf('ASM3_2W_T1_10k_1_Top_00%d%d%d%d.bmp', i, j, k, l);
                    fullFileName = fullfile(directory,bmpfilename);
```

```
                    oneFile= imread(fullFileName,'BMP');
                    output(:,:,:,index) = oneFile(:,:,:);
                    if index == numimages
                        break
                    end
                    index = index + 1;
                end
                if index == numimages
                    break
                end
            end
            if index == numimages
                break
            end
        end
        if index == numimages
            break
        end
    end
toc

%     Restore and save the image array
if (directory == 'Top')
    T = zeros(h,w,3,numimages);
    T(:,:,:,:) = output(:,:,:,:);
    save ('ASM3_2W_T1_10k_1_T.mat','T');
end

% if (directory == 'Side')
%     S = zeros(h,w,3,numimages);
%     S(:,:,:,:) = output(:,:,:,:);
%     save ('ASM3_2W_T1_10k_1_S.mat','S');
% end

% if (directory == 'Bot')
%     B = zeros(h,w,3,numimages);
%     B(:,:,:,:) = output(:,:,:,:);
%     save ('ASM3_2W_T1_10k_1_B.mat','B');
% end

toc
clear i j k l h w r x y index;
clear output numimages directory bmpfilename fullFileName oneFile;
```

FilterAverage

```
%-------------------------------------------------------------------------%
% TRANSIENT TLC
%   Processing Step 2
```

```
%   3 Point Moving Average-Time Series Filtering
%    3x3 Spatial Filter
%    X-Install a Low-Pass Filter to filter out noise
%   Frame Uncertainty
%   Build Time Matrix (t)
%
% LUCKY TRAN & MICHELLE VALENTINO
% Open Publication Project
% Revision 4
% Last Updated 07/08/2011
%-------------------------------------------------------------------------%

%Inputs Required:
%   Top Wall RGB(x,y,z,t) Array                 <-- From Previous Codes
(named 'T')
%   Side Wall RGB(x,y,z,t) Array                <-- From Previous Codes
(named 'S')
%   Bottom Wall RGB(x,y,z,t) Array              <-- From Previous Codes
(named 'B')
%   Camera Speed                                <-- Frames Per Second (Hz)

clc;
close all;
clear all;
tic;

%Set Working Directory if needed
cd ('E:\Documents\Wedges\TLC\Run 2 8_2011\SW\SW_9-1-11\ASM3_2W_T1_10k');

%INPUTS
load ASM3_2W_T1_40k_1_T.mat
load ASM3_2W_T1_40k_1_B.mat
load ASM3_2W_T1_40k_1_S.mat

% time threshold to filter
threshold = 0.0;

%Camera Frame Rate
% 29.97 fps for progressive scan, do not change
cam_speed = 29.97;

%FIND SIZES OF INPUT ARRAYS
[Ty Tx Tw Tz] = size(T);
[Sy Sx Sw Sz] = size(S);
[By Bx Bw Bz] = size(B);

% time series filter
T(:,:,:,2:end-1) = (T(:,:,:,1:end-2)+T(:,:,:,2:end-1)+T(:,:,:,3:end))/3;
S(:,:,:,2:end-1) = (S(:,:,:,1:end-2)+S(:,:,:,2:end-1)+S(:,:,:,3:end))/3;
B(:,:,:,2:end-1) = (B(:,:,:,1:end-2)+B(:,:,:,2:end-1)+B(:,:,:,3:end))/3;
toc
```

```
% 3x3 spatial filter
T(2:end-1,2:end-1,:) = 1/9*(T(1:end-2,1:end-2,:)+T(2:end-1,1:end-
2,:)+T(3:end,1:end-2,:)+T(1:end-2,2:end-1,:)+T(2:end-1,2:end-
1,:)+T(3:end,2:end-1,:)+T(1:end-2,3:end,:)+T(2:end-
1,3:end,:)+T(3:end,3:end,:));
S(2:end-1,2:end-1,:) = 1/9*(S(1:end-2,1:end-2,:)+S(2:end-1,1:end-
2,:)+S(3:end,1:end-2,:)+S(1:end-2,2:end-1,:)+S(2:end-1,2:end-
1,:)+S(3:end,2:end-1,:)+S(1:end-2,3:end,:)+S(2:end-
1,3:end,:)+S(3:end,3:end,:));
B(2:end-1,2:end-1,:) = 1/9*(B(1:end-2,1:end-2,:)+B(2:end-1,1:end-
2,:)+B(3:end,1:end-2,:)+B(1:end-2,2:end-1,:)+B(2:end-1,2:end-
1,:)+B(3:end,2:end-1,:)+B(1:end-2,3:end,:)+B(2:end-
1,3:end,:)+B(3:end,3:end,:));
toc

% a(1:Tz)=T(30,250,2,1:Tz);
% b(1:Tz)=T(30,250,2,1:Tz);
% plot(1:Tz,a,1:Tz,b)
% figure
% plot(1:Tz,a)
% figure
% plot(1:Tz,b)

%BUILD Z MATRICES
% C dummy variable to carry magnitude
% z Matrix carries the index of each peak
z_T = zeros(Ty,Tx,Tw);
z2_T = zeros(Ty,Tx,Tw);
z3_T = zeros(Ty,Tx,Tw);
uT = zeros(Ty,Tx,Tw);
[C,z_T(:,:,:)]=max(T,[],4);

for i = 1:Ty
    for j = 1:Tx
        for k = 1:Tw
            l = z_T(i,j,k);
            T(i,j,k,l) = NaN;
        end
    end
end

[C,z2_T(:,:,:)]=max(T,[],4);

for i = 1:Ty
    for j = 1:Tx
        for k = 1:Tw
            l = z2_T(i,j,k);
            T(i,j,k,l) = NaN;
        end
    end
end

[C,z3_T(:,:,:)]=max(T,[],4);
```

```
for i = 1:Ty
    for j = 1:Tx
        for k = 1:Tw
            uT(i,j,k) = max ([abs(z3_T(i,j,k) - z2_T(i,j,k)) abs(z2_T(i,j,k)
- z_T(i,j,k)) abs(z3_T(i,j,k) - z_T(i,j,k)) ]);
        end
    end
end

z_S = zeros(Sy,Sx,Sw);
z2_S = zeros(Sy,Sx,Sw);
z3_S = zeros(Sy,Sx,Sw);
uS = zeros(Sy,Sx,Sw);
[C,z_S(:,:,:)]=max(S,[],4);

for i = 1:Sy
    for j = 1:Sx
        for k = 1:Sw
            l = z_S(i,j,k);
            S(i,j,k,l) = NaN;
        end
    end
end

[C,z2_S(:,:,:)]=max(S,[],4);

for i = 1:Sy
    for j = 1:Sx
        for k = 1:Sw
            l = z2_S(i,j,k);
            S(i,j,k,l) = NaN;
        end
    end
end
[C,z3_S(:,:,:)]=max(S,[],4);

for i = 1:Sy
    for j = 1:Sx
        for k = 1:Sw
            uS(i,j,k) = max ([abs(z3_S(i,j,k) - z2_S(i,j,k)) abs(z2_S(i,j,k)
- z_S(i,j,k)) abs(z3_S(i,j,k) - z_S(i,j,k)) ]);
        end
    end
end

z_B = zeros(By,Bx,Bw);
z2_B = zeros(By,Bx,Bw);
z3_B = zeros(By,Bx,Bw);
[C,z_B(:,:,:)]=max(B,[],4);

for i = 1:By
    for j = 1:Bx
        for k = 1:Bw
            l = z_B(i,j,k);
```

```
            B(i,j,k,l) = NaN;
        end
    end
end

[C,z2_B(:,:,:)]=max(B,[],4);

for i = 1:By
    for j = 1:Bx
        for k = 1:Bw
            l = z2_B(i,j,k);
            B(i,j,k,l) = NaN;
        end
    end
end

[C,z3_B(:,:,:)]=max(B,[],4);

for i = 1:By
    for j = 1:Bx
        for k = 1:Bw
            uB(i,j,k) = max ([abs(z3_B(i,j,k) - z2_B(i,j,k)) abs(z2_B(i,j,k)
- z_B(i,j,k)) abs(z3_B(i,j,k) - z_B(i,j,k)) ]);
        end
    end
end

toc

% %CONVERT FROM FRAMENUMBER TO TIME (s)
t_T = z_T/cam_speed;
uT = uT/cam_speed;
t_S = z_S/cam_speed;
uS = uS/cam_speed;
t_B = z_B/cam_speed;
uB = uB/cam_speed;

% Filter values based on threshold
for i = 1:Ty
    for j = 1:Tx
        for k = 1:Tw
            if ( t_T(i,j,k) < threshold)
                t_T(i,j,k) = NaN;
            end
        end
    end
end

for i = 1:Sy
    for j = 1:Sx
        for k = 1:Sw
            if ( t_S(i,j,k) < threshold)
                t_S(i,j,k) = NaN;
            end
```

```
        end
    end
end

for i = 1:By
    for j = 1:Bx
        for k = 1:Bw
            if ( t_B(i,j,k) < threshold)
                t_B(i,j,k) = NaN;
            end
        end
    end
end

save('ASM3_2W_T1_40k_1_t_T.mat', 't_T' , 'uT');
save('ASM3_2W_T1_40k_1_t_S.mat', 't_S' , 'uS');
save('ASM3_2W_T1_40k_1_t_B.mat', 't_B' , 'uB');

toc;
%Clean Workspace
%Clears Variables that are no longer needed
clear cam_speed threshold;
clear i j k l
clear Ty Tx Tw Tz;
clear Sy Sx Sw Sz;
clear By Bx Bw Bz;
clear z_T z2_T z3_T z_S z2_S z3_S z_B z2_B z3_B C
clear T S B;
```

HTCProcessing

```
%-------------------------------------------------------------------------%
% TRANSIENT TLC
%   Processing Step 3
%   Heat Transfer Coefficient and Nusselt Number Processing Code

% LUCKY TRAN & MICHELLE VALENTINO
% Open Publication Project
% Revision 4
% Last Updated 07/08/2011
%-------------------------------------------------------------------------%

clc;
close all;
clear all;

%Inputs Required:
%   Time Matrix (t)             <-- From Previous Codes (named 't')
%   Dimensions of Time Matrix   <-- [x,y] - Value of Time (t) in space
%   Wall Temperature (T_wall)   <-- From TLC Calibration (T_MaxG)(Kelvin)
%   Initial Temperature (T_init)<-- From DAQ (One Value)(Kelvin)
```

```
%   Inlet Temperature (T_inlet) <-- From DAQ (T_inlet)(Kelvin)
%   Bulk Temp Curve (T_bulk)    <-- From Excel Fit (fn(x))
%   Channel Mass Flow-Rate      <-- Input From Venturi Sheet (m_dot)(kg/s)
%   Channel Wetted Perimeter    <-- Specific to Case Tested

%Set Working Directory if needed
cd ('E:\Documents\Wedges\TLC\Run 2 8_2011\SW\SW_9-1-11\ASM3_2W_T1_10k');

% Shortcuts
TRUE = 1;
FALSE = 0;

TOP=TRUE;
SIDE=FALSE;
BOTTOM=TRUE;

% Method0=FALSE; % Using inlet temperature as reference temperature
Method1=TRUE; %Interpolation from measured inlet and outlet temperatures

% Shortcuts lead into while statements which are used only to group large
% segments of code together. Otherwise, there is no point to the while
% loop.  Break statements at the end of loop ensures termination of the
% loop upon completion.

% Take advantage of shortcuts to execute parallel threads of MATLAB
% Take due care to make sure that variables are not accessed simultaneously

% Code time matrices
load 'ASM3_2W_T1_10k_t_T.mat'
% load 'A1_2_40k_t_S.mat'
load 'ASM3_2W_T1_10k_t_B.mat'

% Bulk Temperature Curve-Fit Parameters
% Tbulk = (Tf-Ti)(Ax+1)(1-e^(Bt))+Ti
Ti = 23.051025;
Tf = 55.3583903;
A = -0.0131897472;
B = -0.370117751;
save('Tbulk.mat','Ti','Tf','A','B')

%INPUTS
T_wall = [34.8 35.1 35.7]; %From Calibration Don't Touch
T_init = Ti; %Initial Condition

%Acrylic Properties
rho_a = 1400; % kg/m^3
cp_a = 1466; % J/kg/K
k_a = 0.20; % W/m/K
alpha_a = k_a/(rho_a*cp_a); %m^2/s

%L = length of the channel
L = 10; % in.
```

```
% Setup Number of Steps for Superposition
N = 250;

%FIND SIZES OF INPUT ARRAYS
[Ty Tx Tw] = size(t_T);
% [Sy Sx Sw] = size(t_S);
[By Bx Bw] = size(t_B);

% Calculate Resolutions
% needed to calculate bulk temperature from pixel location
RT = L/Tx;
% RS = L/Sx;
RB = L/Bx;

while(Method1 == TRUE && TOP == TRUE)
% TOP SOLUTION
% Superposition
% Method1 : Tref taken by Linear Interpolation
% ============
tic
h1_T(:,:,:) = 100*ones(Ty,Tx,Tw);
vi(1,1,1,1:N)=1:N;
vi = vi./N;
v = vi(ones(Ty,1),ones(Tx,1),ones(Tw,1),:);
wi = t_T(:,:,:).*ones(Ty,Tx,Tw);
w(:,:,:,:) = wi(:,:,:,ones(N,1));
Tau_T(:,:,:,:) = w(:,:,:,:).*v(:,:,:,:);

lh1(1:Tx)= ((A*([1:Tx]*RT)) + 1);
lhs = lh1(ones(Ty,1),:,ones(Tw,1),ones(N,1));
rhs(1:Ty,1:Tx,1:Tw,1:N)=(1 - exp(B*Tau_T(1:Ty,1:Tx,1:Tw,1:N)))*(Tf-Ti);
T_step2 = zeros (Ty,Tx,Tw,N);
T_step2 = lhs(:,:,:,:).*rhs(:,:,:,:);
T_step1=zeros(Ty,Tx,Tw,N);
T_step1(:,:,:,2:N)=T_step2(:,:,:,1:N-1);
delT(:,:,:,:) = T_step2(:,:,:,:) - T_step1(:,:,:,:);
t_prime = t_T(:,:,:,ones(N,1)) - Tau_T(:,:,:,:);

toc
for k = 1:Tw
    for i = 1:Ty
        for j = 1:Tx
            if (isnan(t_prime(i,j,k)))
                h1_T(i,j,k) = NaN;
            else
                h1_T(i,j,k) = fsolve(@(h)(T_init - T_wall(k) + sum((1-
exp(h^2*alpha_a*(t_prime(i,j,k,:))/k_a^2).*erfc(h*sqrt(alpha_a*t_prime(i,j,k,
:))/k_a)).*delT(i,j,k,:),4)),h1_T(i,j,k),optimset('Display','off'));
            end
        end
        [i k]
    end
end
```

```
toc
save('ASM3_2W_T1_10k_h1_T.mat','h1_T')
clear lh1 lhs rhs T_step2 T_step1 delT t_prime vi v wi w Tau_T
break
end

while(Method1 == TRUE && SIDE == TRUE)
% SIDE SOLUTION
% Superposition
% Method1 : Tref taken by Linear Interpolation
% ============
tic
h1_S(:,:,:) = 100*ones(Sy,Sx,Sw);
vi(1,1,1,1:N)=1:N;
vi = vi./N;
v = vi(ones(Sy,1),ones(Sx,1),ones(Sw,1),:);
wi = t_S(:,:,:).*ones(Sy,Sx,Sw);
w(:,:,:,:) = wi(:,:,:,ones(N,1));
Tau_S(:,:,:,:) = w(:,:,:,:).*v(:,:,:,:);

lh1(1:Sx)= ((A*([1:Sx]*RS)) + 1);
lhs = lh1(ones(Sy,1),:,ones(Sw,1),ones(N,1));
rhs(1:Sy,1:Sx,1:Sw,1:N)=(1 - exp(B*Tau_S(1:Sy,1:Sx,1:Sw,1:N)))*(Tf-Ti);
T_step2 = zeros (Sy,Sx,Sw,N);
T_step2 = lhs(:,:,:,:).*rhs(:,:,:,:);
T_step1=zeros(Sy,Sx,Sw,N);
T_step1(:,:,:,2:N)=T_step2(:,:,:,1:N-1);
delT(:,:,:,:) = T_step2(:,:,:,:) - T_step1(:,:,:,:);
t_prime = t_S(:,:,:,ones(N,1)) - Tau_S(:,:,:,:);

toc
for k = 1:Sw
    for i = 1:Sy
        for j = 1:Sx
            if (isnan(t_prime(i,j,k)))
                h1_S(i,j,k) = NaN;
            else
                h1_S(i,j,k) = fsolve(@(h)(T_init - T_wall(k) + sum((1-
exp(h^2*alpha_a*(t_prime(i,j,k,:))/k_a^2).*erfc(h*sqrt(alpha_a*t_prime(i,j,k,
:))/k_a)).*delT(i,j,k,:),4)),h1_S(i,j,k),optimset('Display','off'));
            end
        end
        [i k]
    end
end

toc
save('ASM3_2W_T1_10k_h1_S.mat','h1_S')
clear lh1 lhs rhs T_step2 T_step1 delT t_prime vi v wi w Tau_S
break
end

while(Method1 == TRUE && BOTTOM == TRUE)
% BOTTOM SOLUTION
```

```
% Superposition
% Method1 : Tref taken by Linear Interpolation
% ============
tic
h1_B(:,:,:) = 100*ones(By,Bx,Bw);
vi(1,1,1,1:N)=1:N;
vi = vi./N;
v = vi(ones(By,1),ones(Bx,1),ones(Bw,1),:);
wi = t_B(:,:,:).*ones(By,Bx,Bw);
w(:,:,:,:) = wi(:,:,:,ones(N,1));
Tau_B(:,:,:,:) = w(:,:,:,:).*v(:,:,:,:);

lh1(1:Bx)= ((A*([1:Bx]*RB)) + 1);
lhs = lh1(ones(By,1),:,ones(Bw,1),ones(N,1));
rhs(1:By,1:Bx,1:Bw,1:N)=(1 - exp(B*Tau_B(1:By,1:Bx,1:Bw,1:N)))*(Tf-Ti);
T_step2 = zeros (By,Bx,Bw,N);
T_step2 = lhs(:,:,:,:).*rhs(:,:,:,:);
T_step1 = zeros(By,Bx,Bw,N);
T_step1(:,:,:,2:N)=T_step2(:,:,:,1:N-1);
delT(:,:,:,:) = T_step2(:,:,:,:) - T_step1(:,:,:,:);
t_prime = t_B(:,:,:,ones(N,1)) - Tau_B(:,:,:,:);

toc
for k = 1:Bw
    for i = 1:By
        for j = 1:Bx
            if (isnan(t_prime(i,j,k)))
                h1_B(i,j,k) = NaN;
            else
                h1_B(i,j,k) = fsolve(@(h)(T_init - T_wall(k) + sum((1-
exp(h^2*alpha_a*(t_prime(i,j,k,:))/k_a^2).*erfc(h*sqrt(alpha_a*t_prime(i,j,k,
:))/k_a)).*delT(i,j,k,:),4)),h1_B(i,j,k),optimset('Display','off'));
            end
        end
        [i k]
     end

end

toc
save('ASM3_2W_T1_10k_h1_B.mat','h1_B')
clear lh1 lhs rhs T_step2 T_step1 delT t_prime vi v wi w Tau_B
break
end

%Clean Workspace
%Clears Variables that are no longer needed
clear x y i j N
clear RT RS RB L
clear A B Ti Tf
clear TRUE FALSE TOP BOTTOM SIDE Method0 Method1 Method2
clear lims phch phud
clear rho_a cp_a k_a alpha_a
clear Ty Tx
```

```
clear Sy Sx
clear By Bx
clear T_wall T_init T_inlet
clear m_dot P_wet Dh A_x
clear thigh tlow;
```

MaskProcessing

```
%-------------------------------------------------------------------------%
% TRANSIENT TLC
%   Processing Step 4 ()
%   Heat Transfer Coefficient and Nusselt Number Processing Code
%   Reading Image Mask and
% LUCKY TRAN & MICHELLE VALENTINO
% Open Publication Project
% Revision 3
% Last Updated 06/30/2011
%-------------------------------------------------------------------------%

clc;
close all;
clear all;
% Set Working Directory
cd ('E:\Documents\Wedges\TLC\Run 2 8_2011\JPC2_2W_T1\10k');

% Shortcuts
TRUE = 1;
FALSE = 0;

average = 1;

% Load time matrices
load 'JPC2_2W_T1_10k_2_t_T.mat'
% load 'JPC2_2W_T1_10k_2_t_S.mat'
load 'JPC2_2W_T1_10k_2_t_B.mat'

% Load processed HTC matrices
load JPC2_2W_T1_10k_2_h1_T.mat
% load JPC2_2W_T1_10k_2_h1_S.mat
load JPC2_2W_T1_10k_2_h1_B.mat

%INPUTS
% Bulk Temperature Curve-Fit Parameters
% Tbulk = (Tf-Ti)(Ax+1)(1-e^(Bt))+Ti
load Tbulk.mat

T_wall = [34.8 35.1 35.7]; %From Calibration Don't Touch
T_init = Ti; %Initial Condition

%L = length of the channel
```

```
L = 10; % in.

%FIND SIZES OF INPUT ARRAYS
[Ty Tx Tw] = size(t_T);
% [Sy Sx Sw] = size(t_S);
[By Bx Bw] = size(t_B);

% Calculate Resolutions
% needed to calculate bulk temperature from pixel location
RT = L/Tx;
% RS = L/Sx;
RB = L/Bx;

% Copper Properties
rho = 8800; %kg/m^3
c = 385; % J/kg*K
kcu = 401; %W/m*K

% Rib Parameters
wedgepitch=2*.0254;
SA = 299.76/ 1000^2; %heat transfer surface area of wedge
footprint = 108.16/1000^2; %mm^2
m = rho*(299.96/1000^3); % mass of copper
weight = SA/footprint;

maskimtop = zeros(Ty,Tx,Tw);
maskimbot = zeros(By,Bx,Bw);
masktop = zeros(Ty,Tx);
maskbot = zeros(By,Bx);

t_T_min = zeros(1,Tx,Tw);
t_T_avg = zeros(1,Tx,Tw);
t_T_max = zeros(1,Tx,Tw);

t_B_min = zeros(1,Bx,Bw);
t_B_avg = zeros(1,Bx,Bw);
t_B_max = zeros(1,Bx,Bw);

maskimtop = imread('10kMASKTop3all.bmp','BMP');
maskimbot = imread('10kMASKBot.bmp','BMP');

h1_T_mask = zeros(Ty,Tx,Tw);
h1_B_mask = zeros(By,Bx,Bw);

% PT = zeros(1,Tx);
% PS = zeros(1,Sx);
% PB = zeros(1,Bx);

tic
% Read Mask Images

for i = 1:Ty
    for j = 1:Tx
```

```
        if ( maskimtop(i,j,:) == 255*TRUE(ones(1,1,3)));
            masktop(i,j) = TRUE;
        else
            masktop(i,j) = FALSE;
        end
    end
end
save('masktop.mat','masktop')


for i = 1:By
    for j = 1:Bx
        if ( maskimbot(i,j,:) == 255*TRUE(ones(1,1,3)));
            maskbot(i,j) = TRUE;
        else
            maskbot(i,j) = FALSE;
        end
    end
end
save('maskbot.mat','maskbot')


% Fetch times
% t_min, t_max not used
%
% while (TOP == TRUE)
% for k = 1:Tw
%     for j = 1:Tx
%         if ( masktop(1,j) == TRUE);
%             t_T_min(1,j,k) = nanmin(t_T(:,j,k));
%             t_T_avg(1,j,k) = nanmean(t_T(:,j,k));
%             t_T_max(1,j,k) = nanmax(t_T(:,j,k));
%         end
%     end
% end
% break
% end

% for ribs spanning entire width

% while (BOT == TRUE)
% for k = 1:Bw
%     for j = 1:Bx
%         if ( maskbot(1,j) == TRUE);
%             t_B_min(1,j,k) = nanmin(t_B(:,j,k));
%             t_B_avg(1,j,k) = nanmean(t_B(:,j,k));
%             t_B_max(1,j,k) = nanmax(t_B(:,j,k));
%         end
%     end
% end
% break
% end

% Calculate Tbulk
```

```
Tb(1,1:Tx,1) = (((A*([1:Tx]*RT)) + 1)*(Tf-Ti)+Ti);
Tbulk(1,:,:) = Tb(1,:,ones(1,1,3));

for k = 1:Tw
    for j = 1:Tx
        for i = 1:Ty
            if ( masktop(1,j) == TRUE)
                h1_T_mask(i,j,k) = (m*c)/(SA*t_T(i,j,k))*log((T_init -
Tbulk(1,j,k))/(T_wall(k) - Tbulk(1,j,k)));
                h1_T(i,j,k) = weight*h1_T_mask(i,j,k);
            end
        end
    end
end
clear Tb Tbulk

% Calculate Tbulk
Tb(1,1:Bx,1) = (((A*([1:Bx]*RB)) + 1)*(Tf-Ti)+Ti);
Tbulk(1,:,:) = Tb(1,:,ones(1,1,3));

for k = 1:Bw
    for j = 1:Bx
        for i = 1:By
            if ( maskbot(i,j) == TRUE)
                h1_B_mask(i,j,k) = (m*c)/(SA*t_B(i,j,k))*log((T_init -
Tbulk(1,j,k))/(T_wall(k) - Tbulk(1,j,k)));
                h1_B(i,j,k) = weight*h1_B_mask(i,j,k);
            end
        end
    end
end
clear Tb Tbulk

toc

save('JPC2_2W_T1_10k_2_h1_T_mask3.mat','h1_T')
save('JPC2_2W_T1_10k_2_h1_B_mask.mat','h1_B')
%
save('JPC2_2W_T1_10k_2_tstats.mat','t_T_min','t_T_avg','t_T_max','t_B_min','t
_B_avg','t_B_max')
clear lh1 lhs rhs T_step2 T_step1 delT t_prime vi v wi w Tau_B
```

PostProcessing

```
%-------------------------------------------------------------------------%
% TRANSIENT TLC
%   Post-Processing Step 5 ()
%   Heat Transfer Coefficient and Nusselt Number Processing Code

% LUCKY TRAN & MICHELLE VALENTINO
% Open Publication Project
% Revision 3
```

```
% Last Updated 05/03/2010
%-------------------------------------------------------------------------%

clc;
close all;
clear all;
% Set Working Directory
cd ('E:\Documents\Wedges\TLC\Run 2 8_2011\JPC2_2W_T1\10k');

load JPC2_2W_T1_10k_2_h1_T_mask2.mat
load JPC2_2W_T1_10k_2_h1_S.mat
load JPC2_2W_T1_10k_2_h1_B_mask.mat

% Reynolds number
Re = 10000;
Pr = 0.7;

low= 0;
high= 5;

% Channel Dimensions
H = 0.63*0.0254;     % H = Channel Height (m)
W = 1.26*0.0254;     % W = Channel Width (m)
L = 10*0.0254;       % L = Window Length (m)
A = W*H;             % A Flow Cross Section
P = 2*W+2*H;         % P Wetted Perimeter
Dh = 4*A/P;          % Dh hydraulic diameter

k_air = 0.025;

NuDB = 0.023*Re^0.8*Pr^0.3;


% Array Dimensions
[Ty Tx Tw] = size(h1_T(:,1:end-276,:));
[Sy Sx Sw] = size(h1_S(:,1:end-262,:));
[By Bx Bw] = size(h1_B(:,1:end-259,:));

% Filter Threshold
threshold = 100*NuDB*k_air/Dh;
lowthreshold = 0*NuDB*k_air/Dh;

% Threshold Filter
% Filter Top Wall
for i = 1:Ty
    for j = 1:Tx
        for k = 1:Tw
            if ( h1_T(i,j,k) > threshold)
                h1_T(i,j,k) = NaN;
            end
            if ( h1_T(i,j,k) < lowthreshold)
                h1_T(i,j,k) = NaN;
            end
```

```
        end
    end
end

% Filter Side Wall
for i = 1:Sy
    for j = 1:Sx
        for k = 1:Sw
            if ( h1_S(i,j,k) > threshold)
                h1_S(i,j,k) = NaN;
            end
            if ( h1_S(i,j,k) < lowthreshold)
                h1_S(i,j,k) = NaN;
            end
        end
    end
end

% Filter Bottom Wall
for i = 1:By
    for j = 1:Bx
        for k = 1:Bw
            if ( h1_B(i,j,k) > threshold)
                h1_B(i,j,k) = NaN;
            end
            if ( h1_B(i,j,k) < lowthreshold)
                h1_B(i,j,k) = NaN;
            end
        end
    end
end

Top_Red = h1_T(:,:,1);
Top_Green = h1_T(:,1:end-276,2);
Top_Blue = h1_T(:,:,3);
Side_Red = h1_S(:,:,1);
Side_Green = h1_S(1:end-5,1:end-262,2);
Side_Blue = h1_S(:,:,3);
Bot_Red = h1_B(:,:,1);
Bot_Green = h1_B(5:end-5,1:end-259,2);
Bot_Blue = h1_B(:,:,3);

% load PT.mat
% load PB.mat

SpnT(:,1) = (1:Ty)/Ty-0.5;
SpnS = (1:Sy)/Sy-0.5;
SpnB(:,1) = (1:By)/By-0.5;

xT = ((1:Tx)/Tx)*(L/Dh);
xS = ((1:Sx)/Sx)*(L/Dh);
xB = ((1:Bx)/Bx)*(L/Dh);

figure
```

```
plot(1:Tx, nanmean(Top_Green(:,1:Tx))./(NuDB*k_air/Dh),'g.')
hold on
% plot(PT, nanmean(Top_Blue(:,1:Tx)),'b.')
% plot(PT, nanmean(Top_Red(:,1:Tx)),'r.')
hold off
% xlim([0 2])
ylim([low high])
title ('Top')
xlabel('x/P')
ylabel('Nu/Nuo')

figure
plot(1:Sx, nanmean(Side_Green(:,1:Sx))./(NuDB*k_air/Dh),'g.')
hold on
% % plot(1:Sx, nanmean(Side_Blue(:,1:Sx)),'b.')
% % plot(1:Sx, nanmean(Side_Red(:,1:Sx)),'r.')
% hold off
% xlim([0 8])
ylim([low high])
title ('Side')
xlabel('x/P')
ylabel('Nu/Nuo')

figure
plot(1:Bx, nanmean(Bot_Green(:,1:Bx))./(NuDB*k_air/Dh),'g.')
hold on
% plot(PB, nanmean(Bot_Blue(:,1:Bx)),'b')
% plot(PB, nanmean(Bot_Red(:,1:Bx)),'r')
hold off
% xlim([0 8])
ylim([low high])
title ('Bottom')
xlabel('x/P')
ylabel('Nu/Nuo')

% figure
% plot(PT, nanmean(Top_Green(:,1:Tx)./NuDB),'r.')
% hold on
% plot(PB, nanmean(Bot_Green(:,1:Bx))./NuDB,'b.')
% hold off
% xlim([0 8])
% ylim([low high])
% title ('Top & Bot')
% xlabel('x/P')
% ylabel('Nu/Nuo')
% legend ('Top','Bottom')

NuTr = nanmean(Top_Red)*Dh/k_air;
NuTg = nanmean(Top_Green)*Dh/k_air;
NuTb = nanmean(Top_Blue)*Dh/k_air;
NuSr = nanmean(Side_Red)*Dh/k_air;
NuSg = nanmean(Side_Green)*Dh/k_air;
NuSb = nanmean(Side_Blue)*Dh/k_air;
NuBr = nanmean(Bot_Red)*Dh/k_air;
NuBg = nanmean(Bot_Green)*Dh/k_air;
```

```
NuBb = nanmean(Bot_Blue)*Dh/k_air;

NuT= nanmean([NuTg]);
NuS= nanmean([NuSg]);
NuB= nanmean([NuBg]);
Nua = nanmean([NuT NuT NuS NuB NuB]);

NuAugTOP = ((Top_Green)*Dh/k_air)/NuDB;
NuAugSIDE = ((Side_Green)*Dh/k_air)/NuDB;
NuAugBOT = ((Bot_Green)*Dh/k_air)/NuDB;

etaT= NuT/NuDB;
etaS= NuS/NuDB;
etaB= NuB/NuDB;
eta = mean([NuT NuB])/NuDB;

[etaT etaS etaB eta ]

clear Tw Tx Ty
clear Sw Sx Sy
clear Bw Bx By
clear i j k low high threshold
clear H W P A Dh
clear Dh k_air
% clear NuTr NuTg NuTb
% clear NuSr NuSg NuSb
% clear NuBr NuBg NuBb
```

NLREG Code & Output (Example)

The three columns in the code represent location from the test section, time step, and temperature measured.

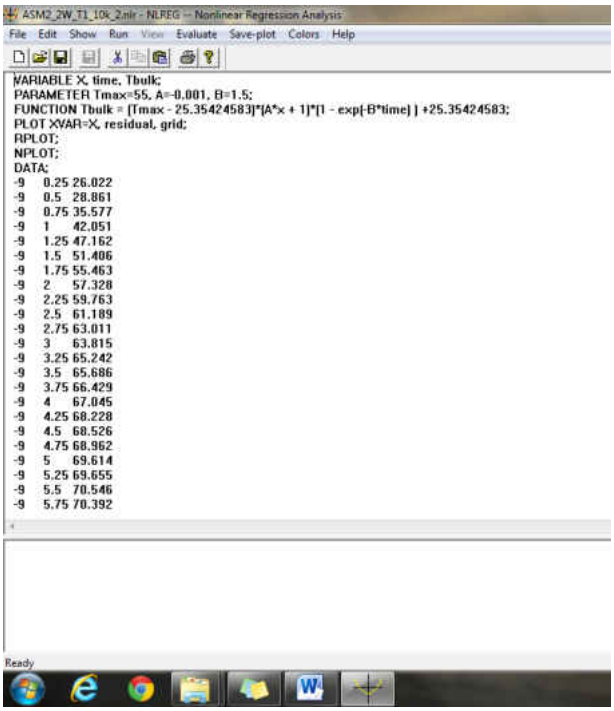

Output: where the “Calculated Parameter Values” are input to the MATLAB htcprocessing code.

```
 1: VARIABLE X, time, Tbulk;
 2: PARAMETER Tmax=55, A=-0.001, B=1.5;
 3: FUNCTION Tbulk = (Tmax - 25.35424583)*(A*x + 1)*(1 - exp(-B*time) ) +25.35424583;
 4: PLOT XVAR=X, residual, grid;
 5: RPLOT;
 6: NPLOT;
 7: DATA;

Beginning computation...
Stopped due to: Both parameter and relative function convergence.


  ----  Final Results  ----

NLREG version 6.5
Copyright (c) 1992-2010 Phillip H. Sherrod.  All rights reserved.
This is a registered copy of NLREG that may not be redistributed.

Number of observations = 720
Maximum allowed number of iterations = 500
Convergence tolerance factor = 1.000000E-010
Stopped due to: Both parameter and relative function convergence.
Number of iterations performed = 11
Final sum of squared deviations = 6.9235290E+003
Final sum of deviations = 4.9835220E+001
Standard error of estimate = 3.10745
Average deviation = 2.50413
```

Maximum deviation for any observation = 9.61802
Proportion of variance explained (R^2) = 0.9088 (90.88%)
Adjusted coefficient of multiple determination (Ra^2) = 0.9086 (90.86%)
Durbin-Watson test for autocorrelation = 0.045
This Durbin-Watson value indicates autocorrelation or inappropriate function.
Analysis completed 24-Sep-2011 11:36. Runtime = 0.14 seconds.

---- Descriptive Statistics for Variables ----

Variable	Minimum value	Maximum value	Mean value	Standard dev.
X	-9	11	-1	7.488517
time	0.25	45	22.625	12.99921
Tbulk	24.987	84.544	68.48111	10.27663

---- Calculated Parameter Values ----

Parameter	Initial guess	Final estimate	Standard error	t	Prob(t)
Tmax	55	71.1821715	0.1383355	514.56	0.00001
A	-0.001	-0.0180314768	0.0003690376	-48.86	0.00001
B	1.5	0.278345791	0.005431992	51.24	0.00001

---- Analysis of Variance ----

Source	DF	Sum of Squares	Mean Square	F value	Prob(F)
Regression	2	69009.47	34504.73	3573.31	0.00001
Error	717	6923.529	9.656247		
Total	719	75933			

APPENDIX B: EXCEL SPREADSHEETS

Friction Factor (also showing venturi calibration for the 1”-38)

MANOMETER CORRECTION					
INPUT			CORRECTED		
	Blue	Gray		Blue	Gray
dP	13.5	70	dP	12.9091	67.1308
P	10	46	P	9.5631	44.0164

Raw	Readings	Voltage	Temp (C)	Run
dP	13.58714286	5	24	40k_2
		Current		
		205		

	DP	SCFM	mdot	
1" 38	Inch H20		lb/min	kg/s
	13.58714286	32.48116046	2.390614882	0.01807273

	FLOWRATE	Reynolds Number
SCFM	32.48116046	40153.26923
mdot (kg/s)	0.01807273	

Temp Step (K)	30	Voltage	Current	Power (W)	Voltage Setting
HEAT	Calculated	#REF!	#REF!	544.8407859	#REF!
	Actual	7.63	193	1472.59	

1	13.55
2	13.65
3	13.61
4	13.65
5	13.52
6	13.61
7	13.52

GEOMETRY	
W (m)	0.032004
H (m)	0.016002
A (X-sect) (m^2)	0.000512128
P (m)	0.096012
Dh	0.021336

0.21336

PROPERTIES		
rho (kg/m^3)	1.184503922	at 70deg F for conversion from SCI
mu (N*s/m^2)	1.87516E-05	
cp (J/(kg*K))	1004.904061	

friction factor	
dp/dx (slope)	504.72
Channel Velocity	29.79262181
f, exerimental	0.02048517
f, blasius	0.022323221
%diff	-8.233808631

deltaP (Pa)	
Chanel Velocity	0

f/fo 0.917661914

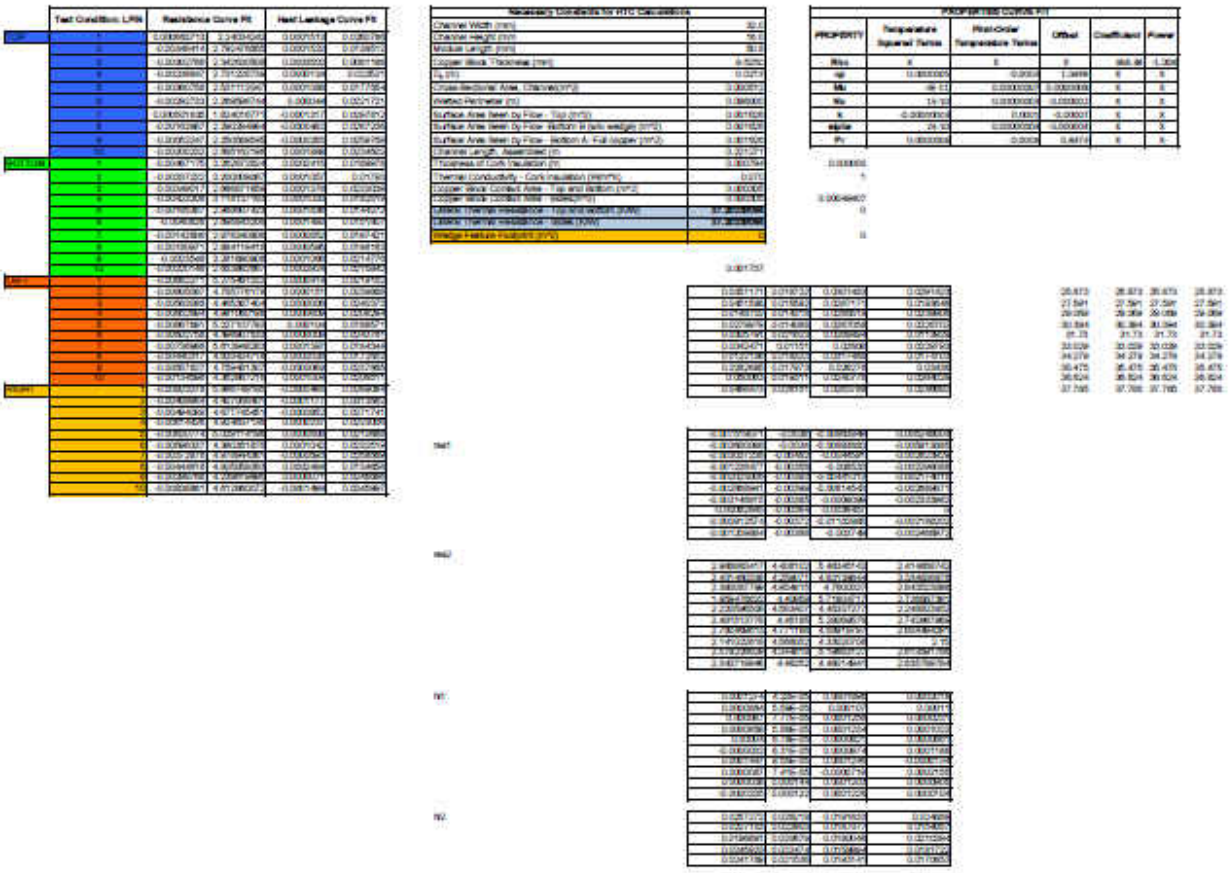

Constants Page for the HTC Processing; next 4 pages show the heat transfer post processing sheet

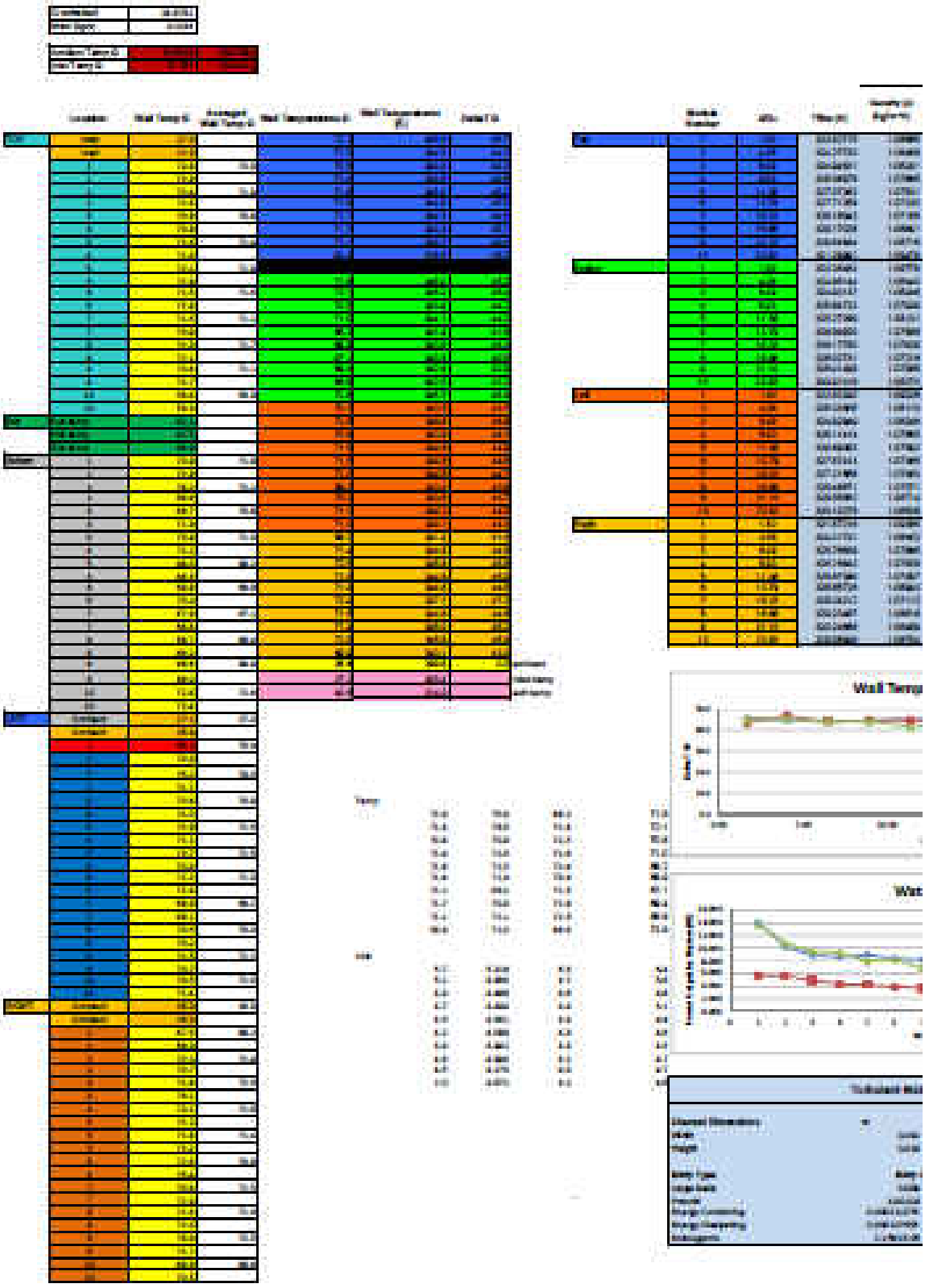


Bulk Temperature

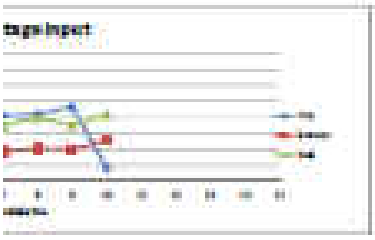

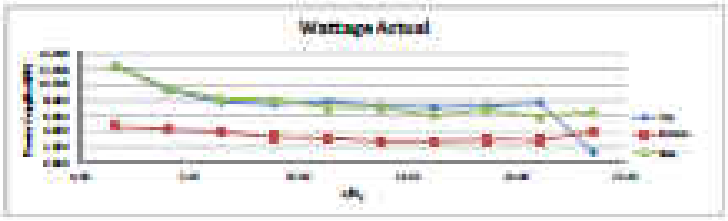
Wattage Actual

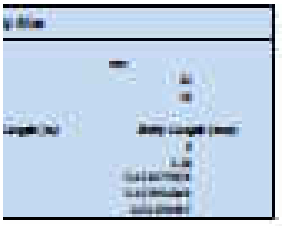

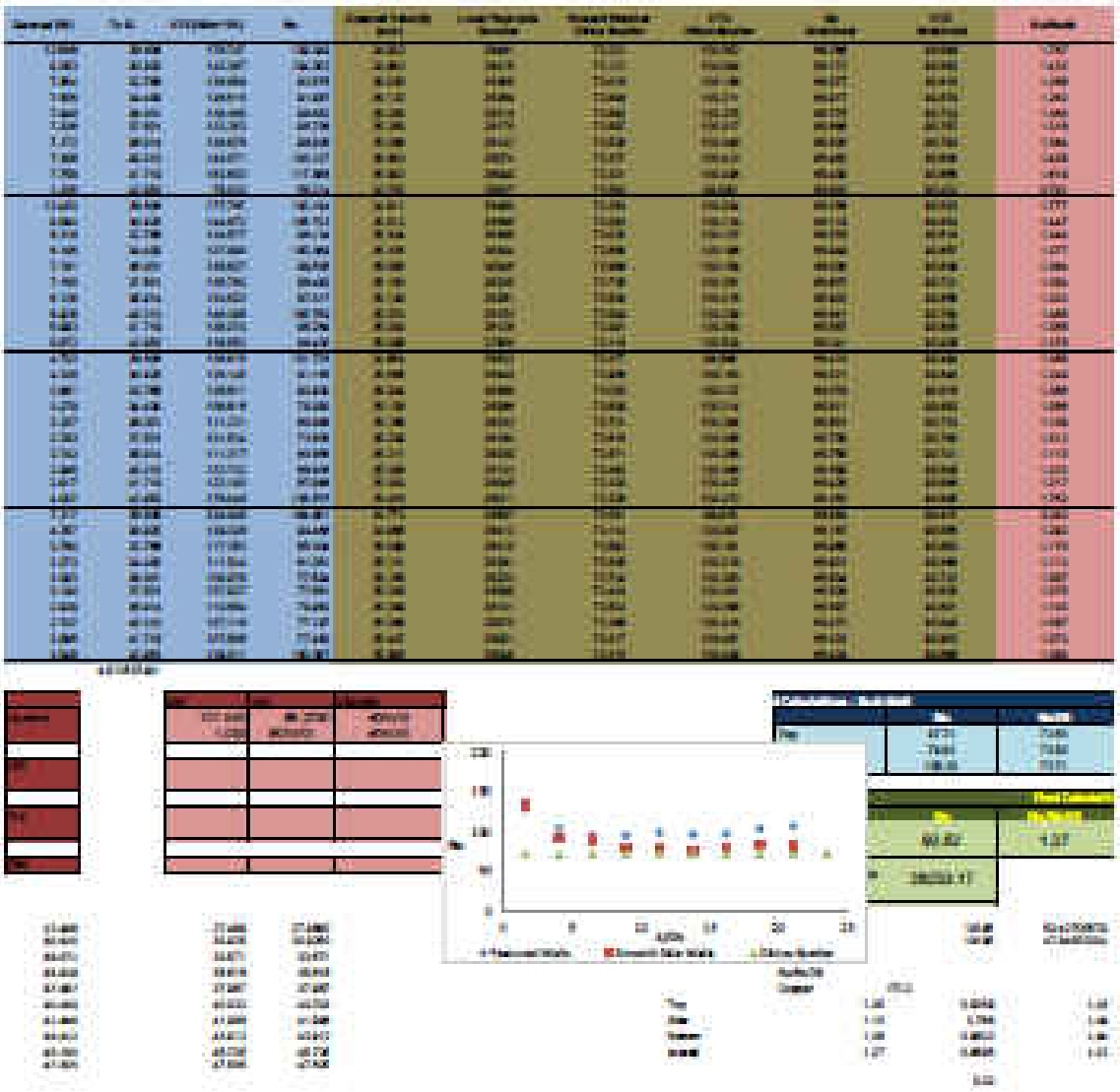

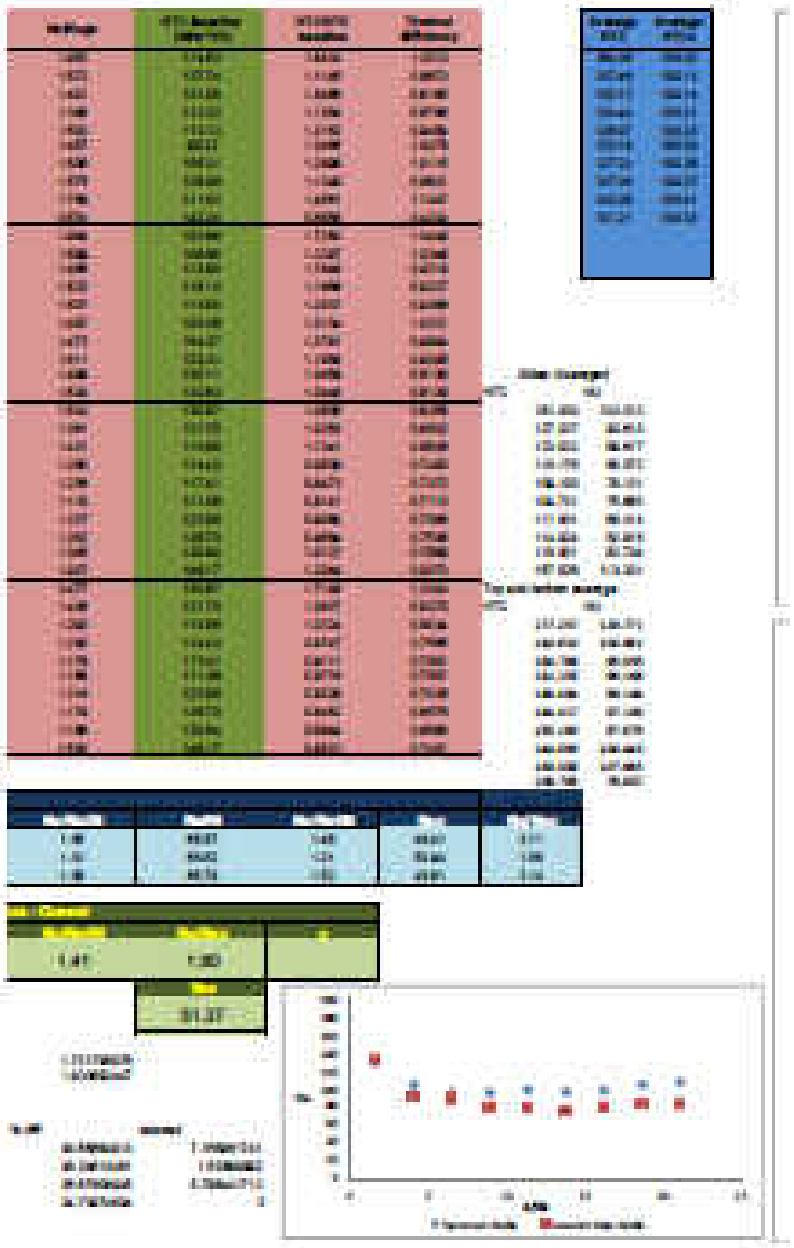

APPENDIX C: UNCERTAINTY (MATHCAD)

Copper-Block HTC

This analysis was completed by Michelle Valentino and Lucky Tran for the *Siemens Transition Duct* Project at UCF-CATER

Calculation of Uncertainty for Transition Duct Testing

For Reference, see Chapter 5 in Figliola and Beasley

ALL DATA AND CALCULATIONS FROM EXCEL

ALL UNCERTAINTY CALCULATIONS

Known Accuracies of Measurement Tools

Omega HHP 805 - (Grey) Digital Manometer

$FSR_{large} := 2.068 \cdot 10^{5} \cdot Pa$ *Manometer range is 0-30psi*

$\mu_{mano\_large} := 0.002 \cdot FSR_{large}$ *Accuracy of Manometer is 0.2% of FSR*

Omega HHP 90 - (Blue) Digital Manometer

$in2pa := 249.08Pa \qquad inh20 := \frac{1}{249.08Pa}$

$$=> \quad inh20 = 4.015 \times 10^{-3} \frac{1}{Pa}$$

$FSR_{small} := 50 \cdot in2pa$

$\mu_{mano\_small}(P_{pa}) := \left[0.002 \cdot (P_{pa}) + 0.002 \cdot FSR_{small} + 1Pa\right]$

Manometer range is 0-30psi

Scanivalve - Measurement Computing DAQ

...uracy of Manometer is 0.2% of ...ading + 0.2% of FSR + 1 LSD

$\mu_{scaniv}(P_{scani}) := 0.0001 \cdot (P_{scani})$ *Accuracy of Transducer*

$\mu_{daq}(P_{scani}) := 0.01 \cdot (P_{scani})$ *Accuracy of DAQ Measuring Transducer Voltage*

Thermocouples - Type T

$B_{Therm} := 1$ *gain 100 --> error (typical 0.01%) (max 0.1%)*

Sperry DM-350A - Digital Multimeter

$u_{volt}(Volt) := 0.005 \cdot Volt$ *Basic AC Voltage Accuracy*

$u_{res}(Res) := 0.0015(Res)$ *Basic Resistance Accuracy*

Calipers

$\mu_{cal} := 0.001 \cdot .0254$ $\mu_{cal} = 2.54 \times 10^{-5}$

$\mu_{cal} = 2.54 \times 10^{-5}$

Testing Measurements

NOTES:

Constant Wall Temperature Testing Conditions
Average Temperatue and Standard Deviation Taken Over Redundant Thermocouples

Channel Geometry

$num\_blocks := 10$ *Number of Blocks Forming Test Section*

$nn := num\_blocks - 1$ *Array Max Index*

$w := .032$ *Channel Width, Unfinned*

$h := 0.016$ *Channel Height, Unfinned*

$l\_block := 2 \cdot .0254$ *Block Thickness*

$ll := l\_block \cdot num\_blocks = 0.508$ *Channel Length*

$A_{top} := w \cdot l\_block = 1.626 \times 10^{-3}$

$k_c := 400$ *Thermal Conductivity of Copper Block*

$$A_{side} := \frac{A_{top}}{2} = 8.128 \times 10^{-4}$$

$$D_h := \frac{4 \cdot w \cdot h}{2 \cdot w + 2 \cdot h} = 0.021$$

$\rho_{high} := 1400$ $k_{low} := .167$ $\rho := 1400$

$\rho_{low} := 1170$ $c_{low} := 1466$ $c := 1466$

$k_{high} := .25$ $c_{high} := 1470$ $k := .2$

$$\mu_k := \frac{k_{high} - k_{low}}{2}$$

$$\alpha := \frac{k}{\rho \cdot c}$$

$$\mu_\rho := \frac{\rho_{high} - \rho_{low}}{2}$$

$$\mu_c := \frac{c_{high} - c_{low}}{2}$$

$$\mu_\alpha := \sqrt{\left(\mu_k \cdot \frac{1}{\rho \cdot c}\right)^2 + \left[\mu_\rho \cdot \left(\frac{k}{\rho^2 \cdot c}\right)\right]^2 + \left(\mu_c \cdot \frac{k}{\rho \cdot c^2}\right)^2} = 2.175 \times 10^{-8}$$

$$uncert_\alpha := \frac{\mu_\alpha}{\alpha} \cdot 100 = 22.317$$ properties of acrylic (uncertainty)

Insulation

$t := .002$ *Insulation Thickness*

$k_{insul} := 0.07$ *Thermal Conductivity of Insulation Material*

$$A_{cs} := w \cdot h = 5.12 \times 10^{-4}$$

$SA_{top} := w \cdot l\_block = 1.626 \times 10^{-3}$ $SA_{right} := h \cdot l\_block = 8.128 \times 10^{-4}$

$SA_{bottom} := SA_{top} = 1.626 \times 10^{-3}$ $SA_{left} := SA_{right} = 8.128 \times 10^{-4}$

$Lat_{res} := \frac{t}{k_{insul} \cdot 0.000610} = 46.838$

Geometry Uncertainties:

$\mu_{Acs} := \sqrt{(w \cdot \mu_{cal})^2 + (h \cdot \mu_{cal})^2} = 9.087 \times 10^{-7}$

$\mu_{SAtop} := \sqrt{(w \cdot \mu_{cal})^2 + (l\_block \cdot \mu_{cal})^2} = 1.525 \times 10^{-6}$ $\mu_{SAside} := \sqrt{(h \cdot \mu_{cal})^2 + (l\_block \cdot \mu_{cal})^2}$

$\mu_{SAbottom} := \mu_{SAtop} = 1.525 \times 10^{-6}$ $\mu_{SAside} = 1.353 \times 10^{-6}$

$\mu_{Lat.res} := \sqrt{(2 \cdot t \cdot \sqrt{2} \cdot \mu_{cal})^2 + [2 \cdot (w + h) \cdot \mu_{cal}]^2} = 2.443 \times 10^{-6}$

$\mu_{Lat.res} = 2.443 \times 10^{-6}$

$uncert_{Latres} := \frac{\mu_{Lat.res}}{Lat_{res}} \cdot 100 = 5.215 \times 10^{-6}$

$\mu_{Dh} := \sqrt{\left[\left[\frac{w \cdot h + (w + h) \cdot h}{(w + h)^2}\right] \cdot \mu_{cal}\right]^2 + \left[\left[\frac{w \cdot h + (w + h) \cdot w}{(w + h)^2}\right] \cdot \mu_{cal}\right]^2} = 2.662 \times 10^{-5}$

Equations to Account for Local Property Variations of Air

NOTE:
All properties taken as a function of T in Kelvin

$\rho(T) := [368.38 \cdot (T)^{-1.008}]$

$Pr(T) := (6 \cdot 10^{-7}) \cdot (T)^2 + -0.0006 \cdot (T) + 0.8373$

$\mu(T) := [(3 \cdot 10^{-11}) \cdot (T)^2 + (7 \cdot 10^{-8}) \cdot (T) + (8 \cdot 10^{-7})]$

$k_f(T) := [(-3 \cdot 10^{-8}) \cdot (T)^2 + (1 \cdot 10^{-4}) \cdot (T) + (-7 \cdot 10^{-5})]$

$c_p(T) := [(5 \cdot 10^{-7}) \cdot (T)^2 + 0.0003 \cdot (T) + 1.0499] \cdot 1000$

10k_1 Case C Data: everything as (top, left, right, bottom)

Voltages

$V_{all} := \begin{pmatrix} 5.0 & 4.978 & 4.5 & 4.9 \\ 4.4 & 4.017 & 4.3 & 5.0 \\ 4.3 & 3.964 & 4.3 & 4.6 \\ 3.6 & 3.891 & 4.0 & 4.3 \\ 4.0 & 3.486 & 3.7 & 4.1 \\ 3.7 & 3.576 & 3.9 & 4.0 \\ 3.9 & 3.402 & 3.6 & 3.7 \\ 3.5 & 3.401 & 3.3 & 3.5 \\ 3.5 & 3.261 & 3.4 & 3.7 \\ 3.3 & 3.522 & 3.3 & 3.6 \end{pmatrix}$

Temperatures

$T_{all} := \begin{pmatrix} 68.7 & 72.1 & 70.3 & 71.3 \\ 69.1 & 70.3 & 70.1 & 69.9 \\ 71.8 & 70.4 & 71.6 & 70.4 \\ 69.6 & 70.2 & 70.4 & 70.1 \\ 71.9 & 70.9 & 72.0 & 71.0 \\ 69.4 & 71.0 & 70.9 & 69.7 \\ 70.5 & 70.9 & 71.2 & 68.6 \\ 70.3 & 70.5 & 70.9 & 68.7 \\ 70.6 & 71.6 & 70.7 & 68.3 \\ 70.2 & 70.8 & 69.3 & 69.9 \end{pmatrix}$

$m_{dot} := .0047$

$T_{inlet} := 26.115$

$T_{amb} := 25.255$

Uncertainty for Data:

Voltages

$\mu_{V.all} := u_{volt}(V_{all}) =$

	0	1	2	3
0	0.025	0.025	0.023	0.025
1	0.022	0.02	0.022	0.025
2	0.022	0.02	0.022	0.023
3	0.018	0.019	0.02	0.022
4	0.02	0.017	0.019	0.021
5	0.019	0.018	0.02	0.02
6	0.02	0.017	0.018	0.019
7	0.018	0.017	0.017	0.018
8	0.018	0.016	0.017	0.019
9	0.017	0.018	0.017	0.018

Temperatures

$\mu_{T.all} :=$ for $i \in 0..3$, for $j \in 0..9$, $\mu_{T_{j,i}} \leftarrow 1$, μ_T

mdot $\mu_{mdot} := 0.1 \cdot m_{dot} = 4.7 \times 10^{-4}$

Inlet temp $\mu_{T.inlet} := 1$ $\mu_{TC} := 1$

Amb temp $\mu_{T.amb} := 1$

$\frac{\mu_{V\_all}}{V_{all}} =$

	0	1	2	3
0	$5 \cdot 10^{-3}$	$5 \cdot 10^{-3}$	$5 \cdot 10^{-3}$	$5 \cdot 10^{-3}$
1	$5 \cdot 10^{-3}$	$5 \cdot 10^{-3}$	$5 \cdot 10^{-3}$	$5 \cdot 10^{-3}$
2	$5 \cdot 10^{-3}$	$5 \cdot 10^{-3}$	$5 \cdot 10^{-3}$	$5 \cdot 10^{-3}$
3	$5 \cdot 10^{-3}$	$5 \cdot 10^{-3}$	$5 \cdot 10^{-3}$	$5 \cdot 10^{-3}$
4	$5 \cdot 10^{-3}$	$5 \cdot 10^{-3}$	$5 \cdot 10^{-3}$	$5 \cdot 10^{-3}$
5	$5 \cdot 10^{-3}$	$5 \cdot 10^{-3}$	$5 \cdot 10^{-3}$	$5 \cdot 10^{-3}$
6	$5 \cdot 10^{-3}$	$5 \cdot 10^{-3}$	$5 \cdot 10^{-3}$	$5 \cdot 10^{-3}$
7	$5 \cdot 10^{-3}$	$5 \cdot 10^{-3}$	$5 \cdot 10^{-3}$	$5 \cdot 10^{-3}$
8	$5 \cdot 10^{-3}$	$5 \cdot 10^{-3}$	$5 \cdot 10^{-3}$	$5 \cdot 10^{-3}$
9	$5 \cdot 10^{-3}$	$5 \cdot 10^{-3}$	$5 \cdot 10^{-3}$	$5 \cdot 10^{-3}$

$$\frac{\mu_{TC}}{T_{inlet}} = 0.038$$

$$\frac{\mu_{TC}}{T_{amb}} = 0.04$$

Input Values for all Curve fits in HL Calculations:

Heat Leakage Data:

$$Res_1 := \begin{pmatrix} -0.001633433 & -0.00432914 & -0.003916107 & -0.002465851 \\ -0.000858822 & -0.004952312 & -0.004242193 & -0.002894409 \\ -0.001318477 & -0.003710133 & -0.003809543 & -0.002745935 \\ -0.00239402 & -0.003463365 & -0.004026412 & -0.001689738 \\ -0.002191872 & -0.003484488 & -0.004697333 & -0.002596696 \\ -0.001913482 & -0.003699719 & -0.00576059 & -0.002417572 \\ -0.002805847 & -0.00395172 & -0.00482514 & -0.002184968 \\ -0.002099379 & -0.003514804 & -0.005061401 & -0.002392388 \\ -0.002678739 & -0.004645559 & -0.004859748 & -0.002749608 \\ -0.002048521 & -0.006075788 & -0.005409027 & -0.003039452 \end{pmatrix}$$

$$Res_2 := \begin{pmatrix} 2.764228177 & 4.517496231 & 4.590872336 & 2.69613759 \\ 2.289273233 & 4.410225669 & 4.658332644 & 3.308507015 \\ 2.292461578 & 4.901399453 & 4.683409065 & 2.966696573 \\ 2.006464837 & 5.011180992 & 5.337865531 & 2.991675112 \\ 2.201806262 & 4.272071987 & 4.449280043 & 2.770937924 \\ 2.402268011 & 4.883875568 & 5.141511838 & 3.024955795 \\ 2.758556867 & 4.789051604 & 4.84067734 & 2.975910415 \\ 2.242347344 & 4.581719937 & 4.449386816 & 2.571323388 \\ 2.665643912 & 4.430458641 & 4.627101411 & 3.10804915 \\ 2.299507599 & 5.626608342 & 4.592629795 & 3.150932403 \end{pmatrix}$$

$$HL_{c1} := \begin{pmatrix} 0.0000804 & 0.0000399 & 0.0002064 & 0.0001073 \\ 0.0000759 & 0.0000563 & 0.0000419 & 0.0000757 \\ 0.0000823 & -0.0000127 & 0.0000739 & 0.0000592 \\ 0.0001283 & 0.0000533 & 0.0001152 & 0.0000387 \\ 0.0001072 & 0.0000401 & 0.0000571 & 0.0000331 \\ 0.0000662 & 0.0000181 & 0.0000562 & 0.000027 \\ 0.0000472 & 0.0003475 & 0.0000315 & 0.0000468 \\ 0.0001368 & 0.0000281 & 0.0000421 & 0.0000447 \\ 0.000058 & 0.0000205 & 0.0000382 & 0.0000299 \\ 0.0000902 & 0.0000429 & 0.000043 & 0.0003185 \end{pmatrix}$$

$$HL_{c2} := \begin{pmatrix} 0.0300111 & 0.0254166 & 0.0196698 & 0.0244988 \\ 0.0234248 & 0.0218198 & 0.0203423 & 0.0202717 \\ 0.01942 & 0.0246955 & 0.0241214 & 0.0199626 \\ 0.017494 & 0.0187772 & 0.0182675 & 0.021864 \\ 0.0198618 & 0.0226647 & 0.0219551 & 0.0205931 \\ 0.021357 & 0.0219223 & 0.0203638 & 0.0215674 \\ 0.0216323 & 0.0051982 & 0.0217821 & 0.0209107 \\ 0.0221571 & 0.0204902 & 0.0209998 & 0.0256531 \\ 0.0220464 & 0.0219639 & 0.0216301 & 0.0240484 \\ 0.0315776 & 0.0223883 & 0.0234661 & 0.0185317 \end{pmatrix}$$

Calculations in Heat Transfer Coeff Chart:

$$Res := augment\left[\overrightarrow{\left(Res_1^{\langle 0\rangle} \cdot T_{all}^{\langle 0\rangle}\right)} + Res_2^{\langle 0\rangle}, \left[\overrightarrow{\left(Res_1^{\langle 1\rangle} \cdot T_{all}^{\langle 1\rangle}\right)} + Res_2^{\langle 1\rangle}\right], \left[\overrightarrow{\left(Res_1^{\langle 2\rangle} \cdot T_{all}^{\langle 2\rangle}\right)} + Res_2^{\langle 2\rangle}\right], \overrightarrow{\left(Res_1^{\langle 3\rangle} \cdot T_{all}^{\langle 3\rangle}\right)} + Res_2^{\langle 3\rangle}\right]$$

Uncertainty for Resistance calc

$Res =$

	0	1	2	3
0	2.652	4.205	4.316	2.52
1	2.23	4.062	4.361	3.106
2	2.198	4.64	4.411	2.773
3	1.84	4.768	5.054	2.873
4	2.044	4.025	4.111	2.587
5	2.269	4.621	4.733	2.856
6	2.561	4.509	4.497	2.826
7	2.095	4.334	4.091	2.407
8	2.477	4.098	4.284	2.92
9	2.156	5.196	4.218	2.938

$$\mu_{res} := \overrightarrow{\left(Res \cdot .05 \cdot \mu_{T.all}\right)} =$$

	0	1	2	3
0	0.133	0.21	0.216	0.126
1	0.111	0.203	0.218	0.155
2	0.11	0.232	0.221	0.139
3	0.092	0.238	0.253	0.144
4	0.102	0.201	0.206	0.129
5	0.113	0.231	0.237	0.143
6	0.128	0.225	0.225	0.141
7	0.105	0.217	0.205	0.12
8	0.124	0.205	0.214	0.146
9	0.108	0.26	0.211	0.147

$\frac{\mu_{res}}{Res} =$

	0	1	2	3
0	0.05	0.05	0.05	0.05
1	0.05	0.05	0.05	0.05
2	0.05	0.05	0.05	0.05
3	0.05	0.05	0.05	0.05
4	0.05	0.05	0.05	0.05
5	0.05	0.05	0.05	0.05
6	0.05	0.05	0.05	0.05
7	0.05	0.05	0.05	0.05
8	0.05	0.05	0.05	0.05
9	0.05	0.05	0.05	0.05

Q input uncertainty:

$$\mu_{Q.inputsquared} := \left[\left[\overrightarrow{\left(\frac{\overrightarrow{(V_{all} + V_{all})}}{Res}\right)} \cdot \mu_{V.all}\right] \cdot \left[\frac{\overrightarrow{(V_{all} + V_{all})}}{Res} \cdot \mu_{V.all}\right]\right] + \left[\overrightarrow{\left(\frac{\overrightarrow{(V_{all} \cdot V_{all})}}{\overrightarrow{(Res \cdot Res)}} \cdot \mu_{res}\right)} \cdot \left[\frac{\overrightarrow{(V_{all} \cdot V_{all})}}{\overrightarrow{(Res \cdot Res)}} \cdot \mu_{res}\right]\right]$$

$$\mu_{Q.input} := \begin{for}\ j \in 0..3 \\ \quad \text{for}\ i \in 0..9 \\ \quad\quad \mu_{Q.input_{i,j}} \leftarrow \sqrt{\mu_{Q.inputsquared_{i,j}}} \\ \mu_{Q.input}\end{for}$$

$Q_{input} := \left[\overrightarrow{\left(\frac{\overrightarrow{(V_{all} \cdot V_{all})}}{Res}\right)}\right] =$

	0	1	2	3
0	9.427	5.893	4.692	9.527
1	8.682	3.972	4.24	8.048
2	8.413	3.386	4.192	7.63
3	7.044	3.175	3.166	6.435
4	7.827	3.019	3.33	6.499
5	6.032	2.767	3.214	5.601
6	5.94	2.567	2.882	4.844
7	5.848	2.669	2.662	5.089
8	4.946	2.595	2.699	4.688
9	5.052	2.387	2.582	4.41

$$Q_{loss} := \overrightarrow{\left[HL_{c1} \cdot \overrightarrow{\left[(T_{all} - T_{amb}) \cdot (T_{all} - T_{amb})\right]}\right]} + \overrightarrow{\left[HL_{c2} \cdot (T_{all} - T_{amb})\right]}$$

$\mu_{Q.input} =$

	0	1	2	3
0	0.481	0.3	0.239	0.486
1	0.443	0.203	0.216	0.41
2	0.429	0.173	0.214	0.389
3	0.359	0.162	0.161	0.328
4	0.399	0.154	0.17	0.331
5	0.308	0.141	0.164	0.286
6	0.303	0.131	0.147	0.247
7	0.298	0.136	0.136	0.26
8	0.252	0.132	0.138	0.239
9	0.258	0.122	0.132	0.225

$\frac{\mu_{Q.input}}{Q_{input}} =$

	0	1	2
0	0.051	0.051	0.051
1	0.051	0.051	0.051
2	0.051	0.051	0.051
3	0.051	0.051	0.051
4	0.051	0.051	0.051
5	0.051	0.051	0.051
6	0.051	0.051	0.051
7	0.051	0.051	0.051
8	0.051	0.051	0.051
9	0.051	0.051	0.051

$Q_{loss} =$

	0	1	2	3
0	1.456	1.278	1.305	1.356
1	1.173	1.097	0.997	1.056
2	1.082	1.089	1.277	1.022
3	1.028	0.952	1.059	1.058
4	1.16	1.118	1.151	1.011
5	1.072	1.041	1.047	1.012
6	1.075	0.961	1.067	0.994
7	1.276	0.985	1.046	1.199
8	1.119	1.062	1.062	1.091
9	1.601	1.109	1.117	1.462

$$\mu_{Q.loss} := \left[\left[\overrightarrow{\left[HL_{c1} \cdot \overrightarrow{\left((T_{all} - T_{amb})\right)}\right]} + \overrightarrow{\left(HL_{c2}\right)}\right] \cdot \mu_{T.all} \cdot \sqrt{2}\right]$$

$\mu_{Q.loss} =$

	0	1	2	3
0	0.047	0.039	0.041	0.042
1	0.038	0.034	0.031	0.033
2	0.033	0.034	0.039	0.032
3	0.033	0.03	0.033	0.033
4	0.035	0.035	0.035	0.031
5	0.034	0.032	0.032	0.032
6	0.034	0.03	0.033	0.032
7	0.04	0.031	0.032	0.039
8	0.035	0.032	0.033	0.036
9	0.05	0.034	0.036	0.046

$T_{all}^{T} =$

	0	1	2	3	4	5	6	7	8	9
0	68.7	69.1	71.8	69.6	71.9	69.4	70.5	70.3	70.6	70.2
1	72.1	70.3	70.4	70.2	70.9	71	70.9	70.5	71.6	70.8
2	70.3	70.1	71.6	70.4	72	70.9	71.2	70.9	70.7	69.3
3	71.3	69.9	70.4	70.1	71	69.7	68.6	68.7	68.3	69.9

$$Q_{lateral} := \left| \begin{array}{l} \text{for } i \in 0 \\ \quad Q_{lat}^{\langle i \rangle} \leftarrow \dfrac{\left[\left(T_{all}^{\,T}\right)^{\langle i+1 \rangle} - \left(T_{all}^{\,T}\right)^{\langle i \rangle}\right]}{Lat_{res}} \\ \text{for } i \in 1..8 \\ \quad Q_{lat}^{\langle i \rangle} \leftarrow \dfrac{\left[\left(T_{all}^{\,T}\right)^{\langle i+1 \rangle} - \left(T_{all}^{\,T}\right)^{\langle i \rangle}\right] + \left[\left(T_{all}^{\,T}\right)^{\langle i-1 \rangle} - \left(T_{all}^{\,T}\right)^{\langle i \rangle}\right]}{Lat_{res}} \\ \text{for } i \in 9 \\ \quad Q_{lat}^{\langle i \rangle} \leftarrow \dfrac{\left[\left(T_{all}^{\,T}\right)^{\langle i-1 \rangle} - \left(T_{all}^{\,T}\right)^{\langle i \rangle}\right]}{Lat_{res}} \\ Q_{lat} \end{array} \right| =$$

	0	1	2	3	4
0	$8.54 \cdot 10^{-3}$	0.049	-0.105	0.096	-0.102
1	-0.038	0.041	-0.058	0.019	-0.013
2	$-4.27 \cdot 10^{-3}$	0.036	-0.058	0.06	-0.058
3	-0.03	0.041	-0.017	0.026	...

Lateral Uncertainty:

$\mu_{Lat.res} = 2.443 \times 10^{-6}$

$Lat_{res} = 46.838$

$$\mu_{Q.lateral} := \left| \begin{array}{l} \text{for } j \in 0..3 \\ \quad \mu_{Q.lat_{0,j}} \leftarrow \sqrt{\left[\dfrac{1}{Lat_{res}} \cdot \left(\sqrt{2}\right) \cdot \mu_{TC}\right]^2 + \left[\dfrac{\left(T_{all_{1,j}} - T_{all_{0,j}}\right)}{\left(Lat_{res}\right)^2} \cdot \mu_{Lat.res}\right]^2} \\ \text{for } j \in 0..3 \\ \quad \mu_{Q.lat_{9,j}} \leftarrow \sqrt{\left[\dfrac{1}{Lat_{res}} \cdot \left(\sqrt{2}\right) \cdot \mu_{TC}\right]^2 + \left[\dfrac{\left(T_{all_{8,j}} - T_{all_{9,j}}\right)}{Lat_{res}^{\,2}} \cdot \mu_{Lat.res}\right]^2} \\ \text{for } i \in 1..8 \\ \quad \text{for } j \in 0..3 \\ \quad\quad \mu_{Q.lat_{i,j}} \leftarrow \sqrt{\left[\dfrac{1}{Lat_{res}} \cdot \left(\sqrt{4}\right) \cdot \mu_{TC}\right]^2 + \left[\dfrac{\left[\left(T_{all_{i+1,j}} - T_{all_{i,j}}\right) + \left(T_{all_{i-1,j}} - T_{all_{i,j}}\right)\right]}{Lat_{res}^{\,2}} \cdot \mu_{Lat.res}\right]^2} \\ \mu_{Q.lat} \end{array} \right|$$

$Q_{lateral} =$

	0	1	2	3	4
0	$8.54 \cdot 10^{-3}$	0.049	-0.105	0.096	-0.102
1	-0.038	0.041	$-6.405 \cdot 10^{-3}$	0.019	-0.013
2	$-4.27 \cdot 10^{-3}$	0.036	-0.058	0.06	-0.058
3	-0.03	0.041	-0.017	0.026	...

$$Q_{lateral} := Q_{lateral}^{\,T}$$

$$Q_{actual} := Q_{input} - Q_{loss} + Q_{lateral}$$

$\mu_{Q.lateral} =$

	0	1	2	3
0	0.03	0.03	0.03	0.03
1	0.043	0.043	0.043	0.043
2	0.043	0.043	0.043	0.043
3	0.043	0.043	0.043	0.043
4	0.043	0.043	0.043	0.043
5	0.043	0.043	0.043	0.043
6	0.043	0.043	0.043	0.043
7	0.043	0.043	0.043	0.043
8	0.043	0.043	0.043	0.043
9	0.03	0.03	0.03	0.03

$Q_{actual} =$

	0	1	2	3
0	7.98	4.576	3.383	8.141
1	7.558	2.916	3.28	7.033
2	7.226	2.291	2.858	6.591
3	6.112	2.243	2.166	5.403
4	6.565	1.888	2.121	5.441
5	5.037	1.722	2.197	4.594
6	4.837	1.599	1.802	3.876
7	4.583	1.716	1.618	3.88
8	3.813	1.493	1.611	3.64
9	3.459	1.296	1.495	2.914

$$\mu_{Q.actualsquared} := \left[\left(\mu_{Q.lateral} \cdot \mu_{Q.lateral}\right) + \left[\left(\mu_{Q.loss} \cdot \mu_{Q.loss}\right)\right] + \left[\left(\mu_{Q.input} \cdot \mu_{Q.input}\right)\right]\right]$$

$$\mu_{Q.actual} := \left| \begin{array}{l} \text{for } j \in 0..3 \\ \quad \text{for } i \in 0..9 \\ \quad\quad \mu_{Q.actual_{i,j}} \leftarrow \sqrt{\mu_{Q.actualsquared_{i,j}}} \\ \mu_{Q.actual} \end{array} \right|$$

$$Q := \left| \begin{array}{l} \text{for } j \in 9 \\ \quad Q^{\langle j \rangle} \leftarrow 0.5 \cdot \left(Q_{actual}^{\,T}\right)^{\langle 9 \rangle} \\ \text{for } j \in 8..0 \\ \quad Q^{\langle j \rangle} \leftarrow 0.5 \cdot \left[\left(Q_{actual}^{\,T}\right)^{\langle j \rangle} + \left(Q_{actual}^{\,T}\right)^{\langle j+1 \rangle}\right] \\ Q^T \end{array} \right|$$

$\mu_{Q.actual} =$

	0	1	2	3
0	0.484	0.304	0.245	0.488
1	0.446	0.21	0.223	0.414
2	0.432	0.181	0.221	0.393
3	0.363	0.17	0.17	0.333
4	0.403	0.163	0.179	0.336
5	0.312	0.151	0.172	0.291
6	0.308	0.141	0.157	0.253
7	0.304	0.146	0.146	0.266
8	0.258	0.143	0.148	0.245
9	0.264	0.13	0.14	0.232

$Q =$

	0	1	2	3
0	7.769	3.746	3.331	7.587
1	7.392	2.603	3.069	6.812
2	6.669	2.267	2.512	5.997
3	6.338	2.066	2.144	5.422
4	5.801	1.805	2.159	5.017
5	4.937	1.661	1.999	4.235
6	4.71	1.658	1.71	3.878
7	4.198	1.604	1.615	3.76
8	3.636	1.394	1.553	3.277
9	1.729	0.648	0.747	1.457

$$\mu_Q := \left| \begin{array}{l} \text{for } j \in 0..3 \\ \quad \mu_{Q_{0,j}} \leftarrow 0.5 \cdot \mu_{Q\,actual_{0,j}} \\ \text{for } i \in 8..0 \\ \quad \text{for } j \in 0..3 \\ \quad\quad \mu_{Q_{i,j}} \leftarrow \sqrt{\left(0.5 \cdot \mu_{Q\,actual_{i+1,j}}\right)^2 + \left(0.5 \cdot \mu_{Q\,actual_{i,j}}\right)^2} \\ \mu_Q \end{array} \right| =$$

	0	1	2	3
0	0.329	0.185	0.165	0.32
1	0.311	0.139	0.157	0.285
2	0.282	0.124	0.14	0.257
3	0.271	0.118	0.123	0.236
4	0.255	0.111	0.124	0.222
5	0.219	0.103	0.116	0.193
6	0.216	0.101	0.107	0.183
7	0.199	0.102	0.104	0.181
8	0.185	0.097	0.102	0.169
9	0.132	0.065	0.07	0.116

$$T_{bulk} := \left| \begin{array}{l} \text{for } j \in 0 \\ \quad T_{bulk_j} \leftarrow T_{inlet} = \dfrac{0.5 \cdot Q_{actual_{0,0}} + 0.5 \cdot Q_{actual_{0,1}} + 0.5 \cdot Q_{actual_{0,2}} + 0.5 \cdot Q_{actual_{0,3}}}{m_{dot} \cdot 1006} \\ \text{for } j \in 0..8 \\ \quad T_{bulk_{j+1}} \leftarrow T_{bulk_j} + \dfrac{\left(0.5 \cdot Q_{actual_{j+1,0}} + 0.5 \cdot Q_{actual_{j,0}} + 0.5 \cdot Q_{actual_{j+1,1}} + 0.5 \cdot Q_{actual_{j,1}} + 0.5 \cdot Q_{actual_{j+1,2}} + 0.5 \cdot Q_{actual_{j,2}} + 0.5 \cdot Q_{actual_{j+1,3}} + 0.5 \cdot Q_{actual_{j,3}}\right)}{\left(m_{dot} \cdot 1006\right)} \\ T_{bulk} \end{array} \right|$$

$\frac{\mu_Q}{Q} =$

	0	1	2	3
0	0.042	0.049	0.05	0.042
1	0.042	0.053	0.051	0.042
2	0.042	0.055	0.056	0.043
3	0.043	0.057	0.058	0.044
4	0.044	0.062	0.057	0.044
5	0.044	0.062	0.058	0.045
6	0.046	0.061	0.063	0.047
7	0.047	0.064	0.064	0.048
8	0.051	0.069	0.065	0.051
9	0.076	0.1	0.093	0.079

$T_{bulk} =$

	0
0	28.661
1	33.406
2	37.61
3	41.299
4	44.677
5	47.803
6	50.517
7	53.045
8	55.409
9	57.495

Uncertainty for Bulk Temperature

$$\mu T_{bulk} = \left| \begin{array}{l} \text{for } i \in 0 \\ \quad \mu T_{bulk_i} \leftarrow \sqrt{\left[\frac{1}{m_{dot} \cdot 1005}\left[\left(0.5 \cdot \mu Q_{actual_{0,2}}\right)^2 + \left(0.5 \cdot \mu Q_{actual_{0,0}}\right)^2 + \left(0.5 \cdot \mu Q_{actual_{0,1}}\right)^2 + \left(0.5 \cdot \mu Q_{actual_{0,1}}\right)^2\right]\right]^2 + \left(\frac{Q_{actual_{0,0}} + Q_{actual_{0,1}} + Q_{actual_{0,2}} + Q_{actual_{0,3}}}{m_{dot} \cdot 1005} \cdot \mu_{T\,inlet}\right)^2 + \left(\mu_{T\,inlet}\right)^2} \\ \text{for } i \in 0..8 \\ \quad \mu T_{bulk_{i+1}} \leftarrow \sqrt{\left[\frac{1}{m_{dot} \cdot 1005}\left[\left(0.5 \cdot \mu Q_{actual_{i+1,0}}\right)^2 + \left(0.5 \cdot \mu Q_{actual_{i,0}}\right)^2 + \left(0.5 \cdot \mu Q_{actual_{i+1,1}}\right)^2 + \left(0.5 \cdot \mu Q_{actual_{i,1}}\right)^2 + \left(0.5 \cdot \mu Q_{actual_{i+1,2}}\right)^2 + \left(0.5 \cdot \mu Q_{actual_{i,2}}\right)^2 + \left(0.5 \cdot \mu Q_{actual_{i+1,3}}\right)^2 + \left(0.5 \cdot \mu Q_{actual_{i,3}}\right)^2\right]\right]^2 + \left(\frac{0.5 \cdot Q_{actual_{i+1,0}} + 0.5 \cdot Q_{actual_{i,0}} + 0.5 \cdot Q_{actual}\right.} \\ \mu T_{bulk} \end{array} \right|$$

$$hA = \frac{Q_{actual}}{augment\left(T_{all}^{\langle 0 \rangle} - T_{bulk}^{\langle 0 \rangle}, T_{all}^{\langle 1 \rangle} - T_{bulk}^{\langle 1 \rangle}, T_{all}^{\langle 2 \rangle} - T_{bulk}^{\langle 2 \rangle}, T_{all}^{\langle 3 \rangle} - T_{bulk}^{\langle 3 \rangle}\right)}$$

$hA =$

	0	1	2	3
0	0.199	0.105	0.081	0.191
1	0.212	0.079	0.089	0.193
2	0.211	0.07	0.084	0.201
3	0.216	0.078	0.074	0.188
4	0.241	0.072	0.078	0.207
5	0.233	0.074	0.095	0.21
6	0.242	0.078	0.087	0.214
7	0.266	0.088	0.091	0.248
8	0.251	0.092	0.105	0.262
9	0.272	0.087	0.127	0.235

$\mu T_{bulk} =$

	0
0	1.003500
1	1.008967
2	1.014480
3	1.018469
4	1.021950
5	1.025062
6	1.027451
7	1.029677
8	1.031715
9	1.033500

$$hA_{permodule} := \left| \begin{array}{l} \text{for } k \in 0..9 \\ \quad hA_{sum_k} \leftarrow \sum_{n=0}^{3} hA_{k,n} \\ hA_{sum} \end{array} \right.$$

	0
0	0.577
1	0.573
2	0.566
3	0.556
4	0.597
5	0.612
6	0.622
7	0.702
8	0.731
9	0.731

$hA_{permodule} =$

$$hA_{case} := \frac{\sum_{n=1}^{9} hA_{permodule_n}}{9} = 0.632$$

$$N := \frac{hA_{case}}{m_{dot} \cdot 1006} = 0.134$$

where N=hA/mdot*cp

Uncertainty for hA (per block):

$$\mu_{hA.block} := \left| \begin{array}{l} \text{for } j \in 0..3 \\ \quad \text{for } i \in 0..9 \\ \quad\quad \mu_{block_{i,j}} \leftarrow \sqrt{\left[\left(\frac{1}{T_{all_{i,j}} - T_{bulk_i}}\right) \cdot \left(\mu_{Q_{i,j}}\right)\right]^2 + \left[\frac{Q_{i,j}}{\left(T_{all_{i,j}} - T_{bulk_i}\right)^2} \cdot \sqrt{\left(\mu_{T.bulk_i}\right)^2 + \left(\mu_{T.all_{i,j}}\right)^2}\right]^2} \\ \mu_{block} \end{array} \right.$$

	0	1	2	3
0	0.011	$5.101 \cdot 10^{-3}$	$4.815 \cdot 10^{-3}$	$9.557 \cdot 10^{-3}$
1	0.012	$4.637 \cdot 10^{-3}$	$5.366 \cdot 10^{-3}$	0.011
2	0.012	$4.835 \cdot 10^{-3}$	$5.145 \cdot 10^{-3}$	0.011
3	0.015	$5.396 \cdot 10^{-3}$	$5.569 \cdot 10^{-3}$	0.012
4	0.015	$5.664 \cdot 10^{-3}$	$6.142 \cdot 10^{-3}$	0.013
5	0.018	$6.271 \cdot 10^{-3}$	$7.363 \cdot 10^{-3}$	0.015
6	0.02	$7.581 \cdot 10^{-3}$	$7.721 \cdot 10^{-3}$	0.02
7	0.023	$9.557 \cdot 10^{-3}$	$9.311 \cdot 10^{-3}$	0.025
8	0.026	$9.693 \cdot 10^{-3}$	0.012	0.031
9	0.019	$7.181 \cdot 10^{-3}$	$9.722 \cdot 10^{-3}$	0.017

$\mu_{hA.block} =$

Uncertainty for hA (per module):

$$\mu_{hA.module} := \left| \begin{array}{l} \text{for } k \in 0..9 \\ \quad \mu_{hA.sum_k} \leftarrow \sqrt{\sum_{n=0}^{3} \left(\mu_{hA.block_{k,n}}\right)^2} \\ \mu_{hA.sum} \end{array} \right.$$

	0
0	0.016
1	0.018
2	0.018
3	0.021
4	0.021
5	0.026
6	0.03
7	0.037
8	...

$\mu_{hA.module} =$

Uncertainty for case hA value:

$$\mu_{hA.case} := \sqrt{\frac{\sum_{n=1}^{9} \left(\mu_{hA.module_n}\right)^2}{9}} = 0.028$$

$$\frac{\mu_{hA.case}}{hA_{case}} = 0.044$$

Uncertainty for N:

$$\mu_N := \sqrt{\left(\frac{1}{m_{dot} \cdot 1006} \cdot \mu_{hA.case}\right)^2 + \left[\frac{hA_{case}}{\left(m_{dot}^2 \cdot 1006\right)} \cdot \mu_{mdot}\right]^2} = 0.015$$

$$uncertaintyN := \frac{\mu_N}{N} \cdot 100 = 10.936$$

FINDING NUSSELT NUMBER

$$T_{bulk} := \begin{pmatrix} 28.35150929 & 28.35150929 & 28.35150929 & 28.35150929 \\ 32.42355404 & 32.42355404 & 32.42355404 & 32.42355404 \\ 36.00281178 & 36.00281178 & 36.00281178 & 36.00281178 \\ 39.17133077 & 39.17133077 & 39.17133077 & 39.17133077 \\ 42.10611021 & 42.10611021 & 42.10611021 & 42.10611021 \\ 44.76920898 & 44.76920898 & 44.76920898 & 44.76920898 \\ 47.04101783 & 47.04101783 & 47.04101783 & 47.04101783 \\ 49.21806415 & 49.21806415 & 49.21806415 & 49.21806415 \\ 51.24530235 & 51.24530235 & 51.24530235 & 51.24530235 \\ 52.98384363 & 52.98384363 & 52.98384363 & 52.98384363 \end{pmatrix}$$

$$T_f := \frac{\overrightarrow{(T_{bulk} + T_{all})}}{2} + 273.15 =$$

	0	1	2	3
0	321.676	323.376	322.476	322.976
1	323.912	324.512	324.412	324.312
2	327.051	326.351	326.951	326.351
3	327.536	327.836	327.936	327.786
4	330.153	329.653	330.203	329.703
5	330.235	331.035	330.985	330.385
6	331.921	332.121	332.271	330.971
7	332.909	333.009	333.209	332.109
8	334.073	334.573	334.123	332.923
9	334.742	335.042	334.292	334.592

$k_{air} :=$ for $i \in 0..9$, for $j \in 0..3$, $k_{air_{i,j}} \leftarrow k_f(T_{f_{i,j}})$, k_{air}

$k_{air} =$

	0	1	2	3
0	0.029	0.029	0.029	0.029
1	0.029	0.029	0.029	0.029
2	0.029	0.029	0.029	0.029
3	0.029	0.029	0.029	0.029
4	0.03	0.03	0.03	0.03
5	0.03	0.03	0.03	0.03
6	0.03	0.03	0.03	0.03
7	0.03	0.03	0.03	0.03
8	0.03	0.03	0.03	0.03
9	0.03	0.03	0.03	0.03

$Nu :=$ for $j \in 0..9$, for $i \in 0,3$, $Nu_{j,i} \leftarrow \left(\frac{D_h}{A_{top} \cdot k_{air_{j,i}}}\right) \cdot (hA_{j,i})$, for $i \in 1..2$, $Nu_{j,i} \leftarrow \left(\frac{D_h}{A_{side} \cdot k_{air_{j,i}}}\right) \cdot (hA_{j,i})$, Nu

$Nu =$

	0	1	2	3
0	90.211	94.915	73.392	86.112
1	95.251	70.987	80.301	86.597
2	94.257	62.437	75.014	89.811
3	96.19	69.073	66.225	83.491
4	106.643	63.774	68.659	91.515
5	103.124	65.51	83.937	92.718
6	106.526	69.025	76.61	94.571
7	116.593	86.305	79.502	109.028
8	109.83	80.574	92.211	123.952
9	118.918	84.999	110.757	102.655

$\mu_{Nu} :=$ for $k \in 0..9$, for $j \in 0,3$, $\mu_{Nu_{k,j}} \leftarrow \sqrt{\left(\mu_{hA.block_{k,j}} \cdot \frac{D_h}{A_{top} \cdot k_{air_{k,j}}}\right)^2 + \left(\mu_{Dh} \cdot \frac{hA_{k,j}}{A_{top} \cdot k_{air_{k,j}}}\right)^2}$, for $j \in 1..2$, $\mu_{Nu_{k,j}} \leftarrow \sqrt{\left(\mu_{hA.block_{k,j}} \cdot \frac{D_h}{A_{side} \cdot k_{air_{k,j}}}\right)^2 + \left(\mu_{Dh} \cdot \frac{hA_{k,j}}{A_{side} \cdot k_{air_{k,j}}}\right)^2}$, μ_{Nu}

$uncert_{Nublock} :=$ for $j \in 0..9$, for $i \in 0..3$, $uncert_{j,i} \leftarrow \frac{\mu_{Nu_{j,i}}}{Nu_{j,i}} \cdot 100$, $uncert$

$\mu_{Nu} =$

	0	1	2	3
0	4.85	4.598	4.35	4.311
1	5.395	4.166	4.822	4.798
2	5.168	4.321	4.591	4.991
3	6.599	4.804	4.956	5.53
4	6.455	5.017	5.432	5.913
5	8.067	5.534	6.499	6.809
6	8.837	6.671	6.79	8.737
7	10.231	8.389	8.169	10.942
8	11.246	8.473	10.181	13.702
9	8.121	6.27	8.505	7.215

$uncert_{Nublock} =$

	0	1	2	3
0	5.376	4.844	5.927	5.007
1	5.664	5.868	6.005	5.54
2	5.483	6.921	6.121	5.557
3	6.86	6.954	7.484	6.623
4	6.053	7.867	7.912	6.461
5	7.823	8.448	7.742	7.344
6	8.296	9.664	8.864	9.239
7	8.775	9.72	10.275	10.036
8	10.239	10.515	11.041	11.054
9	6.829	7.376	7.679	7.029

$$Nu_{average} := \left| \begin{array}{l} Nu_{top} \leftarrow \dfrac{\sum_{i=3}^{8} Nu_{i,0}}{6} \\ Nu_{side} \leftarrow \dfrac{\sum_{i=3}^{8} \left(\dfrac{Nu_{i,1} + Nu_{i,2}}{2} \right)}{6} \\ Nu_{bot} \leftarrow \left| \begin{array}{l} Nu_{bot} \leftarrow 0 \\ \text{for } i \in 4,6,8 \\ \quad Nu_{bot} \leftarrow Nu_{bot} + Nu_{i,3} \\ Nu_{bot} \leftarrow \dfrac{Nu_{bot}}{3} \end{array} \right. \\ Nu_{average} \leftarrow \dfrac{Nu_{top} + Nu_{bot} + Nu_{side}}{3} \\ Nu_{average} \end{array} \right.$$

$Nu_{average} = 94.982$

DOF: n-1 = 23 $t_{0.025} := 2.571$

$St_{DevTOP} := Stdev(Nu_{3,0}, Nu_{4,0}, Nu_{5,0}, Nu_{6,0}, Nu_{7,0}, Nu_{8,0}) = 6.792$

$St_{DevBOTTOM} := Stdev(Nu_{3,1}, Nu_{4,1}, Nu_{5,1}, Nu_{6,1}, Nu_{7,1}, Nu_{8,1}) = 8.994$

$St_{DevLEFT} := Stdev(Nu_{3,2}, Nu_{4,2}, Nu_{5,2}, Nu_{6,2}, Nu_{7,2}, Nu_{8,2}) = 9.666$

$St_{DevRIGHT} := Stdev(Nu_{3,3}, Nu_{4,3}, Nu_{5,3}, Nu_{6,3}, Nu_{7,3}, Nu_{8,3}) = 14.687$

Uncertainties for Side Walls Individually:

Top

$$U_{TOP} := t_{0.025} \cdot \left(\frac{St_{DevTOP}}{\sqrt{6}} \right) = 7.129$$

Bottom

$$U_{BOTTOM} := t_{0.025} \cdot \left(\frac{St_{DevBOTTOM}}{\sqrt{6}} \right) = 9.441$$

Left

$$U_{LEFT} := t_{0.025} \cdot \left(\frac{St_{DevLEFT}}{\sqrt{6}} \right) = 10.146$$

Right

$$U_{RIGHT} := t_{0.025} \cdot \left(\frac{St_{DevRIGHT}}{\sqrt{6}} \right) = 15.415$$

All Walls Together:

$$St_{Dev} := Stdev\left(Nu_{3,0}, Nu_{4,0}, Nu_{5,0}, Nu_{6,0}, Nu_{7,0}, Nu_{8,0}, Nu_{3,1}, Nu_{4,1}, Nu_{5,1}, Nu_{6,1}, Nu_{7,1}, Nu_{8,1}, \frac{Nu_{3,2}}{2}, \frac{Nu_{4,2}}{2}, \frac{Nu_{5,2}}{2}, \frac{Nu_{6,2}}{2}, \frac{Nu_{7,2}}{2}, \frac{Nu_{8,2}}{2}, \frac{Nu_{3,3}}{2}, \frac{Nu_{4,3}}{2}, \frac{Nu_{5,3}}{2}, \frac{Nu_{6,3}}{2}, \frac{Nu_{7,3}}{2}, \frac{Nu_{8,3}}{2}\right) = 27.26$$

$t_{0.025all} := 2.069$

$$U_{allNu} := t_{0.025all} \cdot \left(\frac{St_{Dev}}{\sqrt{24}} \right) = 11.513$$

$Nu =$

	0	1	2	3
0	90.211	94.915	73.392	86.112
1	95.251	70.987	80.301	86.597
2	94.257	62.437	75.014	89.811
3	96.19	69.073	66.225	83.491
4	106.643	63.774	68.659	91.515
5	103.124	65.51	83.937	92.718
6	106.526	69.025	76.61	94.571
7	116.593	86.305	79.502	109.028
8	109.83	80.574	92.211	123.952
9	118.918	84.999	110.757	102.655

FF & Augmentations

Friction Factor Uncertainty

Case C 10k_1

Known Accuracies of Measurement Tools

Omega HHP 805 - (Grey) Digital Manometer

$FSR_{large} := 2.068 \cdot 10^{5} \cdot Pa$ *Manometer range is 0-30psi*

$\mu_{mano\_large} := 0.002 \cdot FSR_{large}$ *Accuracy of Manometer is 0.2% of FSR*

Omega HHP 90 - (Blue) Digital Manometer

$in2pa := 249.08Pa$ $inh20 := \frac{1}{249.08Pa}$

$$=> \quad inh20 = 4.015 \times 10^{-3} \frac{1}{Pa}$$

$FSR_{small} := 50 \cdot in2pa$

$\mu_{mano\_small}(P_{pa}) := \left[0.002 \cdot (P_{pa}) + 0.002 \cdot FSR_{small} + 1Pa\right]$

Manometer range is 0-30psi

Scanivalve - Measurement Computing DAQ

racy of Manometer is 0.2% of
...ding + 0.2% of FSR + 1 LSD

$\mu_{scaniv}(P_{scani}) := 0.0001 \cdot (P_{scani})$ *Accuracy of Transducer*

$\mu_{daq}(P_{scani}) := 0.01 \cdot (P_{scani})$ *Accuracy of DAQ Measuring Transducer Voltage*

Calipers

$\mu_{cal} := 0.001 \cdot .0254$ $\mu_{cal} = 2.54 \times 10^{-5}$

$\mu_{cal} = 2.54 \times 10^{-5}$

Channel Geometry

num_blocks := 10 — *Number of Blocks Forming Test Section*

nn := num_blocks − 1 — *Array Max Index*

w := .032 — *Channel Width, Unfinned*

h := 0.016 — *Channel Height, Unfinned*

l_block := 2·.0254 — *Block Thickness*

ll := l_block·num_blocks = 0.508 — *Channel Length*

$A_{top} := w \cdot l\_block = 1.626 \times 10^{-3}$

$k_c := 400$ — *Thermal Conductivity of Copper Block*

$A_{side} := \frac{A_{top}}{2} = 8.128 \times 10^{-4}$

$D_h := \frac{4 \cdot w \cdot h}{2 \cdot w + 2 \cdot h} = 0.021$

Properties of Acrylic Uncertainties

$\rho_{high} := 1400$ $k_{low} := .167$ $\rho := 1400$

$\rho_{low} := 1170$ $c_{low} := 1466$ $c := 1466$

$k_{high} := .25$ $c_{high} := 1470$ $k := .2$

$$\mu_k := \frac{k_{high} - k_{low}}{2} \qquad \alpha := \frac{k}{\rho \cdot c}$$

$$\mu_\rho := \frac{\rho_{high} - \rho_{low}}{2}$$

$$\mu_c := \frac{c_{high} - c_{low}}{2}$$

$$\mu_\alpha := \sqrt{\left(\mu_k \cdot \frac{1}{\rho \cdot c}\right)^2 + \left[\mu_\rho \cdot \left(\frac{k}{\rho^2 \cdot c}\right)\right]^2 + \left(\mu_c \cdot \frac{k}{\rho \cdot c^2}\right)^2} = 2.175 \times 10^{-8}$$

$$uncert_\alpha := \frac{\mu_\alpha}{\alpha} \cdot 100 = 22.317$$

$$A_{cs} := w \cdot h = 5.12 \times 10^{-4}$$

$$SA_{top} := w \cdot l\_block = 1.626 \times 10^{-3} \qquad SA_{right} := h \cdot l\_block = 8.128 \times 10^{-4}$$

$$SA_{bottom} := SA_{top} = 1.626 \times 10^{-3} \qquad SA_{left} := SA_{right} = 8.128 \times 10^{-4}$$

$$\mu_{Acs} := \sqrt{(w \cdot \mu_{cal})^2 + (h \cdot \mu_{cal})^2} = 9.087 \times 10^{-7}$$

$$\mu_{SAtop} := \sqrt{(w \cdot \mu_{cal})^2 + (l\_block \cdot \mu_{cal})^2} = 1.525 \times 10^{-} \qquad \mu_{SAside} := \sqrt{(h \cdot \mu_{cal})^2 + (l\_block \cdot \mu_{cal})^2}$$

$$\mu_{SAbottom} := \mu_{SAtop} = 1.525 \times 10^{-6} \qquad \mu_{SAside} = 1.353 \times 10^{-6}$$

$$\mu_{Dh} := \sqrt{\left[\left[\frac{w \cdot h + (w + h) \cdot h}{(w + h)^2}\right] \cdot \mu_{cal}\right]^2 + \left[\left[\frac{w \cdot h + (w + h) \cdot w}{(w + h)^2}\right] \cdot \mu_{cal}\right]^2} = 2.662 \times 10^{-5}$$

FF Case Data:

$DP := 4620.5$ in Pascals, from venturi reading

$DP_{inh20} := 18.55$ in inchesH20 from venturi reading

Pscani:

$$P_{scani} := \begin{pmatrix} -0.021616667 \\ -0.023296667 \\ -0.024956667 \\ -0.026056667 \\ -0.026596667 \\ -0.027606667 \\ -0.028306667 \\ -0.029296667 \\ -0.029756667 \\ -0.031686667 \\ -0.032466667 \end{pmatrix}$$

$P_{Pa} := P_{scani} \cdot 6894.7 =$

	0
0	-149.04
1	-160.624
2	-172.069
3	-179.653
4	-183.376
5	-190.34
6	-195.166
7	-201.992
8	-205.163
9	-218.47
10	-223.848

Locations:

$$x_m := \begin{pmatrix} 0.254 \\ 0.3048 \\ 0.3556 \\ 0.381 \\ 0.4064 \\ 0.4318 \\ 0.4572 \\ 0.4826 \\ 0.508 \\ 0.5588 \\ 0.5842 \end{pmatrix}$$

$$dl := x_{m_{10}} - x_{m_0} = 0.33 \qquad \mu_{dl} := \sqrt{\left(\mu_{cal}\cdot x_{m_0}\right)^2 + \left(\mu_{cal}\cdot x_{m_{10}}\right)^2} = 1.618 \times 10^{-5}$$

$$dP := P_{Pa_{10}} - P_{Pa_0} = -74.807 \qquad \mu_{dP} := \sqrt{\left(\mu_{daq}\left(P_{scani_{10}}\right)\cdot P_{Pa_0}\right)^2 + \left(\mu_{daq}\left(P_{scani_0}\right)\cdot P_{Pa_{10}}\right)^2} = 0.068$$

$$\frac{dP}{dl} = -226.552$$

$$\mu_{dpdl} := \sqrt{\left[\mu_{dl}\cdot\left(\frac{-dP}{dl^2}\right)\right]^2 + \left[\mu_{dP}\cdot\left(\frac{1}{dl}\right)\right]^2} = 0.208 \qquad uncert_{dpdl} := \frac{\mu_{dpdl}}{\frac{dP}{dl}}\cdot 100 = -0.092$$

Uncertainty in Velocity:

$$U := \frac{mdot}{A\cdot\rho} \qquad mdot := SCFM\cdot\frac{.4536}{60}\cdot.0736 \qquad .0736\cdot\frac{.4536}{60} = 5.564 \times 10^{-4}$$

$$\rho_a := 1.192187648$$

$$\mu_{mano\_small}(4620.5Pa) = 35.149\,Pa$$

$$uncert_{DP} := \frac{\mu_{mano\_small}(4620.5Pa)}{4620.5Pa} = 7.607 \times 10^{-3}$$

$$SCFM := DP^{0.4467}\cdot 2.2499 = 97.539 \qquad SCFM_{inh20} := DP_{inh20}{}^{.4467}\cdot 2.2499 = 8.293$$

$$\mu_{SCFM} := \sqrt{\left(\mu_{mano\_small}(4620.5Pa)\cdot\frac{1.00503033}{DP^{0.5533}}\right)^2} = 0.331\,Pa$$

$$\mu_{SCFM} := \frac{0.331Pa}{Pa}$$

$$uncert_{SCFM} := \frac{\mu_{SCFM}}{SCFM} = 3.394 \times 10^{-3}$$

$$\mu_{mdot} := \sqrt{\left(\mu_{SCFM}\cdot 5.564 \times 10^{-4}\right)^2} = 1.842 \times 10^{-4}$$

$$mdot := SCFM_{inh20}\cdot 5.564\cdot 10^{-4} = 4.614 \times 10^{-3}$$

$$uncert_{mdot} := \frac{\mu_{mdot}}{mdot} = 0.04$$

$$\mu_U := \sqrt{\left(\mu_{mdot}\cdot\frac{1}{A_{cs}\cdot\rho_a}\right)^2 + \left(\mu_{Acs}\cdot\frac{mdot}{\rho_a\cdot A_{cs}^{\,2}}\right)^2}$$

$$U := \frac{mdot}{A_{cs}\cdot\rho_a} = 7.56$$

$$uncert_U := \frac{\mu_U}{U}\cdot 100 = 3.995$$

$$\mu_{ff} := \sqrt{\left(\mu_U\cdot\frac{4\cdot D_h\cdot\frac{dP}{dl}}{\rho_a\cdot U^3}\right)^2 + \left[\mu_{dpdl}\cdot\left(\frac{2\cdot D_h}{\rho_a\cdot U^2}\right)\right]^2 + \left[\mu_{Dh}\cdot\left(\frac{2\cdot\frac{dP}{dl}}{\rho_a\cdot U^2}\right)\right]^2} \qquad ff := \frac{\frac{-dP}{dl}\cdot D_h}{0.5\cdot\rho_a\cdot U^2}$$

$$uncert_{ff} := \frac{\mu_{ff}}{ff}\cdot 100 = 7.992$$

$$\mu := 1.86523E\text{-}05$$

$$\mu_{Re} := \sqrt{\left(\mu_U\cdot\frac{\rho_a\cdot D_h}{\mu}\right)^2 + \left(\mu_{Dh}\cdot\frac{\rho_a\cdot U}{\mu}\right)^2} \qquad Re := \frac{\rho_a\cdot U\cdot D_h}{\mu}$$

$$uncert_{Re} := \frac{\mu_{Re}}{Re}\cdot 100 = 3.997$$

$$\mu_{ffo} := \sqrt{\left(\mu_{Re}\cdot\frac{0.079}{Re^{1.25}}\right)^2} \qquad ffo := 0.316\cdot Re^{-0.25} = 0.031$$

$$uncert_{ffo} := \frac{\mu_{ffo}}{ffo}\cdot 100 = 0.999$$

$$\mu_{ffaug} := \sqrt{\left(\mu_{ff}\cdot\frac{1}{ffo}\right)^2 + \left(\mu_{ffo}\cdot\frac{ff}{ffo^2}\right)^2} = 0.364 \qquad ffaug := \frac{ff}{ffo}$$

$$uncert_{ffaug} := \frac{\mu_{ffaug}}{ffaug}\cdot 100 = 8.054$$

$Pr := .7$

$Nu_{average} := 94.98$ $\qquad \mu_{Nu} := 10$ Input from the other sheet

$$\mu_{NuDB} := \sqrt{\left(\mu_{Re}\cdot\frac{.0184\cdot Pr^{0.4}}{Re^{0.2}}\right)^2} = 1.035 \qquad Nu_{DB} := .023\cdot Re^{0.8}\cdot Pr^{0.4}$$

$$uncert_{NuDB} := \frac{\mu_{NuDB}}{Nu_{DB}}\cdot 100 = 3.198$$

$$\mu_{Nuaug} := \sqrt{\left(\mu_{Nu}\cdot\frac{1}{Nu_{DB}}\right)^2 + \left(\mu_{NuDB}\cdot\frac{Nu_{average}}{Nu_{DB}^2}\right)^2} \qquad Nuaug := \frac{Nu_{average}}{Nu_{DB}}$$

$$uncert_{Nuaug} := \frac{\mu_{Nuaug}}{Nuaug}\cdot 100 = 11.003$$

$$\mu_{\eta} := \sqrt{\left(\mu_{ffaug}\cdot\frac{Nuaug}{3\cdot ffaug^{\frac{4}{3}}}\right)^2 + \left(\mu_{Nuaug}\cdot\frac{1}{ffaug^{\frac{1}{3}}}\right)^2} \qquad \eta := \frac{Nuaug}{ffaug^{\frac{1}{3}}}$$

$$uncert_{\eta} := \frac{\mu_{\eta}}{\eta}\cdot 100 = 11.326$$

TLC Uncertainty

M.Valentino
10-3-11

$\mu_{TC} := 0.5$

$\mu_{time} := 0.15$

Case C 10K Pixel (35,450,2) bottom wall

$t\_peak := 27.9613$ peak time

$T_{wall} := 35.1$ temp=35.1C

$T_i := 24.3649$

$T_f := 58.9966439$

$A := -0.027902245$

$B := -0.34548502$

$Px := 450$

$P_{tot} := 531$

$x_{sw} := \frac{Px}{P_{tot}} \cdot .254 = 0.215$

$x_{sw1} := \frac{448}{P_{tot}} \cdot .254 = 0.214$

Properties of Acrylic Uncertainties

$\rho_{high} := 1400$ $k_{low} := .167$ $\rho := 1400$

$\rho_{low} := 1170$ $c_{low} := 1466$ $c := 1466$

$k_{high} := .25$ $c_{high} := 1470$ $k := .2$

$\mu_k := \frac{k_{high} - k_{low}}{2}$

$\mu_\rho := \frac{\rho_{high} - \rho_{low}}{2}$

$\mu_c := \frac{c_{high} - c_{low}}{2}$

$\alpha := \frac{k}{\rho \cdot c} = 9.745 \times 10^{-8}$

$$\mu_\alpha := \sqrt{\left(\mu_k \cdot \frac{1}{\rho \cdot c}\right)^2 + \left[\mu_\rho \cdot \left(\frac{k}{\rho^2 \cdot c}\right)\right]^2 + \left(\mu_c \cdot \frac{k}{\rho \cdot c^2}\right)^2} = 2.175 \times 10^{-8}$$

$$uncert_\alpha := \frac{\mu_\alpha}{\alpha} \cdot 100 = 22.317$$

Calipers

$\mu_{cal} := 0.001 \cdot .0254$ $\mu_{cal} = 2.54 \times 10^{-5}$

$\mu_{cal} = 2.54 \times 10^{-5}$

Channel Geometry

$num\_blocks := 10$ *Number of Blocks Forming Test Section*

$nn := num\_blocks - 1$ *Array Max Index*

$w := .032$ *Channel Width, Unfinned*

$h := 0.016$ *Channel Height, Unfinned*

$l\_block := 2 \cdot .0254$ *Block Thickness*

$ll := l\_block \cdot num\_blocks = 0.508$ *Channel Length*

$A_{top} := w \cdot l\_block = 1.626 \times 10^{-3}$

$A_{cs} := w \cdot h = 5.12 \times 10^{-4}$

$SA_{top} := w \cdot l\_block = 1.626 \times 10^{-3}$ $SA_{right} := h \cdot l\_block = 8.128 \times 10^{-4}$

$SA_{bottom} := SA_{top} = 1.626 \times 10^{-3}$ $SA_{left} := SA_{right} = 8.128 \times 10^{-4}$

$$\mu_{Acs} := \sqrt{(w \cdot \mu_{cal})^2 + (h \cdot \mu_{cal})^2} = 9.087 \times 10^{-7}$$

$\mu_{SAtop} := \sqrt{(w \cdot \mu_{cal})^2 + (l\_block \cdot \mu_{cal})^2} = 1.525 \times 10^{-}$ $\mu_{SAside} := \sqrt{(h \cdot \mu_{cal})^2 + (l\_block \cdot \mu_{cal})^2}$

$\mu_{SAbottom} := \mu_{SAtop} = 1.525 \times 10^{-6}$ $\mu_{SAside} = 1.353 \times 10^{-6}$

$$\mu_{Dh} := \sqrt{\left[\left[\frac{w \cdot h + (w + h) \cdot h}{(w + h)^2}\right] \cdot \mu_{cal}\right]^2 + \left[\left[\frac{w \cdot h + (w + h) \cdot w}{(w + h)^2}\right] \cdot \mu_{cal}\right]^2} = 2.662 \times 10^{-5}$$

$L_{wedge} := 20.8mm$

$W_{wedge} := 20.8mm$

$A_{wedge} := 0.5 W_{wedge} \cdot L_{wedge} = 2.163 \times 10^{-4}\ m^2$

$$\mu_{Awedge} := \sqrt{(0.5 \cdot L_{wedge} \cdot \mu_{cal})^2 + (0.5 \cdot W_{wedge} \cdot \mu_{cal})^2} = 3.736 \times 10^{-7}\ m$$

$$uncert_{Awedge} := \frac{\mu_{Awedge}}{A_{wedge}} \cdot 100 = 0.173\ \frac{1}{m}$$

$$A_{sw} := SA_{bottom} - \frac{A_{wedge} \cdot 1}{m^2} = 1.409 \times 10^{-3}$$

$$\mu_{ASW} := \sqrt{(\mu_{Awedge} \cdot SA_{bottom})^2 + \left(\mu_{SAbottom} \cdot \frac{A_{wedge}}{m}\right)^2} = 6.911 \times 10^{-10}\ m$$

$$uncert_{ASW} := \frac{\mu_{ASW}}{A_{sw}} \cdot 100 = 4.904 \times 10^{-5}\ m$$

$$T_b := (T_f - T_i)\cdot\left(A\cdot x_{sw}\cdot\frac{1}{.0254} + 1\right)\cdot\left(1 - e^{B\cdot t\_peak}\right) + T_i$$

$$T_b = 51.504$$

$N := 250$

$i := 0..N$

$$T_{bulk}(t) := (T_f - T_i)\cdot\left(A\cdot x_{sw}\cdot\frac{1}{.0254} + 1\right)\cdot\left[1 - e^{B\cdot(t)}\right] + T_i$$

$$\tau_i := \frac{t\_peak\cdot i}{N} \qquad m := 1..N$$

$$\Delta T_m := T_{bulk}(\tau_m) - T_{bulk}(\tau_{m-1}) \qquad \sum_{i=1}^{N}\Delta T_i = 27.139$$

$HTC := 100$

Given

$$T_{wall} - T_i = \sum_{i=1}^{N}\left[\left[1 - e^{\left[\frac{HTC^2\alpha\cdot(t\_peak-\tau_j)}{k^2}\right]}\cdot erfc\left[\frac{HTC\cdot\sqrt{\alpha\cdot(t\_peak-\tau_j)}}{k}\right]\right]\cdot\Delta T_j\right]$$

$h_{sw} := Find(HTC)$

$$h_{sw} = 110.782$$

zz

$$\theta := \frac{T_{wall} - T_i}{T_b - T_i}$$

$$\mu_\theta := \sqrt{\left(\frac{-1}{T_i - T_b}\cdot\mu_{TC}\right)^2 + \left[\mu_{TC}\cdot\left[\frac{T_{wall} - T_i}{(T_b - T_i)^2} - \frac{1}{(T_b - T_i)}\right]\right]^2 + \left[\mu_{TC}\cdot\left[\frac{T_i - T_{wall}}{(T_i - T_b)^2}\right]\right]^2} = 0.023$$

lets say $$\zeta := \frac{h_{sw}\cdot\sqrt{\alpha\cdot t\_peak}}{k}$$

$$\mu_\zeta := \sqrt{\left[\mu_\theta\cdot\left[\left(e^{\zeta^2}\right)\cdot\frac{2}{\sqrt{\pi}}\cdot e^{(\zeta^2)} - 2\cdot\zeta\cdot erfc(\zeta)\cdot e^{\zeta^2}\right]\right]^2}$$

$$\mu_\zeta = 0.038$$

$$\mu_{hsw} := \sqrt{\left(\mu_\zeta \cdot \frac{k}{\sqrt{\alpha \cdot t\_peak}}\right)^2 + \left(\mu_k \cdot \frac{\zeta}{\sqrt{\alpha \cdot t\_peak}}\right)^2 + \left[\mu_\alpha \cdot \frac{k \cdot t\_peak \cdot \zeta}{2 \cdot (t\_peak \cdot \alpha)^{\frac{3}{2}}}\right]^2 + \left[\mu_{time} \cdot \frac{\alpha \cdot k \cdot \zeta}{2 \cdot (\alpha \cdot t\_peak)^{\frac{3}{2}}}\right]^2}$$

$$uncertHTC := \frac{\mu_{hsw}}{h_{sw}} \cdot 100 = 24.383$$

uncertainty in the lumped capacitace portion:

properties of copper:

$$\rho_{cu} := 8800 \qquad cp_{cu} := 385 \qquad k_{cu} := 401 \qquad SA := \frac{426.47}{1000^2} \qquad m_{cu} := \rho_{cu} \cdot \left(\frac{599.93}{1000^3}\right)$$

$$footprint := \frac{216.32}{1000^2} = 2.163 \times 10^{-4}$$

$$weight := \frac{SA}{footprint}$$

$$T_{blc} := (T_f - T_i) \cdot (A \cdot x_{sw} + 1) \cdot \left(1 - e^{B \cdot t\_lc}\right) + T_i$$

$$h_{LC} := \frac{m_{cu} \cdot cp_{cu}}{SA \cdot t\_lc} \cdot \ln\left[\frac{(T_i - T_{blc})}{T_{wall} - T_{blc}}\right] = 65.851$$

$$\mu_{hlc} := \sqrt{\left(\mu_{cal} \cdot \frac{cp_{cu} \cdot m_{cu} \cdot \ln\left(\frac{T_{blc} - T_i}{T_{blc} - T_{wall}}\right)}{t\_lc \cdot SA^2}\right)^2 + \left(\mu_{time} \cdot \frac{cp_{cu} \cdot m_{cu} \cdot \ln\left(\frac{T_{blc} - T_i}{T_{blc} - T_{wall}}\right)}{SA \cdot t\_lc^2}\right)^2 + \left[\mu_{TC} \cdot \frac{cp_{cu} \cdot m_{cu} \cdot (T_{wall} - T_{blc}) \cdot \left[\frac{1}{T_{wall} - T_{blc}} - \frac{T_i - T_{blc}}{(T_{wall} - T_{blc})^2}\right]}{SA \cdot t\_lc \cdot (T_i - T_{blc})}\right]^2 + \left[\mu_{TC} \cdot \frac{cp_{cu} \cdot m_{cu}}{SA \cdot t\_lc \cdot (T_{blc} - T_i)}\right]^2 + \left[\mu_{TC} \cdot \frac{cp_{cu} \cdot m_{cu}}{SA \cdot t\_lc \cdot (T_{blc} -}\right.}$$

$$uncert_{hlc} := \frac{\mu_{hlc}}{h_{LC}} \cdot 100 = 9.266$$

$$h_{lc} := weight \cdot h_{LC} = 129.823$$

$$A_{tot} := 10 \cdot 1.26 = 12.6$$

$$\mu_{Atot} := \sqrt{(\mu_{cal} \cdot 1.26)^2 + (\mu_{cal} \cdot 10)^2} = 2.56 \times 10^{-4}$$

$$A_{lc} := \text{footprint} \cdot \frac{1}{.0254^2} \cdot 5 = 1.676$$

$$A_{sw} := A_{tot} - A_{lc} = 10.924$$

$$h_{TLC} := \frac{h_{sw} \cdot A_{sw} - h_{lc} \cdot A_{lc}}{A_{tot}}$$

$$\mu_{htlc} := \sqrt{\left(\mu_{cal} \cdot \frac{h_{lc}}{A_{tot}}\right)^2 + \left(\mu_{cal} \cdot \frac{h_{sw}}{A_{tot}}\right)^2 + \left(\mu_{hlc} \cdot \frac{A_{lc}}{A_{tot}}\right)^2 + \left[\mu_{Atot} \cdot \left(\frac{h_{sw} \cdot A_{sw} - h_{lc} \cdot A_{lc}}{A_{tot}^2}\right)\right]^2 + \left(\mu_{hsw} \cdot \frac{A_{sw}}{A_{tot}}\right)^2}$$

$$\text{uncert}_{HTLC} := \frac{\mu_{htlc}}{h_{TLC}} \cdot 100 = 29.748$$

from other sheet:

$$D_h := .021 \qquad k_{air} := .03$$

$$\mu_{Dh} := 2.662 \times 10^{-5}$$

$$D_h := .021 \qquad k_{air} := .03$$

$$\mu_{Dh} := 2.662 \times 10^{-5}$$

$$\mu_{NuTLC} := \sqrt{\left(\mu_{htlc} \cdot \frac{D_h}{k_{air}}\right)^2 + \left(\mu_{Dh} \cdot \frac{h_{TLC}}{k_{air}}\right)^2} = 16.403$$

$$Nu_{TLC} := \frac{h_{sw} \cdot D_h}{k_{air}} = 77.547$$

$$\text{uncert}_{nutlc} := \frac{\mu_{NuTLC}}{Nu_{TLC}} \cdot 100 = 21.152$$

$$\text{uncert}_{\eta} := \frac{\mu_{\eta}}{\eta} \cdot 100 = 11.326$$

$$\mu_{NuTLC} := 16.4 \qquad Nu_{TLC} := 77.54$$

$$\mu NuaugTLC := \sqrt{\left(\mu_{NuTLC} \cdot \frac{1}{Nu_{DB}}\right)^2 + \left(\mu_{NuDB} \cdot \frac{Nu_{TLC}}{Nu_{DB}^2}\right)^2} = 0.512$$

$$\text{uncertNuaugTLC} := \frac{\mu NuaugTLC}{\frac{Nu_{TLC}}{Nu_{DB}}} \cdot 100 = 21.391$$

+

APPENDIX D: Y+ CALCULATION

$L := 1.25in$

$H := 0.63in$

$W := 1.26in$

$A := H \cdot W = 5.121 \times 10^{-4}\,m^2$

$P := 2H + 2W$

$D_h := \frac{4A}{P}$

$\rho := 1.19\,\frac{kg}{m^3}$

$\mu := 1.84 \cdot 10^{-5} \cdot \frac{N \cdot s}{m^2}$

$\tau_w := \frac{2273\,\frac{Pa}{m} \cdot W \cdot H}{L} = 36.664 \cdot \frac{N}{m^2}$ $\qquad \frac{L}{D_h} = 1.488$

$y_p := .0005in$

$u_\tau := \sqrt{\frac{\tau_w}{\rho}} = 5.551\,\frac{m}{s}$

$yplus := \frac{\rho \cdot u_\tau \cdot y_p}{\mu} = 4.559072469$

$y_p \cdot \left(\frac{1 - 1.05^8}{1 - 1.05}\right) = 1.213 \times 10^{-4}\,m$ prism layer thickness absolute size

$x_p := 50 \cdot y_p$

$x_p = 6.35 \times 10^{-4}\,m$

APPENDIX E: PUBLICATIONS

Conference Publications

Slabaugh, C., Valentino, M., Ricklick, M., Kapat, J.S. Heat Transfer and Friction Augmentation in a Narrow Rectangular Duct with Ribs Applied to One Wall. Joint Propulsion Conference. 2010.

Valentino, M., Slabaugh, C., Ricklick, M., Kapat, J.S. Heat Transfer and Friction Augmentation in a Narrow Rectangular Duct with Ribs Applied to One Wall. Florida Center for Advanced Aero-Propulsion (FCAAP) – Annual Technical Symposium 2010.

Valentino, M., Tran, L., Ricklick, M., Kapat, J.S. A Study of Heat Transfer Augmentation for Recuperative Heat Exchangers: Comparison between Two Dimple Geometries. Turbo Expo 2011.

Tran, L., Valentino, M., Saha, A., Ricklick, M., Slabaugh, C., Kapat, J.S., Basu, S. Detailed Flow Visualization in a Narrow Rectangular Channel with Dimples Applied to One Wall. Turbo Expo 2011.

Tran, L., Valentino, M., Ricklick, M., Kapat, J.S. Overall Thermal Performance of Transport Promoters in Internal Cooling Channels of Various Rotating Machineries. (Draft Submitted). IGTC 2011.

Valentino, M., Tran, L., Ricklick, M., Kapat, J.S. Comparison of Heat Transfer and Friction Augmentation for Symmetric and Non-Symmetric Wedge Turbulators on Two Opposite Wall. Joint Propulsion Conference 2011

Tran, L., Valentino, M., Ricklick, M., Kapat, J.S. Effect of Varying the Rib Width and Number of Ribbed Walls on Heat Transfer and Friction in High Aspect Ratio Channel. Joint Propulsion Conference 2011.

Presentations

Slabaugh, C., Valentino, M., Ricklick, M., Kapat, J.S. Heat Transfer and Friction Augmentation in a Narrow Rectangular Duct with Ribs Applied to One Wall. Joint Propulsion Conference. 2010.

Valentino, M., Slabaugh, C., Ricklick, M., Kapat, J.S. Heat Transfer and Friction Augmentation in a Narrow Rectangular Duct with Ribs Applied to One Wall. Florida Center for Advanced Aero-Propulsion (FCAAP) – Annual Technical Symposium 2010.

Valentino, M., Tran, L., Ricklick, M., Kapat, J.S. A Study of Heat Transfer Augmentation for Recuperative Heat Exchangers: Comparison between Two Dimple Geometries. Turbo Expo 2011.

In-Progress

Valentino, M., Tran, L., Ricklick, M., Kapat, J. A Study of Heat Transfer Augmentation for Recuperative Heat Exchangers: Comparison between Two Dimple Geometries. (Submitted). Journal of Engineering for Gas Turbines and Power.

REFERENCES

(n.d.). Retrieved 8 23, 2011, from GE Aviation: http://www.geae.com/genxrightnow/

Carman, B., Kapat, J., Chow, L., & An, L. (2002). Impact of a Ceramic Microchannel Heat Exchanger on a Micro Turbine. *Turbo Expo.* Amsterdam: ASME.

Chandra, P. R., Alexander, C. R., & Han, J. C. (2003). Heat Transfer and Friction Behaviors in Rectangular Channels with Varying numbers of Ribbed Walls. *International Journal of Heat and Mass Transfer, 46*, 481-495.

Chen, Y., Fiebig, M., & Mitra, N. (2000). Heat Transfer Enhancement of Finned Oval Tubes with Staggered Punched Longitudinal Vortex Generators. *International Journal of Heat and Mass Transfer, 43*, 417-435.

Cho, H. H., Lee, S. Y., & Wu, S. J. (2001). The Combined Effect of Rib Arrangements and Discrete Ribs on Local Heat/Mass Transfer in a Square Duct. *ASME 46th Annual International Gas Turbineand Aeorengine Congress and Exhibition*, (pp. 1-11). New Orleans, LA.

Chompookham, T., Thianpong, C., Kwankaomeng, S., & Promvonge, P. (2009). Heat Transfer Augmentation in a Wedge-Ribbed Channel Using Winglet Vortex Generators. *International Communications in Heat and Mass Transfer*, 163-169.

Chyu, M., Ding, H., Downs, J., & Soechting, F. (1998). Determination of Local Heat Transfer Coefficient Based on Bulk Mean Temperature Using a Transient Liquid Crystals Technique. *Experimental Thermal and Fluid Science*, 142-149.

European Petroleum Technology. (n.d.). Retrieved 8 23, 2011, from Siemens SGT-750: http://www.german-oilgas-expo.com/e-news-siemens-new-gasturbine-17112010.htm

Gas Turbine International, LLC. (n.d.). Retrieved 8 24, 2011, from GE LM2500 Twin Shank: http://www.itrademarket.com/GAS_TURBINE_INTL/1997346/ge-lm2500-twin-shank.htm

Han, J. (1984). Heat Transfer and Friction in Channels With Two Opposite Rib-Roughened Walls. *Journal of Heat Transfer*, 774-781.

Han, J. (1988). Heat Transfer and Friction Characteristics in Rectangular Channels With Rib Turbulators. *Journal of Heat Transfer*, 321-328.

Han, J. C., Huang, J. J., & Lee, C. P. (1993). Augmented Heat Transfer in Square Channels with Wedge-Shaped and Delta-Shaped Turbulence Promoters. *Enhanced Heat Transfer, 1*(1), 37-52.

Han, J., & Park, J. (1988). Developing Heat Transfer in Rectangular Channels with Rib Turbulators. *Int. J. Heat Mass Transfer, 31*(1), 183-195.

Han, J., Glicksman, L., & Rohsenow, W. (1978). An Investigation of Heat Transfer and Friction for Rib-Roughened Surfaces. *Int. J. Heat Mass Transfer*, 1143-1156.

Han, J., Huang, J., & Lee, C. (1993). Augmented Heat Transfer in Square Channels with Wedge-Shaped and Delta-Shaped Turbulence Promoters. *Enhanced Heat Transfer, 1*(1), 37-52.

Han, J., Park, J. S., & Lei, C. (1985). Heat Transfer Enhancement in Channels With Turbulence Promoters. *Journal of Engineering for Gas Turbines and Power, 107*(3), 628-635.

Han, J.-C., Dutta, S., & Ekkad, S. V. (2000). *Gas Turbine Heat Transfer and Cooling Technology.* New York, New York, United States of America: Taylor and Francis.

Henze, M., & von Wolfersdorf, J. (2011). Influence of Approach Flow Conditions on Heat Transfer Behind Vortex Generators. *International Journal of Heat and Mass Transfer, 54*, 279-287.

Henze, M., Dietz, C., Neumann, S., von Wolfersdorf, J., & Weigand, B. (2005). Heat Transfer Enhancement From Single Vortex Generators. *ASME Turbo Expo 2005: Power for Land, Sea and Air.* Reno-Tahoe: ASME.

Henze, M., Dietz, C., von Wolfersdorf, J., & Weigand, B. (2007). Heat Transfer Around Longitudinal and Parallel Arranged Wedge-Shaped Vortex Generators. *ASME Turbo Expo 2007: Power for Land, Sea and Air.* Montreal: ASME.

Henze, M., von Wolfersdorf, J., Dietz, C., & Neumann, S. (2010). Flow and Heat Transfer Characteristics Behind Vortex Generators- A Benchmark Dataset. *International Journal of Heat and Fluid Flow*.

Henze, M., von Wolfersdorf, J., Weigand, B., Dietz, C., & Neumann, S. (2010). Flow and Heat Transfer Characteristics Behind Vortex Generators - A Benchmark Dataset. *International Journal of Heat and Fluid Flow* .

Kline, S. J., & McClintock, F. A. (1953). *Mechanical Engineering, 75*, 3-8.

Ligrani, P. M., & Mahmood, G. I. (2003). Spatially Resolved Heat Transfer and Friction Factors in a Rectangular Channel With 45-Deg Angled Crossed-Rib Turbulators. *Journal of Turbomachinery*, 575-584.

Liou, T., Chen, C., & Tsai, T. (2000). Heat Transfer and Fluid Flow in a Square Duct With 12 Different Shaped Vortex Generators. *Journal of Heat Transfer*, 327-335.

Metzger, D. E., & Larson, D. E. (1986). Use of Melting Point Surface Coatings for Local Convection Heat Transfer Measurements in Rectangular Channel Flows with 90 degree Turns. *Journal of Heat Transfer, 108*, 48-54.

Pauly, W., & Eaton, J. (1988). Experimental Study of the Development of Longitudinal Vortex Pairs Embedded in a Turbulent Boundary Layer. *AIAA, 26*, 816-823.

PowerSmith Group. (n.d.). Retrieved 8 23, 2011, from PowerSmith ISCC: http://powersmithgroup.com/SolarGasTurbineHybrid.aspx

Promvonge, P., & Thianpong, C. (2008). Thermal Performance Assessment of Turbulent Channel Flows Over Different Shaped Ribs. *International Communications in Heat and Mass Transfer*, 1327-1334.

Saha, P., & Biswas, G. (2010). Numerical Simulation of Turbulent Flow in a Rectangular Channel With Periodically Mounted Longitudinal Vortex Generators. *14th International Heat Transfer Conference.* Washington, D.C.: ASME.

Solugas. (n.d.). Retrieved 8 23, 2011, from http://www.solugas.com/index/overview.html

Taslim, M. E., Li, T., & Spring, S. D. (1998). Measurements of Heat Transfer Coefficients and Friction Factors in Passages Rib-Roughened on All Walls. *Journal of Turbomachinery, 120*(3), 564-570.

Taslim, M., Li, T., & Kercher, D. (1996). Experimental Heat Transfer and Friction in Channels Roughened With Angled, V-Shaped, and Discrete Ribs on Two Opposite Walls. *Journal of Turbomachinery*, 20-28.

Thianpong, C., Chompookham, T., Skullong, S., & Promvonge, P. (2009). Thermal Characterization of Turbulent Flow in a Channel with Isosceles Triangular Ribs. *International Communications in Heat and Mass Transfer, 36*, 712-717.

Tiggelbeck, S., Mitra, N., & Fiebig, M. (1994). Comparison of Wing-Type Vortex Generators for Heat Transfer Enhancement in Channel Flows. *Journal of Heat Transfer, 116*, 880-885.

Tran, L., Valentino, M., Ricklick, M., & Kapat, J. (2011). Effect of Rib Aspect Ratio on Heat Transfer and Friction in Rectangular Channels. *Joint Propulsion Conference* . San Diego: AIAA.

Wright, L., & Gohardani, A. (2008). Effect of Turbulator Width and Spacing on the Thermal Performance of Angled Ribs in a Rectangular Channel (AR=3:1). *ASME International Mechanical Engineering Congress and Exposition.* Boston: ASME.